# Reconstruction of energy spectra for different mass groups of high-energy cosmic rays

Zur Erlangung des akademischen Grades eines

DOKTORS DER NATURWISSENSCHAFTEN

von der Fakultät für Physik des

Karlsruher Instituts für Technologie (KIT)

genehmigte

DISSERTATION

von

Dipl.-Phys. Marcel René Finger
aus Landau in der Pfalz

Tag der mündlichen Prüfung: 20. Mai 2011

Referent: Prof. Dr. Johannes Blümer,
Institut für Kernphysik und Institut für Experimentelle Kernphysik
Korreferent: Prof. Dr. Wim de Boer,
Institut für Experimentelle Kernphysik

## Zusammenfassung

Das KASCADE-Grande-Experiment auf dem Gelände des Campus Nord des Karlsruher Instituts für Technologie ist ein Multi-Detektor-Aufbau zur Messung von ausgedehnten Luftschauern, bestehend aus dem ursprünglichen KASCADE-Experiment und dessen Erweiterung Grande. Das Hauptziel des Experiments ist die Vermessung des Energiespektrums und die Bestimmung der Zusammensetzung der kosmischen Strahlung im Energiebereich von $10^{15}$ eV bis $10^{18}$ eV. Das Energiespektrum im Messbereich des KASCADE-Experiments weist bei $\approx 4 \times 10^{15}$ eV eine Indexänderung auf, welche als das „Knie“ im Spektrum der kosmischen Strahlung bezeichnet wird und zu deren Entstehung verschiedene Theorien existieren. Um diese Theorien bestätigen oder widerlegen zu können, ist nicht nur eine genaue Kenntnis des Gesamtenergiespektrums, sondern auch der Spektren einzelner Massengruppen (H, He, C, Si, Fe) notwendig. Ein Vergleich der Position des Knies im Gesamtspektrum mit den Kniepositionen von Wasserstoff und Helium zeigt, dass das Knie vor allem durch diese leichte Komponente verursacht wird. Unter der Annahme einer Massen- oder Ladungszahlabhängigkeit der Kniepositionen der Elemente erwartet man, ausgehend von Wasserstoff, eine erneute Indexänderung im Bereich von $10^{17}$ eV, welche im Messbereich des Grande-Detektorfeldes liegt und durch die schwere Komponente (Eisen) verursacht wird. Die Existenz des Eisenknies konnte bisher nicht bestätigt werden. Die Bestimmung der Energiespektren einzelner Massengruppen im Energiebereich um $10^{17}$ eV kann daher einen wichtigen Beitrag zur Erforschung des Eisenknies liefern.

In der vorliegenden Arbeit wird eine Entfaltungsanalyse vorgestellt, welche auf KASCADE- und KASCADE-Grande-Daten basiert und die zur Bestimmung der Spektren einzelner Massengruppen und des Gesamtspektrums dient. In der Analyse wird ein iteratives Verfahren (Gold-Algorithmus) verwendet. Basis der Analyse ist das gemessene zweidimensionale Schauergrößenspektrum der Elektronen- und Myonenzahlen. Die zur Entfaltung der Daten benötigten Antwortfunktionen werden aus Simulationen gewonnen.
Die Untersuchung der entfalteten Energiespektren basierend auf KASCADE-Daten zeigt, dass die rekonstruierten Einzelspektren stark vom verwendeten Wechselwirkungsmodell abhängen, die Gesamtspektren jedoch innerhalb der Unsicherheiten sehr gut miteinander übereinstimmen. Die mit verschiedenen Wechselwirkungsmodellen (QGSJET01, QGSJETII, EPOS1.99 und SIBYLL) bestimmten Gesamtspektren weisen alle eine Indexänderung (Knie) im Bereich um $4 \times 10^{15}$ eV auf. Die Position dieses Knies variiert jedoch etwas von Modell zu Modell. Zudem zeigen alle rekonstruierten Einzelspektren der leichten Elemente (H, He) knieähnliche Strukturen auf, welche mit einer Rigiditätsabhängigkeit der einzelnen Kniepositionen vereinbar sind. Durch die Erweiterung der Entfaltungsanalyse auf KASCADE-Grande-Daten kann die Existenz einer knieähnlichen Struktur im Verlauf des Spektrums der Eisengruppe bei etwa $9 \times 10^{16}$ eV bestätigt werden, wobei das Gesamtspektrum in diesem Bereich keine Indexänderung aufweist. Auch das Abknicken des Eisenspektrums ist mit einer Rigiditätsabhängigkeit vereinbar.

## Abstract

The KASCADE-Grande experiment located at the Karlsruher Institute of Technology (Campus North) is a multi detector system for the measurement of extensive air showers, consisting of the former KASCADE experiment and its extension Grande. Main goal of the experiment is the measurement of the energy spectrum and the composition of cosmic rays in the energy range from $10^{15}$ to $10^{18}$ eV. The energy spectrum exhibits in the measurement range of KASCADE at $\approx 4 \times 10^{15}$ eV a change of slope, which is referred to as the "knee" in the energy spectrum of cosmic rays. Its origin is still unknown, but there exist several theories which try to explain this structure. To confirm or falsify some scenarios a precise knowledge of the energy spectra of individual elemental groups and of the all-particle spectrum is indispensable. The data measured by the KASCADE experiment allows the reconstruction of the energy spectra of individual mass groups (H, He, C, Si, Fe). A comparison of the knee position of the all-particle spectrum with the knee position of the hydrogen and helium reveals that the knee in the all-particle spectrum originates from the kink of these spectra of the light elements. Assuming an dependence of the knee positions of the individual elements on the mass number or on the valence, another kink in the energy spectrum is expected at an energy of some $10^{17}$ eV, which is caused by the heavy component and therefore referred to as the iron knee. Up to now the existence of the iron knee was not confirmed and for this reason the determination of the spectra of the individual mass groups in the region around $10^{17}$ eV can contribute to investigating the iron knee.

The present work deals with the deconvolution of KASCADE and KASCADE-Grande data, which allows the reconstruction of the all-particle energy spectrum and the determination of the energy spectra of individual mass groups. In the analysis an iterative deconvolution procedure is applied (Gold algorithm), based upon the measured two-dimensional shower size spectrum of electron and muon numbers. By means of simulations the response functions, which are necessary for the deconvolution analysis, are determined. The analysis comprises the results of the KASCADE deconvolution analysis on the basis of different interaction models (QGSJET01, QGSJETII, EPOS1.99 and SIBYLL) as well as the results of the KASCADE-Grande deconvolution analysis on the basis of QGSJETII.
The examination of the KASCADE unfolding results derived by the use of different hadronic high energy interaction models indeed reveals a strong dependency of the individual energy spectra on the hadronic high-energy interaction model used, but the reconstructed all-particle fluxes agree well within the uncertainties. The all-particle spectra, originating from different interaction models, exhibit a knee (change of index) around $4 \times 10^{15}$ eV, slightly varying from one model to the other. Additionally all results show knee-like features in the energy spectra of the light primaries (H and He) and suggest a rigidity dependence of the knee positions of the individual elements. An extension of the unfolding analysis to KASCADE-Grande data confirms the existence of a knee-like structure in the iron spectrum, but the all-particle energy spectrum does not exhibit such a feature. The kink in the iron spectrum is as well compatible with a rigidity dependence.

# Contents

# Chapter 1

# Introduction

With the discovery of cosmic rays in 1912 Victor Franz Hess opened the field of astroparticle physics, which combines astrophysics with particle physics. The phenomenon of cosmic rays plays a decisive role in particle physics, since the cosmic ray particles can reach energies, which can not be reached by man-made particle accelerators. Thus new particles, like for example the positron, the muon and the $\pi$ meson, were detected in the cosmic radiation. But after almost one century of investigating cosmic rays, the most essential questions of cosmic ray physics are still not solved. For example the sources of cosmic rays as well as the acceleration and propagation mechanisms are still relevant topics in current research.
The energy spectrum of cosmic rays spans a large range in both the energy and the flux. The course of the energy spectrum of cosmic rays can be described by an inverse power law ($dN/dE \propto E^{\gamma}$), with only a few remarkable changes of the index $\gamma$. The change of slope at an energy of $\approx 4 \times 10^{15}\,\mathrm{eV}$, which is called the "knee" in the energy spectrum of cosmic rays, is among the most prominent structures of the energy spectrum. The knee is supposed to be caused by the steepening of the spectra of the light elements, especially by hydrogen and helium. Although several theories exist, trying to explain the knee, its true origin is still unknown.
At an energy around $10^{17}\,\mathrm{eV}$ another kink in the energy spectrum is expected, originating from the steepening of the heavy component and therefore being referred to as the iron knee. Until now there is no consensus on its existence.
Due to the steep spectrum ($\gamma \approx -3$) the flux of cosmic rays decreases rapidly with increasing energy. This leads to the necessity of instrumenting large ground-based detector arrays for the measurement of extensive air showers, being induced by cosmic ray primaries such as for example hydrogen and iron.
The KASCADE-Grande experiment investigates extensive air showers in the energy range from $10^{15}$ to $10^{18}\,\mathrm{eV}$ and thus covers the region of the knee and the possible iron knee. The detailed knowledge of the all-particle energy spectrum in combination with the reconstructed energy spectra of the individual mass groups allows the exclusion or the verification of existing theories about the knee. Thus, the reconstruction of energy spectra can grant experimental access to the most frequently discussed questions, such as the question on the origin and the acceleration and propagation mechanisms.

In the present thesis the all-particle energy spectrum as well as the energy spectra of individual mass groups, i. e. the composition, are determined by means of deconvolution. Basis of the analysis is the two-dimensional shower size spectrum of electron and muon numbers measured by the KASCADE array and the Grande array. The data, collected by the KASCADE experiment, allows the reconstruction of the energy spectra between $10^{15}$ and $10^{17}\,\mathrm{eV}$, the

region of the knee. The Grande extension, exceeding the energy range of KASCADE by one order of magnitude, is designed to investigate the energy spectrum around the iron knee and measures from $10^{16}$ to $10^{18}$ eV.

# Chapter 2

# Cosmic rays and extensive air showers

The Earth's atmosphere is continuously hit by cosmic ray particles with a rate of about 1000 per square meter per second. Almost all of these particles are ionized nuclei (98 %) and only a small fraction are electrons (2 %). Up to energies of several TeV the cosmic ray flux is sufficiently high for direct measurements of the elemental distribution and the energy spectrum of cosmic rays by balloon and satellite experiments. At higher energies due to the power law spectrum the flux becomes so small that indirect measurements of so-called extensive air showers (see Section 2.5) with large ground based detectors become necessary. The phenomenon of extensive air showers was discovered in 1938 by Pierre Auger via coincidence measurements at the Jungfraujoch in the Bernese Alps. Measuring extensive air showers is up to now the only possibility of observing cosmic rays at the highest energies with sufficient statistics.

## 2.1 The energy spectrum

The energy spectrum of cosmic rays spans a large range in energy as well as in flux and can be described by a broken power law $dN/dE \propto E^{\gamma}$, with several changes of the spectral index $\gamma$. Figure 2.1 shows the differential energy spectrum of cosmic rays multiplied by $E^{2.5}$ for a better illustration of structures. At an energy of $\approx 4 \times 10^{15}$ eV the spectral index $\gamma$ changes from $\gamma \approx -2.7$ to $\gamma \approx -3.1$. This steepening of the slope is known as the 'knee' in the energy spectrum of cosmic rays. In [Ant05] it was shown that the knee is caused by the light elements, especially by hydrogen and helium. The origin of the knee is still unknown, but a lot of models exist which try to explain it. Several models are discussed in Section 2.4.1.
At an energy of some $10^{17}$ eV the spectrum is supposed to steepen again to an index $\gamma \approx -3.3$, which is called the second knee [Ber07]. Evidence for a second knee was shown for example by the High Resolution Fly's Eye (HiRes) [Bir93, Bir94], the HiRes/MIA hybrid experiment [Abu01], Akeno [Nag92] and Haverah Park [Law91, Ave03].
Another feature established in literature is the so called ankle at $\approx 3 \times 10^{18}$ eV, where the cosmic ray spectrum flattens again. The ankle is supposed to mark the transition from galactic to extragalactic cosmic rays. Above the ankle the radius of gyration $r_g$ of a proton exceeds the thickness of the galactic disc and therefore galactic cosmic rays escape out off and extragalactic cosmic rays get into the Galaxy.
The GZK (Greisen-Zatsepin-Kuz'min) cutoff [Gre66, Zat66] at an energy of $\approx 5 \times 10^{19}$ eV describes an upper limit on the energy of cosmic rays from faraway sources and is at present one of the most discussed questions. The reason for this sharp cutoff are interactions of

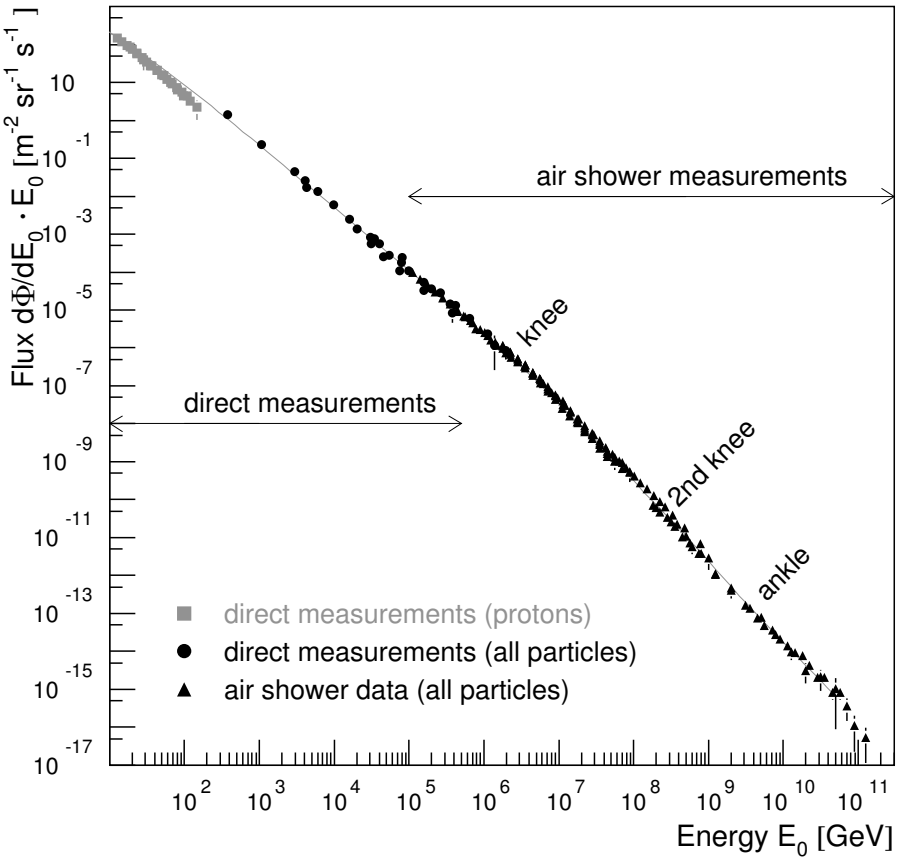


Figure 2.1: Energy spectrum of cosmic rays multiplied by $E_0$ (taken from [Blu09]).

protons with the cosmic microwave background during their propagation from the source to Earth. The first observation of such a cutoff was achieved by the HiRes [Ave08] collaboration and a limit similar to the GZK cutoff was later reported by the Auger experiment [Abr08].

## 2.2 The composition of cosmic rays

All elements from the periodic table are present in galactic cosmic rays. About 87% are protons, 12% are alpha particles and only 1% are heavier nuclei. Up to energies of some TeV the relative abundances of cosmic rays can be studied well with satellite and balloon experiments. In figure 2.2 the relative abundances of cosmic ray nuclei with a valence up to $Z = 32$ are compared to the relative abundances in the solar system. In general both distributions agree well, which suggests the same origin, namely stellar nucleosynthesis. But there are also some characteristic deviations. The elements Li, Be, B below carbon and the elements Sc, Ti, V, Cr below iron are more abundant in cosmic rays than in the solar system. This effect can be explained by spallation processes of the more common elements C, N, O and Fe while propagating through the Galaxy. Fragments arising from such interactions are known as secondary cosmic rays. The number of secondaries together with the knowledge of the cross sections of this processes allow the calculation of the amount of matter the cosmic rays have travelled through. With this information an estimation of the mean residence time of cosmic rays in the Galaxy is possible [Gai90]. A more precise method for obtaining the length of stay of cosmic rays within the Galaxy

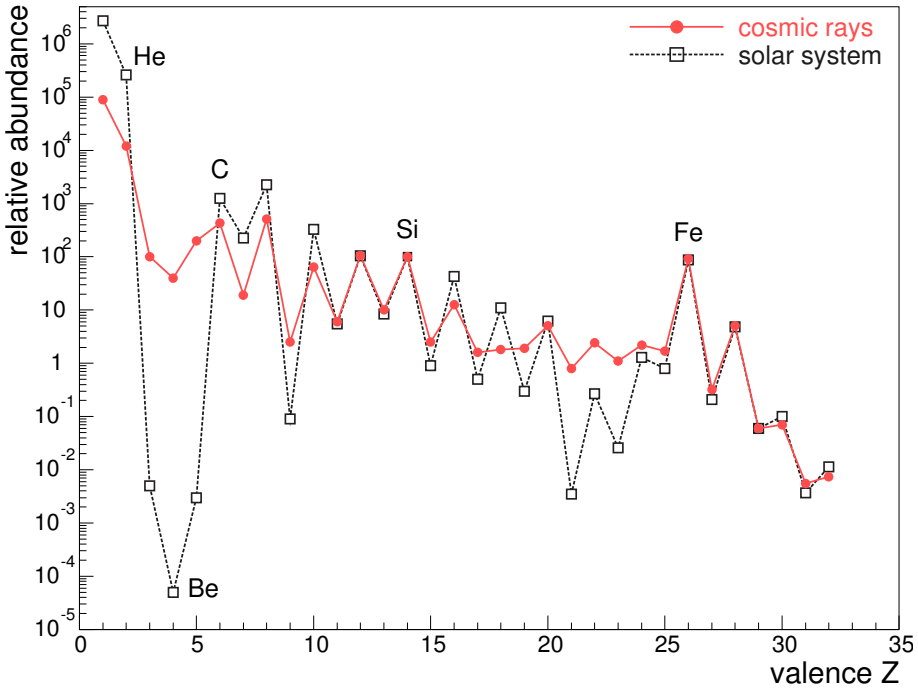


Figure 2.2: Relative abundances (normalised to Si=100) of galactic cosmic rays with a valence up to $Z = 32$ compared to the solar system [Mül03].

is the use of the ratio of radioactive isotopes, for example the measurement of the $Be^9/Be^{10}$ ratio suggest a time of approximately $10^6$ a [Gai90].
Another crucial point is the difference in the relative abundances of H and He. These two elements are less abundant in cosmic rays compared to the solar system. On the one hand these differences can be explained by the high ionization energy of these two elements and connected to this by the more difficult acceleration. On the other hand the disagreement of the relative abundances of hydrogen and helium can also be interpreted by a different composition at the source.
The composition of cosmic rays changes with energy. These alterations in the composition of cosmic rays are of great interest, because they can give hints on the sources, the propagation and the acceleration mechanisms. Above several TeV only the all-particle spectrum but not the composition is known in detail. In this energy region the direct determination of the composition of cosmic rays is very difficult, because direct measurements are hardly possible due to the steep spectrum. Besides hydrogen and helium the elements nitrogen, oxygen, neon, magnesium, silicon and iron are the most abundant elements in cosmic rays. Using KASCADE array data or Grande array data, respectively, deconvolution techniques offer one possibility to obtain the energy spectra of different mass groups.

## 2.3 Sources, acceleration and propagation of cosmic rays

### Sources and acceleration of cosmic rays

The questions about the sources and the acceleration mechanisms of cosmic rays are still among the foremost questions in astroparticle physics and are closely related to each other. Cosmic rays cover a large range in energy and their spectrum can be described by a power law, which indicates a non-thermal origin. In 1949 Enrico Fermi proposed a mechanism for the acceleration

of cosmic rays, which is known as second order Fermi acceleration. The particles gain energy in head-on collisions with randomly distributed plasma clouds in the interstellar medium and those particles involved in tail-end collisions loose energy. On average head-on collisions are more probable. The energy gain of the original Fermi mechanism is of second order $\Delta E \propto \beta^2 E$ with $\beta = \frac{v_s}{c}$ and $v_s$ is the velocity of the shock. For that reason this mechanism is slow and inefficient and only plays a minor role in cosmic ray acceleration.
But this theory led to today's picture of an acceleration at strong shock waves propagating at supersonic, but non-relativistic speed through the interstellar medium. Particles crossing from the shocked to the unshocked region and back gain energy. Since head-on collisions are more likely, a particle that passes the shock front repeatedly gains energy very fast. This mechanism, referred to as first order Fermi acceleration, is more efficient ($\Delta E \propto \beta E$) for the acceleration of cosmic rays and naturally leads to a power law spectrum $E^\gamma$ with index $\gamma \approx -2$, which is, in contrast to second order Fermi acceleration, not dependent on local details of the environment. The measured spectrum with an index $\gamma \approx -3$ is steeper than the predicted one. This change of index can be explained by energy losses of the particles while travelling through the interstellar medium, so it is an effect of propagation. Particles accelerated at shock fronts reach their maximum energy $E_{max} \propto Ze\frac{v_s}{c}BTv_s$, where $Ze$ is the charge of the particle, $v_s$ the velocity of the shock, $B$ the magnetic field and T the time the particle stays in the acceleration region. Most of the cosmic ray particles are supposed to be accelerated in blast waves of supernova remnants. Only a small fraction of $\approx 10\%$ of the kinetic energy of the supernova explosion is transferred to cosmic rays. Protons accelerated in supernova remnants are supposed to reach under realistic conditions energies up to 100 TeV [Gai90].
The sources and also the acceleration mechanisms that are able to accelerate particles up to the highest energies are still under discussion. Due to the enormous energy range of cosmic rays different sources seem to be imaginable. With shock wave acceleration higher energies can be reached, if higher magnetic fields and longer acceleration times are assumed. Candidates are pulsars, young supernovae, binary stars and galactic winds [Gai90]. Acceleration in jets of active galactic nuclei (AGN) or the acceleration in polar caps of fast rotating neutron stars [Che86] are other possible scenarios to accelerate particles to the highest energies.
In [Sig03] an overview of the so-called 'top-down' models can be found. In these 'top-down' scenarios cosmic rays with the highest energies are produced in decay or annihilation processes of super massive particles or cosmological relics, e.g. topological defects, magnetic monopoles or wimpzillas. The majority of the 'top-down' models can be excluded by present measurements of the Pierre Auger Collaboration, especially the scenarios based on the decay of super massive particles as all the models predict a high photon flux at the highest energies, which is not observed [Abr08a] .

### Propagation of cosmic rays

Another interesting question in cosmic ray physics is the propagation of cosmic rays. With the ratio of spallation products such as Be, B to their primary nuclei C,N the matter traversed by cosmic rays in the GeV region can be estimated to $5 - 10\,\mathrm{gcm}^{-2}$. If the matter along a line through the galaxy is summed up, you come to only $10^{-3}\,\mathrm{gcm}^{-2}$ which leads to the assumption that cosmic rays stay within the galaxy for a very long time. The matter traversed by cosmic rays decreases with increasing energy, what let us assume that the particles were first accelerated and then propagate through the interstellar medium. After being accelerated the cosmic ray particles propagate in a diffusive process through our galaxy being deflected by randomly distributed magnetic fields. The development of the particle density with energy and position can be described by a transport equation, which is in general solved by simplified

models. The most simple model is the so called 'leaky box model', that describes the free propagation in a containment volume with a time independent probability for escaping [Sha70]. In the 'nested leaky box model' [Cow73] and the 'closed galaxy model' [Ran95] near the sources there are confinement regions with relatively high density, where particles diffuse for a short energy dependent time. More realistic models than the 'leaky box' models do not treat the diffusion operator as a constant [Gin80]. For many purposes both theories come to similar results.

## 2.4 The knee and the iron knee

### 2.4.1 Models of the knee

Since its discovery in 1958 by Kulikov and Khristiansen [Kul58] from observations of the size spectrum of extensive air showers, the knee was subject of many investigations. The propagation and the acceleration mechanisms of cosmic rays are still unknown and therefore the knee is of great interest and still object of research. Various theories exist that try to explain the origin of this kink in the spectrum. In [Hör04] a survey of such models can be found. They can be divided into four groups. Three groups explain the knee by astrophysical reasons, describing the knee as an intrinsic characteristic of the energy spectrum, whereas the fourth category assumes the knee to be caused by indirect measurements via extensive air showers. In the last group of theories the knee does not exist in the primary energy spectrum.

Models of the first group are based upon acceleration mechanisms and the maximum energy that can be reached by these processes. Common to the models of the first group is the dependence of the knee positions of the individual elements on the valence Z ($E_Z^{knee} \propto Z \cdot E_{prot}^{knee}$).
The model after Berezhko and Ksenofonotov [Ber99] deals with the acceleration in supernova remnants.
Stanev et al. [Sta93] propose a model where the particles are accelerated at three different main sites. The blast waves driven by normal supernovae explosions accelerate protons to $10^{14}$ eV. Explosions of stars into their former stellar wind are able to accelerate protons to approximately $9 \times 10^{16}$ eV and iron nuclei to approximately $3 \times 10^{18}$ eV. The particles with energies exceeding $10^{17}$ eV come from extragalactic sources.
Kobayakawa et al. [Kob02] describe a slightly modified version of the standard diffusive acceleration of particles in supernova remnants with shocks, which are in general perpendicular to the magnetic field lines. This theory is extended for magnetic field lines oriented arbitrarily to the velocity of the shock and the particles are therefore accelerated to higher energies.
The model by Sveshnikova [Sve03] is based upon the standard acceleration model and the latest data on supernovae explosions. In this theory the energy spectrum is the sum over all different types of supernovae explosions.
In the single source model after Erlykin and Wolfendale [Erl01] the knee is assumed to be caused by a single nearby supernova remnant, whose spectrum is superimposed to the background of many sources. The knee in the all-particle spectrum is a two-kink structure, which is due to the cut off of oxygen and iron nuclei from this single source.
Another possible explanation for the knee is the model by Völk and Zirakashvili [Völ03], which discusses the reacceleration of cosmic rays in the galactic wind. The knee in the all-particle spectrum cannot be explained by propagation processes, but is a feature of the source spectrum itself.
Plaga discusses a mechanism to accelerate cosmic ray hadrons in the baryonic plasma, ejected

in bipolar supernova explosions, which is referred to as 'cannonballs' [Pla02]. The original cannonball model was proposed by Dar and De Rújula [Dar00] to explain the phenomenon of gamma ray bursts. Two possible scenarios are presented. The first describes the acceleration of cosmic rays up to energies of the knee via ultra-relativistic shocks driven by cannonballs. The second scenario is based upon second order Fermi acceleration inside the turbulent plasma. With this mechanism energies up to $Z \times 10^{20}$ eV can be reached.

Models of the second category explain the origin of the knee by propagation processes of cosmic rays through the interstellar medium.
The basis of the minimum pathlength model by Swordy [Swo95] is the 'Leaky Box model'. The pathlength $\lambda_e$ for escaping from the Galaxy is described by a rigidity dependent decrease, which has a minimum value. The obtained spectra are characterised by a smooth change of slope and a dip below the knees of the individual spectra.
Lagutin et al. [Lag01] relate the origin of the knee to anomalous diffusion of cosmic rays in the magnetic field of the Galaxy, assuming an inhomogeneous interstellar medium. The diffusion coefficient depends on the rigidity of the particles. Like in the model discussed before the change of slope is very soft.
The next three attempts to explain the origin of the knee adopt similar approaches, taking into account the regular and the irregular galactic magnetic fields, and antisymmetric diffusion.
In Ptuskin et al. [Ptu93] it is shown that the knee can be traced back to Hall diffusion of the particles in the global regular magnetic field of the Galaxy. The effect of the Hall diffusion in the GeV energy range has a negligible effect on the leakage of cosmic rays from the Galaxy, but at approximately 3 PeV it becomes dominant, what results in the knee. Ogio and Kakimoto discuss in [Ogi03] the diffusion in turbulent galactic magnetic fields. The regular and the irregular components are assumed to have the same field strength. Not only the regular magnetic field in the Galaxy, but also the irregularities of roughly the same strength are taken into account. Above $10^6$ GeV the heavy component (iron) dominates the all-particle energy spectrum. The spectra derived using this diffusion model show a smooth knee structure.
The model after Roulet et al. [Rou03] deals with diffusion of cosmic rays in the regular and irregular component of the galactic magnetic field. For energies below the knee ($E < Z \times E_K$) perpendicular diffusion dominates, while at higher energies hall diffusion is the dominant mechanism for escaping. At an energy of $E \approx Z \times E_K$ both diffusion coefficients (Hall diffusion and perpendicular diffusion) are comparable.

The models depicted in the third category consider interactions of cosmic rays with various background particles in the Galaxy to be the origin of the knee.
Tkaczyk [Tka01] describes the knee to be caused by a combination of photo-disintegration and diffusion. The energy loss of cosmic ray particles can be described by three processes, which are pair production, pion photo-production and photo-disintegration of nuclei. The steepening of the all-particle spectrum can be explained by photo-disintegration and by leakage from the Galaxy. In this model protons dominate the all-particle spectrum above $10^8$ GeV.
Candia et al. [Can02] see photo-disintegration of cosmic ray nuclei by optical and UV photons in the source region to be the cause of the knee. For the energy loss of cosmic ray particles below an energy of $10^{18}$ eV mainly photo-disintegration is responsible. The energy at which photo-disintegration becomes efficient is dependent on the mass number A ($E_0 \geq A \times 10^{15}$ eV).
In Dova et al. [Dov01] the knee is caused by a mechanism similar to the GZK-cut-off. The interaction of cosmic rays with massive background neutrinos in the galactic halo ($\mathrm{p}+\nu \rightarrow \nu+\Delta$ and $\Delta \rightarrow \mathrm{p}+\pi$) is accountable for the steepening in the energy spectrum.

Adopting a completely different approach the theories of the fourth group try to explain the knee structure by new physics in the atmosphere. The knee is not present in the primary energy spectrum, but is an effect of indirect measurements, so called extensive air shower measurements (see Section 2.5). Energy is transferred to one component of the shower that cannot or not yet be detected. As described by Kazanas and Nicolaidis possible candidates for carrying away the lacking energy are the lightest supersymmetric particles [Kan01] or gravitons [Kan01a]. The knee is therefore a threshold effect.

Although most of the models discussed in this chapter predict similar all-particle spectra, the energy spectra of individual elements vary considerably. Some show a smooth change of spectral index, others are characterized by a sharp cut-off. According to indirect measurements via extensive air showers the change of index at the knee seems to be sharp. For excluding or verifying theories a precise knowledge of the spectra of the individual elements is indispensable. Currently the experimental results cannot approve an exact conclusion about the origin of the knee, but astrophysical reasons are preferred.

### 2.4.2 From the knee to the iron knee

With the KASCADE experiment (see Chapter 3.1), measuring in the energy region of the knee, it was for the first time possible to determine the energy spectra of individual mass groups [Ant05]. As mass groups H, He, C, Si and Fe were chosen. The knee in the all-particle energy spectrum was found at an energy of $\approx 4 \times 10^{15}$ eV. The graphs in Figure 2.3 display two examples of unfolded energy spectra, obtained on basis of different hadronic high-energy interaction models (QGSJET01/GHEISHA on the left and SIBYLL2.1/GHEISHA on the right). As shown in the depiction, the origin of the knee in the all-particle energy spectrum is linked to the steepening of the light component, mainly to hydrogen and helium. Since it is unknown which combination of hadronic interaction models describes the shower development and the resulting distributions best, the exact courses of the energy spectra and the abundances of the individual elements can not be definitely determined. In order to make more general statements on the abundances, on the knee positions and on the models of the knee, the analysis of further interaction models is indispensable.
Taking into account only the astrophysical models, an iron knee is assumed to exist at an energy of $E_{Fe} \approx 26 \times 4 \times 10^{15}$ eV adopting a dependence on the valence or at an energy of

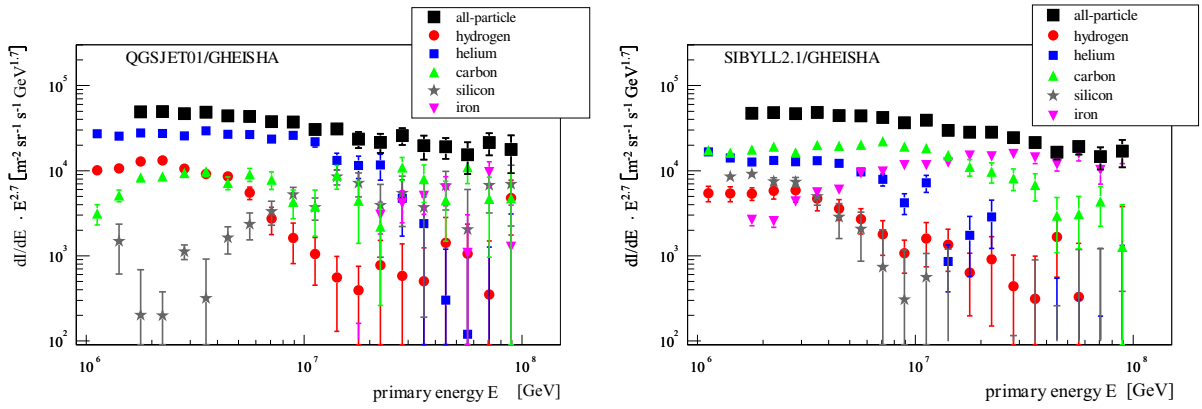


Figure 2.3: Energy spectra for H, He and C using QGSJET01/GHEISHA (left) and SIBYLL2.1/GHEISHA (right).

$E_{Fe} \approx 56 \times 4 \times 10^{15}$ eV for a dependence on the mass number. Until now there is no evidence for the existence of an iron knee in the energy spectrum and it is still not clarified if the iron knee is equivalent to the second knee. The KASCADE-Grande experiment (see Chapter 3), consisting of the former KASCADE experiment and the extension to Grande, is able to reconstruct air showers with an energy from $10^{14}$ up to $10^{18}$ eV and covers the energy region of the first and the second knee.
Measurements in this energy range are of greatest interest, because they are supposed to give information about the propagation and acceleration mechanisms and are subject of this thesis.

## 2.5 Extensive air showers

The cosmic ray flux below an energy of $10^{14}$ eV is sufficiently high for direct measurements with balloons or satellites, but at higher energies due to the steep spectrum and therefore the low flux at high energies, indirect measurements via extensive air showers become necessary. This measurement technique allows the operation of large ground based detectors for collecting sufficient statistics at that high energies.
Interacting with the air molecules of the Earth's atmosphere, mainly nitrogen and oxygen, a cosmic ray primary particle (ionized nucleus) induces a cascade of particles, a so-called extensive air shower. In the interactions with the primary particle mainly $\pi$ mesons, with an equal amount in all charged states, but also strange particles for example K- and $\Lambda-$ mesons and particle-antiparticle pairs like $p-\bar{p}$ and $n-\bar{n}$ are produced. These secondaries can either undergo further interactions or decay, depending on the traversed amount of matter as well as the lifetime of the particles. Apart from hadrons also electrons, photons, muons and neutrinos are produced by decay.
The atmospheric depth in which the first interaction occurs is dependent on the interaction length of the primary particles in air and is at fixed energies liable to strong fluctuations, which also lead to fluctuations in the shower sizes. For protons at an energy of $10^{15}$ eV the interaction length is about $65\,\mathrm{gcm}^{-2}$, whereas for iron nuclei it is $16\,\mathrm{gcm}^{-2}$.
The average number of particles produced in such cascades scales with the energy. The particles, travelling with nearly speed of light, reach ground in a curved shower disc with only a few meters of thickness (see left part of Figure 2.4). The lateral spread of an extensive air shower is affected by Coulomb scattering, by deflection in the Earth's magnetic field and by the transverse momentum, originating from interactions and decays. Being dependent on the energy of the particle, the lateral spread of an air shower can extend several 100 meters.
The particles produced in an extensive air shower can be classified into three components, the hadronic, the muonic, and the electromagnetic component (see right part of Figure 2.4). At sea level the bulk of particles in an air shower, about 90%, arise from the electromagnetic component, the muonic component accounts for 9% and only 1% of the particles are hadrons. In the following paragraphs these three components are shortly introduced.

### 2.5.1 The hadronic component

The hadronic component forms the core of an extensive air shower and is generally accountable for the energy transport during the shower development. The muonic and the electromagnetic component are induced by the hadronic component via decay processes, and are therefore affected directly by fluctuations in the development of the hadronic component. Due to the small transverse momentum transferred in hadronic interactions the hadrons can mainly be found in a distance of 10 m to 20 m to the shower axis. Only low energetic hadrons, in general neutrons, can travel longer distances away from the shower axis.

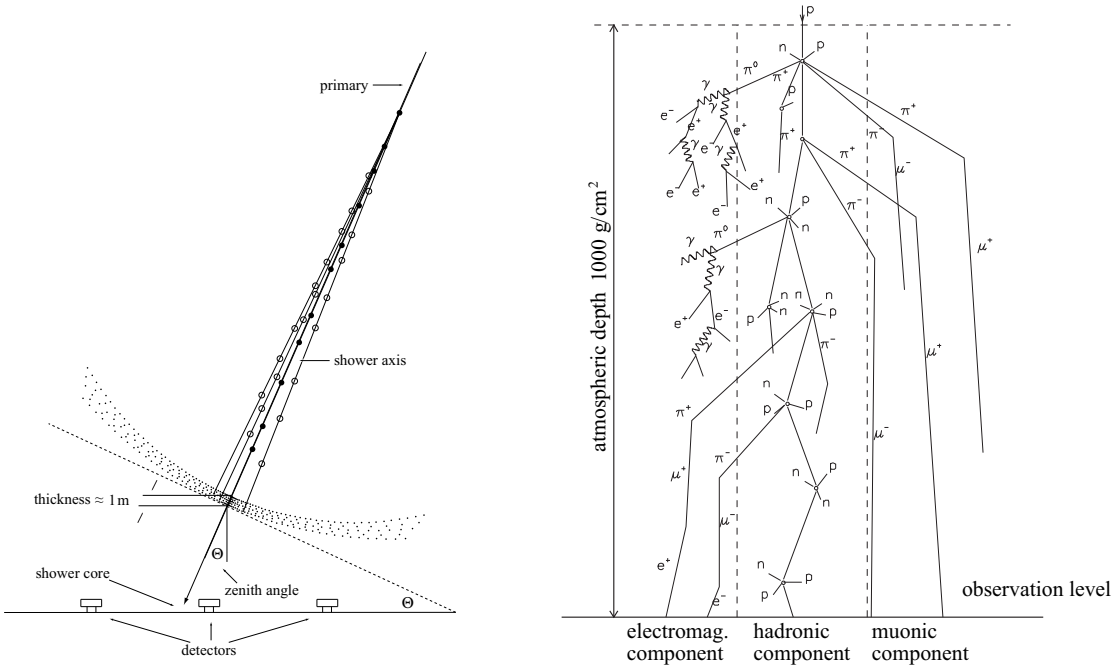


Figure 2.4: Schematic representation of an extensive air shower. On the left an illustration of the curved shower front can be seen, on the right the shower development with its three components is depicted.

### 2.5.2 The muonic component

The mesons produced in hadronic processes, mostly pions, decay via weak interaction with a lifetime of $\tau \approx 2.55 \times 10^{-8}$ s into muons and neutrinos according to

$$\pi^{\pm} \rightarrow \mu^{\pm} + \nu_{\mu}(\bar{\nu}_{\mu}). \tag{2.1}$$

At the beginning of the shower development the number of muons increases slowly, because most of the hadrons of the first generation are undergoing further hadronic interactions (instead of decaying). This can be explained by the large Lorentz factors of the hadrons, which lead to a suppression of decay. K-mesons produce muons in analogous decay processes, whereas their contribution to the production of muons is dependent on energy and converges for high energies asymptotically towards 27% [Gai90].
The majority of muons produced during the shower development reaches the observation level, what is due to the small cross sections and the long lifetimes of relativistic muons. Only a few low energetic muons decay the following way

$$\mu^{\pm} \rightarrow e^{\pm} + \nu_{e}(\bar{\nu}_{e}) + \bar{\nu}_{\mu}(\nu_{\mu}) \tag{2.2}$$

and therefore account for the electromagnetic component. Originating from decays of mesons the muons are produced close to the shower axis. Because of the higher mass of muons in comparison to electrons, Coulomb scattering and bremsstrahlung are suppressed by a factor of $(m_e/m_{\mu})^2 \approx 10^{-5}$. The trajectories of muons remain therefore hardly unchanged, and their production height can be easily determined using simple geometry. Hence muons allow to draw conclusions on the early stage of the air shower development.
Having the largest lateral spread of the three components, even muons of a 1 PeV shower can be detected at distances exceeding 1 km.

### 2.5.3 The electromagnetic component

The electromagnetic component predominantly arises from the decay of the neutral pion $\pi^0$ in two photons. In presence of a nucleus $X$ these photons produce $e^+ - e^-$ pairs according to

$$\gamma + X \rightarrow e^+ + e^- + X. \tag{2.3}$$

The conversion length of photons $\lambda_{ph}$ in air, which is about 48 gcm$^{-2}$ is mainly affected by $e^+ - e^-$ pair creation, whereas the contribution of $\mu^+ - \mu^-$ pair production is negligible. In the vicinity of a nucleus electrons and positrons create via bremsstrahlung

$$e^{\pm} + X \rightarrow e^{\pm} + \gamma + X \tag{2.4}$$

further photons, which for their part again produce $e^+ - e^-$ pairs. Due to the small radiation length $X_0$ in air of $\approx 37$gcm$^{-2}$ and the low critical energy of $\approx 84$ MeV the number of electrons increases very fast, coming up to its maximum when the bulk of electrons/positrons has reached the critical energy. Below the critical energy the particles loose energy in general by ionisation processes, leading to an exponential decrease after having reached the shower maximum.
The number of electrons in a $\gamma$ induced air shower is approximately given by

$$N_e(E_0, t) = \frac{0.31}{\sqrt{\beta}} \cdot e^{t(1-1.5\ \ln s)} \tag{2.5}$$

$$\text{with } t = \frac{X}{X_0},\ \beta_0 = \ln \frac{E_0}{E_{krit}} \text{ und } s = \frac{3t}{t + 2\beta_0}, \tag{2.6}$$

with $X$ being the atmospheric depth and $E_0$ displaying the initial energy of the photon [Gre66]. The parameter $s$ characterises the stage of development of the shower, whereas at an age of $s = 0$ the first electromagnetic particle is produced, at $s = 1$ the maximum number of particles is achieved and at $s = 2$ less than one particle is present.
The lateral distribution of electrons (see Section 2.5.5) can be described in an analytical way by the NKG function [Kam57, Gre66]

$$\rho_e(r) = \frac{\Gamma(4.5 - s)}{\Gamma(s)\Gamma(4.5 - s)} \frac{N_e}{2\pi r^2} \left(\frac{r}{r_m}\right)^{s-2} \left(1 + \frac{r}{r_m}\right)^{s-4.5}. \tag{2.7}$$

$\rho_e$ represents the lateral particle density of the electrons, $r$ is the distance to the showers core and $N_e$ is the number of electrons at the observation level. The Moliere unit $r_m$, which is affected by multiple scattering, characterises the lateral spread of an electromagnetic air shower.

### 2.5.4 The longitudinal distribution

One possibility of observing extensive air showers is the measurement of the longitudinal distribution as it is done for example by the fluorescence telescopes of the Auger experiment. The number of particles as a function of the atmospheric depth is referred to as longitudinal distribution. Figure 2.5 shows the average longitudinal profile of electrons and muons for 50 proton and iron induced air showers at an energy of 1 PeV (qualitatively not very different for varying energies). Air showers induced by different primary particle types develop in different ways. Iron induced air showers reach their maximum earlier than proton induced air showers due to the higher cross section. The amount of traversed matter between the initial interaction of the primary particle and the shower maximum is almost independent of the primary particle type, but dependent on the initial energy $E_0$.
In the shower maximum proton and iron induced air showers have nearly the same number of

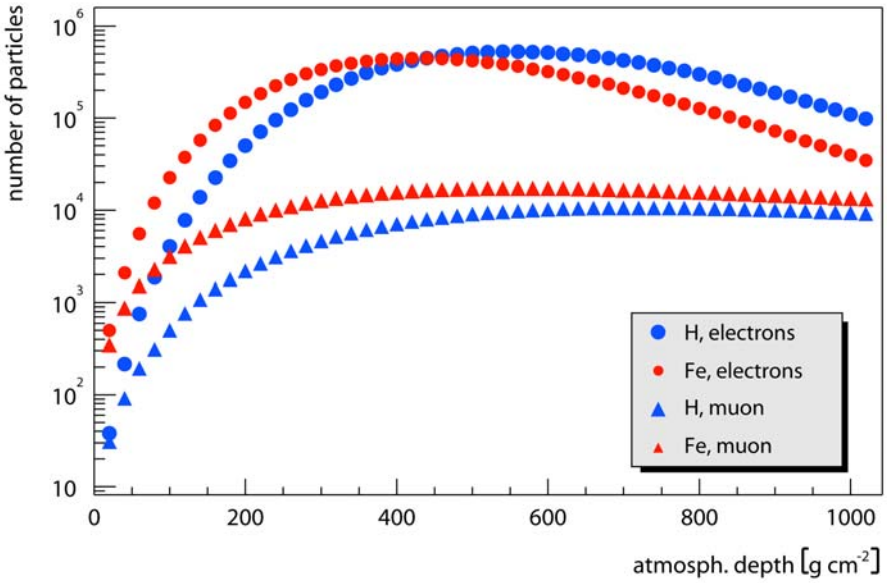


Figure 2.5: Average longitudinal distribution of electrons and muons for 50 proton and iron induced air showers with an energy of 1 PeV at vertical incidence.

electrons, which also holds for the total number of charged particles, since the bulk of particles produced in an air shower are electrons. After having reached the maximum a fast decrease in the electromagnetic component can be observed. The total number of particles allows to draw a conclusion on the energy of the primary particle and the atmospheric depth of the maximum gives a hint on the identity of the primary particle.
For both primary particle types the number of muons $N_\mu$ increases more slowly than the number of electrons $N_e$. In contrast to the electron number the number of muons remains more or less constant after the maximum. This leads to smaller fluctuations in the muon number compared to those fluctuations in the number of electrons and hadrons. For that reason the number of muons in an air shower can be used as an estimator for the primary energy.
The correlation of both, the number of electrons and the number of muons, is a crucial parameter to identify the primary particle.

### 2.5.5 The lateral distribution

The observation of the lateral distribution is another possibility to measure extensive air showers. The particle densities as a function of the distance to the shower core are known as lateral distribution. Figure 2.6 displays the average lateral distributions of electrons and muons for 50 proton and iron initiated air showers at an energy of 1 PeV (qualitatively not very different for varying energies).
Air showers induced by iron nuclei hold at observation level less electrons compared to proton initiated showers with the same energy. Having a closer view it becomes obvious that the lateral distributions for different primary particle types show different curvatures. For example at a distance of 20 m to the shower core the electron densities differ by a factor of 5, whereas the densities at a distance of 200 m differ only by a factor of 2.
On the contrary for muons near the shower core differences are hardly found, but with increasing

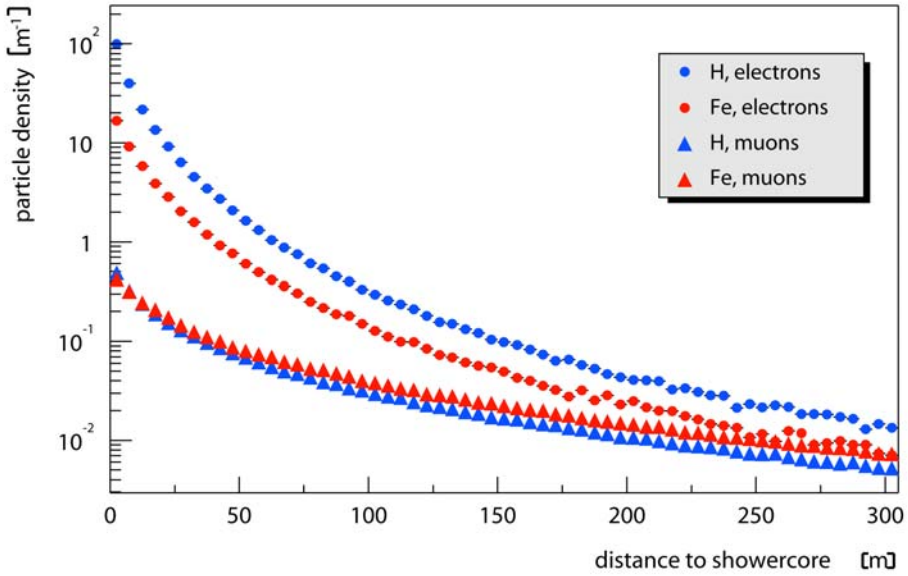


Figure 2.6: Average lateral distribution of electrons and muons for 50 proton and iron induced air showers with an energy of 1 PeV at vertical incidence.

distance to the shower core the lateral distributions of different primary particle types vary. Due to the larger cross section an iron initiated air shower develops in higher altitude. Muons are barely affected by interactions (Coulomb scattering, bremsstrahlung) on their way through the atmosphere. Muons that are produced at lower atmospheric depths can travel longer distances away from the shower core and therefore the lateral distribution of muons for iron induced air showers is flatter compared to the one of proton initiated showers.

# Chapter 3

# The KASCADE-Grande experiment

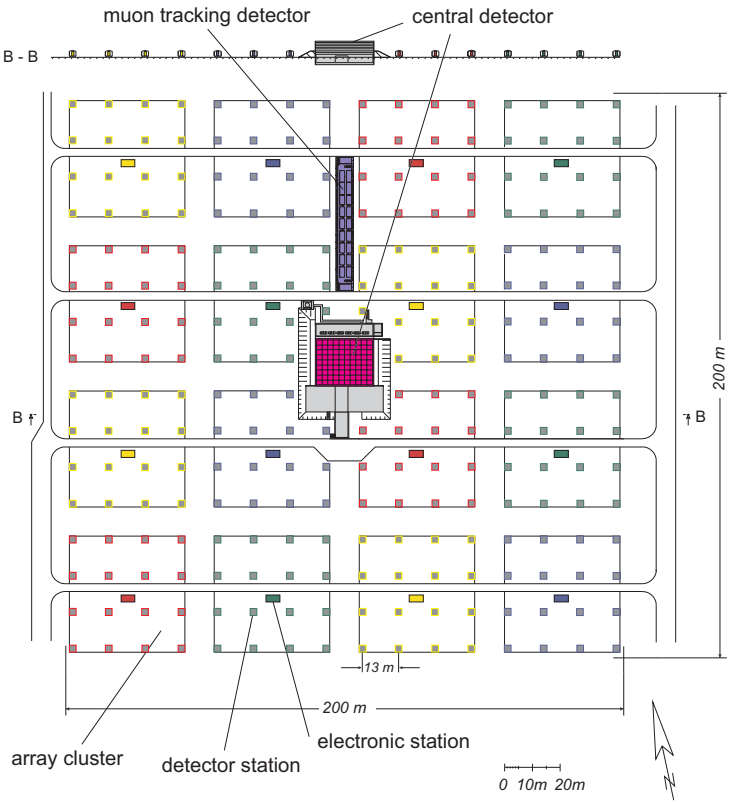


Figure 3.1: Layout of the KASCADE experiment.

The KASCADE-Grande experiment, located on the Campus North of the Karlruhe Institute of Technology (KIT), is a multi-detector facility consisting of the original KASCADE experiment (KArlsruhe Shower Core and Array DEtector) and the Grande array. The energy range of KASCADE from $10^{14}$ to $10^{17}$ eV was extended by Grande up to $10^{18}$ eV. Being composed of several detector types the KASCADE-Grande experiment offers the possibility of observing the three different components of extensive air showers simultaneously. Main goals of the experiment are the measurement of the energy spectrum and the determination of the composition of cosmic rays in the energy range of the first and the second knee (see Chapter 2.4.1). The measurement of different quantities also provides the opportunity of testing several hadronic low and high energy interaction models and can therefore contribute to the improvement of these models. In

the following sections the KASCADE experiment [Ant03] and the Grande array [Ape10] will be introduced.

## 3.1 KASCADE

### 3.1.1 The KASCADE array

The KASCADE array consists of 252 detector stations, arranged on a quadratic grid with 13 m spacing, on an area of $200 \times 200\,\mathrm{m}^2$. The detector stations are electronically organized in 16 clusters of 16 stations each, aside from the four inner clusters, containing only 15 stations (see figure 3.1). Each cluster is able to take data independently. Data is collected in the electronic station of each cluster and then transmitted to the main building. Each detector station is equipped with four e/$\gamma$ detectors [Völ92] for the measurement of the electromagnetic component and four detectors for the observation of the muonic component [Kri92]. A schematic view of one detector station can be found in Figure 3.2. The e/$\gamma$ detectors are installed above a lead/iron absorber (10 cm Pb and 4 cm Fe), corresponding to $20X_0$. For electrons the energy threshold, arising from the materials used, is about 5 MeV. Below the iron/lead absorber, which stops the electromagnetic component, the muon detectors are mounted. For vertical muons the absorbers result in a threshold of 230 MeV. The twelve outer clusters contain only 2 e/$\gamma$ detectors per station. The four inner clusters are not equipped with muon detectors, because of punch-through effects of the electromagnetic component close to the shower core.

Above an circular aluminium tub with 1m diameter, filled up to an height of 5 cm with liquid scintillator, a light collection cone is mounted. The liquid scintillator consists of 2 g/l PMP (1-phenyl-3-mesityl-2-pyrazoline) in 80% paraffine and 20% pseudocumene. On top of the cone a light collector of lucite and above that a 3" photomultiplier is installed. The cone is filled with argon to prevent the liquid scintillator from oxidation. A wide dynamic range can be achieved by picking up the signal from the anode and one of the dynodes, what allows to detect up to 2000 minimum ionizing particles (m.i.p.). At 12 MeV, which is the mean energy deposit of a m.i.p., the energy resolution is about 8%. The time resolution of the detector is 0.77 ns.

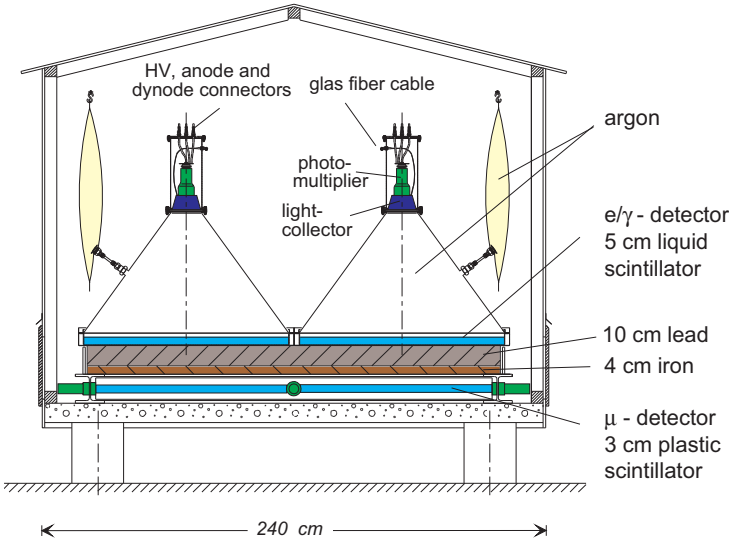


Figure 3.2: Sketch of a KASCADE array detector station.

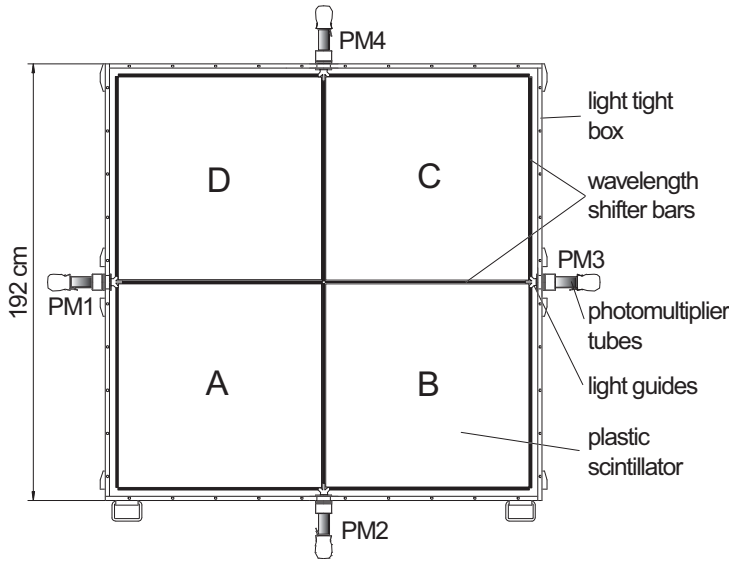


Figure 3.3: Sketch of a KASCADE muon detector.

In Figure 3.3 the layout of the muon detectors is shown. The muon detectors consist of four plastic scintillators of the type Bicron BD-416 ($90 \times 90\,\mathrm{cm}^2$) with a thickness of 3 cm. Wavelength shifter bars are applied on all four sides and the light is transferred by lucite light guides to four 1.5" photomultipliers. At 8 MeV the energy resolution of the detector is approximately 10% and the time resolution is determined to 2.9 ns.

When a multiplicity condition in one of the clusters is fulfilled, a trigger is created and the data acquisition for all clusters and the other detector components is started. With a multiplicity condition of $n_i = 20$ out of 60 e/$\gamma$ detectors for the inner clusters and $n_i = 10$ out of 32 e/$\gamma$ detectors for the outer clusters the trigger rate for the array is about 3 events per second [Sch96].

### 3.1.2 The central detector

In the centre of the KASCADE array the central detector with an area of $16 \times 20\,m^2$ can be found (see figure 3.1). Main component of the central detector is the hadron sampling calorimeter [Eng99]. For the observation of the hadronic component 8 tiers of iron absorber and 9 layers of warm-liquid scintillator are installed. The calorimeter consists of in total 11000 liquid ionization chambers, filled with tetramethylsilane (TMS) or tetramethylpentane (TMP). The thickness of the absorbers corresponds to 11.5 nuclear interaction lengths.

The first layer of liquid ionisation chambers above the absorber is the so-called top layer, with full surface coverage, for the observation of electromagnetic cores and mainly small showers. Above the top layer the top cluster with 25 scintillation counters is installed. With a coverage of 7.5% the top layer serves as a trigger source for small, e.g. proton induced, air showers.

Below the third layer of absorbers a layer of scintillation detectors, the so-called trigger layer, is mounted. This layer serves as a trigger for the ionisation chambers, as well as for the muon detectors in the basement and is also used for the reconstruction of the arrival time distributions. The thickness of the absorbers above, resulting in an energy threshold for

vertical muons of 490 MeV, corresponds to 30 $X_0$ and shields the trigger layer against the electromagnetic component.

In the basement of the central detector two layers of multi-wire proportional chambers, for the measurement of the positions and the angles of energetic muons, are installed. The chambers are filled with $Ar/CH_4$ as counting gas. The precision for the position determination is 1.1 cm. The distance between the two layers of 38 cm translates to an angular resolution of 1.5°. For the reduction of ambiguities at higher densities a layer of limited streamer tubes has been installed below the multi-wire proportional chambers.

### 3.1.3 The muon tracking detector

The muon tracking detector [Dol02], in the North of the central detector, is designed for the measurement of muon tracks. The tracking detector consists of 3 layers of limited streamer tubes with a spacing between the horizontal planes of 82 cm and a total length of 48 m. The effective detection area for vertical particles is 128 $m^2$. As counting gas a mixture of 20% argon, 60% isobutane, and 20% $CO_2$ is used. This configuration allows to reconstruct the muon track, and therefore the determination of the production height of the muons by means of triangulation. The shielding (concrete, iron, and soil) above corresponds to 18 $X_0$ in vertical direction and an energy threshold of 0.8 GeV.

## 3.2 Grande

### 3.2.1 The Grande array

The Grande array consists of 37 detector stations on a triangular grid with an average distance of 137m to each other. The detector threshold is 3 MeV for charged particles. The instrumented area is approximately $700 \times 700\,m^2$ (see Figure 3.4). Each detector station has an effective area

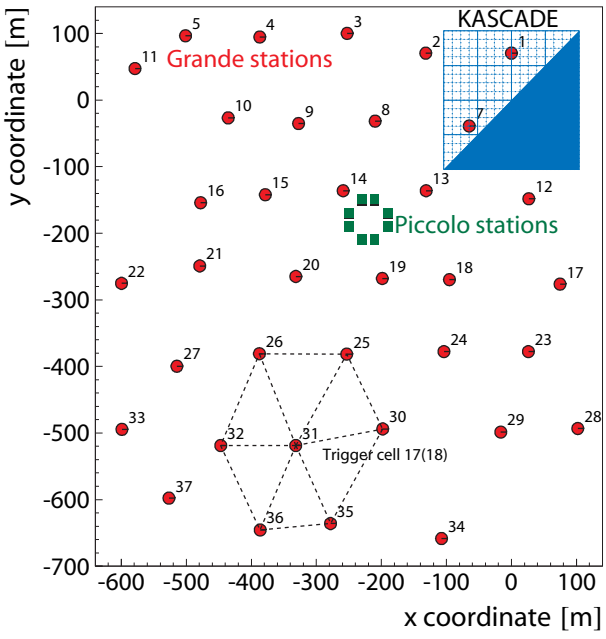


Figure 3.4: Sketch of the Grande array.

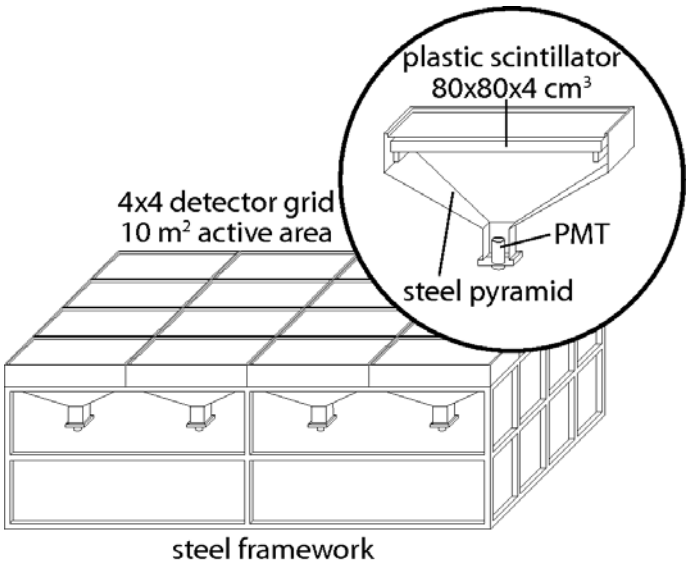


Figure 3.5: Sketch of a Grande detector station.

of $10\,\mathrm{m}^2$ and consists of 16 panels ($80 \times 80 \times 4\,\mathrm{cm}^3$) of plastic scintillator (NE102A) mounted on a steel framework. A schematic view of a station can be found in Figure 3.5. Below the plastic scintillators, on a $4 \times 4$ detector grid, 16 light collecting pyramids with 16 high gain (1.6 pC/m.i.p.) photomultipliers (Philips XP3462) are installed for the detection of low particle densities. The four central units are additionally equipped with low gain (0.08 pC/m.i.p.) photomultipliers for the measurement of high particle densities. The signals of the photomultipliers are already added up by 2 passive mixers (CAEN 169), one for the signals from the 16 high gain PMTs, the other for the signals from the four low gain PMTs. The module for the high gain PMTs has two outputs. One output is passed on a double threshold discriminator for trigger and time measurement purposes, with a threshold of -12 mV for timing and -24 mV for triggering. The other output is transmitted together with the output of the mixer for the low gain PMTs to a shaping amplifier (CAEN N442), which produces output signals proportional to the total charge. The three outputs of the shaping amplifier correspond to three different amplification factors, two for the signal from the high gain PMTs and one for the signal from the low gain PMTs, resulting in a large dynamic range. For the high gain PMTs the amplification factors are $A_{\mathrm{HG}} = 2.5\,\mathrm{mV/pC}$ and $A_{\mathrm{HG}\times 10} = 25\,\mathrm{mV/pC}$ and for the low gain PMTs $A_{\mathrm{LG}} = 5\,\mathrm{mV/pC}$. The Grande stations are organized in 18 overlapping trigger hexagons, consisting of 7 stations, with one central station. The data acquisition can be triggered by either a 4/7 coincidence (3 outer stations and the central station) or a 7/7 coincidence. The former configuration leads to a trigger rate of $\approx 5\,\mathrm{Hz}$, the latter, being used as trigger for KASCADE, to a rate of about 0.5 Hz. The whole experiment can also be triggered by an external trigger provided by the KASCADE central trigger (Chapter 3.1), resulting in a trigger rate of $\approx 3.5\,\mathrm{Hz}$.
The Grande DAQ (**D**ata **A**c**Q**uisition) station is located in the center of the Grande array. All detector stations are connected to the DAQ station via 5 cables with a length of 700 m for the signal, two cables for high voltage and two optical fibers [Ape10].

### 3.2.2 The Piccolo array

The enlarged array of Grande with the KASCADE array in the northeastern corner leads to events with large distances to the former KASCADE array. For these distant events the trigger

signal generated by Grande is too late to start the data acquisition of the muon devices at the central detector and the muon tracking detector of KASCADE. The Piccolo array, consisting of 8 stations with 10 $m^2$ of plastic scintillator placed on a octagon with a distance of 20 m of each other, is designed to solve these problems. Piccolo provides a fast external trigger to KASCADE. The trigger condition for Piccolo is 2 out of 8 stations. The threshold of the detector is 3 MeV for charged particles.

## 3.3 The reconstruction of observables

The KASCADE array and the Grande array are in principle two stand-alone experiments. The detectors of the KASCADE array, being equipped with electron and muon detectors, allow the reconstruction of electron and muon numbers of extensive air showers. Since the Grande detectors, not having any shielding, can only measure the energy deposits of all charged particles in the scintillators, without having any further information, it is only possible to reconstruct the number of the charged particles. But the additional information, coming from the muon detectors of the KASCADE array, allows also the separation of electrons and muons for showers measured with KASCADE-Grande. The reconstruction algorithms are explained in the following sections. Relevant shower parameters, like for example the number of electrons and muons, the arrival direction of the air shower (azimuth and zenith angle) and the core position are reconstructed using KRETA (**K**ASCADE **R**econstruction for **E**x**T**ensive **A**irshowers), a code especially developed for KASCADE. In this work solely data from the KASCADE array and the combined measurement of the KASCADE and the Grande array are used.

### 3.3.1 KASCADE

The reconstruction of air shower properties for showers measured with KASCADE is an iterative process, being subdivided into three levels.

#### 3.3.1.1 Level 1

In a first step the shower core is determined via a neural network [May92] and the shower direction by means of a gradient method, using the arrival times of the first particles in the detector stations [May93]. With an empirical sum formula a first approximation of the electron and the muon number is possible. The parameters obtained in this first step serve as starting values for the next reconstruction level.

#### 3.3.1.2 Level 2

In the second step of the procedure the measured energy deposits are corrected with so-called LECFs (Lateral Energy Correction Functions) [Web99] and converted into particle densities. In the $e/\gamma$ detectors and the $\mu$ detectors respectively, not only electrons and muons, but also other particles are registered. To account for the contributions of other particles and to convert the measured energy deposits into particle densities, LECFs, obtained by Monte Carlo simulations, are used. They describe the energy deposits of different particles in the detector as a function of the distance to the shower core. For KASCADE four different LECFs exist, two for the energy deposits of the muons in the $e/\gamma$ detectors and in the $\mu$ detectors respectively, two others for the energy deposits of electrons, gammas and hadrons in both detector types.
As a next step the reconstruction of the shower direction is improved. The adopted method [Kra96, Mai03] compares the measured arrival times relative to the shower core with the medians

of the arrival time distributions, which were parameterised as a function of the number of particles registered in one station and as a function of the distance to the shower core in shower coordinates. Via a $\chi^2$ minimisation the shower direction, which transforms best the measured arrival times into the shower plane, is obtained.
With the improved information on the shower direction and the particle densities the lateral distribution is determined using a modified NKG function [Ant06]. The modified NKG function given by

$$\rho_{e,\mu}(r) = C(s) \cdot N_{e,\mu} \left( \frac{r}{r_m^{e,\mu}} \right)^{s-\alpha} \left( 1 + \frac{r}{r_m^{e,\mu}} \right)^{s-\beta} \tag{3.1}$$

with

$$C(s) = \frac{\Gamma(\beta - s)}{2\pi r_m^2 \Gamma(s - \alpha + 2)\Gamma(\alpha + \beta - 2s)}$$

is adopted to determine simultaneously the shower core, the electron number $N_e$, and the age parameter $s$ of the electron lateral distribution. In case of the lateral distribution only the muon number $N_\mu$ is a free parameter. For muons the age parameter $s$ is defined by a parameterisation as a function of the electron number. The Molière radii $r_m$ as well as $\alpha$ and $\beta$ for both, electrons and muons, are determined by means of Monte Carlo simulations ($r_m = 89$ m for electrons and $r_m = 420$ m for muons).

#### 3.3.1.3 Level 3

In the last step of the procedure the energy deposits are calculated again, using the LECFs and the improved information on the shower core and the shower direction from Level 2. With these newly gained particle densities the shower reconstruction is performed again. Afterwards the NKG functions are adapted to the lateral distributions of electrons and muons. The electron number is determined taking into account the number of muons from Level 2, to correct for the contributions of muons in the $e/\gamma$ detectors, whereas the number of muons is obtained like in Level 2.

Instead of the muon number $N_\mu$ the truncated muon number $N_\mu^{tr.}$ is used, i. e. only muons in the range from 40 - 200 m with respect to the shower core are taken into account. Whereas the lower limit is defined by the 'punch-through effect' of the electrons near the shower core, the upper limit is given by the dimension of the array.

### 3.3.2 KASCADE-Grande

The energy deposit in a Grande detector station is dominated by charged leptons, more precisely by electrons and muons. Not only these charged leptons, but also converted gammas and hadrons contribute to the energy deposits. To account for these effects a LECF, describing the energy deposit per charged lepton as a function of the core distance, is used. The left part of Fig. 3.6 displays such an LECF, describing the average energy loss per charged particle in the Grande detectors as a function of the core distance (see [Ape10]). Above 450 m the LECF takes a constant value, corresponding to the mean energy deposit of a vertical incident muon. The depicted function is obtained by CORSIKA simulations (Chapter 3.4) and a detailed detector simulation based on GEANT [GEA93]. The dependence of the LECF on the primary particle mass, the energy and the inclination is negligible. The Grande detectors can only measure the total amount of charged particles. For a determination of the number of electrons and muons the muon detectors of the KASCADE array are used. The LECF for muons, displayed in the right part of Fig.3.6, is obtained averaging over simulated proton and iron induced air showers with energies

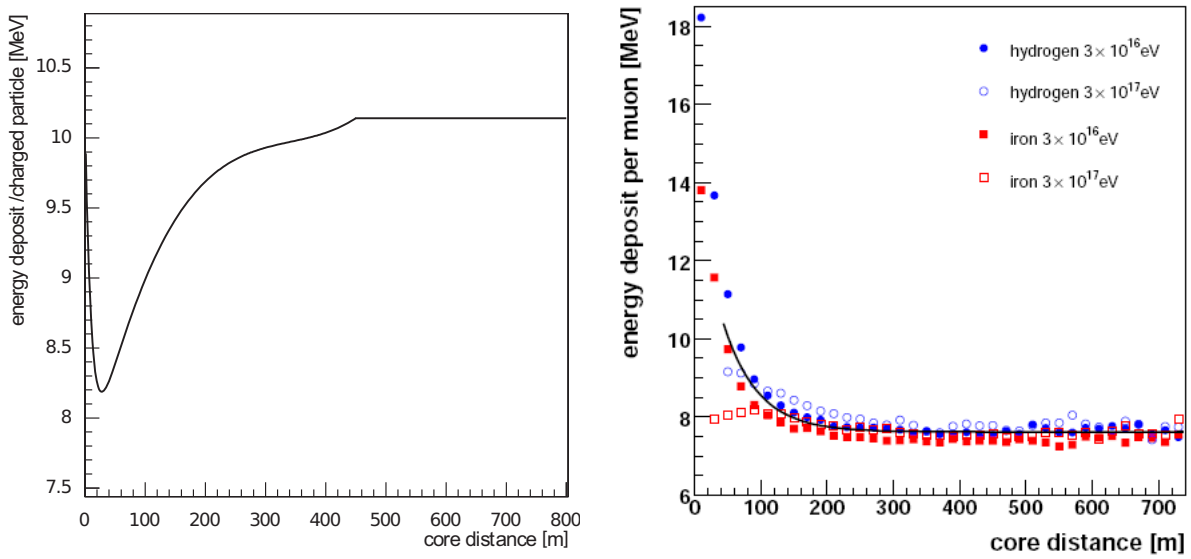


Figure 3.6: Left: LECF describing the average energy loss per charged particle in the Grande detectors subject to the distance to the core. The LECF is valid for all energies and inclinations [Ape10]. Right: LECFs of muons for iron and proton initiated air showers with different energies at a zenith angle of 22° [Van06].

of 30, 100, and 300 PeV at an inclination of 22°. For small core distances and high energies the energy deposit per muon is smaller due to the punch-through of the electromagnetic component.

The reconstruction of air shower observables with KRETA is again arranged in three levels.

**Level 1**

In the first level the arrival direction and the core position of the extensive air shower are roughly estimated. The shower core is determined by a center of gravity method, using the coordinates of the station weighted with the energy deposits. If this method fails, the coordinates of the Grande station with the highest energy deposits are taken as shower core.
In the first method for reconstructing the arrival direction the shower front is assumed to be planar with the estimated shower direction being perpendicular to the plane, characterized by the arrival times of the three detectors with the highest energy deposits. The second procedure implemented in KRETA is based upon a $\chi^2$ minimization and is only applicable if the shower core is known. The arrival times, measured by the Grande stations, are weighted with the locally observed particle densities. By means of simulations, assuming primary protons with an energy of $10^{17}$eV at an zenith angle of 22°, a theoretical shower front and its time spread is derived. With the differences of the measured arrival times and the one obtained by simulations a $\chi^2$ minimization is performed.
For a first estimate of the total amount of charged particles and muons and all further calculations a transformation in shower disc coordinates is performed. The z-axis of the new coordinate system is represented by the shower axis and perpendicular to the plane spanned by the new x- and y-axis.
After having corrected for the contribution of hadrons and photons, and having converted the

energy deposits into particle densities, as described in the first part of this chapter, a first estimation of the total number of charged particles and muons is possible. The sum of particles, either charged particles (electrons + muons) or only muons, measured in n detector stations can be written as

$$\sum_{i=1}^{n} n_{p_i} = \sum_{i=1}^{n} N_x \cdot f_i(r) \cdot A \text{ ($x$ represents charged particles or muons)} \tag{3.2}$$

with $n_{x_i}$ being the number of particles measured in a detector station, $N_x$ the total number of particles, and A the effective area. $f_i(r)$ represents the discretized values of the LDF of the particles normalized to 1. Equation 3.2 can be solved for the number of particles $N_x$

$$N_x = \frac{\sum\limits_{i=1}^{n} n_{p_i}}{\sum\limits_{i=1}^{n} \cdot f_i(r) \cdot A}. \tag{3.3}$$

For the determination of the number of charged particles, the function $f(r)$ is given by

$$f(r) = C \cdot \left(\frac{r}{r_0}\right)^{p_1} \cdot \left(\frac{r}{r_0}\right)^{2p_2} \cdot \left(\frac{r}{r_0}\right)^{3p_3}, \tag{3.4}$$

where $r_0 = 90\,\text{m}$ is the scaling radius for charged leptons, $p_1 = -2.462$, $p_2 = -4.16$, and $p_3 = 0.098$. These parameters were obtained by simulation studies of proton and iron induced air showers. For a first estimation of the total amount of muons a modified Lagutin function [Lag01] given by

$$f(r) = \left(\frac{0.28}{r_0^2}\right) \cdot \left(\frac{r}{r_0}\right)^{-0.69} \cdot \left(\frac{r}{r_0}\right)^{-2.39} \cdot \left(1 + \left(\frac{r}{10 \cdot r_0}\right)^2\right)^{-1}, \tag{3.5}$$

with scaling radius $r_0 = 320\,\text{m}$ and $N_\mu \cdot f(r)$, is used.
The results obtained in level 1 serve as starting values for further calculations.

**Level 2**

In the second level the observables like the number of charged particles $N_{ch}$, the core position, and the slope of the lateral distribution function s are determined using a modified NKG function

$$\rho_{ch}(r) = \frac{\Gamma(\beta - s)}{\Gamma(s - \alpha + 2)\Gamma(\alpha + \beta - 2s - 2)} \frac{N_{ch}}{2\pi r_0^2} \left(\frac{r}{r_m}\right)^{s-\alpha} \left(1 + \frac{r}{r_m}\right)^{s-\beta}, \tag{3.6}$$

with $\alpha = 1.6$, $\beta = 3.4$ and $r_0 = 30\,\text{m}$. The determination of the shower observables is an iterative process:

- Determination of the core position via a $7 \times 7$ detector grid with a 8 m spacing is used. The LDFs are fitted, taking into consideration all 49 ($7 \times 7$) possible core positions, and the core position minimising $\chi^2$ is kept. Free parameters are the shower age s and $N_{ch}$.
- The obtained core position is then used in the time fit for the reconstruction of the arrival times, already explained in Section 3.3.2

- With fixed core position and arrival direction the LDF is fitted again leaving number of charged $N_{ch}$ and the shower age $s$ as free parameters.
- The LDF fit is performed again with free core coordinates $x_c$ and $y_c$
- For the determination of the final results of $N_{ch}$, the arrival direction and the shower age $s$, the iteration steps 3 and 4 are repeated with fixed core coordinates.

In a last step in level 2 the muon number is determined, fitting the particle densities measured in the muon detectors of the KASCADE array with a modified Lagutin function, described by

$$\rho(r) = N_\mu \cdot \left(\frac{0.28}{r_0^2}\right) \cdot \left(\frac{r}{r_0}\right)^{-0.69} \cdot \left(\frac{r}{r_0}\right)^{-2.39} \cdot \left(1 + \left(\frac{r}{10 \cdot r_0}\right)^2\right)^{-1}. \tag{3.7}$$

The fitting procedure is performed with fixed core coordinates and arrival direction.

**Level 3**

In level 3 the electron number is obtained on basis of a NKG function. The particle density $\rho_{ch}(r) = \rho_e(r) + \rho_\mu(r)$ is fitted with the sum of a Lagutin function, whose parameters where determined in level 2 , and a NKG function. The result of this procedure is the number of electrons. The number of muons $N_\mu$ is taken from level 2.

## 3.4 Shower simulations with CORSIKA

Ground based detector systems, such as KASCADE-Grande, just take random samples of the shower disc, due to the spacing of the detector stations.
Measures like the energy deposits in the detectors or the arrival times allow the reconstruction of important air shower observables, such as the number of particles produced in an air shower and the direction of the primary particle(zenith and azimuth angle). Since the main goal of KASCADE-Grande is the determination of the energy spectrum and the composition of cosmic rays, it is essential to derive information on the energy and the identity of the primary particle from the reconstructed air shower observables. For the determination of the relations between these different quantities so called Monte Carlo methods are indispensable. CORSIKA (**CO**smic **R**ay **SI**mulation for **KA**scade) [Hec98], an air shower simulation tool, was originally designed to model the development of air showers for the KASCADE experiment, but is meanwhile used worldwide by most experiments for the interpretation of air shower data.
The shower development in the Earth's atmosphere is a statistical process, which consists of several subprocesses and is liable to strong fluctuations. Although the description of various subprocesses in general works well, the superposition of these processes can not be described in an analytical way. The different steps in the shower development are treated independently, choosing possible results via random numbers. The most important parts of air shower simulations are the production of secondary particles in collisions with nuclei, the determination of the travelled distance until the next interaction, and the transport of particles, taking into account continuous energy loss, and the deflection due to scattering or the Earth's magnetic field. The particles are tracked through the atmosphere until they undergo further interactions or decay. In particle decays all branches down to a 1% ratio are taken into account.

Being well understood up to the highest energies, electromagnetic interactions can be described and simulated precisely. By default electromagnetic interactions are treated with a

modified version of the EGS4 code (**E**lectron **G**amma **S**hower system version **4**) [Nel85] adapted to air shower simulations, which gives detailed information on all electromagnetic particles.
The development of extensive air showers is strongly constrained on hadronic interactions, i. e. on interactions of mesons, baryons, and nuclei with the molecules of the air. Hadronic interactions can be studied with collider experiments. The maximum energy attainable by cosmic accelerators exceeds the one of colliders on Earth by several orders of magnitude, and therefore an extrapolation of hadronic interactions to higher energies based on theoretical models is necessary . Another problem is that in collider experiments the particles in extreme forward direction are not registered and vanish undetected. But just these particles with low transverse momentum are of greatest interest for air shower development.
To get an idea about the uncertainties arising from these two problems several hadronic low and high energy interaction models are implemented in CORSIKA.
The majority of hadronic high energy interaction models, such as DPMJET [Ran95], neXus [Dre99], QGSJet [Kal93], and VENUS [Wer93], are based upon the Gribov-Regge-Theory, which describes the interaction at high energies via Pomeron exchange. In DPMJET, neXus, and QGSJet additionally hard processes, which correspond to the jets observed in collider experiments, are taken into consideration. The absence of this jet mechanism in the VENUS model is compensated by increased Pomeron exchange. These four interaction models treat the Gribov-Regge approach in a different way, so that the results for different models partly show large deviations. The interaction program SIBYLL [Fle94] is based upon the minijet model. Each projectile nucleus interacts with the nuclei of the air molecules independently and is described by the superposition principle.
The HDPM model [Cap89] is a phenomenological program, extrapolating experimental result in the low energy region to higher energies, what leads to large uncertainties if the reachable collider energies are exceeded.
Newly developed models are QGSJetII [Ost06] and EPOS [Wer08].
EPOS is a multiple scattering approach based on partons and Pomerons (parton ladders) and is the successor of the neXus model.
QGSJetII is an update of QGSJet01. In QGSJetII additionally non-linear interaction effects are taken into account and the model tuning to fixed target experiments has improved.
As hadronic low energy interaction models FLUKA [Fas00], GHEISHA [Fes85], and URQMD [Bas98] are available. Fluka is based on well tested microscopic models and therefore each step in hadronic interaction modelling is self-consistent and has a solid physical basis. The performance of FLUKA is optimized, using data of collider experiments.
GHEISHA is a model using parameterisations in the full range of hadronic shower energies for the modelling of cross sections and interactions. GEANT-GHEISHA can not handle the reaction kinematics properly, as the sum of the energies of the secondary particles and their energy deposits are often larger than the energy of the primary particle.
The URQMD (**U**ltrarelativistic **Q**uantum **M**olecular **D**ynamics) model, a microscopic model based on a phase space description of the reaction, has many free parameters that have to be determined by experimental data.

In the standard version of CORSIKA all particles are tracked until they decay or undergo further interactions. The required disc space and the computing time for air shower simulations scale linearly with the energy of the primary particle. The so-called thinning algorithm [Hil81, Hil97] provides faster simulations, but has the disadvantage that thinned showers can not be used in a detector simulation of KASCADE-Grande. The point at which this algorithm starts, is characterised by the thinning level $\epsilon_{thin} = E_{thin}/E_{prim}$. If the sum of

all $j$ particles drops below the thinning energy

$$\epsilon_{thin} \cdot E_0 > \sum_j E_j \tag{3.8}$$

only one of these particles is tracked and all the others are discarded. The particle selected with the probability $p_i = E_i / \sum_j E_j$ gets a weighting and is the representative of the discarded particles.

To get a detector response the fully simulated (without thinning) air showers are processed with CRES (**C**osmic **R**ay **E**vent **S**imulation), a detector simulation based upon the GEANT3 program [GEA93]. Taking into consideration all detector components, CRES produces an output equal to the raw data, measured with KASCADE-Grande, and provides measures such as the energy deposits and the arrival times of the particles.
After the detector simulation both true and reconstructed shower observables are known and therefore detailed studies of the reconstruction properties are possible.

# Chapter 4

# The principle of unfolding

An often occurring problem in physics is the determination of the original distribution of an observable, which is not affected by any measurement effect. In general the measured distribution differs from the original distribution due to statistical fluctuations and the limited resolution of the detector, in general the measurement device (error of measurement). By means of deconvolution these distortions can be corrected for. The concepts of deconvolution have been developed for optical image reconstruction, radio astronomy, crystallography and medical imaging, but can also be applied in particle physics. In the following chapter the problem of unfolding in general and the solution strategies, mainly in context with particle physics, are introduced. The description follows mostly the overview on unfolding in [Cow98].

## 4.1 The unfolding problem

The true values of a measure $x$ are assumed to be distributed according to the probability density function (p.d.f.) $f_{true}(x)$. Instead of the true value, arisen by statistical fluctuations and measurement errors, the observable $y$ is measured. The corresponding probability density function is characterized by $g(y)$. For continuous probability density functions the relation between true and measured variables is given by

$$g(y) = \int_a^b A(y|x) f(x) \mathrm{d}x, \text{ with } a \leq x \leq b. \tag{4.1}$$

Equation 4.1 is a Fredholm integral equation of first kind with the so-called kernel or response function $A(x, y)$. By means of deconvolution equation 4.1 can be solved for the sought after distribution $f(x)$, if the kernel or response function $A(y|x)$ is known. The kernel function $A(y|x)$ itself can also be described by an integral equation $A(y|x) = s(y|x)\epsilon(x)$, being composed of the resolution function $s(y|x)$ ($\int s(y|x)\mathrm{d}x = 1$) and the detection efficiency $\epsilon(x)$. The function $s(y|x)$ displays the conditional p.d.f. for a measured value $y$ given the occurrence that the true value was $x$.

The probability density functions $f(x)$ and $g(y)$ can either be described in a functional way or by normalized histograms, which are commonly used in particle physics. Using data the measured distribution $g(x)$ is available as a histogram Therefore equation 4.1 has to be discretised, i. e. the functions $f(x)$, $g(x)$, and $A(y, x)$ are replaced by histograms.

The number of events measured in the $i$th bin is given

$$\begin{aligned}\nu_i &= \mu_{tot} P(\text{event observed in bin i}) \\ &= \mu_{tot} \int P\left(\begin{array}{c|c}\text{observed} & \text{true value y and} \\ \text{in bin i} & \text{event detected}\end{array}\right) \epsilon(x) f_{true}(y) \\ &= \mu_{tot} \int\limits_{bin\ i} \mathrm{d}x \int \mathrm{d}y s(y|x)\epsilon(x) f_{true}(y),\end{aligned} \tag{4.2}$$

with $\mu_{tot}$ being the total number of events. Expanding equation 4.2 by the number of events $\mu_j$ in the $j$th bin of the true distribution and breaking the integral over y into a sum over bins, the number of events observed in bin $i$ can be written as

$$\begin{aligned}\nu_i &= \sum_{j=1}^{M} \frac{\int_{\text{bin } i} \mathrm{d}x \int_{\text{bin } i} \mathrm{d}y s(y|x)\epsilon(x) f_{true}(y)}{(\mu_j/\mu_{\text{tot}})} \mu_j \\ &= \sum_{j=1}^{M} R_{ij}\mu_j.\end{aligned} \tag{4.3}$$

The elements of the so-called response matrix $R$ are given by

$$\begin{aligned}R_{ij} &= \frac{\int_{\text{bin } i} \mathrm{d}x \int_{\text{bin } j} \mathrm{d}y s(y|x)\epsilon(x) f_{true}(y)}{\int_{\text{bin } j} \mathrm{d}y f_{true}(y)} \\ &= \frac{P(\text{observed in bin i and true value in bin j})}{P(\text{observed in bin i})} \\ &= P(\text{observed in bin i}|\text{true value in bin j}).\end{aligned} \tag{4.4}$$

According to the first line of equation 4.4 for the calculation of the elements of the response matrix $R_{ij}$, not only the response function $A(y|x) = s(y|x)\epsilon(x)$, but also the sought after distribution $f_{true}(y)$ is required. As the determination of $f_{true}(y)$ is the main aim of the deconvolution analysis, it is unknown. Choosing the bin size of the unfolded histogram rather small, in the way that $s(y|x)$ and $\epsilon(x)$ are approximately constant over the bin of x, the dependence on $f_{true}(y)$ is negligible.

## 4.2 Solution by matrix inversion

A unique solution of the matrix equation does not exist, if the system is underdetermined, i. e. if the number of measured channels M is smaller than the number of channels of the sought-after distribution. But also in the overdetermined case usually no exact solution can be found.
In general the matrix equation $\nu = R\mu$ can be solved for $\mu$ by direct matrix inversion, if $R$ is a non-singular quadratic matrix. The solution obtained by direct inversion has good statistical properties, it is for example not biased. But practically the inversion only works, if the matrix is dominated by the diagonal elements. If a large migration to the neighbouring bins can be found, the results look unsatisfactorily and show large oscillations. Another crucial point is the symmetry of the matrix along the diagonal, which leads to a close to singular matrix with $\det R \approx 0$. For a completely singular matrix no unique solution exists, for an almost singular matrix the results are often far off truth and do not lead to a stable solution.

The system that has to be solved is a so-called ill-conditioned system, i. e. small perturbations cause a relatively large change in the solution.
Another problem arises from statistical uncertainties in the measured distribution, what leads to the fact that the system will never be exactly fulfilled and therefore a solution close to the truth can not be expected.

## 4.3 The method of correction factors

One of the most simple approaches for the estimation of the true distribution is the method of correction factors. Assuming the true and the reconstructed distribution to have the same number of bins and the response matrix to be diagonal, an estimator for one bin $i$ of the true distribution is

$$\mu_i = C_i(n_i - \beta_i). \tag{4.5}$$

In this equation $\beta_i$ is the background and $C_i$ is a correction factor. Without background $\beta_i$ the correction factors are given by

$$C_i = \frac{1}{R_{ii}}. \tag{4.6}$$

For negligible resolution effects the response matrix is diagonal and the method of correction factors is applicable. In case of KASCADE-Grande due to effects of resolution the response matrix is not diagonal and therefore this procedure is not applicable and not further discussed.

## 4.4 Forward unfolding

Another possibility to determine the true distribution is the maximisation of a log-likelihood function or the minimisation of the $\chi^2$ functional. If the shape of the function $f(y)$ is known and can be parameterized using the parameters $\alpha_k (k = 0, 1, ...l)$, by minimising

$$\chi^2 = \sum \frac{\nu_i - \sum_j R_{ij} f(y, \alpha_k)}{\sigma^2} \tag{4.7}$$

the parameters $\alpha_k$ can be determined. The disadvantage of those minimising and maximising algorithms is that the shape of the true distribution (the fit function) has to be known. Therefore an application of those methods does not allow the discovery of any unknown features in the sought-after function, i. e. the energy spectrum, and is therefore not used for unfolding KASCADE-Grande data.

## 4.5 Regularised unfolding

A system of linear equations can be solved using a log-likelihood or a least squares expression. The $\chi^2$ expression is similar to the one discussed in section 4.4, but instead of a parametric fit function $f(y)$, the bin contents $\mu_i$ of the true distribution are used. The $\chi^2$ functional is given by

$$\chi^2 = \sum \frac{\nu_i - \sum_j R_{ij} \mu_i}{\sigma^2}. \tag{4.8}$$

For a true histogram $\mu$ and a data histogram $\nu$ with the same number of bins, i. e. for a quadratic response matrix, the solution of equation 4.9 is equivalent to the results obtained by direct matrix inversion. The direct solution may show large fluctuations in $\mu$, which can be reduced by applying a method called regularisation. By regularisation additional constraints on $\mu$ are

introduced, which lead to a smoothing of the solution. In general the solution with the highest degree of smoothness out of the acceptable solutions is chosen. The $\chi^2$ functional modified using the regularisation function $S(\mu)$ and the regularisation parameter $\alpha$ can be described by

$$\chi^2_{mod} = \alpha \sum \frac{\nu_i - \sum_j R_{ij}\mu_i}{\sigma^2} + S(\mu). \tag{4.9}$$

The function $S(\mu)$ is a measure for the smoothness. The regularisation strength is controlled via the parameter $\alpha$. A large $\alpha$ corresponds to a weak regularisation, $\alpha = 0$ leads to the smoothest distribution possible, completely ignoring data. The parameter $\alpha$ may also be attached to the regularisation function $S(\mu)$.

### 4.5.1 Regularisation functions

#### 4.5.1.1 Tikhonov regularisation

A regularisation method commonly used is the Tikhonov regularisation, suggested independently by Phillips [Phi62] and Tikhonov [Tik63]. The regularisation term is given by

$$S[f_{true}(y)] = \int \left( \frac{d^k f_{true}(y)}{dy^k} \right)^2 dy. \tag{4.10}$$

In general a linear combination of terms with different derivatives can be used, but practically one value of $k$ is chosen, usually $k = 2$. For example for $k = 2$ and equal bin width $\delta y_i$ the regularisation function $S(\mu)$ is

$$S(\mu) = \frac{1}{\Delta y_i^2} \sum_{i=1}^{M-1} (-\mu_i + 2\mu_{i+1} - \mu_{i+2})^2. \tag{4.11}$$

With the symmetric matrix of constants in matrix notation the regularisation parameter can be written as

$$S(\mu) = \vec{\mu}^T G \vec{\mu}. \tag{4.12}$$

Using the error matrix $C_{ij} = \delta_{ij}/\sigma(\nu_i)$, the $\chi^2$ expression can also be formulated as a matrix equation

$$\chi^2 = \alpha[C(\vec{\nu} - R\vec{\mu})]^T[C(\vec{\nu} - R\vec{\mu})] + \vec{\mu}^T G \vec{\mu}. \tag{4.13}$$

This formulation leads to a system of linear equations, which can be solved by using, for example, the damped least square algorithm.
Since all bin contents of an energy spectrum are expected to be positive, the original Tikhonov algorithm can not be applied, because it does not guarantee the positiveness of the solution. Considering also the positiveness of the solution leads to non-linear equations and therefore the matrix formalism has to be given up.

#### 4.5.1.2 Regularisation based on entropy

Another regularisation function is based upon the entropy. The entropy $H$ of a probability distribution $p = (p1, ..., p_M)$ [Sha48] is given by

$$H = -\sum_{i=1}^{M} p_i \lg p_i. \tag{4.14}$$

It can be interpreted as a measure of smoothness of a histogram $\mu = (\mu_1, ..., \mu_M)$. Based upon the so-called principle of maximum entropy, as regularisation function

$$S(\mu) = H(\mu) = -\sum_{i=1}^{M} \frac{\mu_i}{\mu_{tot}} \lg \frac{\mu_i}{\mu_{tot}} \tag{4.15}$$

is used. The entropy $S(\mu)$ has a maximum, if all bin contents are equal and a minimum, if all events $\mu_{tot}$ are concentrated in one bin. The advantage of this method guarantees the positiveness of the solution and for this reason can also be used for unfolding KASCADE-Grande data.

## 4.6 Iterative algorithms

Systems of linear equations according to equation 4.3, can also be solved for the true values by means of iterative procedures. Iterative methods converge to the exact solution of the problem with increasing number of iterations. Reproducing statistical data fluctuations, the exact solution is not of interest. Therefore a stop criterion has to be introduced. More information about the stop criterion can be found in section 4.8

### 4.6.1 The Van Cittert procedure

For a quadratic, positive definite response matrix $R$ the basic form of the iterative Van Cittert method [Cit33] is given by

$$\mu_i^{k+1} = \mu_i^k + \alpha(\nu_i - \sum_j R_{ij}\mu_j). \tag{4.16}$$

Here $k$ is the number of iterations and $\alpha$ the so-called relaxation factor.
If the response matrix is not quadratic, i. e. if data vector and solution vector are not of the same dimension, the following substitutions are done

$$R \Leftrightarrow R^T R \quad , \qquad \vec{\nu} \Leftrightarrow R^T \vec{\nu}. \tag{4.17}$$

For consideration of the statistical uncertainties of the data the error matrix, defined by $C_{ij} = \delta_{ij}/\sigma(\nu_i)$, is used. The modified response matrix $\tilde{R}$ and the modified data vector $\vec{\tilde{\nu}}$ are

$$\tilde{R} = CR \quad , \qquad \vec{\tilde{\nu}} = C\vec{\nu}. \tag{4.18}$$

For convergence of equation 4.16 the condition

$$0 < \alpha < \frac{2}{\lambda_{max}} \tag{4.19}$$

has to be fulfilled, where $\lambda_{max}$ represents the largest eigenvalue of the response matrix $R$.
This algorithm does not guarantee positive solutions and is therefore not applied to data.

### 4.6.2 The Gold algorithm

The Gold algorithm [Gol64] is a further development of the Van Cittert procedure and provides only positive solutions. The Gold deconvolution is characterized by its stability and robustness against oscillation effects, arising from ill-conditioned response matrices.
The requirement for the Gold algorithm is a quadratic non-singular response matrix with only

positive elements and non-zero diagonal elements. Additionally the positive definiteness of the matrix is required. In case of a non-quadratic or non-positive definite matrix a substitution according to equation 4.17 is performed. The recursion formula for the $(k+1)$th iteration step is

$$\mu_i^{k+1} = \frac{\mu_i^k \nu_i}{\sum_{j=1}^{n} R_{ij}\mu_j^k}, \tag{4.20}$$

with $\mu_i^k$ being the component of the solution vector from the last iteration step. For taking into account the statistical uncertainties of the data both sides of $\vec{\mu} = R\vec{\nu}$ can be multiplied by the error matrix $C$, which is defined by $C_{ij} = \delta_{ij}/\sigma(\nu_i)$. Its robustness and simplicity lead to favouring this algorithm in the unfolding analysis of KASCADE-Grande data.

### 4.6.3 The Bayesian unfolding

Another iterative unfolding approach is based on Bayes' Theorem [Ago95]. For independent causes ($C_i, \quad i = 1, ...., n_c$) with their initial probability $P_0(C_i)$ and the conditional probability $P(E_j|C_i)$ of the $i$th cause to produce the $j$th effect $E_j$, the Bayes formula can be written as

$$P(C_i|E_j) = \frac{P(E_j|C_i)P_0(C_i)}{\sum_{l=1}^{n_c} P(E_j|C_l)P_0(C_l)}. \tag{4.21}$$

The expected number of events $n(C_i)$ assigned to a cause $C_i$ can be calculated to

$$n(C_i) = \sum_{j=1}^{n_E} P(C_j|E_i)n(E_i). \tag{4.22}$$

$n(E_i)$ represents the number of events of several possible effects.
With a first guess of the initial distribution $\vec{\mu^0}$ in matrix notation the probabilities $P(C_i|E_j)$ are given by

$$P(\mu_i|\nu_j) = \frac{R(\nu_j|\mu_i)\mu_i^0}{\sum_{l=1}^{n_\mu} R(\nu_j|\mu_l^0)\mu_l^0}, \tag{4.23}$$

where the probabilities $P(\nu_j|\mu_i)$, with $\mu_i$ being the elements of the sought-after vector and $\nu_j$ being the elements of the data vector, are represented by the elements of the response matrices $R_{ji}$ and the probabilities $P_0(C_i)$ can be written as $\mu_i^0/\mu_{tot}^0$, whereas $\mu_{tot}^0$ cancels out. The initial distribution for example can be chosen from the best knowledge of process. Equation 4.23 leads to a better estimation for the probabilities $P(\mu_i|\nu_j)$ and therefore to a better estimate of the solution $\vec{\mu}$. As recursion formula

$$\mu_j^{k+1} = \sum_{i=1}^{n_\mu} P(\mu_j^k|\nu_i)\nu_i \tag{4.24}$$

is obtained. For taking into account the efficiencies equation 4.24 has to be modified to

$$\mu_j^{k+1} = \frac{1}{\epsilon_j}\sum_{i=1}^{n_\nu} P(\mu_j^k|\nu_i)\nu_i, \tag{4.25}$$

with the efficiencies $\epsilon_j$

$$\epsilon_j = \sum_{j=1}^{n_\mu} P(\nu|\mu_j^k) = \sum_{j=1}^{n_\mu} R_{ij}. \tag{4.26}$$

Compared to the Gold algorithm the implementation of the Bayesian unfolding is more complex, because more steps for the calculation are required, but both algorithms provide similar results.

## 4.7 Estimation of errors

### 4.7.1 Statistical errors (variances)

For the estimation of the statistical uncertainties of the unfolding procedure, arising from statistical data fluctuations, a random generator is used. Therefore the measured distribution is interpreted as a probability density function, according to which k new sets of distributions are created. The produced simulation sets contain the same number of events as the measured distribution and reproduce the statistical fluctuations of the original distribution. Each of these simulation sets is unfolded. With $\mu_{i,k}$ being the value of the $i$th bin of the $k$th unfolded solution, the statistical uncertainty of each bin is given by the standard deviation

$$\sigma_i = \sqrt{\frac{1}{K}\sum_{k=1}^{K}(\mu_{i,k} - \bar{\mu_i})^2}, \quad \text{with} \quad \bar{\mu} = \frac{1}{K}\sum_{k=1}^{K}\mu_{i,k}. \tag{4.27}$$

### 4.7.2 Systematic bias

The shift of the solution with respect to the true distribution is referred to as bias. For its determination a similar approach as for the statistical errors is used (see 4.7.1).
Therefore k new data sets are generated and unfolded. The mean values of the unfolded solutions are considered to be the true quantities. The mean of the i$th$ bin averaged over all k sets is given by

$$\bar{\mu_i} = \sum_{k=1}^{K}\mu_{i,k}. \tag{4.28}$$

The convolution of the k solutions with the response matrices leads to k new calculated distributions, which can be deconvolved. $\mu^{re}_{i,k}$ is the $i$th bin content of the $k$th set of re-unfolded energy spectra. The bias of the $i$th bin of the solution can then be calculated to

$$b_i = \frac{1}{K}\sum_{k=1}^{K}(\mu^{re}_{i,k} - \bar{\mu_i}). \tag{4.29}$$

## 4.8 Stop criterion and the regularisation parameter

The regularisation parameter $\alpha$ is a measure for the smoothness of the distribution and indicates a compromise between bias and variance of the estimator. The tradeoff between bias and variance defines the regularisation parameter.
For iterative algorithms the stop criterion, that means the number of iterations until the iterative process is stopped, has to be determined. With increasing number of iterations the solution converges towards the exact solution of the system, i. e. the bias decreases. Since the solution reproduces statistical fluctuations in the data, the statistical uncertainties rise with the number of iterations. Therefore the iteration has to be stopped at a certain level.
For the determination of the stop criterion as well as for the determination of the regularisation parameter several criteria can be found.

One possibility is the minimisation of the mean squared error, averaged over all bins, which is defined as

$$\mathrm{MSE} = \frac{1}{M}\sum_{i=1}^{M}(\sigma_i^2 + b_i^2), \tag{4.30}$$

where $M$ is the dimension of the solution vector and for the $i$th component of the solution vector $\sigma_i$ represents the variance and $b_i$ the bias.
Alternatively the so-called 'weighted mean squared error' (WMSE) can be used. The difference to MSE is that the different bins contribute differently. The WMSE is defined as

$$\mathrm{WMSE} = \frac{1}{M}\sum_{i=1}^{M}\frac{\sigma_i^2 + b_i^2}{\mu_i}, \tag{4.31}$$

with $\mu_i$ being the $i$th component of the solution estimate.
Another approach for the determination of the regularisation parameter is based on the requirement that the bias squared is not larger than the variance

$$\chi_b^2 = \frac{1}{M}\sum_{i=1}^{M}\frac{b_i^2}{\sigma_i^2}. \tag{4.32}$$

The sought-after tradeoff is characterized by a value of $\chi_b^2 \approx 1$. For the determination of the regularisation parameter $\alpha$, the values of the WMSE, MSE or $\chi_b^2$ can be plotted versus the regularisation parameter.
In case of iterative algorithms the so-called iteration level, equivalent to the number of iterations, has to be determined. Therefore the WMSE, MSE or $\chi_b^2$ subject to the number of iterations or the $\Delta\chi^2$ between the results of sequent iteration steps is plotted.

# Chapter 5

# Ansatz of the analysis

## 5.1 The two-dimensional shower size spectrum

The two-dimensional shower size spectra of electron and muon numbers measured by KASCADE (see Fig. 5.2) and KASCADE-Grande (see Fig. 5.3) contain air showers of different energies and of all primary particles from proton up to iron and can therefore be understood as superposition of all these showers. For illustration purposes the probability density functions of three different primary particle masses (H, C and Fe) with different energies are shown as contours in Fig. 5.1 for zenith angles from 0 to 18°. Showers induced by heavy primary particles produce more muons. Since the muons orginate directly from the decay of $\pi$ mesons, this can be explained by the larger number of nucleons taking part in hadronic interactions. With increasing mass of the primary particle the number of electrons reaching the detector level decreases. This is due to the higher interaction height of heavy primary particles, which leads to an energy deposit of the electromagnetic component higher in the atmosphere and therefore to fewer electrons at ground level. Beside these two effects the probability distributions for higher energies are shifted to larger shower sizes.
In addition, it becomes obvious that the fluctuations in the electron and the muon number reduce with increasing primary particle mass. This effect can be explained by the principle of superposition, according to which an iron induced air shower can be described by 56 proton induced air showers each with an energy of $E_{prot} = \frac{E_0}{56}$. Hence, an iron induced air shower is an averaging over 56 proton induced air showers and shows less fluctuations. In addition a decrease of the relative shower fluctuations with increasing energy can be observed.
Furthermore, the probability distributions of different primary particle types and different energies overlap and a separation of different primary particle masses and energies is rather difficult.

## 5.2 Ansatz of the analysis

The aim of the unfolding analysis is the the reconstruction of energy spectra of cosmic rays for different mass groups. To disentangle the information on the nature of the primary particle and its energy deconvolution techniques are indispensable. The analysis is based upon the two-dimensional shower size spectrum of electron and muon numbers measured by KASCADE (Fig. 5.2) and KASCADE-Grande (Fig. 5.3). The content of one cell $i$ of this distribution can be described by

$$N_i = 2\pi A_s T_m \sum_{A=1}^{N_A} \int_{\theta_1}^{\theta_2} \int_{-\infty}^{+\infty} \frac{dJ_A}{\mathrm{dlg}E}\, p_A((\lg N_e, \lg N_\mu^{tr.})_i | \lg E) \sin\theta \cos\theta \,\mathrm{dlg}E \,\mathrm{d}\theta, \qquad (5.1)$$

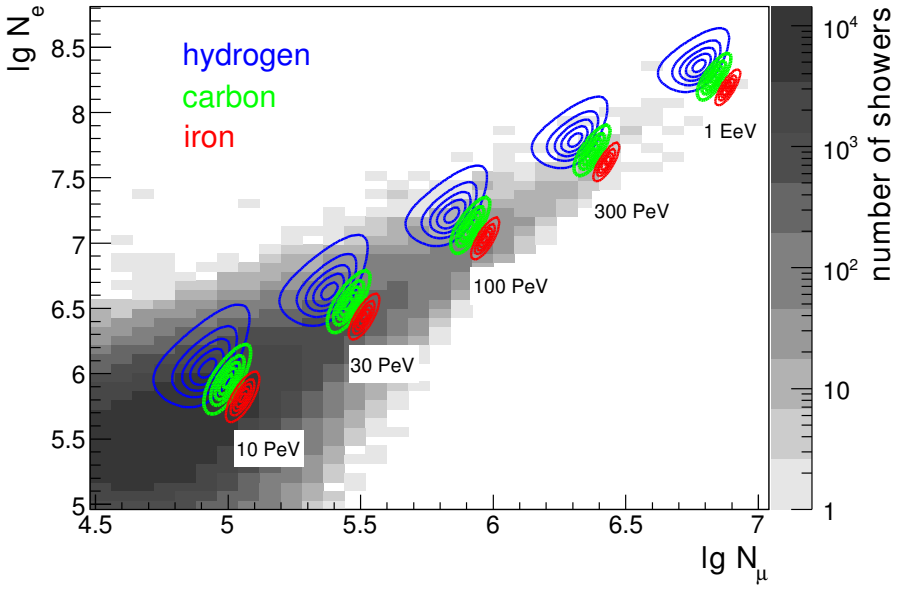


Figure 5.1: Probability density functions for proton, carbon and iron induced air showers with different energies for zenith angles from 0 to 18°.

where $dJ_A/\mathrm{dlg}E$ represents the differential flux of an element with mass number $A$, $A_s$ is the detection area and $T_m$ is the measurement period. $p_A$ is the probability for a given energy to reconstruct the shower sizes lg $N_e$ and lg $N_\mu^{tr.}$ and is often referred to as response function. The last term is taking into account the decrease of the effective detection area with increasing zenith angles. In case of the unfolding of KASCADE-Grande data in Equation 5.1 the truncated muon number lg $N_\mu^{tr.}$ is replaced by the total number of muons lg $N_\mu$
Equation 5.1 describes a set of coupled Fredholm integral equations of 1st kind. The system of linear equations can be solved for the differential flux $dJ_A/\mathrm{dlg}E$ by means of unfolding techniques (see Chapter 4), if the probability $p_A$ is known. The probability $p_A$ is given by a convolution integral

$$p_A = \int_{-\infty}^{+\infty}\int_{-\infty}^{+\infty} s_A \epsilon_A r_A \,\mathrm{dlg}N_e^{true}\mathrm{dlg}N_\mu^{true}. \tag{5.2}$$

Here $s_A = s_A(\lg N_e^{true}, \lg N_\mu^{true} | \lg E)$ stands for the shower fluctuations, i. e. the probability that an air shower induced by a primary particle with energy $E$ and mass number $A$ holds the true electron number lg $N_e^{true}$ and the true muon number lg $N_\mu^{true}$ (see Section 6.1). $\epsilon_A = \epsilon_A(\lg N_e^{true}, \lg N_\mu^{true})$ depicts the combined trigger and reconstruction efficiency (see Section 6.3.1). The function $r_A = r_A(\lg N_e, \lg N_\mu^{tr.} | \lg N_e^{true}, \lg N_\mu^{tr.,true})$ includes reconstruction uncertainties (see Section 6.2.1).

## 5.3 Quality cuts

To guarantee a good quality of the reconstructed events, several quality cuts are applied to the reconstructed data. The quality cuts are applied to both, measured and simulated data. Since the deconvolution is applied to KASCADE as well as KASCADE-Grande data, the quality

criteria for both experiments are discussed in the following section.
In general the cuts can be separated into cuts concerning data selection, which are independent on the reconstruction procedure, and into reconstruction cuts. The criteria can be defined and studied on basis of Monte Carlo simulations.

### 5.3.1 KASCADE

The following cuts are independent on the reconstruction:

- Data selection is just started, when in case of the outer clusters 10 detectors or in case of the inner cluster 20 detectors lie above threshold;
- Only events are taken, for which all clusters were active.

After having reconstructed all events, fulfilling the trigger condition, further criteria can be found to improve the quality of the data. The reconstruction criteria for the KASCADE experiment are:

- All events are successfully reconstructed on the third level;
- Events with misreconstructed cores at the border of the KASCADE array are reduced by the fiducial area cut (a circle around the center of the KASCADE array with a radius of 91 m);
- For the reconstructed age parameter $s$ values between 0.2 and 2.1 are required, because due to correletations of the parameters of the NKG function misreconstructed shower cores lead to unphysical values of the age parameters $s$.

The efficiencies for KASCADE are affected by single detectors that do not work properly. Whereas large showers are not affected by this effect, the reconstruction of small showers suffers from single broken detector stations. Therefore only showers with an electron number higher than $N_e \geq 10^{4.8}$ and a muon number higher than $N_\mu^{tr.} \geq 10^{3.6}$ are taken into account.

### 5.3.2 KASCADE-Grande

Criteria independent on the reconstruction:

- At least one trigger hexagon has all 7 stations fired;
- Not all events measured by Grande are air shower events. Some originate from the synchrotron radiation source ANKA. The information about ANKA is stored in a database, what allows to exclude the periods when ANKA was active;
- All 18 trigger hexagons are active;
- KASCADE array is active (required for reconstruction of electron and muon number);
- More than 19 stations show a valid TDC hit.

All events surviving the above mentioned cuts are reconstructed, but not all of them successfully. For exclusion of badly reconstructed events additional quality criteria are defined:

- Successfull reconstruction on the third level is required;
- To reduce events with misreconstructed cores at the border of the Grande array, as fiducial area a circle around the center of the Grande array with a radius of 250 m is chosen;

- Events whose reconstructed age parameter s (see equation 3.6) reaches its mathematical limits, are discarded, because in that case the fit is not reliable;
- A reconstruction criterion using the relation of the energy sum in the detectors and the shower size reduces further misreconstructed events.

In this analysis nearly full trigger and reconstruction efficiency is required. The detector efficiencies for KASCADE-Grande are discussed in Section 6.3.2. The KASCADE-Grande experiment is fully efficient at $\lg(N_e) \geq 6$ and $\lg(N_\mu) \geq 5$.

## 5.4 Data

### 5.4.1 KASCADE

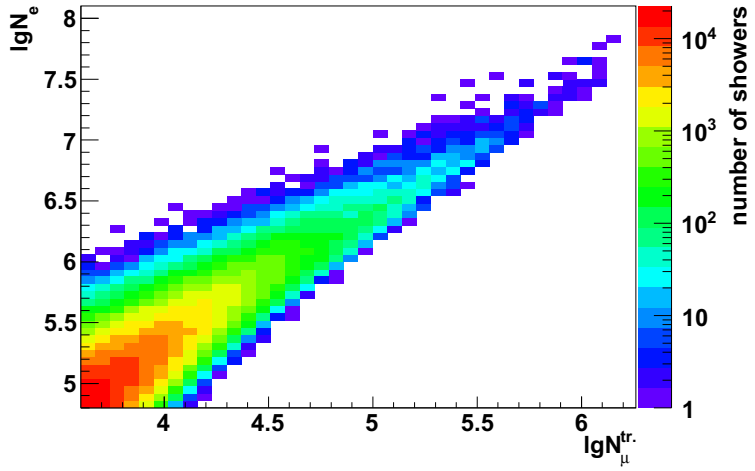


Figure 5.2: Two-dimensional size spectra measured with the KASCADE array in the zenith angle range from 0° to 18° after all cuts. The measurement period of 833.9 days results in 639865 events.

After all cuts and in the region of full efficiency 639865 events remain in the zenith angle range from 0° to 18°. The measurement period for the shown histogram is approximately 834 days. Fig. 5.2 shows the two-dimensional size spectra of electron and muon numbers, whereby for KASCADE instead of the muon number $N_\mu$ the truncated muon number $N_\mu^{tr.}$ is used. The displayed distribution does not include all of the data available for KASCADE, but exceeds the statistics, existing for Grande, by a multiple.

### 5.4.2 KASCADE-Grande

In the zenith angle range from 0° to 18°, after having applied all cuts, 76433 events remain in the region of full efficiency. Fig. 5.3 shows color coded the number of measured showers for the Grande array as a function of the muon number lg $N_\mu$ and the electron number lg $N_e$. It becomes obvious that with increasing shower size, i. e. with increasing energy, the number of reconstructed showers decreases. The difference in the atmospheric depth between 0° and 18° is approximately 5%. A projection along the lg $N_e$ axis or the lg $N_\mu$ axis respectively results in the one dimensional shower size spectra.

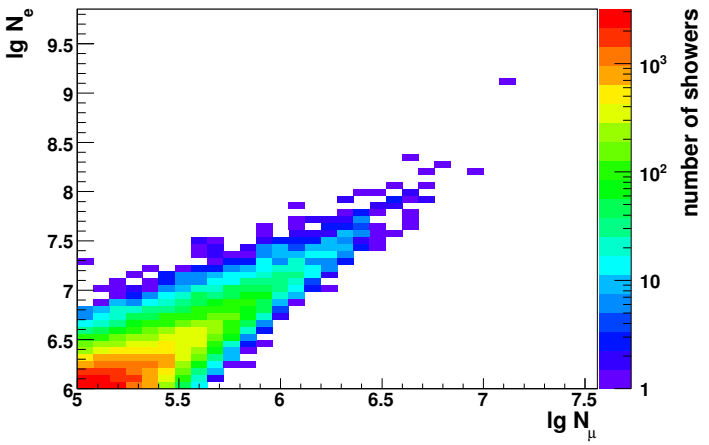


Figure 5.3: Two-dimensional size spectra of electron and muon numbers in the zenith angular range 0 - 18° measured by KASCADE-Grande. In the measurement time of approximately 1270 days 89604 events are successfully reconstructed.

## 5.5 Simulations

The determination of the probabilities $p_A$ given by equation 5.2 are discussed more in detail in the next chapter. At this point solely the different simulations sets, being essential for the calculation of $p_A$, are overviewed. Whereas the computing time of an fully simulated air shower roughly scales with the energy, the file size per energy decade increases by approximately a factor of 15. On average, the simulation of an event with an energy of $10^{17}$ eV takes approximately 11 hours and the allocated storage space is about 3 GB. Thus, the production of sufficient statistics is rather time and memory space consuming. The standard KASCADE-Grande set consist of CORSIKA showers fully simulated with a continuous spectrum and a spectral index $\gamma = 2$. The energies reach from $10^{14}$ eV up to $10^{18}$ eV, in order to cover the entire measurement range of the KASCADE-Grande experiment. Afterwards the showers are processed with CRES to get the response of the detectors (KASCADE and Grande). In the standard set as primary particles hydrogen, helium, carbon as representative of the CNO group, silicon as representative of the medium heavy elements and iron as representative of Fe, Co and Ni are chosen. On basis of this standard sets the contribution of the reconstruction uncertainties $r_A$ and the efficiencies $\epsilon_A$ can be determined.
With the standard simulation set the determination of the shower fluctuations at high energies is hardly possible, which originates mainly from the inverse power law ($E^{-2}$), leading to a rapid decrease of the number of simulated showers with increasing energy. To investigate the intrinsic shower fluctuations a large statistics is required. For this reason new simulation sets are produced, which only comprise thinned showers simulated at fixed energies (see section Table 6.1). The thinning algorithm is shortly discussed in Section 3.4. Based upon this thinned simulations the intrinsic fluctuations in the true electron and the true muon number can be parameterized. The simulation procedure has to be repeated for each individual hadronic interaction model.

# Chapter 6

# The probabilities $p_A$ and the response matrices

The probabilities $p_A$ are indispensable for the reconstruction of the energy spectra of different elemental groups by means of deconvolution. $p_A$ describes the probability for a primary particle with mass number $A$ to reconstruct in a defined energy interval the certain pair of electron and muon numbers. As already mentioned in Section 5.2, $p_A$ can be described by a convolution integral according to Equation 5.2, consisting of the shower fluctuations $s_A$, the reconstruction uncertainties $r_A$ and the combined trigger and reconstruction efficiencies $\epsilon_A$. These functions do not only depend on the number of electrons and muons, but are also dependent on the zenith angle, thus different angular ranges have to be treated separately. In the deconvolution analysis presented here only events in the zenith angle range from 0° to 18° are used, but in former analysis the results of different angular ranges have been investigated [Ape09] (see also Section 8.3.2). The procedure of determining the response matrices is based on the general ideas described in [Ant05].

## 6.1 Determination of shower fluctuations $s_A$

For the determination of the shower fluctuations CORSIKA simulations are used. These simulations were produced, using the so-called thinning algorithm (see Section 3.4), being implemented in CORSIKA. The use of the thinning algorithm allows a fast simulation with sufficiently enough statistics for the parameterization of the shower fluctuations.
For each primary particle mass (H, He, C, Si and Fe) a certain number of showers is simulated at different fixed energies. For KASCADE-Grande the chosen fixed energies and the corresponding number of showers can be found in Table 6.1. In case of KASCADE, due to the lower energy range of the experiment, additionally showers at energies of $10^{14}$eV (8000 events) and $5 \cdot 10^{14}$eV (6400 events) are produced.
The parameterization of the shower fluctuations in the logarithmic electron number $\lg N_e$ and the logarithmic muon number $\lg N_\mu$, respectively the truncated muon number $\lg N_\mu^{tr.}$ in case of

| primary energy [PeV] | 2 | 5 | 10 | 31.6 | 100 | 316 | 1000 | 3160 |
|---|---|---|---|---|---|---|---|---|
| number of showers | 6400 | 4800 | 3200 | 2400 | 1600 | 1200 | 800 | 400 |

Table 6.1: Fixed energies chosen for KASCADE-Grande and number of simulated showers per energy.

KASCADE (see Section 3.3.1), are done the same way as described in [Ant05].

### 6.1.1 The $\lg N_e$-distribution

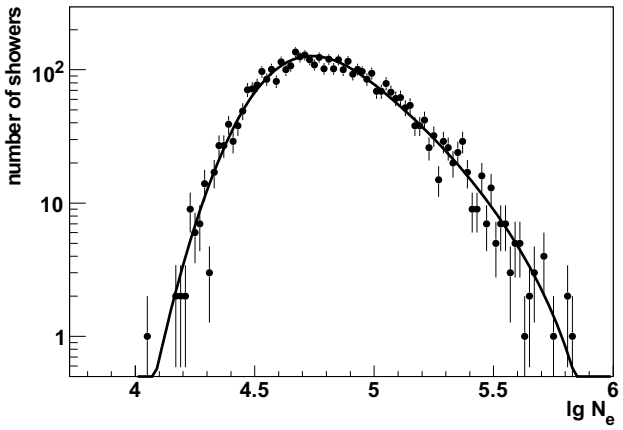


Figure 6.1: $\lg N_e$-distribution for proton induced air showers at an energy of 1 PeV for zenith angles from 0 ° to 18 °. The line displays the corresponding fit according to Equation 6.1.

Figure 6.1 shows the shower fluctuations in the logarithmic electron number $\lg N_e$ for proton induced air showers $(0 - 18°)$ at an energy of 1 PeV. The line illustrates the parameterization used. In the simulations, underlying the depiction, QGSJET01 was used as hadronic high-energy model and FLUKA describes the hadronic low-energy interactions. Qualitatively the use of other interaction models does not change the shape of these fluctuations, but the mean values vary. Although all showers depicted in Figure 6.1 hold the same energy, they underlie strong fluctuations. These fluctuations are mainly due to the stochastic process of the shower development. Additionally, the height of the first interaction is liable to fluctuations. Both processes are responsible for fluctuations in the number of particles in an air shower.
The probability density function, which is used for the parameterization of the $\lg N_e$-distribution is given by

$$\begin{aligned} p(\lg N_e|\lg E) =& g_0 \cdot \operatorname{erf}\left(\frac{\lg N_e - g_1}{g_2}\right) \\ & \times \exp\left(g_3 \cdot (\lg N_e - g_4)\right) \\ & \times (g_4 - \lg N_e)^{g_5} \,. \end{aligned} \tag{6.1}$$

$c_0$ is the scale factor of the function. The other parameters characterize the shape of the distribution and vary with energy. Due to the lack of statistics the exact shape of the distributions at the edges can hardly be predicted and will cause a systematic uncertainty in the reconstruction of the elemental spectra, which will be discussed in Chapter 8.

### 6.1.2 The $\lg N_\mu^{tr}$-distribution for KASCADE

As already mentioned in Section 3.3.1 for KASCADE the number of truncated muons is used as observable. The parametrization of the intrinsic shower fluctuations in the truncated muon number proves to be more challenging, since the number of electrons and the truncated number

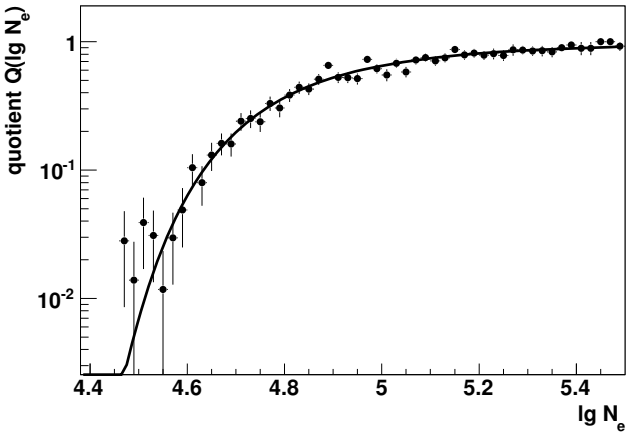


Figure 6.2: Quotient of the number of showers above a certain threshold (here: $\lg N_\mu^{tr.} > 3.5$) and the number of all simulated showers subject to the true number of electrons $\lg N_e$. For this plot only proton induced air showers with an energy of 1 PeV in the zenith angle range from 0 ° to 18 ° are used.

of muons are correlated. The discussion on this section is based upon simulations, using as interaction models QGSJET01 and FLUKA. The application of other interaction models does qualitatively not change the procedure of describing the fluctuations in the truncated muon number. This correlation becomes obvious when looking at the quotient of the number of showers with a truncated muon number above a certain threshold and the number of all simulated events subject to the electron number $N_e$ . Figure 6.2 displays the quotient for proton induced air showers of 1 PeV for zenith angles from 0 ° to 18 ° and a threshold of $\lg N_\mu^{tr.} > 3.5$. The plotted line displays the fit function according to

$$Q(\lg N_e, \lg N_\mu^{tr.} | \lg E) = \mathrm{erf}\left(\frac{\lg N_e - \lg N_0}{g_6 - g_7(\lg N_0 - \lg N_e)}\right). \tag{6.2}$$

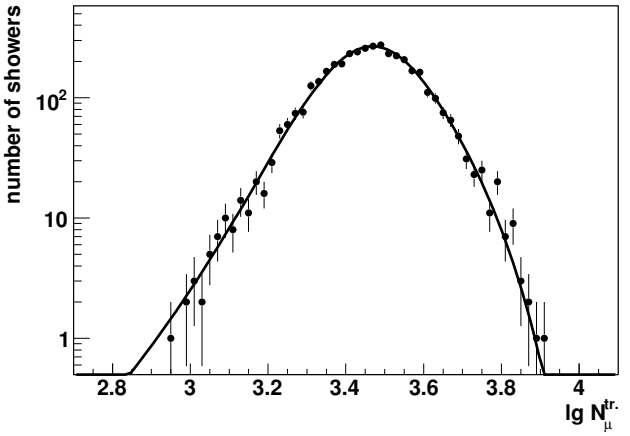


Figure 6.3: $\lg N_\mu^{tr.}$-distribution with the corresponding fit function according to Equation 6.6 for proton induced air showers at an energy of 1 PeV for zenith angles from 0 ° to 18 °.

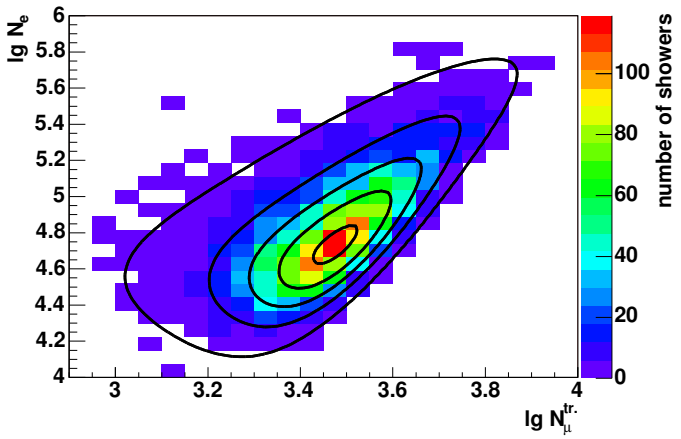


Figure 6.4: $\lg N_e$ - $\lg N_\mu^{tr.}$-distribution for proton induced events with an energy of 1 PeV in the zenith angle range $0 - 18°$. The contour lines display the corresponding two-dimensional parameterization according to Equation 6.5.

$\lg N_0$ is dependent on the threshold $\lg N_\mu^{tr.,0}$. This interrelation can be described by a polynomial of second order

$$\lg N_0 = g_8 + g_9 \cdot \lg N_\mu^{tr.,0} + g_{10} \cdot (\lg N_\mu^{tr.,0})^2. \tag{6.3}$$

Parameter $p_6$ and $p_7$ are adopted to be independent of the threshold $\lg N_\mu^{tr.,0}$. Together with Equation 6.1 this results in the probability to reconstruct showers with an electron number $\lg N_e$ and a truncated muon number above $\lg N_\mu^{tr.,0}$

$$P(\lg N_e, \lg N_\mu^{tr.} \geq \lg N_\mu^{tr.,0} | \lg E) = Q(\lg N_e, \lg N_\mu^{tr.,0}) \cdot p(\lg N_e | \lg E)\, \mathrm{d} \lg N_e. \tag{6.4}$$

The probability for a shower with an electron number $\lg N_e$ and a truncated muon number $\lg N_\mu^{tr.}$ is given by

$$\begin{aligned} P(\lg N_e, \lg N_\mu^{tr.} | \lg E) = \big(&Q(\lg N_e, \lg N_\mu^{tr.}) - Q(\lg N_e, \lg N_\mu^{tr.} + \mathrm{d} \lg N_\mu^{tr.})\big) \\ &\times p(\lg N_e | \lg E)\, \mathrm{d} \lg N_e. \end{aligned} \tag{6.5}$$

Using the already determined parameters of the $\lg N_e$-distribution (equation 6.1) a function according to

$$P(\lg N_\mu^{tr.} | \lg E) = \int_{-\infty}^{+\infty} P(\lg N_e, \lg N_\mu^{tr.} | \lg E)\, \mathrm{d} \lg N_e \tag{6.6}$$

is adjusted to the $\lg N_\mu^{tr.}$-distribution. The $\lg N_\mu^{tr.}$-distribution with the corresponding fit function is shown in Figure 6.3 for proton induced air showers with an energy of 1 PeV. In Figure 6.4 the correlated $\lg N_e$ - $\lg N_\mu^{tr.}$ - distribution and the corresponding two-dimensional function are displayed. The parameters of function 6.6 are determined for all energies. By means of interpolation the values of the parameters are determined over the whole energy range. The values of some parameters have to be fixed due to stability problems of the fitting procedure, being caused by the large number of parameters. The parameterizations of $g_1, ..., g_{10}$ can be found in the Appendix A, using as interaction models QGSJETII and FLUKA.

### 6.1.3 The $\lg N_\mu$-distribution for KASCADE-Grande

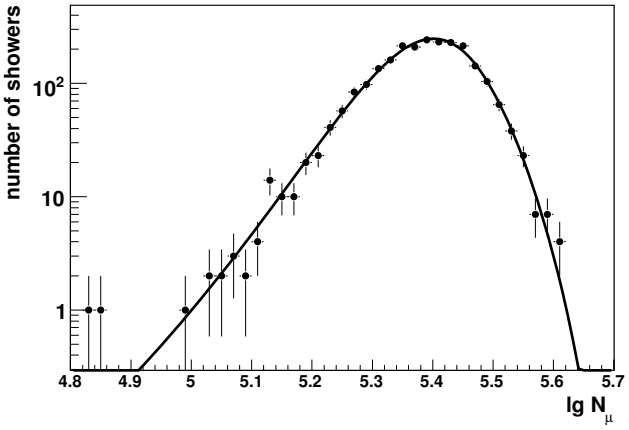


Figure 6.5: lg $N_\mu$-distribution with the corresponding fit function according to Equation 6.6 for proton induced air showers at an energy of $3 \cdot 10^{16}$ eV for zenith angles from 0° to 18°.

In case of KASCADE-Grande the total number of muons $N_\mu$ is reconstructed. The function used for the parameterization of the fluctuations in $\lg N_\mu$ is the same as used for the parameterization of the $\lg N_\mu^{tr.}$-distribution. As an example Figure 6.5 shows the $\lg N_\mu$-distribution on basis of the interaction models QGSJETII and FLUKA for proton induced air showers at an energy of $3 \cdot 10^{16}$ eV. The corresponding parameterizations of $g_1, ..., g_{10}$ can be found in the Appendix A.

## 6.2 The reconstruction uncertainties $r_A$

For the determination of the reconstruction uncertainties fully simulated CORSIKA showers followed by a detector simulation are used. The detector simulation CRES (**C**osmic **R**ay **E**vent **S**imulation), which is based upon the GEANT3 detector simulation tool [GEA93] , produces an output in the same format as the raw data, taking into account all components of the detector. The presence of the true and the reconstructed electron and muon numbers allows to analyse the reconstruction properties of the detector. The reconstructed particle numbers are afflicted by reconstruction uncertainties, which can be subdivided into systematic and statistical uncertainties. In the following sections the reconstruction characteristics for both detectors, KASCADE and KASCADE-Grande, are discussed. Whereas the discussion on KASCADE is, due to the large statistics in these simulation sets, based upon QGSJET01 and FLUKA, for the same reason in case of KASCADE-Grande QGSJETII and FLUKA is used. The use of different hadronic interaction models does again not change the quintessence of the discussion.

### 6.2.1 The reconstruction uncertainties in $N_e$ for KASCADE

Figure 6.6 displays the systematic reconstruction uncertainties in the electron number. On the left the systematic uncertainties are shown subject to the true number of electrons $\lg N_e^{true}$. Over a large range the systematic uncertainties are smaller than 12%, but at small and large electron numbers the uncertainties increase. The small extent of showers with small electron numbers combined with the distance of the detector stations does not allow a proper measurement of the lateral distribution. The reconstructed lateral distribution is too steep what results in an overestimation of the electron number for electron poor showers. The underestimation at large

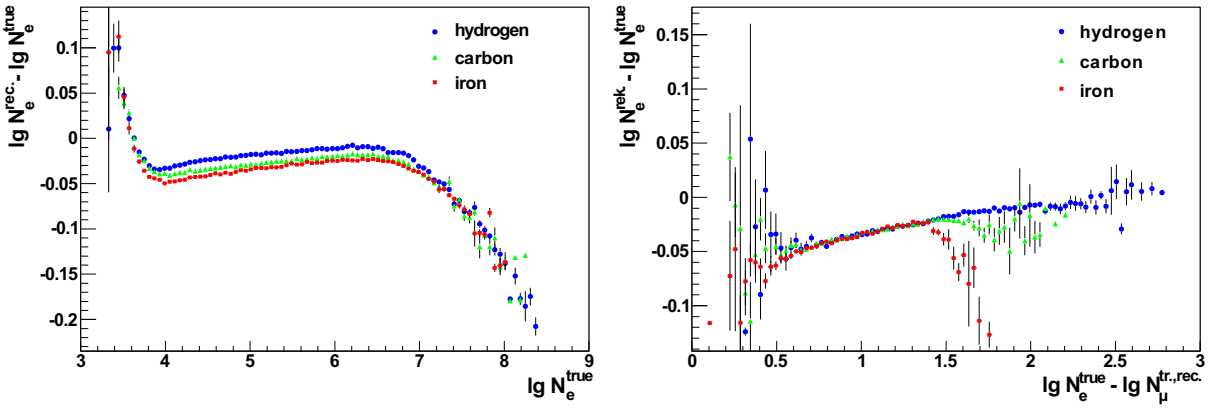


Figure 6.6: Systematic reconstruction uncertainties (lg $N_e^{rec.}$ - lg $N_e^{true}$) in the zenith angle range 0 - 18° subject to the true number of electrons lg $N_e^{true}$ (on the left) and subject to lg $N_e^{true}$ - lg $N_\mu^{tr.,rec}$ (on the right).

electron numbers can be explained by saturation effects. For these showers the detector stations close to the shower center are saturated and can provide only limited information on the particle density, what leads to an underestimation of the electron numbers. In addition this plot reveals a dependence of the reconstruction uncertainties on the primary particle type.
Over a wide range this primary particle dependence can be eliminated using as abscissa lg $N_e^{true}$ - lg $N_\mu^{tr.,rec}$, what is displayed in Figure 6.6 on the right. The strong correlation of the size of the systematic uncertainties with the fitted age parameter and the correlation of the age parameter with the distance to the shower maximum $X_{max}$. $X_{max}$ can be described by lg $N_e^{true}$ - lg $N_\mu^{tr.,true}$. Considering all correlations the size of the reconstruction uncertainties in the electron number can be characterised by a dependence on lg $N_e^{true}$ − lg $N_\mu^{tr.,true}$. The description improves by using lg $N_\mu^{tr.,rec.}$ instead of lg $N_\mu^{tr.,true}$, because of additionally taking into account a systematics due to a wrong correction of the electron number on muons. The advantage of the elimination of the primary particle dependence is the usage of only one correction function for all primary

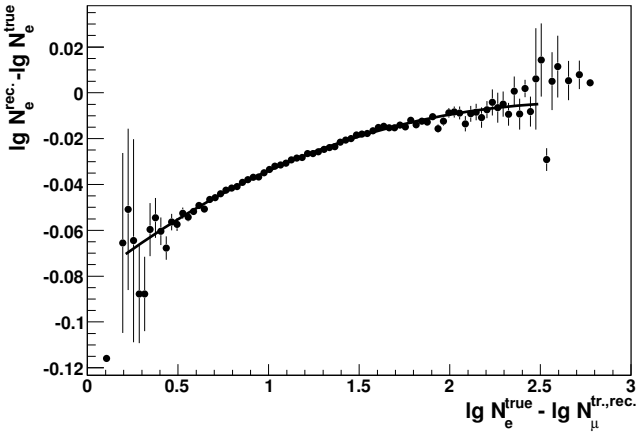


Figure 6.7: Systematic uncertainties averaged over all primary particle types subject to lg $N_e^{true}$ − lg $N_\mu^{tr.,rec}$ for zenith angles from 0 ° to 18 °.

particle types. Up to values of lg $N_e^{true}$ - lg $N_\mu^{tr.,rec} \approx 1.4$ no dependence on the primary particle mass can be found (see right part of Figure 6.6), but at higher lg $N_e^{true}$ - lg $N_\mu^{tr.,rec}$ values a split-up of the uncertainties dependent on the primary particle type can be observed, which is mainly due to showers with electron numbers lg $N_e^{true} > 6.5$. Figure 6.7 shows the systematic uncertainties averaged over all primary particle types subject to lg $N_e^{true}$ – lg $N_\mu^{tr.,rec}$ for zenith angles from 0 ° to 18 °. For correcting systematic reconstruction effects, a polynomial of third order is fitted and denoted as $C_e$(lg $N_e^{true}$, lg $N_\mu^{tr.,rec}$). The solid line in Figure 6.7 represents the parameterization of $C_e$. After having corrected for the systematic shift by applying the function $C_e$, the uncertainties in lg $N_e$ are mostly consistent with zero, solely at low and high electron numbers large systematic uncertainties are remaining. They are displayed in Figure 6.8. On the left hand side of Figure 6.8 the remaining systematics are shown for three different primary particle types (H, He and C). On the right the remaining systematics averaged over all primary particle types can be seen. The solid line displays the parameterization of the remaining

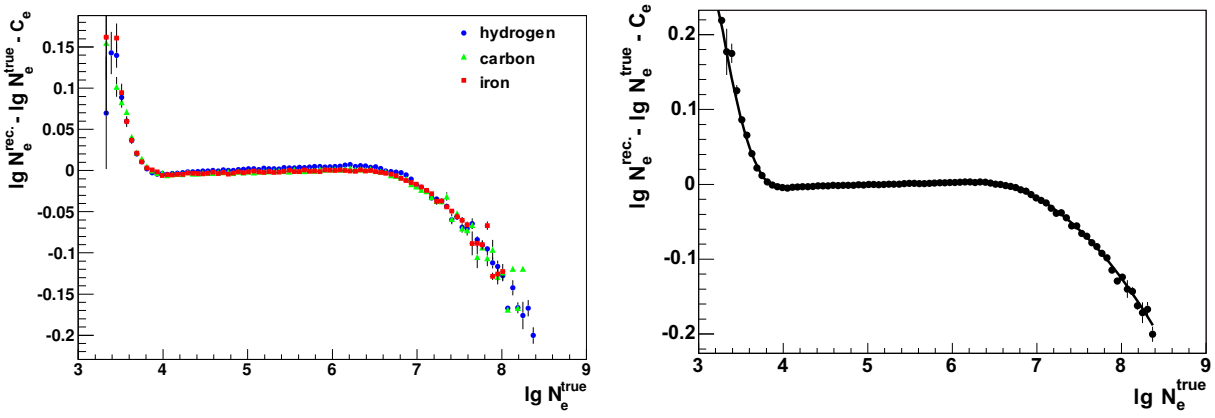


Figure 6.8: Remaining systematic uncertainties, after having applied the correction function $C_e$ in the zenith angle range 0 - 18° subject to the true number of electrons lg $N_e^{true}$ for H, C and Fe (on the left) and and averaged over all particles (on the right).

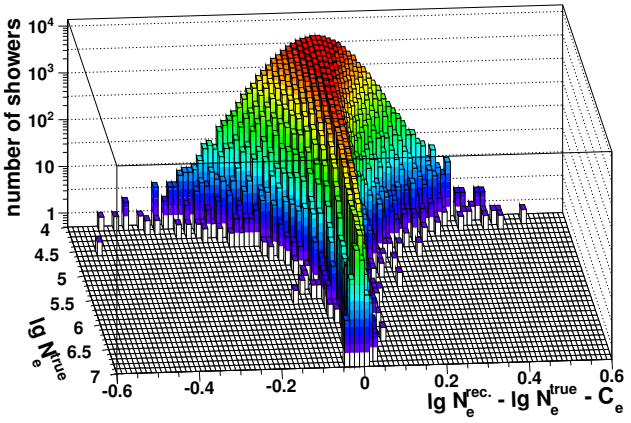


Figure 6.9: Distribution of the lg $N_e$ uncertainties as a function of lg $N_e^{true}$ after the correction of the systematics. The depictions contains events from 0 ° to 18 ° and of all primary particle types.

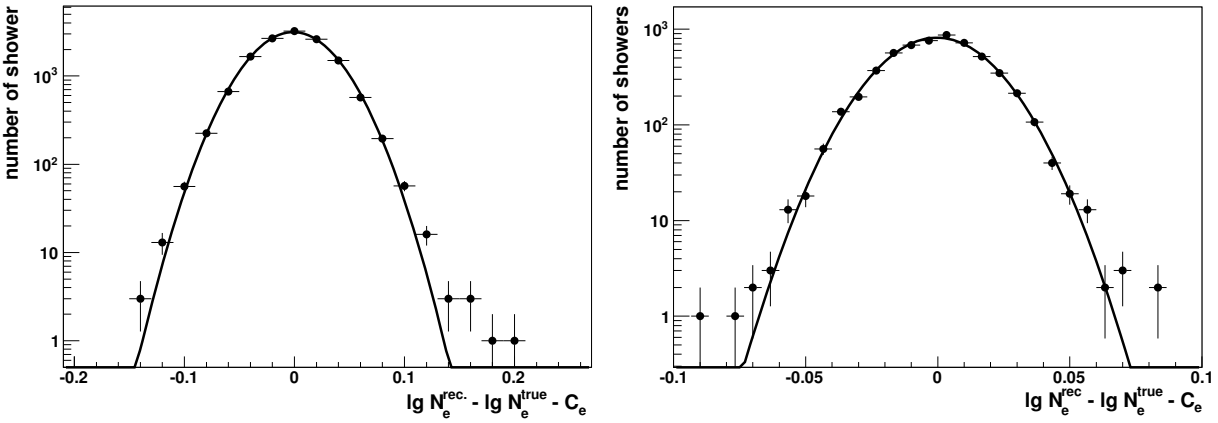


Figure 6.10: Distribution of the reconstruction uncertainties for two different lg $N_e^{true}$ intervals. $4.55 \leq \lg N_e^{true} \leq 4.6$ on the left and $5.05 \leq \lg N_e^{true} \leq 5.1$ on the right with the corresponding parameterization according to Equation 6.8.

systematic uncertainties according to

$$f(\lg N_e^{true}) = \begin{cases} p_2 + p_1 \cdot (\lg N_e^{true} - p_0)^2 & : \quad \lg N_e^{true} \leq p_0 \\ p_2 + p_3 \cdot (\lg N_e^{true} - p_0) & : \quad p_0 < \lg N_e^{true} < p_4 \\ p_2 + p_3 \cdot (p_4 - p_0) + (p_5 \cdot (\lg N_e^{true} - p_4)^2 & : \quad \lg N_e^{true} \geq p_4 \end{cases} \tag{6.7}$$

Figure 6.9 represents the distribution of the lg $N_e$ uncertainties as a function of lg $N_e^{true}$ after the correction of the systematics . The two-dimensional histogram illustrates again a consistency of the mean values of the distribution with zero and reveals a reduction of the distribution width with increasing electron number. The increase of the electron number leads to a more precise adjustment of the fitted function, whereby the width of the distribution diminishes. Each slice of this distribution, i. e. each lg $N_e^{true}$ − lg $N_\mu^{tr.,rec} - C_e$-distribution of a certain lg $N_e^{true}$ interval, can be parameterized by a Gaussian function according to

$$p(x) = n_0 \cdot \exp\left(-\frac{(x - e_1)^2}{2 \cdot e_2^2}\right). \tag{6.8}$$

The distribution of the reconstruction uncertainties for two different lg $N_e^{true}$ intervals is depicted in Figure 6.10. The parameter $n_0$ is the scaling parameter. The parameters $e_1$, $e_2$ and $e_3$ are determined for each lg $N_e^{true}$ interval and interpolated, so that the parameters are known for each electron number. The parameterizations of the reconstruction uncertainties for QGSJETII/ FLUKA are listed in Appendix B.1.

### 6.2.2 The reconstruction uncertainties in $N_\mu^{tr.}$ for KASCADE

The determination of the reconstruction uncertainties in the truncated number of muons is following the same procedure as described in the section before.
The primary particle dependence of the correction function can be eliminated using as abscissa the true electron number lg $N_e^{true}$ instead of the true number of truncated muons lg $N_\mu^{tr.,true}$. This effect is found to be due to the parameterization of the age parameter $s$, which is determined by simulations and averaged over all primary particles, and its dependence on the lg $N_e$. The systematic deviations and the correction functions $C_\mu$ (polynomial of third order) for zenith

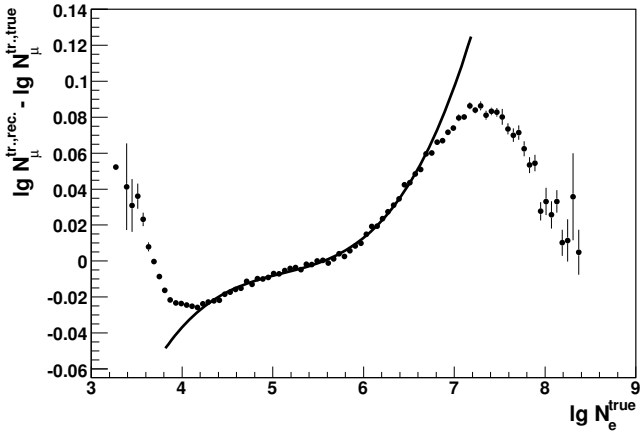


Figure 6.11: Systematic deviation of lg $N_\mu^{tr.,rec}$ and lg $N_\mu^{tr.,true}$ averaged over all primary particle types and the appendant parametrization for zenith angles from 0 ° to 18 °.

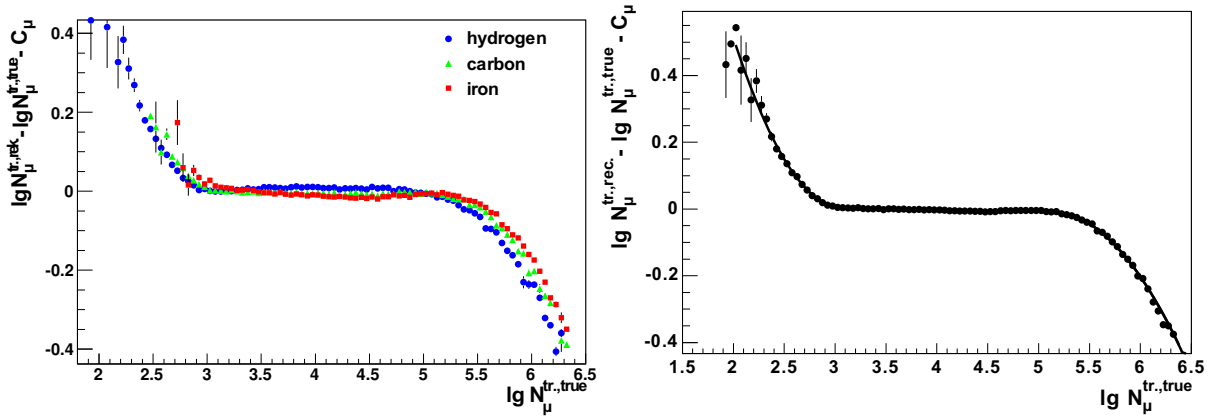


Figure 6.12: Remaining systematics, after having applied the correction function, in the zenith angle range 0 - 18° subject to the true number of muons lg $N_\mu^{true}$ for H, He and C (on the left) and averaged over all particles (on the right).

angles from 0 ° to 18 ° are shown in Figure 6.11. After having corrected the systematic deviations, the remaining systematic uncertainties for $2.9 \leq \lg N_\mu^{tr.,true} \leq 5.3$ are approximately zero (see Figure 6.12). The remaining systematic uncertainties can again be paramterised by a function according to 6.7. At low and high muon numbers an overestimation and an underestimation can be found, respectively. Whereas the overestimation at small number of muons can be related to the small number of responding detectors in small-sized events, the underestimation at high muon numbers originates from saturation effects, as it was already described for the electrons in the section before.
The distributions of the reconstruction uncertainties in $N_\mu^{tr.}$ are shown in Figure 6.13 for two different lg $N_\mu^{tr.,true}$ intervals. Up to lg $N_\mu^{tr.,true} \approx 4$ the statistical reconstruction uncertainties can be described by an asymmetric function given by

$$p(x) = \begin{cases} n_0 \cdot \exp\left(-\frac{(x-m_1)^2}{2 \cdot m_2^2}\right) & : \quad x > m_1 - \frac{m_2^2}{m_3} \\ n_1 \cdot \exp\left(\frac{x}{m_3}\right) & : \quad x \leq m_1 - \frac{m_2^2}{m_3} \end{cases} \tag{6.9}$$

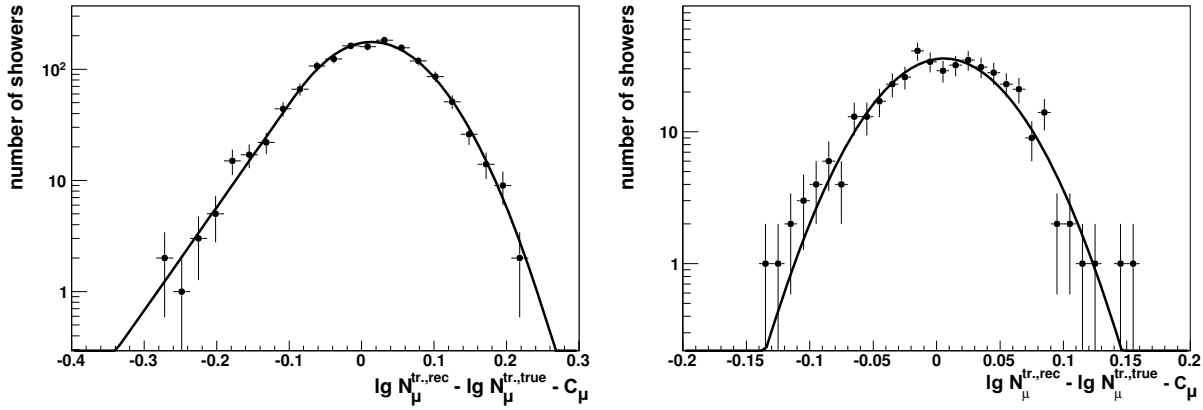


Figure 6.13: Distribution of the reconstruction uncertainties in lg $N_\mu^{tr.}$ for $3.75 < \lg N_\mu^{tr.,true} \leq 3.8$ (left) and for $4.3 < \lg N_\mu^{tr.,true} \leq 4.35$ (right).

The choice of the parameters $n_0$ and $n_1$ is defined by the requirement of continuous differentiability. At larger number of muons in a good approximation a Gaussian distribution can be assumed. For all lg $N_\mu^{true}$ intervals the parameters of the asymmetric and the Gaussian function are determined and interpolated. In the Appendix B.1 the parameterizations of the reconstruction uncertainties for QGSJETII/ FLUKA can be found.

### 6.2.3 The reconstruction uncertainties in $N_e$ for KASCADE-GRANDE

The reconstruction uncertainties for KASCADE-Grande are determined in a similar manner, as it was already explained for KASCADE in the previous sections.
In a first step the systematic reconstruction uncertainties are parameterized. The systematic deviations of lg $N_e^{rec}$ and lg $N_e^{true}$ subject to lg $N_e^{true}$ are shown on the left in Figure 6.14 for three different primary particles. The right side of Figure 6.14 displays the bias averaged over all primary particles. The plotted line displays exemplarily the correction function $C_e(\lg N_e^{true})$

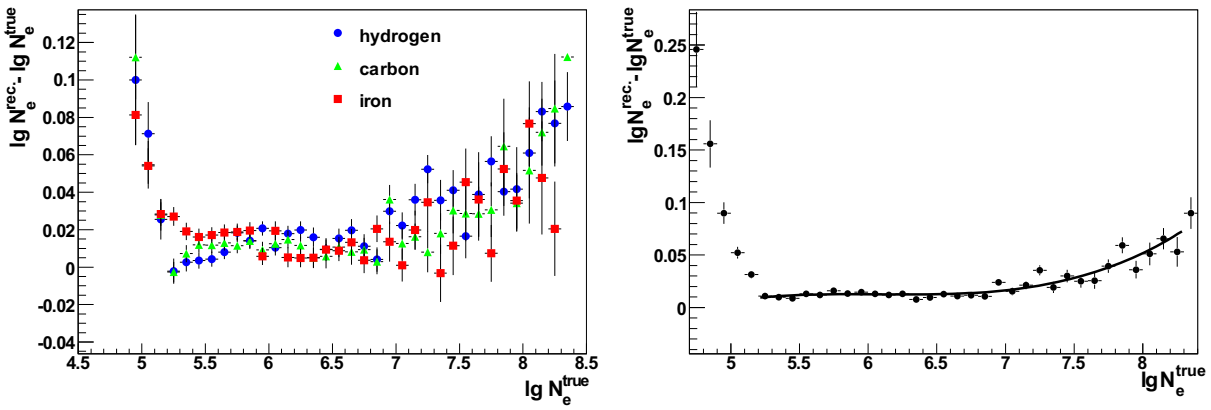


Figure 6.14: Systematic deviation of lg $N_e^{rec}$ and lg $N_e^{true}$ subject to lg $N_e^{true}$ for three different primary particle types in the zenith angle range from 0° to 18° (left) and averaged over all primary particle types (right).

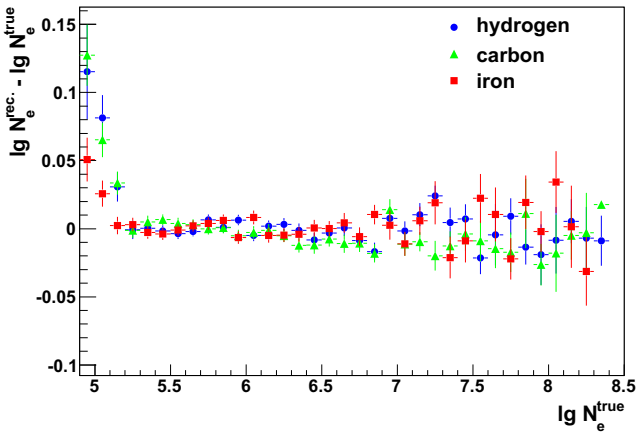


Figure 6.15: Remaining systematics subject to lg $N_e^{true}$ for three different primary particle types after the correction with a polynomial of third order $C_e$.

(averaged over all primary particle masses), which is given by a polynomial of third order. Due to the different reconstruction properties the systematic uncertainties for different primary particle types are determined separately. The overestimation at small electron numbers can be explained by the small number of triggered detector stations, resulting in a worse reconstruction. After having applied the correction function $C_e$, there are still systematic uncertainties remaining, which are shown in Figure 6.15 for three different primary particles. The remaining differences for different primary particle masses can be neglected due to the chosen bin width in the electron number of 0.08 and regarding the statistical error. While for electron numbers lg $N_e^{true}$ above approximately 5.2 the remaining bias is consistent with zero, at small electron numbers an overestimation can be observed.

The distribution of the reconstruction uncertainties in the electron number, after the correction of the bias, are displayed in Figure 6.16 for two different electron number intervals. A difference in the shape of the distribution of the reconstruction uncertainties for different primary masses

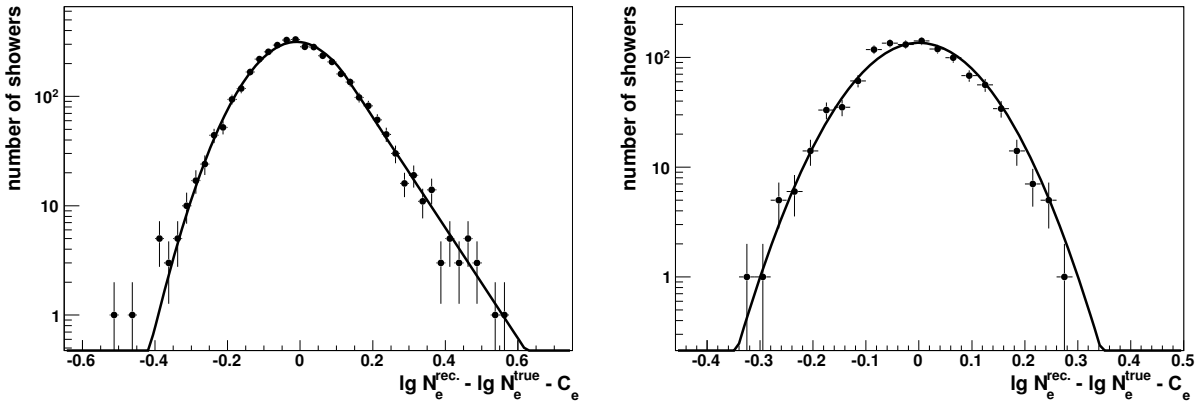


Figure 6.16: Distribution of the reconstruction uncertainties for two different lg $N_e^{true}$ intervals. $6.0 \leq \lg N_e^{true} \leq 6.1$ on the left and $6.7 \leq \lg N_e^{true} \leq 6.8$ on the right with the corresponding parameterization according to Equation 6.10. Here $C_e$ is the correction function, a polynomial of third order.

can not be observed. As in case of KASCADE the reconstruction uncertainties in the electron number can be parameterized by an asymmetric function according to.

$$p(x) = \begin{cases} n_0 \cdot \exp\left(-\frac{(x-e_1)^2}{2 \cdot e_2^2}\right) & : \quad x < e_1 - \frac{e_2^2}{e_3} \\ n_1 \cdot \exp\left(\frac{x}{e_3}\right) & : \quad x \geq e_1 - \frac{e_2^2}{e_3} \end{cases} \tag{6.10}$$

This asymmetric function passes into a Gaussian for $\lg N_e^{true} \geq 6.3$. Comparing the width of the distributions for KASCADE (see Figure 6.10) and for KASCADE-Grande it becomes obvious that the resolution in the electron number reconstruction for KASCADE-Grande is not as good as for KASCADE. The width of the distributions have a large effect on the response matrices and on the deconvolution results since they determine the resolution of the detector. The effect of the resolution on the results of the unfolding analysis will be discussed in Chapter 7. In the Appendix B.2 the parameterizations of the reconstruction uncertainties for QGSJETII/ FLUKA are shown.

### 6.2.4 The reconstruction uncertainties in $N_\mu$ for KASCADE-GRANDE

On the left side of Figure 6.17 the bias of the reconstruction of the muon number for KASCADE-Grande is shown for three different primary particle types. The averaging of the systematic uncertainties over all simulated primary particle masses is displayed in the right part of Figure 6.17. As an example the correction function $C_\mu$ (averaged over all primary particle masses) is displayed as solid line. As correction function a polynomial of third order is used. Again the systematic uncertainties for different primary particle types are determined separately due to the different reconstruction properties of the systematic uncertainties. After having applied the correction function $C_\mu$, there are still some systematics remaining. The remaining bias subject to $\lg N_\mu^{true}$ is shown in Figure 6.18 for three different primary particles. After the correction the remaining bias still shows an oscillating behaviour. Regarding the chosen bin width in the unfolding analysis ($\Delta lg\, N_\mu = 0.08$), the bias for muon numbers $\lg N_\mu^{true} > 4.4$ is after the correction consistent with zero and therefore insignificant.
Figure 6.19 displays the distribution of the reconstruction uncertainties in the muon number for two different $\lg N_\mu^{true}$ intervals. As parameterization an asymmetric function according to

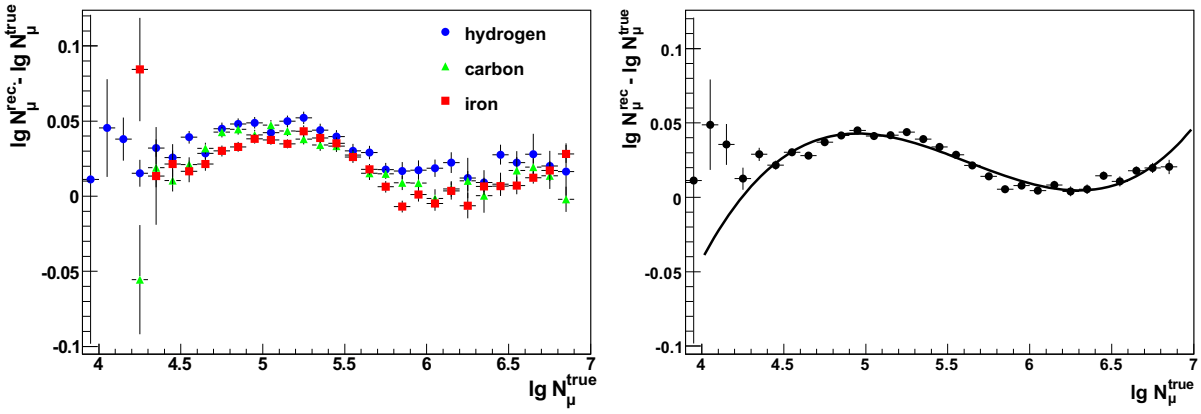


Figure 6.17: Systematic deviation of $\lg N_\mu^{rec}$ and $\lg N_\mu^{true}$ subject to $\lg N_\mu^{true}$ for three different primary particle types in the zenith angle range from 0° to 18° (left) and averaged over all primary particle types (right).

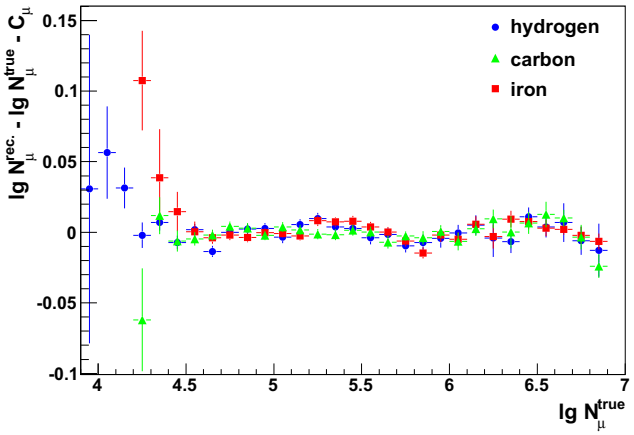


Figure 6.18: Systematics remaining after the correction with a polynomial of third order $C_\mu$ subject to lg $N_\mu^{true}$ for three different primary particles.

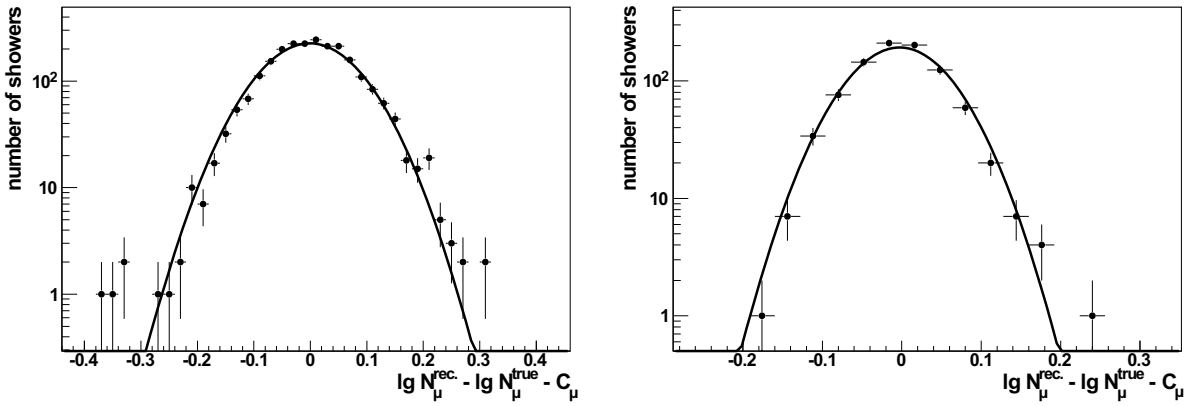


Figure 6.19: Distribution of the reconstruction uncertainties for two different lg $N_\mu^{true}$ intervals. $5.3 \leq \lg N_\mu^{true} \leq 5.4$ on the left and $5.7 \leq \lg N_\mu^{true} \leq 5.8$ on the right, both with the corresponding parameterization according to Equation 6.8. Here $C_\mu$ is the correction function, a polynomial of third order.

Equation 6.9 is used up to muon numbers lg $N_\mu^{true} = 5.2$ and for larger muon numbers a Gaussian is used. The distributions, being closely related to the detector resolution, play a prominent role in the determination of the response matrices and have a large effect on the results of the analysis.
The effect of the resolution on the results of the deconvolution are discussed in Chapter 7. Exemplarily the parameterizations of the reconstruction uncertainties for QGSJETII/ FLUKA are shown in Appendix B.2.

## 6.3 The combined trigger and reconstruction efficiencies

For the determination of the combined trigger and reconstruction efficiencies in dependence on the electron number lg $N_e$ and on the muon number lg $N_\mu$ the same simulation sets as for the determination of the reconstruction uncertainties are used. The combined trigger and

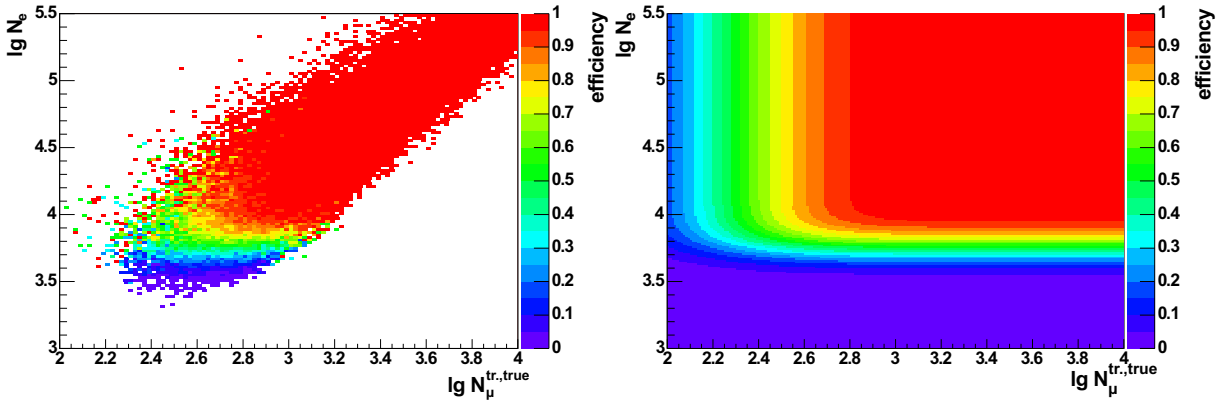


Figure 6.20: Two-dimensional efficiency (averaged over all primary particles) subject to lg $N_e^{true}$ and lg $N_\mu^{tr.,true}$ determined using simulations (on the left) and the fitted two-dimensional function according to 6.11 (on the right) for showers from 0 - 18 °

reconstruction efficiency gives the probability that an event with a certain electron or muon number, or a certain energy triggers the measurement and is properly reconstructed. Like in the discussion of the reconstruction uncertainties the efficiencies in case of KASCADE are discussed on basis of simulations with QGSJET01 in combination with FLUKA, while in case of KASCADE-Grande the efficiencies are reviewed on basis of QGSJETII and FLUKA.

### 6.3.1 The efficiencies of KASCADE

In addition to the shower fluctuations and the reconstruction uncertainties the trigger and reconstruction efficiencies have to be taken into consideration. Whereas the trigger efficiencies describe above which shower size, i. e. above which electron and muon number, respectively, the air showers trigger the detector, the reconstruction efficiencies characterize the shower size which is necessary for a proper reconstruction. In the following the combined trigger and reconstruction efficiencies are discussed.
The correlation of the reconstructed electron and muon number plays, due to its mass sensitivity, a key role in composition studies by means of deconvolution. The left part of Figure 6.20 shows the combined trigger and reconstruction efficiency in dependence on the electron and the truncated muon numbers based on simulations. The projections along the lg $N_e^{true}$ and the lg $N_\mu^{tr.,true}$ axis provide the efficiencies subject to lg $N_{e^{true}}$ and lg $N_\mu^{tr.,true}$, respectively. The right part of Figure 6.20 shows the parametrization used. As parameterization a two-dimensional Gauss error function according to

$$\epsilon(\lg N_e^{true}, \lg N_\mu^{tr.,true}) = \mathrm{erf}\left(\frac{\lg N_e - p_0}{p_1}\right) \cdot \mathrm{erf}\left(\frac{\lg N_\mu^{tr.,true} - p_2}{p_3}\right) \tag{6.11}$$

is used.
Figure 6.21 shows a comparison of the efficiencies of proton and iron induced events subject to lg $N_e^{true}$ (on the left) and lg $N_\mu^{tr.,true}$ (on the right) determined directly from simulations. The efficiencies calculated, taking into consideration the parameters $p_0 - p_3$ are displayed as solid lines. A good agreement of calculated and directly determined efficiencies can be found. The efficiencies for proton and iron induced air showers exhibit only small differences. These can be explained by the fact that the electromagnetic component, representing the bulk of

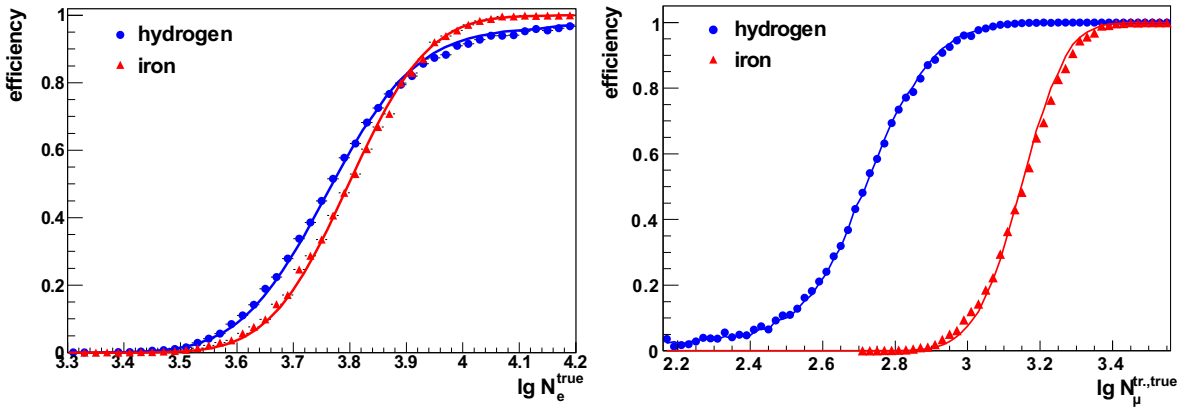


Figure 6.21: Comparison of directly determined and calculated efficiency subject to the electron number (on the left) and subject to the truncated muon number (on the right) for zenith angles from 0 ° to 18 °.

particles produced in an air shower, is primarily accountable for triggering the measurement and therefore the efficiencies subject to the electron number lg $N_e$ for different primary particle types show a similar behaviour. Whereas the efficiency for iron can be described by a pure error function, the efficiencies for proton feature a slightly flatter course for electron numbers in the range of $3.8 \leq \lg N_e^{true} \leq 4.6$. Proton induced air showers already hold at lower energies the same number of electrons as iron initiated air showers, but because of the lower energy and the lower cross section a less amount of muons is produced. The smaller number of muons and the fluctuations in the muon number lead to misreconstructed events, which cause a flatter course of the efficiencies.

The efficiencies subject to the truncated muon numbers lg $N_\mu^{tr.,true}$ for different primary particle masses(see right part of Figure 6.21) differ. Also here the reasons for the difference can be found in the applied trigger. The electromagnetic component is in general responsible

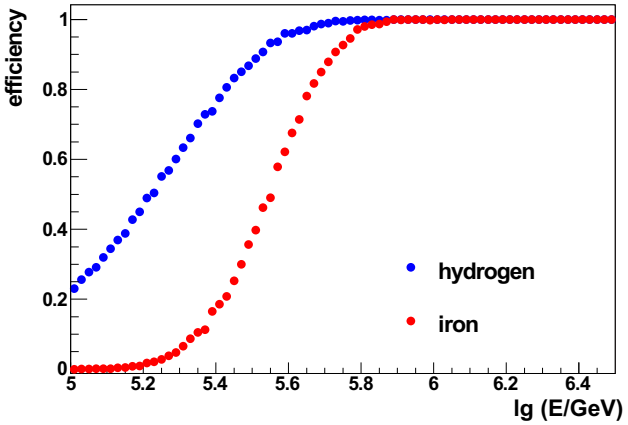


Figure 6.22: Efficiency for hydrogen and iron induced air showers subject to the true energy lg $E$.

for triggering the measurement. Since a proton induced air shower, holding the same number of electrons as an iron induced one, usually has a lower energy and for that reason and due to the smaller hadronic interaction cross section also a smaller number of muons, the efficiency in case of protons is shifted towards smaller muon numbers.

For completeness Figure 6.22 displays the efficiencies for hydrogen and iron induced air showers subject to the true energy lg $E$. The shift of the efficiencies of different primary particle types can be explained by the same reason as in case of the muon efficiencies. Proton induced air showers hold more electrons at observation level than iron induced air showers, i. e. the efficiency for protons is shifted to lower energies.

For shower in the zenith angle range from 0° to 18° the experiment is fully efficient above an electron number lg $N_e$ of approximately 4.5, a truncated muon number lg $N_\mu^{tr.}$ of about 3.4 and an energy lg $E$ of circa 5.8 (in GeV).
Both, the parameterization of the efficiencies subject to the electron number and the truncated muon number, are used for the calculation of the response functions (see Section 6.4). In the Appendix C.1 the parameters of the efficiencies based upon QGSJETII/ FLUKA simulations can be found for all primary masses.

### 6.3.2 The efficiencies of KASCADE-Grande

In the left part of Figure 6.23 the two-dimensional efficiency subject to lg $N_e^{true}$ and lg $N_\mu^{true}$ (averaged over all primary particles) is shown, the right part comprises the two-dimensional parameterization according to Equation 6.11. The trigger and reconstruction efficiencies subject to the electron number lg $N_e^{true}$ and the muon number lg $N_\mu^{true}$ can be found in Figure 6.24. The drawn lines display the parameterizations used, which are determined in a similar approach as already described in Section 6.3.1. The efficiencies as a function of the electron and the muon number both differ for different primary particles. The efficiencies subject to the electron number lg $N_e^{true}$ for hydrogen and iron induced air showers are displayed in the right part of Figure 6.24. Proton induced air showers, having the same energy as iron induced events, hold at observation level more electrons but fewer muons and therefore the efficiency subject to the electron number lg $N_e^{true}$ for hydrogen is shifted to higher electron numbers, whereas the

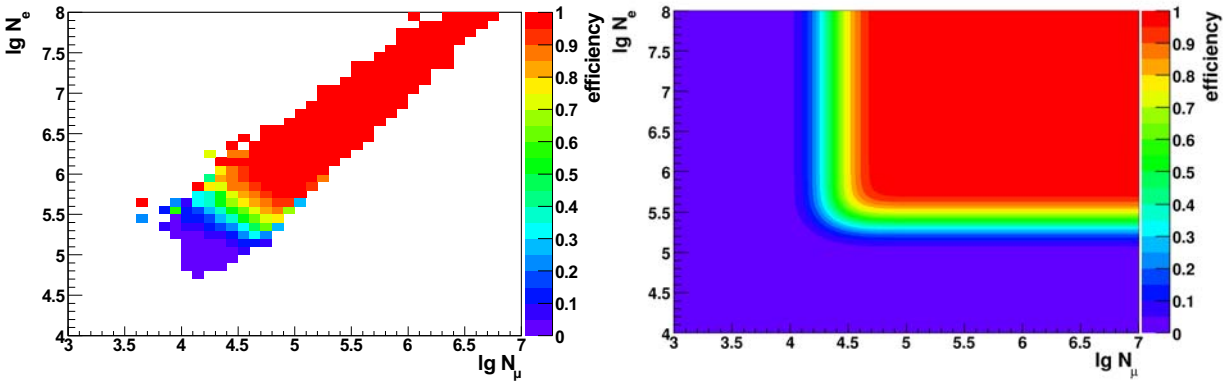


Figure 6.23: Two-dimensional efficiency averaged over all primary particles (0 - 18°) can be found in the left part and the corresponding parametrization is displayed on the right.

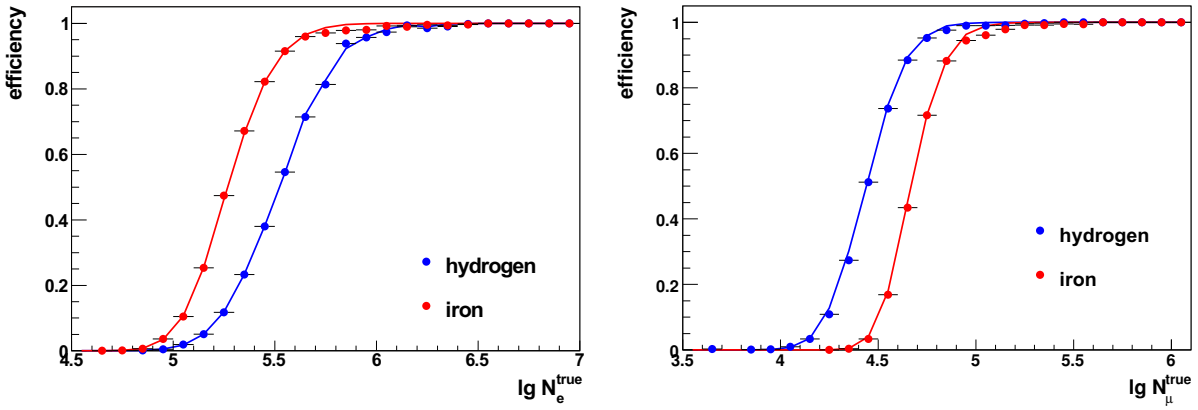


Figure 6.24: Comparison of directly determined and calculated efficiency subject to the electron number (on the left) and subject to the muon number (on the right) for a zenith angle range 0 - 18 °.

efficiency subject to the muon number lg $N_\mu^{true}$ is shifted to smaller muon numbers, both with respect to iron. Both effects can be explained by the trigger and reconstruction characteristics of the Grande detector. In case of KASCADE mainly the electrons are responsible for triggering the measurement. The Grande array is triggered by the total number of charged particles, i. e. by the sum of electrons and muons. For that reasons the efficiencies of different primary particle types subject to the number of charged particles lg $N_{ch}^{true}$ show only small differences, what is displayed in the left part of Figure 6.25. The occurrence of small deviations can be explained by the reconstruction of the muon number, which is performed using the muon detectors of the KASCADE array. Proton induced events have, at the same energy, less muons than iron induced air showers. Furthermore iron nuclei interact earlier in the atmosphere and the muons can, due to their higher production height, travel larger distances away from the shower core, so that, if the shower core is far away from the KASCADE array, more muons (with respect to hydrogen) reach the muon detectors. These two effects result in a slight shift of the efficiency

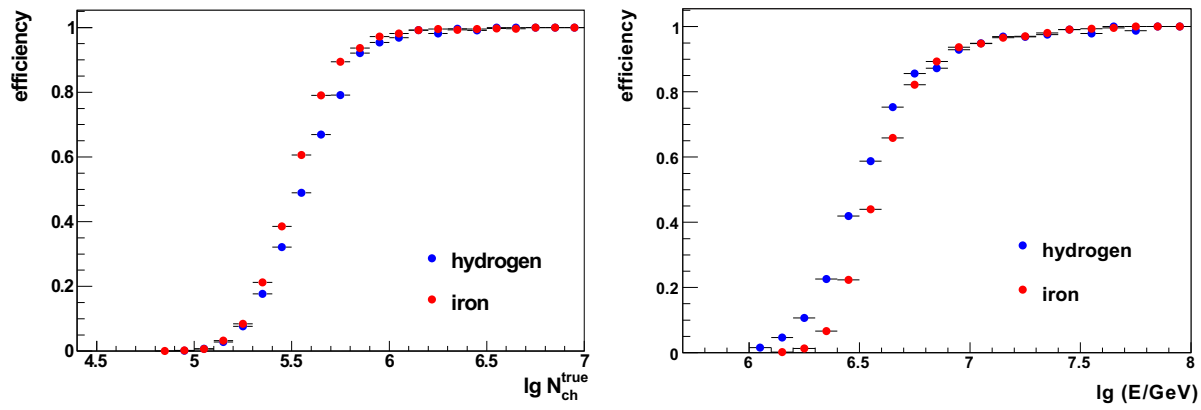


Figure 6.25: Efficiency of proton and iron induced air showers subject to the the number of charged particles lg $N_{ch}^{true}$ (on the left) and subject to the true energy lg $E$ (on the right) for showers from 0 ° to 18 °.

subject to lg $N_{ch}^{true}$ of iron induced showers to lower charged particle numbers.
The efficiency subject to the true energy lg $E$ can be found in the right part of Figure 6.25. The slight differences of the efficiencies of different primary particle masses can be traced back to the different amount of electrons and muons, characterising showers of different primary particle masses at observation level. Since electrons account for the main part of particles produced in an air shower cascade and showers initiated by hydrogen contain at the same energy at observation level more electrons, the efficiency for hydrogen is slightly shifted to lower energies.
For the determination of the response functions (see Section 6.4) only the efficiencies as a function of the number of electrons lg $N_e^{true}$ and the number of muons lg $N_\mu^{true}$ are taken into account. In the Appendix C.2 the parameters of the efficiencies based upon QGSJETII/ FLUKA simulations are listed.

## 6.4 The response matrices

Most essential for the unfolding analysis are the so-called response functions or response matrices. After having determined the shower to shower fluctuations and the reconstruction properties in the electron and muon number (reconstruction uncertainties and efficiencies), as it was described in the sections before, the response functions or response matrices can be calculated.
The two-dimensional size spectra of electron and muon numbers (see Figure 5.2 and 5.3) displays the data vector $\vec{Y}$ in the matrix equation $\vec{Y} = \mathbf{R}\vec{X}$. The content of each cell of the lg $N_e$-lg $N_\mu$-distribution and the lg $N_e$-lg $N_\mu^{tr.}$-distribution, respectively, corresponds to one component $Y_j$ of the data vector. The indexing starts at the lower left corner of the histogram and continues line by line from the left to the right. The vector of unknowns $\vec{X}$, including contributions of 5 different primary particle types(H, He, C, Si and Fe), represents the sought-after energy spectra and consists of 5 subvectors. For that reason the response matrices $\mathbf{R}$ are composed of 5 submatrices.
The vector of unknowns $\vec{X}$ and the response matrices can be written as

$$\mathbf{R} = (\mathbf{R}^{\mathrm{H}} \;\; \mathbf{R}^{\mathrm{He}} \;\; \mathbf{R}^{\mathrm{C}} \;\; \mathbf{R}^{\mathrm{Si}} \;\; \mathbf{R}^{\mathrm{Fe}}) \qquad \text{and} \qquad \vec{X} = \begin{pmatrix} \vec{X}^{H} \\ \vec{X}^{He} \\ \vec{X}^{C} \\ \vec{X}^{Si} \\ \vec{X}^{Fe} \end{pmatrix}. \tag{6.12}$$

The elements of the response matrix $\mathbf{R}^A$ of an element with mass number $A$ is calculated according to

$$R_{ij}^{A} = \frac{\int_{\lg E_j}^{\lg E_j + \Delta \lg E} d\lg E \, p_A(\lg N_e, \lg N_\mu | \lg E) J_A(\lg E)}{\int_{\lg E_j}^{\lg E_j + \Delta \lg E} d\lg E J_A(\lg E)}. \tag{6.13}$$

The probability $p_A$, consisting of the shower fluctuations $s_A$, the reconstruction uncertainties $r_A$ and the efficiencies $\epsilon_A$, in general defines the energy resolution of the resolution of the analysis. In Equation 6.13 the term $J_A(\lg E)$ stands for the flux of a particle with mass number $A$, in principle the sought-after vector $\vec{X}$.
The large statistics of the measurement in combination with the precise reconstruction allows an energy binning of $\Delta \lg E = 0.1$ for KASCADE, whereas the number of reconstructed events and the reconstruction properties of KASCADE-Grande lead to an enlarged binning ($\Delta \lg E = 0.14$). For the calculation of the response functions each energy bin is itself subdivided into intervals, each with a width of 0.01 in logarithmic scale. As the sought-after flux $J_A$ of each primary particle with mass number A is essential for the calculation of the response functions (see 6.13),

an energy spectrum $\propto E^{-3}$ is adopted for all elements. Due to the sufficiently small binning within each energy bin, the exact shape of the flux plays only an inferior role for the calculation of the response matrices.
As for the determination of the probability $p_A$ simulations are applied, the response matrices strongly depend on the underlying hadronic interaction models. The impact of different interaction models on the results of the analysis is discussed in Chapter 8.

# Chapter 7

# Test of the method

Goal of the present deconvolution analysis is the determination of the energy spectra for different mass groups for KASCADE as well as for KASCADE-Grande and the reconstruction of the all-particle spectrum. Both experiments differ significantly in the reconstruction characteristics. Whereas the KASCADE detector is able to reconstruct the shower sizes very precisely, the determination of the electron and the muon number in case of KASCADE-Grande can not be performed with the same precision as for KASCADE. The reconstruction properties, especially the distribution of the reconstruction uncertainties (see Chapter 6), can affect the results of the analysis enormously. The width of the distribution of the reconstruction uncertainties is in the following sections denoted as detector resolution or just resolution. Figure 7.1 comprises the width (sigma) of the shower fluctuations and the resolution in the electron number subject to lg $N_e$ for KASCADE and KASCADE-Grande. The graphs are completely based on simulations, using as hadronic high-energy interaction model QGSJETII and as low-energy interaction model FLUKA. The use of other interaction models does qualitatively not change this diagram. As it can be seen in Figure 7.1 the resolution in the electron number for KASCADE is small in comparison with the intrinsic shower fluctuations of hydrogen as well as iron. For KASCADE-Grande the resolution is of comparable size to the shower fluctuations of iron initiated air showers and smaller than the fluctuations of hydrogen induced showers. In Figure 7.2 the same relations

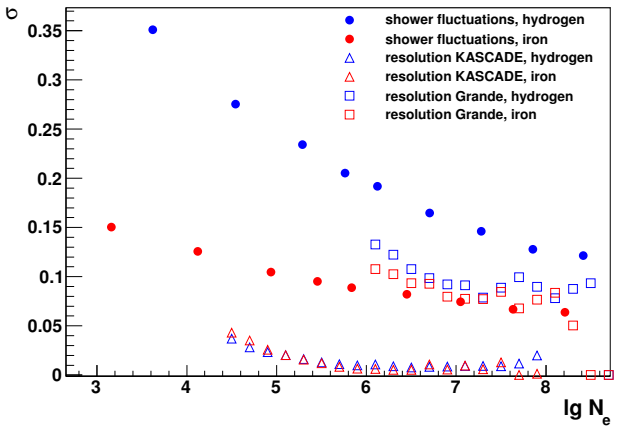


Figure 7.1: Comparison of the spread $\sigma$ of the shower fluctuations in the electron number and the resolution for KASCADE and KASCADE-Grande subject to the electron number lg $N_e$. In the simulations the interaction models QGSJET01 and FLUKA are used.

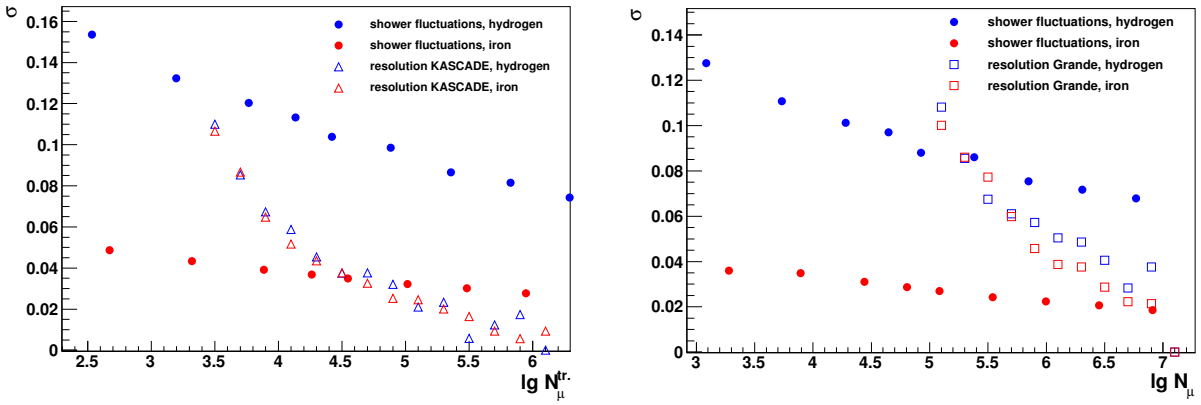


Figure 7.2: Comparison of the spread $\sigma$ of the shower fluctuations and the resolution in the muon number lg $N_\mu$. For KASCADE instead of the muon number lg $N_\mu$ the truncated muon number lg $N_\mu^{tr.}$ is used. In the simulations the interaction models QGSJETII and FLUKA are applied.

are shown for muons. Since KASCADE uses as observable the truncated muon number $N_\mu^{tr.}$ and KASCADE-Grande the total number of muons $N_\mu$ a combined depiction is not feasible. For KASCADE (see left part of Figure 7.2) the resolution at small truncated muon numbers is larger than the width of the shower fluctuations of iron induced showers, but for hydrogen both quantities are of comparable size. With increasing shower size the resolution as well as the shower fluctuations of both elements decrease, whereat the resolution drops faster and reaches at large truncated muon numbers even smaller values than the shower fluctuations of iron induced events. For KASCADE-Grande (see right part of Figure 7.2) at small muon numbers the reconstruction uncertainties exceed the shower fluctuations of both elements, but with increasing muon number the resolution converges to the width of the shower fluctuations of iron. Like for KASCADE the resolution decreases faster than the width of the shower fluctuations. Regarding Figure 7.1 and Figure 7.2 it becomes obvious that both experiments differ significantly in the reconstruction quality of the electron number, but the difference in the muon reconstruction is less pronounced. As a result of the reconstruction properties of the KASCADE-Grande experiment, which are not as good as for KASCADE, achieving results of similar quality for both experiments is not expected. For an evaluation of the unfolding results the use of Monte Carlo methods is indispensable. Furthermore, the use of Monte Carlo data allows the comparison of the true and the reconstructed energy spectra and therefore offers the possibility of studying the systematic uncertainties, also denoted as bias, as well as the statistical uncertainties of the method for different sets of test spectra. The application of the Gold deconvolution, an iterative method, requires in addition the determination of a stop criterion. Subject of the following sections are the estimations of the statistical uncertainties, the bias and the stop criterion for KASCADE and KASCADE-Grande. In addition the reconstruction of energy spectra is discussed for both experiments on basis of different test sets.

## 7.1 Monte Carlo tests

By means of Monte Carlo methods the deconvolution technique itself as well as the effect of the resolution and the data statistics on the results of the analysis can be tested. On basis of a

| element | $\gamma_1$ | $\gamma_2$ | $E_{knee}$ in PeV | $\epsilon$ |
|---|---|---|---|---|
| hydrogen | -2.9 | -4.4 | 4.0 | 3.0 |
| helium | -2.7 | -4.0 | 8.0 | 3.0 |
| carbon | -2.7 | -4.0 | 24.0 | 3.0 |
| silicon | -2.5 | -4.0 | 56.0 | 3.0 |
| iron | -2.5 | -2.5 | 104.0 | 3.0 |

Table 7.1: Parameters of the (KASCADE-like) energy spectra, which are generated according to equation 7.1.

random generator different sets of energy spectra can be produced according to

$$\frac{dI(E)}{dE} \propto E^{\gamma_1} \left(1 + \left(\frac{E}{E_{knee}}\right)^{\epsilon}\right)^{(\gamma_2-\gamma_1)/\epsilon} . \tag{7.1}$$

In equation 7.1 the variable $E_{knee}$ denotes the energy of the knee, $\gamma_1$ is the spectral index before the knee, $\gamma_2$ the index after the knee and $\epsilon$ assigns the width of the knee region. The variation of these parameters allows the simulation of energy spectra with different knee positions and different shapes for the individual elements. Furthermore, an additional scaling factor offers the possibility of varying the composition and the statistics. Again with the help of a random generator the two dimensional size spectrum of electron and muon numbers can be generated, using the produced energy spectra and the calculated response functions. The deconvolution of the resulting lg $N_e$-lg $N_\mu$-distributions allows the comparison of true (simulated) and reconstructed energy spectra.

## 7.2 KASCADE

### 7.2.1 Statistical uncertainties, bias and stop criterion

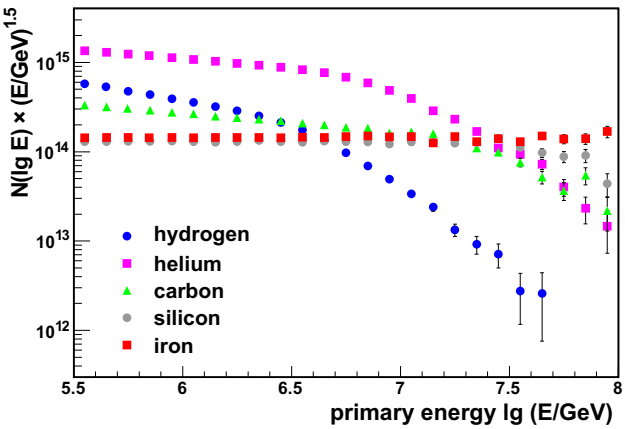


Figure 7.3: Test spectra, which are used for the discussion of the statistical uncertainties, the bias and the stop criterion for the KASCADE analysis.

The estimation of the statistical uncertainties and of the bias of the method is a crucial point in the deconvolution analysis. As described in Section 4.7 for their determination a frequentist

approach is used. Both, statistical uncertainties and bias, are indispensable for the determination of the stop criterion or the choice of regularisation parameter, discussed in Section 4.8. The following sections deal with the estimation of the statistical uncertainties, the bias and the determination of the stop criterion (weighted mean squared error WMSE) for the Gold deconvolution, which is the unfolding method used in this analysis.
Using Monte Carlo data provides the opportunity of comparing the "true" and the estimated quantities. For the determination of the "true" quantities, on basis of a random generator, K subsets of energy spectra of different primary particle types (hydrogen, helium, carbon, silicon and iron) and the corresponding two dimensional size spectra of electron and muon numbers are generated. The parameters according to Table 7.1 are identical for each of the K subsets, but the initialisation parameter of the random generator, also known as random seed, is varied for each of the K subsets. Thus, the underlying probability density functions are identical, but a variation of the seed leads to K different test sets, being compatible within the statistical uncertainties. The knowledge of the unfolded energy spectra as well as of the true energy spectra allows the determination of the bias, the statistical uncertainties and the stop criterion without estimation. The K data sets are unfolded with different iteration levels, corresponding to a different number of iterations. The statistical uncertainty of each bin is the spread of the K solutions and the bias is given by the mean value of the differences of the unfolded and the true spectra. The results based upon this data sets are in the following referred to as "true" statistical uncertainties, "true" bias and "true" WMSE. As specification of the iteration level, different measures are conceivable. Here the $\Delta\chi^2$ value, which characterises the difference in the $\chi^2$/n.d.f. of two successive iteration steps, is used.
In case of measured data solely the two-dimensional size spectrum of electron and muon numbers is known. In order to simulate the reality, only one lg $N_e$-lg $N_\mu$-distribution, the original distribution, is produced and the true spectra of the individual elements are unknown. To estimate the statistical uncertainties this single two-dimensional distribution is interpreted as a probability density function, according to which K new lg $N_e$-lg $N_\mu$-distributions are generated. The estimation of the statistical uncertainties can be performed in a similar manner, as it was described for the true quantities. The K sets are unfolded and the spread in each energy bin describes the statistical uncertainties. An estimation of the systematic uncertainties is more difficult, since the true spectra are unknown. Thus, the original distribution is unfolded for different iteration levels, leading to the knowledge of the individual energy spectra. The solutions, being assumed to reflect the truth, are used as basis or pattern for the generation of K new data subsets. The K subsets belonging to the different patterns are unfolded for different $\Delta\chi^2$ and compared to the pattern, which are now treated like the true spectra. Results derived by the use of these data sets are denoted as estimated statistical uncertainties, estimated bias and estimated WMSE.
Subject of the following sections is the comparison of the "true" and the estimated quantities for KASCADE. The energy spectra, being used for the discussion of the statistical uncertainties, the bias and the stop criterion of KASCADE, can be found in Figure 7.3 and Table 7.1. The abundances are chosen similarly to the results of the unfolding analysis of KASCADE data (see Chapter 8.3), which are obtained using in the analysis as hadronic high-energy interaction model QGSJET01 and for the description of hadronic low-energy interactions FLUKA. The choice of an identical index $\gamma$ before and after the knee in case of the iron spectrum does not have any effect on the simulated spectra, as the knee position of 104 PeV is not inside the measurement range of KASCADE.

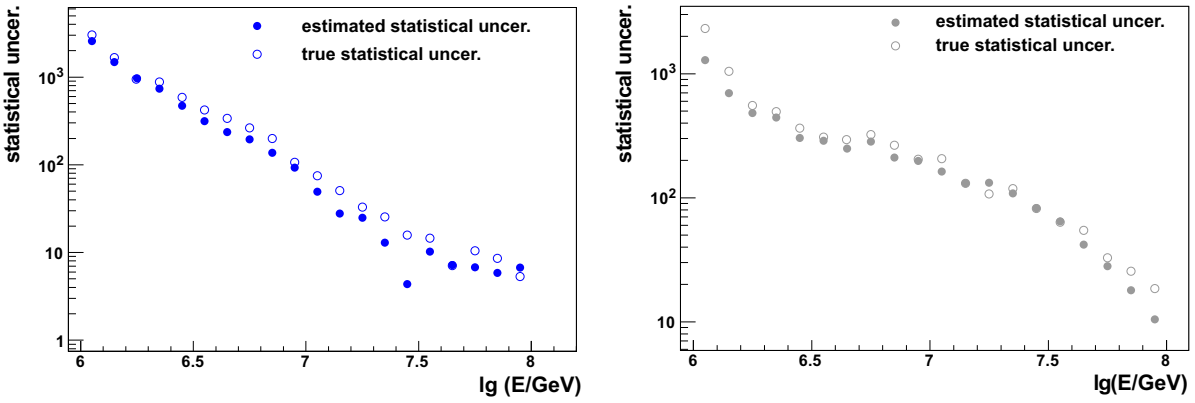


Figure 7.4: True and estimated statistical uncertainties of the hydrogen spectrum (on the left) and the silicon spectrum (on the right) at an iteration level $\Delta\chi^2 = 0.0008$.

#### 7.2.1.1 Statistical uncertainties

The statistical uncertainty of the unfolding method in each energy bin is defined as

$$\sigma_i = \sqrt{\frac{1}{K}\sum_{k=1}^{K}(\mu_{i,k} - \bar{\mu_i})^2}, \quad \text{with} \quad \bar{\mu} = \frac{1}{K}\sum_{k=1}^{K}\mu_{i,k}. \tag{7.2}$$

In this formula $\bar{\mu_i}$ represents the mean value of the $ith$ energy bin of the reconstructed energy spectrum and $\mu_{i,k}$ displays the $ith$ bin content of the $kth$ reconstructed subset. The upper limit of the sum ($K = 50$) is chosen to find a good trade-off between sufficient statistics and short computing time. In Figure 7.4 a comparison of the true and the estimated statistical uncertainties of the hydrogen spectrum (on the left) and of the silicon spectrum (on the right) can be found. The graphs of hydrogen and silicon are chosen as representatives, but the shapes of the statistical uncertainties do not differ qualitatively for the other primary particle types. Silicon is chosen instead of iron as representative of the heavier primary particles, since in the test set the silicon spectrum seems to be affected by larger uncertainties than the iron spectrum (see 7.9). For the calculation of the two-dimensional shower size spectra as well as for the deconvolution the hadronic interaction models QGSJET01 and FLUKA are used. Figure 7.4 depicts the absolute statistical uncertainties subject to the logarithmic energy for an iteration level $\Delta\chi^2 = 0.0008$. The choice of the iteration level, which is equivalent to the stop criterion, is explained later in this chapter. The graphs illustrate a good agreement of true and estimated uncertainties and evidence that the estimation of the statistical uncertainties works quite successfully. Using other interaction models, for example EPOS1.99 instead of QGSJET01, does not change this finding. As the estimated statistical uncertainties are directly used as uncertainties of the reconstructed spectra, they have to be recalculated for each new data set.

#### 7.2.1.2 Bias

The bias of each bin is given by

$$b_i = \frac{1}{K}\sum_{k=1}^{K}(\mu_{i,k} - \bar{\mu_i}). \tag{7.3}$$

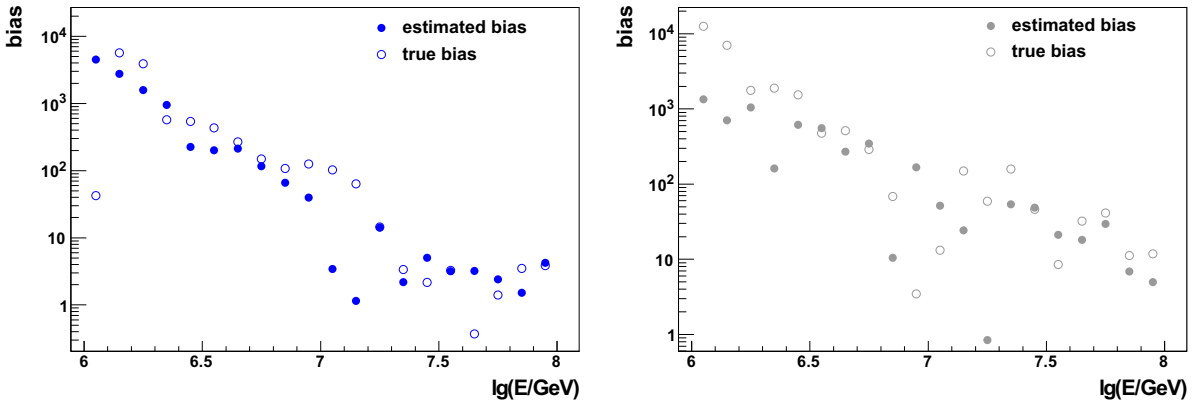


Figure 7.5: True and estimated bias of the hydrogen spectrum on the left and the silicon spectrum on the right at an iteration level $\Delta\chi^2 = 0.0008$.

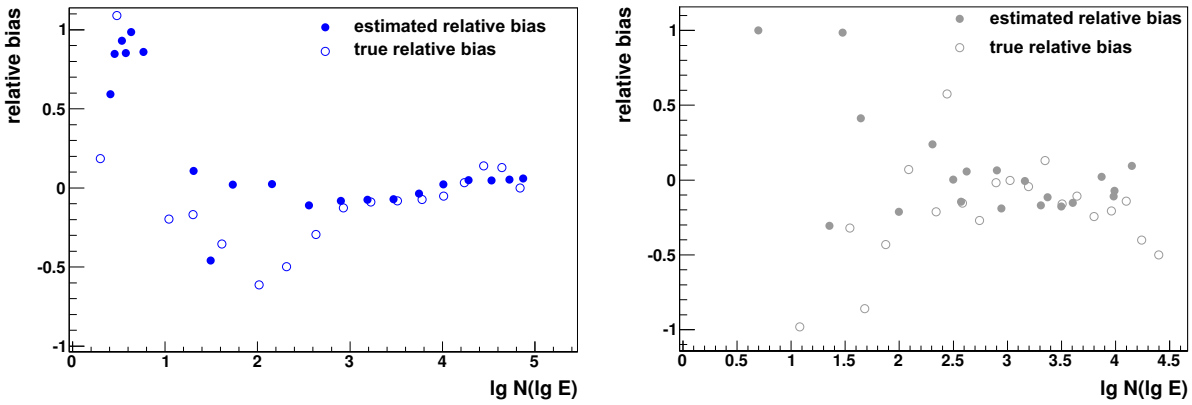


Figure 7.6: True and estimated relative bias subject to the logarithm of the number of showers lg $N(\lg E)$ in a certain energy bin at an iteration level $\Delta\chi^2 = 0.0008$. The relative bias for the hydrogen spectrum is shown on the left and for the silicon spectrum it can be found on the right part, using as hadronic interaction models QGSJET01 and FLUKA.

$\mu_{i,k}$ represents the i$th$ bin content of the k$th$ unfolded subset of energy spectra. $\bar{\mu}_i$ is calculated differently for the two different data sets (one for the "true", the other for the estimated quantities).
The knowledge of the true spectra allows the determination of the systematic uncertainties with respect to the true values, i. e. in this case $\bar{\mu}_i$ represents the i$th$ bin content of the true spectrum. The bias, obtained with this data set, is referred to as the true bias.

For the second data set, which is supposed to simulate the measured data, the true energy spectra are unknown. To estimate the bias anyway, the data is unfolded with an iteration level $\Delta\chi^2 = 0.0008$ and the solutions serve as patterns in order to represent the truth. In that case $\bar{\mu}_i$ stands for the mean value of the i$th$ bin averaged over all K sets. The bias obtained using this data is called the estimated bias.
For an iteration level $\Delta\chi^2 = 0.0008$ the bias subject to the energy is shown in Figure 7.5 for hydrogen and silicon induced air showers. The sign of the bias can not be definitely determined,

for which reason the absolute values of the bias are displayed. The general trend can indeed be reproduced, but the comparison of the true and the estimated values also reveals large differences. Thus, the necessity of an absolute bias becomes obvious.
Figure 7.6 displays the relative bias of the hydrogen and the silicon spectrum subject to the logarithm of the number of showers lg $N(\lg E)$ in a certain energy, without using the absolute values. As abscissa now lg $N(\lg E)$ is used instead of the lg $E$ to make clear below which number of reconstructed events in a single energy bin, a proper reconstruction is no longer possible. On basis of this depiction the bias on the reconstructed spectra can be roughly estimated to $\approx 30\%$. In regions where the relative bias exceeds 30 per cent, the total uncertainty of the method is dominated by the contribution of the statistical uncertainty, so that the exact shape of the bias is not of interest. If in a certain energy bin less than 10 showers are reconstructed the bias is assumed to be 10. This estimation is valid for all energy spectra and leads to a rapid increase of the bias in the depiction of the energy spectra multiplied by $E^{2.5}$, if less than 10 events are reconstructed in one bin.
The unfolded spectra, including the statistical and systematic uncertainties, are discussed in Section 7.2.2.

#### 7.2.1.3 Stop criterion

The choice of the stop criterion, characterising the trade-off between statistical uncertainties and bias, plays a fundamental role in the deconvolution analysis. When the iteration is stopped both, statistical uncertainties and bias, are of the same order of magnitude. As explained in Section 4.8 several criteria are conceivable for the determination of the stop criterion, but in the following as criterion the so-called weighted mean squared error WMSE is used. A proper determination of the stop criterion requires a good estimation of the uncertainties (statistical uncertainties and bias) and vice versa. After having estimated the uncertainties the WMSE can be calculated via

$$\mathrm{WMSE} = \frac{1}{M} \sum_{i=1}^{M} \frac{\sigma_i^2 + b_i^2}{\mu_i}, \tag{7.4}$$

where $\sigma_i$ is the statistical uncertainty and $b_i$ the bias of the $ith$ bin of the energy spectrum. The upper limit of the sum $M$ is given by the number of energy bins of an energy spectrum. A comparison of true and estimated WMSEs can be found in Figure 7.7. The WMSE calculated

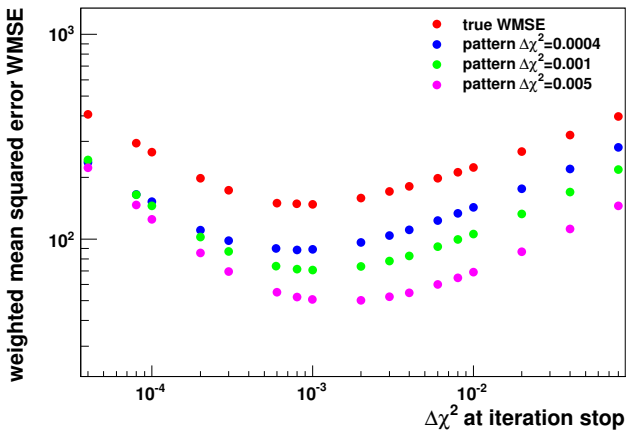


Figure 7.7: Comparison of the true and the estimated weighted mean squared error WMSE.

using the "true" statistical uncertainties, the "true" bias and as weighting $\mu_i$ the mean value of the $ith$ bin of the K spectra, is referred to as "true" WMSE. The other graphs originate from different patterns. A minimum can be found in each course of the WMSE. The positions of the minima are slightly shifted for different patterns. If the $\Delta\chi^2$ value of the pattern is larger than the $\Delta\chi^2$ value at the minimum, the estimation is not useful, because the iteration was aborted too early and therefore the pattern was not properly reconstructed. For patterns with a $\Delta\chi^2$ value smaller than or equal to the $\Delta\chi^2$ value at the minimum, the estimation is valid. The true and the estimated WMSE (obtained on basis of a pattern of $\Delta\chi^2 = 0.0004$) agree well with respect to the position of the minimum, but differ in their absolute values by approximately a factor of 2, which is for the choice of the stop criterion not of any importance. The difference in the true and the estimated WMSE can be explained by the use of the true spectrum in the calculation on the one hand and the estimated spectrum on the other hand. The minimum of the WMSE, which characterises the trade-off between bias and statistical uncertainty, can be determined to $\Delta\chi^2 \approx 0.0008$, whereas with an increasing number of iteration steps the $\Delta\chi^2$ value decreases. The $\chi^2$ of the $i$th cell of the two-dimensional size spectrum of electron and muon numbers is calculated according to

$$\chi_i^2 = \frac{(N_{meas,i} - N_{rec,i})^2}{\sigma_i^2}, \tag{7.5}$$

with $N_{meas,i}$ being the measured and $N_{rec,i}$ the reconstructed number of showers in the $i$th cell and $\sigma_i$ the statistical error of the $i$th cell of the measured distribution. $N_{rec,i}$ is determined by means of forward folding of the reconstructed energy spectra with the response matrices. The $\Delta\chi^2$ value describes the difference of $\sum_i \chi_i^2/n.d.f.$ of two sequent iteration steps.

### 7.2.2 Reconstruction of energy spectra

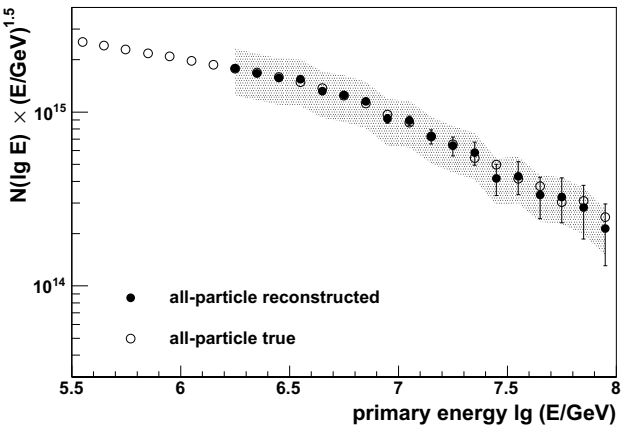


Figure 7.8: True and reconstructed all-particle spectrum.

For the reconstruction of energy spectra the knowledge of the stop criterion as well as of the uncertainties of the method is of importance. The stop criterion, the statistical uncertainties and the bias, are determined as described in the previous sections. The discussed test set contains approximately the same number of events as the KASCADE data set used and is compatible to the set on basis of which the uncertainties and the stop criterion are estimated. Figure 7.8 comprises the true and the reconstructed all-particle spectra, which are built up by summing the

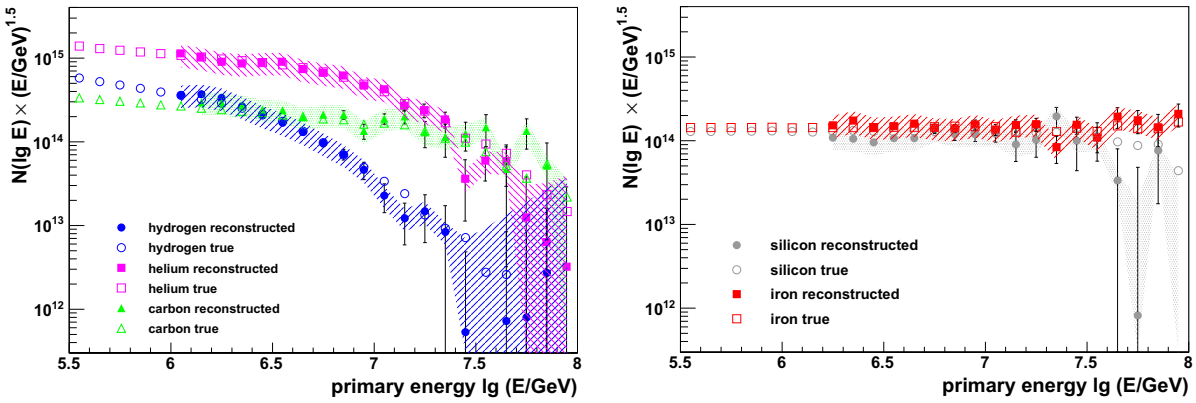


Figure 7.9: True and reconstructed energy spectra of hydrogen, helium and carbon (on the left) and of silicon and iron (on the right) at an iteration level $\Delta\chi^2 = 0.0008$.

energy spectra of the individual elements. The error bars display the statistical uncertainties (see Section 7.2.1.1) and the error band represents the bias (see Section 7.2.1.2). For the calculation of the two-dimensional shower size spectra as well as for the deconvolution the hadronic interaction models QGSJET01 and FLUKA are used. The graph reveals a good agreement of the energy spectra and evidences a very good reconstruction quality for the all-particle spectrum, being obtained by means of deconvolution.

Figure 7.9 shows the true and the reconstructed energy spectra of 5 different primary particle types at an iteration level $\Delta\chi^2 = 0.0008$. In the left part of Figure 7.9 the true energy spectra of hydrogen, helium and carbon are shown together with the reconstructed spectra. The true and reconstructed silicon and iron spectra are shown in the right part of the depiction. The results of the deconvolution reveal a good agreement of reconstructed and true energy spectra within the estimated statistical and systematic uncertainties for all elements. A reconstruction probability below 0.2 can cause problems in the energy spectra reconstructing and for this reason the first point of the carbon spectrum and the first two points of the silicon and the iron spectrum are left out. The reconstruction probabilities for different mass groups can vary from one model to the other and lead to different energy spectra starting at slightly different energies.

### 7.2.3 The effect of statistics

Since the statistics is supposed to be a crucial point in an unfolding analysis, its effect on the results can be studied easily by means of Monte Carlo methods. For this purpose test spectra with the same knee positions, the same indices and the same relative abundances as the spectra shown in Figure 7.9 are produced, but with the difference that the number of events in this data set is enlarged by a factor of 5. For this data set true and reconstructed energy spectra are displayed in Figure 7.10. All true and reconstructed spectra reveal a good agreement. Solely at high energies, where the statistics is still low, a slight betterment of the reconstruction characteristics compared to the spectra in Figure 7.9 can be observed, but in general an increase of the statistics does not further improve the reconstruction performance.

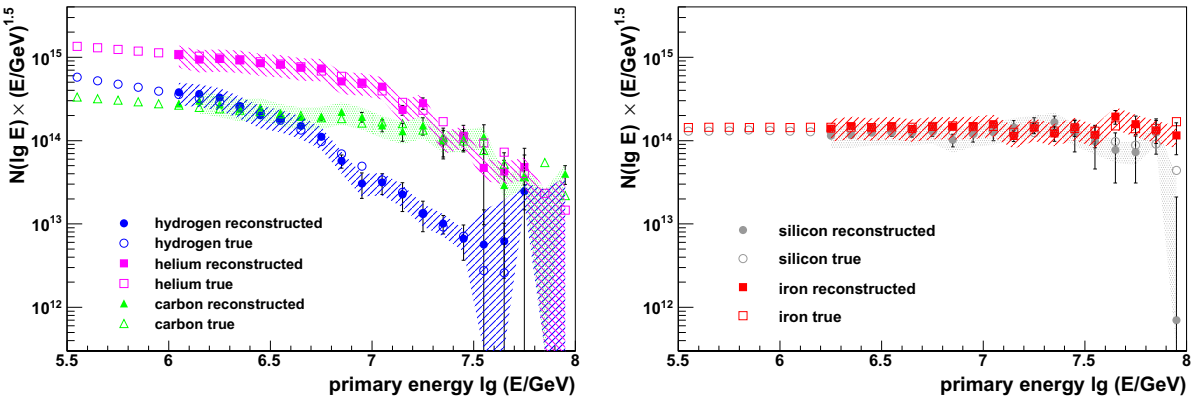


Figure 7.10: True and reconstructed energy spectra of hydrogen, helium and carbon (on the left) and of silicon and iron (on the right) at an iteration level $\Delta\chi^2 = 0.0008$. The shape of the energy spectra is equivalent to the spectra shown in Figure 7.3, but the statistics is 5 times higher.

### 7.2.4 The effect of the detector resolution

Figure 7.1 and 7.2, which comprise a comparison of the detector resolution and the intrinsic shower fluctuations of KASCADE and KASCADE-Grande, lead to the assumption that in case of KASCADE the reconstruction uncertainties do not effect the results of the analysis, because the width of the response matrices is in general dominated by the shower fluctuations. Whereas the efficiencies and the systematic reconstruction uncertainties of the experiment can be corrected for, the distributions of the reconstruction uncertainties in the electron and the muon number can indeed be parameterised, but not eliminated. Thus, detector effects, especially the detector resolution, may have an impact on the unfolded spectra. Using Monte Carlo methods offers the possibility to switch off detector effects, such as the reconstruction uncertainties and

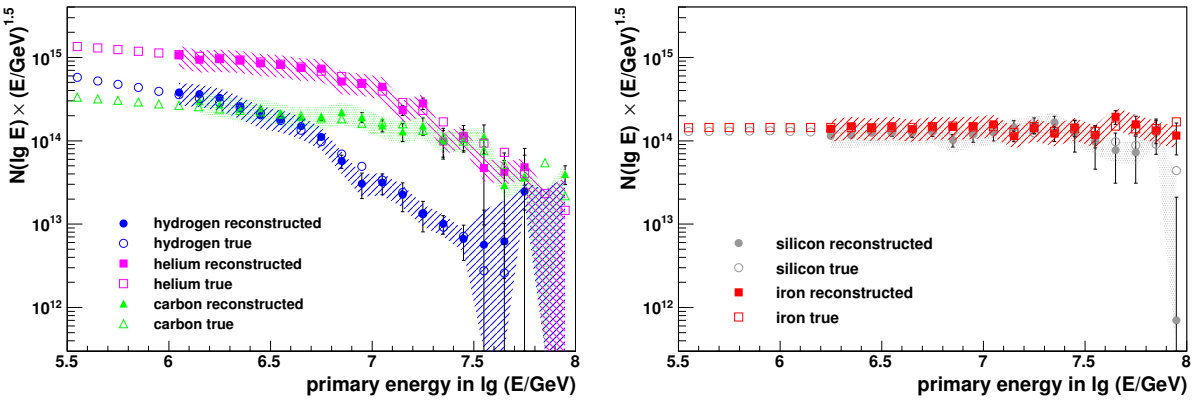


Figure 7.11: True and reconstructed energy spectra of hydrogen, helium and carbon (on the left) and of silicon and iron (on the right) at an iteration level $\Delta\chi^2 = 0.0008$. The shape of the energy spectra is equivalent to the spectra shown in Figure 7.3, but the reconstruction uncertainties are switched off.

the efficiencies, and recalculate the response functions, which then only take into account the shower fluctuations. Based upon this newly acquired determined response functions the two-dimensional size spectrum of electron and muon numbers is generated and unfolded. Switching off all detector effects is in general equivalent to a reduction of the reconstruction uncertainties, i. e. the resolution of the detector (in the electron and the muon number). The energy spectra of this set are consistent with the energy spectra of the standard set, displayed in Figure 7.3. The results of the deconvolution are depicted in Figure 7.11. Compared to Figure 7.9 no obvious improvement can be observed, which leads to the conclusion that for KASCADE detector effects play a minor role in the reconstruction of energy spectra.

## 7.3 KASCADE-Grande

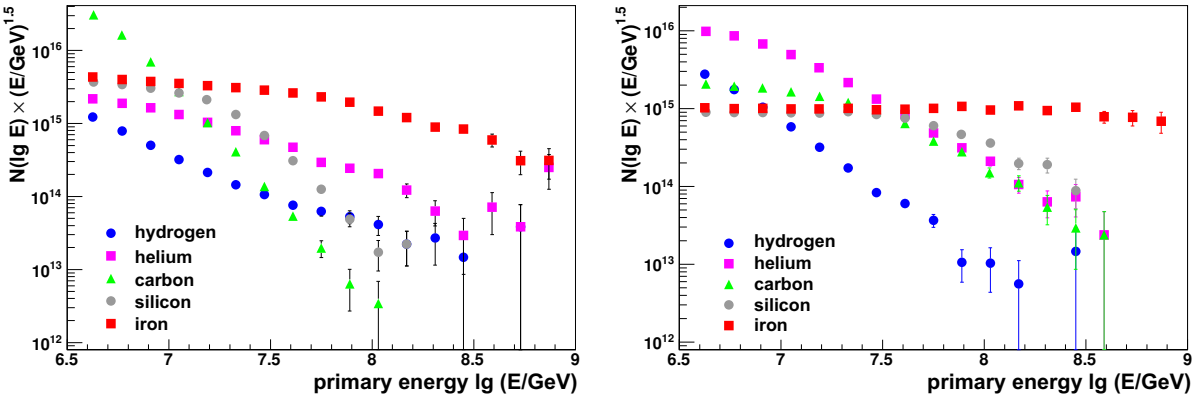


Figure 7.12: Different sets of test spectra, used for the discussion on the reconstruction characteristics of energy spectra by means of unfolding. The test spectra in the left part of the depiction are chosen similarly to the obtained KASCADE-Grande unfolding results (see Chapter 8.6), using as hadronic interaction models QGSJETII and FLUKA (for the parameters cf. Table 7.2). The right part of the figure shows the test spectra, which are chosen according to the parameters in Table 7.1, but with a lower statistics.

Whereas for KASCADE the reconstruction of the electron number lg $N_e$ and the muon number lg $N_\mu$ is very precise and no considerable effect of the detector resolution on the results of the analysis is seen, the resolution in the electron and the muon number for KASCADE-Grande is not as good as for KASCADE, which leads to the expectation that the resolution will have an impact on the results of the analysis. Both experiments also differ considerably in the number of measured air shower events, i. e. in the overall statistics.
Not only the detector resolution and the total statistics are assumed to affect the results of the unfolding analysis, but also the choice of the energy spectra, more precisely the elemental abundances, the slope and the knee positions of the individual spectra. According to the KASCADE results, which are shown in Section 8.1 for different interaction models, the spectra of the light component (H, He and C) steepen after the knee. In some cases, dependent on the interaction model used, the silicon spectrum also changes its spectral index. In the measurement range of the Grande array the index changes result in small elemental abundances, with the exception of iron. The small relative abundances of the elements with respect to iron can cause problems in the unfolding analysis. For an investigation different sets of energy spectra varying in

| element | $\gamma_1$ | $\gamma_2$ | $E_K$ in PeV | $\epsilon$ |
|---|---|---|---|---|
| hydrogen | -3.9 | -3.4 | 20.0 | 3.0 |
| helium | -2.7 | -3.4 | 8.0 | 3.0 |
| carbon | -2.7 | -5.6 | 4.0 | 3.0 |
| silicon | -2.7 | -5.5 | 20.0 | 3.0 |
| iron | -2.7 | -3.4 | 70.0 | 3.0 |

Table 7.2: Parameters of the (Grande-like) energy spectra, which are generated according to equation 7.1.

the abundances, the knee positions and the slopes, are generated. One set, which is used for testing the reconstruction characteristics of the energy spectra of different elemental groups, is chosen similarly to the spectra, obtained by the deconvolution analysis of KASCADE-Grande data (using QGSJETII and FLUKA). This set, characterised by a very steep carbon and silicon spectrum (see left part of Figure 7.12 and Table 7.2), is also used for the discussion on the uncertainties and the stop criterion.

Another set is chosen according to the energy spectra used for the discussion of the KASCADE unfolding analysis (see right part of Figure 7.12 and Table 7.1), i. e. the relative abundances, the knee positions and the slopes are identical to the KASCADE test spectra, but the total number of simulated showers corresponds approximately to the number of showers measured by the Grande array. In this special set no knee in the iron spectrum is assumed, because solely from an extrapolation of the KASCADE results a knee-like structure can not be expected.

Additionally two sets of test spectra with an equally mixed composition, i. e. equal abundance of each primary particle type without any knee-like features, are chosen, one with a spectral index $\gamma = -2.0$ and the other with an index $\gamma = -3.0$. A further set for discussing the reconstruction properties is arbitrarily chosen.

In the following sections the impact of different test sets, varying in the shapes, the abundances and the knee positions of the individual spectra, as well as the effect of the resolution and the overall statistics are discussed. In addition, the estimation of the statistical uncertainties, the bias and the stop criterion are overviewed.

### 7.3.1 Statistical uncertainties, bias and stop criterion

The systematic and statistical reconstruction uncertainties and the weighted mean squared error WMSE, which is used for the determination of the stop criterion, are determined the same way as discussed in detail for KASCADE. They are discussed on basis of the test spectra displayed in the left part of Figure 7.12.

#### 7.3.1.1 Statistical uncertainties

The absolute true and estimated statistical uncertainties of the hydrogen and the silicon spectrum are displayed in Figure 7.13. In the discussion on the uncertainties of the method silicon is chosen instead of iron as representative of the heavy primary particles, because in almost all test sets the reconstruction of the silicon flux is affected by larger uncertainties than the iron flux. The statistical error of each energy bin of the individual energy spectra is given by equation 7.2. A good agreement of true and estimated statistical uncertainties is obvious for both elements, which confirms the validity of the estimation also for KASCADE-Grande. For both elements some values of the true uncertainties are missing, because the true energy spectra do not have any entries for this energy (poor statistics). In case of hydrogen a step in the course of the true

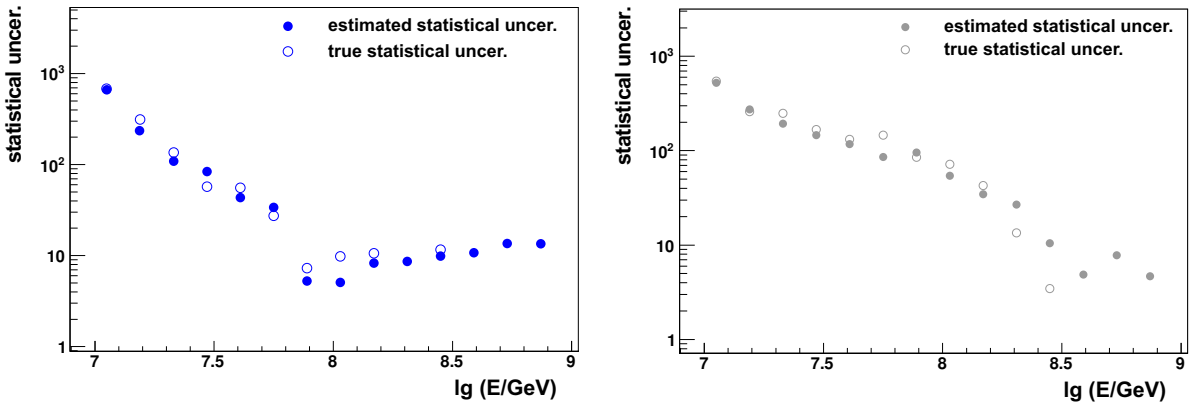


Figure 7.13: True and estimated statistical uncertainties of the hydrogen spectrum (on the left) and the silicon spectrum (on the right) at an iteration level $\Delta\chi^2 = 0.0006$.

as well as the estimated statistical uncertainties is visible at an logarithmic energy between 7.8 and 8.0, which is again due to the low statistics.

#### 7.3.1.2 Bias

Figure 7.14 comprises a comparison of the true and the estimated systematic reconstruction uncertainties of the hydrogen spectrum (on the left) and the silicon spectrum (on the right). The bias in each energy bin of the individual energy spectra is given by equation 7.3. The sign of the bias can not be exactly determined and due to illustration purposes the absolute values are plotted. The true and the estimated systematic uncertainties of the hydrogen spectrum reasonably agree and the general trend is reproduced. In case of the silicon spectrum some larger deviations between true and estimated bias occur, which reveal the difficulties in the estimation of the systematic reconstruction uncertainties without the knowledge of the true energy spectra. As already explained in Section 7.2.1 for measured data the true energy spectra are unknown and therefore cannot be used in the determination of the systematic uncertainties.

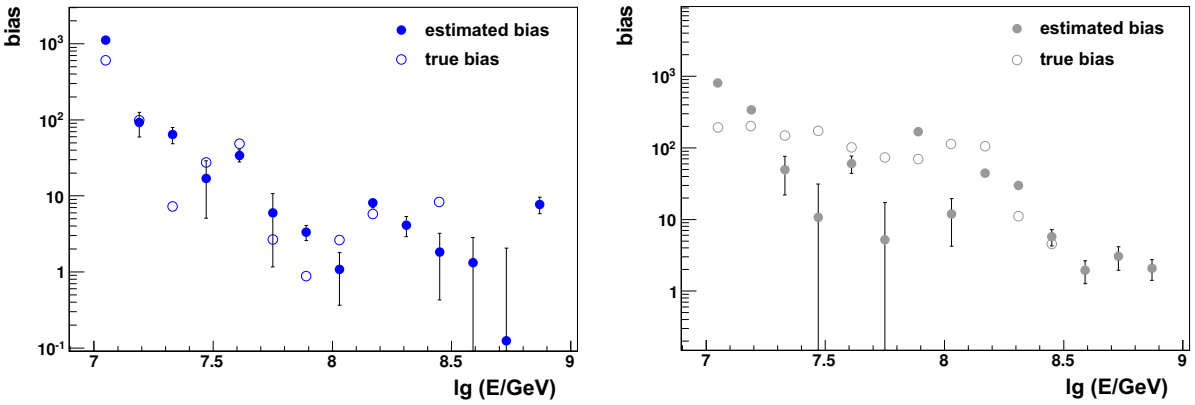


Figure 7.14: True and estimated bias of the reconstruction of the hydrogen spectrum (on the left) and the silicon spectrum (on the right) at an iteration level $\Delta\chi^2 = 0.0006$.

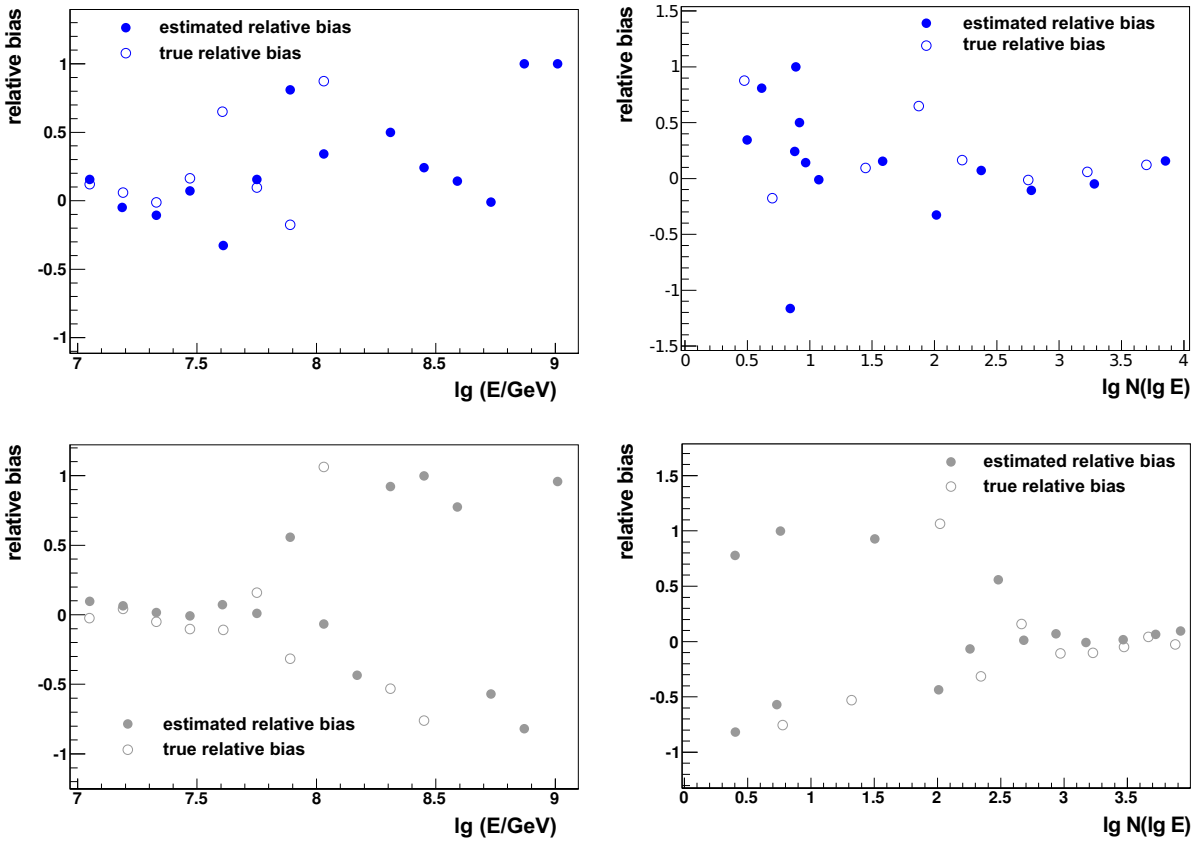


Figure 7.15: True and estimated systematic uncertainties of the reconstruction of the hydrogen spectrum (blue) and the silicon spectrum (grey) at an iteration level $\Delta\chi^2 = 0.0006$. The graphs on the left side of the Figure comprise the systematic reconstruction uncertainties subject to the logarithm of the energy, the graphs on the right side show the bias subject to the logarithm of the number of showers in a certain energy bin.

The circuitous way of using the unfolded solution at a certain $\Delta\chi^2$ value (which is referred to as pattern) instead of the true energy spectra is applied. It is obvious that this method can sometimes, if the reconstruction fails, produce large differences in the individual energy bin, but the general trend is also in case of silicon reproduced.
In Figure 7.15 the relative bias of the reconstruction of the hydrogen and the silicon spectrum is shown. On the left side of the depiction as abscissa the logarithm of the energy is chosen, whereas the graphs on the right side comprise the true and the estimated relative bias subject to the logarithm of the number of showers $\lg N(\lg E)$ in a certain energy bin. On basis of these graphs the absolute bias is estimated to 40 %. If $N(\lg E)$ is smaller than 30, which corresponds to $\approx 1.5$ in logarithmic scale, the bias is assumed to be equal to 30. This estimation leads to a rapid increase of the systematic uncertainties for $N(\lg E) < 30$.

#### 7.3.1.3 Stop criterion

Figure 7.16 comprises a comparison of the true WMSE and the WMSE estimated on basis of different patterns. The minimum of the course of the WMSE can be found at a $\Delta\chi^2$ value of approximately 0.0006. True and estimated WMSE (see pattern $\Delta\chi^2$=0.0006) agree well

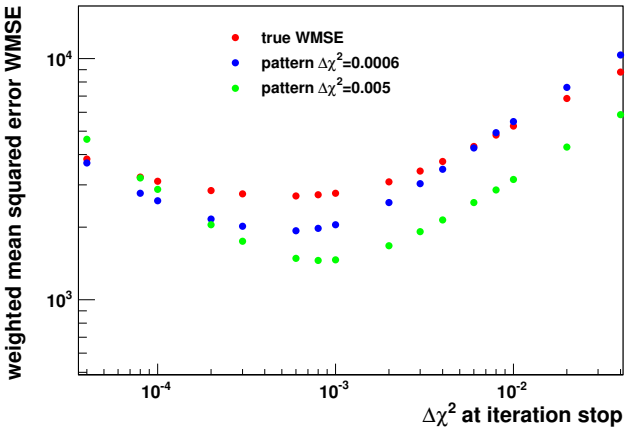


Figure 7.16: Comparison of the true and the estimated weighted mean squared error WMSE.

concerning the position of the minimum, but differ in their absolute values, as it can also be observed for KASCADE.

### 7.3.2 Reconstruction of energy spectra

In the following sections a comparison of the true and the reconstructed energy spectra of different mass groups is discussed for a variety of test sets. A reconstruction of all simulated test sets will evidence that an unfolding analysis is possible for KASCADE-Grande data, but also reveal deficiencies in reconstructing the energy spectra.

#### 7.3.2.1 KASCADE-like energy spectra

In this section the reconstruction of the energy spectra, which are extrapolated from the KASCADE results based upon the interaction models QGSJET01 and FLUKA, are discussed. The parameters of the individual energy spectra, i. e. the knee positions, the indices and the abundances of the elements, are chosen identically to the parameters of the test spectra, used for the

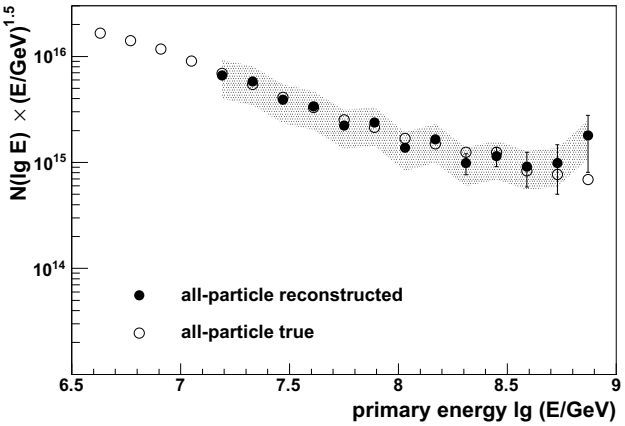


Figure 7.17: True and reconstructed all-particle energy spectrum at an iteration level $\Delta\chi^2 = 0.0006$. The data set is based upon the energy spectra shown in the right part of Figure 7.12.

discussion of the KASCADE unfolding, but differ in statistics. The Monte Carlo set contains approximately the same number of events as the data set measured and reconstructed by the Grande array.
In Figure 7.17 the true and the reconstructed all-particle spectrum is depicted together with the bias, displayed by the error band and the statistical uncertainties, being represented by the error bars.

It is obvious that the reconstruction of the all-particle spectrum works very precisely, almost up to $10^{18}$ eV.
The true and the unfolded fluxes of the individual elements can be found in Figure 7.9. The left part of Figure 7.18 comprises a comparison of the true and the unfolded energy spectra of hydrogen, helium and carbon and in the right part the energy spectra of silicon and iron are depicted. Within the bias and the statistical uncertainties all true and reconstructed energy spectra agree well. Hydrogen, being the least abundant element, is well reconstructed up to an energy of approximately 7.8 in lg (E/GeV). At higher energies the statistical as well as the systematic uncertainties are very large. Due to the statistics at energies above 8.2 in lg (E/GeV) almost no hydrogen induced events can be found in the true, but in the reconstructed spectrum. This can be explained by the positive definiteness of the Gold algorithm, which implies the reconstruction of only positive numbers (and no zeros) and the increasing statistical uncertainties of the two-dimensional shower size spectrum of electron and muon numbers with increasing shower size. The spectrum of helium, being the most abundant nuclei in this simulation set, is reconstructed well up to energies of $\approx 10^8$ GeV, but for higher energies the spectrum is liable to large statistical fluctuations. The true and the reconstructed carbon fluxes of this simulation set are compatible within the uncertainties. For energies above 8.3 in lg (E/GeV) the reconstruction suffers from the low statistics.
In the right part of Figure 7.18 the true and the reconstructed spectra of silicon and iron are depicted. The energy spectra of both elements are reconstructed well and the agreement within the statistical uncertainties and the bias is very good. The reconstruction of iron, the most abundant element in this simulation set, works rather well over the whole energy range. The first point of the iron spectrum is left out due to the reconstruction probability smaller than 0.3, which can cause large deviations.

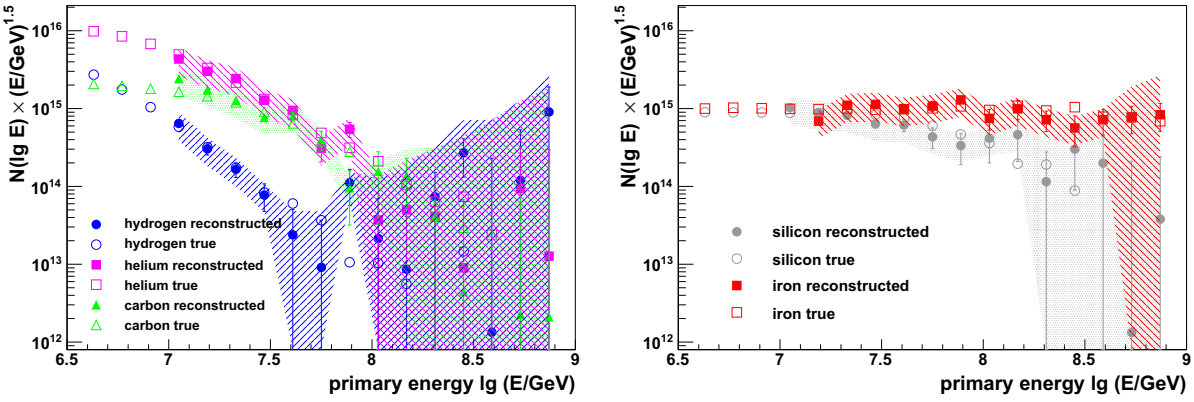


Figure 7.18: True and reconstructed energy spectra of hydrogen, helium and carbon (on the left) and of silicon and iron (on the right) at an iteration level $\Delta\chi^2 = 0.0006$. The data set is chosen according to the energy spectra shown in the right part of Figure 7.12.

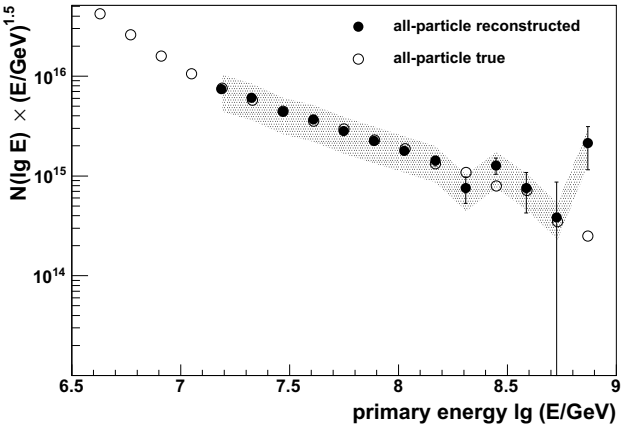


Figure 7.19: True and reconstructed all-particle energy spectrum at an iteration level $\Delta\chi^2 = 0.0006$. The data set is based upon the energy spectra shown in the left part of Figure 7.12.

#### 7.3.2.2 Grande-like energy spectra

Another set of test spectra, which is used to study the effect of the parameters of the energy spectra (knee positions, indices and abundances), approximately corresponds to the unfolded KASCADE-Grande spectra, listed in Table 7.2. The Monte Carlo set is characterised by a steep carbon and silicon spectrum. This test is aimed to analyse the reproducibility of the finally unfolded spectra.
Figure 7.19 comprises a comparison of the true and the reconstructed all-particle energy spectrum with the error bands representing the bias and the error bars depicting the statistical uncertainties. For this set a good agreement of reconstructed and true all-particle energy spectrum is given up to the highest energies.
The true and the reconstructed hydrogen, helium and carbon spectra can be found in the left part of Figure 7.20 together with the systematic uncertainties (error bands) and the statistical uncertainties (error bars). In general the true and the reconstructed fluxes agree well within the

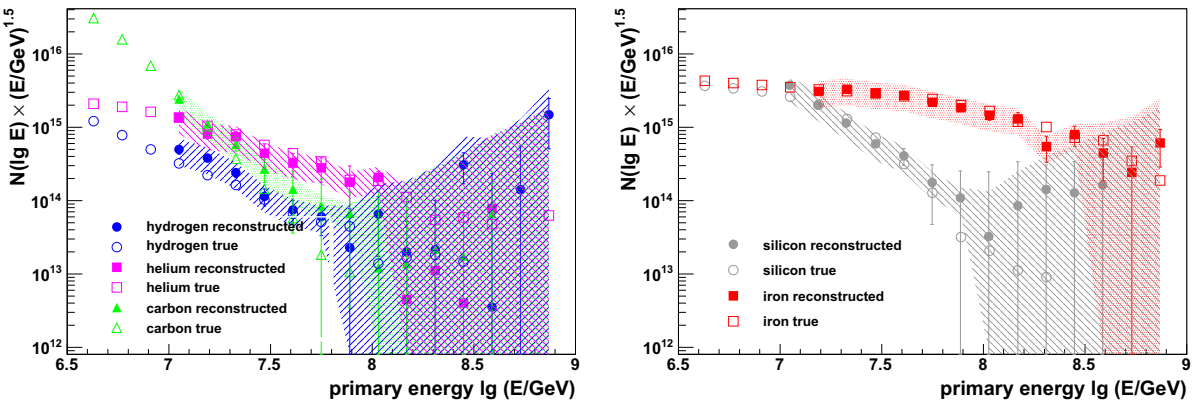


Figure 7.20: True and reconstructed energy spectra of hydrogen, helium and carbon (on the left) and of silicon and iron (on the right) at an iteration level $\Delta\chi^2 = 0.004$. The data set corresponds to the energy spectra shown in the left part of Figure 7.12.

bias and the statistical uncertainties. But a more careful examination reveals the same problems at energies above $10^8$ GeV, already discussed in the last section, originating from the small relative abundances in this energy region. The largest deviations can be found in case of the carbon spectrum. In this test set for energies higher than 7.5 in lg (E/GeV) the unfolded carbon flux is overestimated, but regarding the size of the statistical and systematic uncertainties reconstructed and true flux are compatible. The right part of Figure 7.20 shows the true and the unfolded silicon and iron spectra. The silicon flux is reconstructed well up to an energy of $10^8$ GeV. For larger energies the reconstructed silicon flux is highly overestimated, but considering the bias and the statistical uncertainties true and reconstructed spectra are consistent. Like in the simulation set discussed earlier, iron is at the highest energies the most abundant primary particle. This results in a good reconstruction of the iron flux over the total energy range.

#### 7.3.2.3 Equally mixed composition

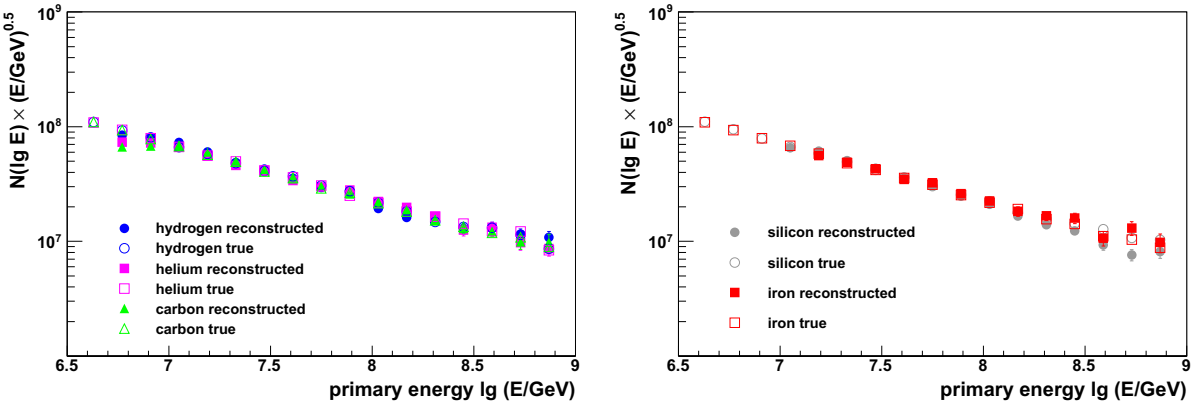


Figure 7.21: True and reconstructed energy spectra of hydrogen, helium and carbon (on the left) and of silicon and iron (on the right) at an iteration level $\Delta\chi^2 = 0.004$. The composition in the data set is equally mixed, without any knee-like features and the same index $\gamma = -2.0$ over the whole energy range.

An equally mixed composition, i. e. same abundance of all primary particle types, is another commonly used set of test spectra. The discussed sets are characterised by two different spectral indices ($\gamma = -2.0$ and $\gamma = -3.0$) and do not exhibit any knee-like features (power law with constant index). The number of events is chosen according to the total number of events measured with the Grande array. Due to illustration purposes the systematic uncertainties are not depicted, but the statistical uncertainties are shown as error bars.
Figure 7.21 comprises the true and the reconstructed test spectra with a spectral index of $\gamma = -2.0$. The good agreement of the true and the reconstructed energy spectra of all five primary particle types even for energies above $10^8$ GeV can be traced back to the flat spectrum with a spectral index $\gamma = -2.0$ and as a consequence the large abundances even at high energies.

Figure 7.22 contains the true and the unfolded fluxes of an equally mixed composition, but now with a spectral index $\gamma = -3.0$. Here the reconstruction of the energy spectra of all primary particle types works well up to an energy of lg (E/GeV) $\approx 8.2$. At higher energies the true as well as the reconstructed energy spectra suffer from the low statistics due to the steeper spectra ($\gamma = -3.0$), which is also represented by the large statistical uncertainties (error bars).

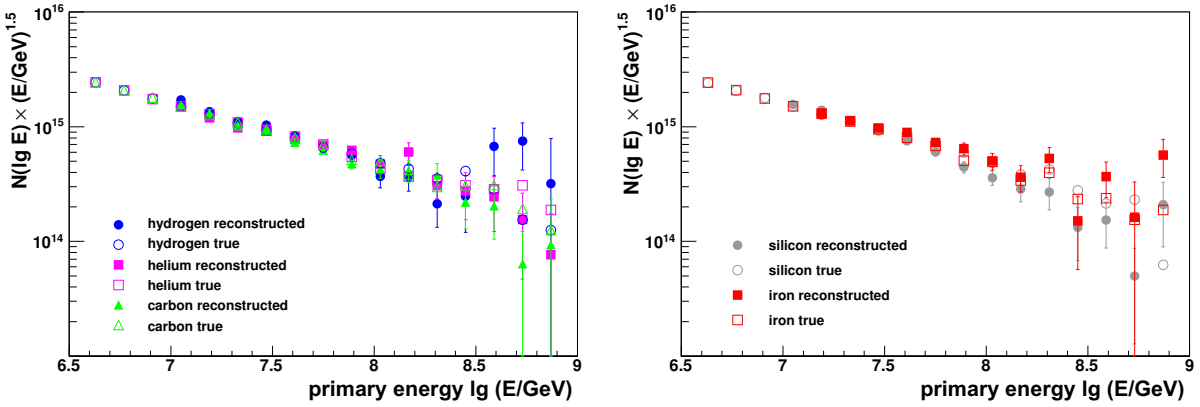


Figure 7.22: True and reconstructed energy spectra of hydrogen, helium and carbon (on the left) and of silicon and iron (on the right) corresponding to an equally mixed composition, without any knee-like features and an index $\gamma = -3.0$ for all primary particle types.

#### 7.3.2.4 Arbitrarily chosen test spectra

Although for almost all of the chosen test spectra the deconvolution works properly and the test spectra can be well reconstructed, there are also some special test spectra, for which a reconstruction of the individual energy spectra is not possible with sufficient precision. The test spectra discussed in this section are only slightly varied with respect to the test set, whose parameters are listed in Table 7.2. The index of the carbon spectrum after the knee was changed to $\gamma = -4.6$, i. e. the spectrum is flatter, and the abundances are slightly altered.
In Figure 7.23 the true and the reconstructed all-particle flux is depicted. Like for all test spectra, discussed in the sections before, the well matching reconstructed and true all-particle spectra reveal the robustness of the reconstruction of the all-particle flux by means of deconvolution.

The stop criterion ($\Delta\chi^2 = 0.00005$), being chosen with the help of the WMSE, indicates that for the reconstruction more iterations are necessary. A larger number of iterations improves in-

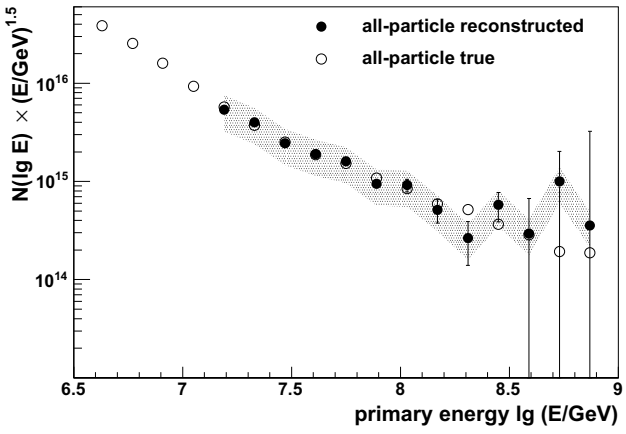


Figure 7.23: True and reconstructed all-particle energy spectra at an iteration level $\Delta\chi^2 = 0.00005$.

deed the systematic reconstruction uncertainties, but with the consequence of larger statistical uncertainties.
The true and the reconstructed energy spectra of the individual mass groups can be found in Figure 7.24. The left panel of the depiction comprises the energy spectra of the elements hydrogen, helium and carbon. The true and the unfolded graphs of hydrogen and carbon reveal a good agreement within the statistical and systematic uncertainties. Whereas for carbon the reconstructed flux disappears for $\lg(E/GeV) > 8$, the helium flux is highly overestimated in this region. The large uncertainties in this energy range are reflected in the large statistical (error bars) and systematic uncertainties (error bands). A comparison of the true and the unfolded helium flux shows that the reconstruction does not work as good as for hydrogen and carbon. At energies above 7.8 in $\lg(E/GeV)$ the reconstructed helium flux is affected by large fluctuations and then is smaller than the scale of the plot, although the true spectrum exhibits entries.
The right part of Figure 7.24 depicts the true and the reconstructed spectra of silicon and iron. Compared to the reconstruction of the energy spectra of the other elements the reconstruction of the silicon flux does not work satisfactorily. The unfolded silicon flux is highly overestimated at low values. The estimated systematic uncertainties are too small, which can be explained by the estimation technique itself. If the reconstruction of an individual energy spectrum fails systematically, the method of estimating the bias by an frequentist approach will always underestimate the systematic uncertainty. In view of the large statistical uncertainties the reconstructed flux in the energy range $7.3 < \lg(E/GeV) < 8$ is compatible with the true spectra. In contrast to silicon the iron flux is well reconstructed, with exception of the first point, which is highly underestimated. This underestimation can be explained by the simultaneous overestimation of the silicon flux in this region.
The reconstruction of the energy spectra of 5 mass groups for this special set of test spectra is not possible with the same precision as for the test spectra discussed in the previous sections. The origin of these uncertainties in the reconstruction can mainly be traced back to the resolution of the experiment in combination with the choice of the abundances and the shapes of the test spectra and is therefore an interplay of different facts. Since the arbitrarily chosen energy spectra are not that far off of the results of the unfolding analysis, a successful reconstruction of the fluxes can not be guaranteed in all cases. A better performance can be achieved by using 5 primary particle types for the deconvolution, but then summing up the medium elements to

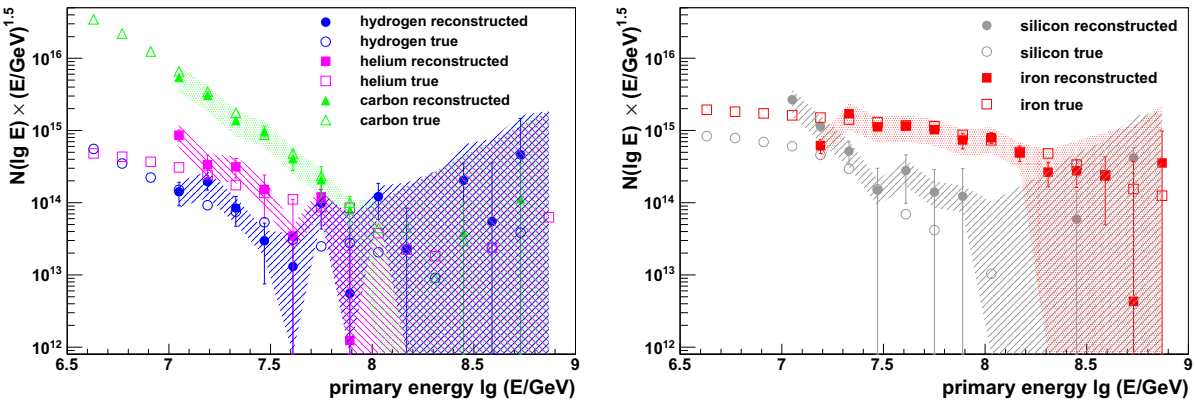


Figure 7.24: True and reconstructed energy spectra of hydrogen, helium and carbon (on the left) and of silicon and iron (on the right) at an iteration level $\Delta\chi^2 = 0.00005$. The choice of the data set is described in section 7.3.2.4.

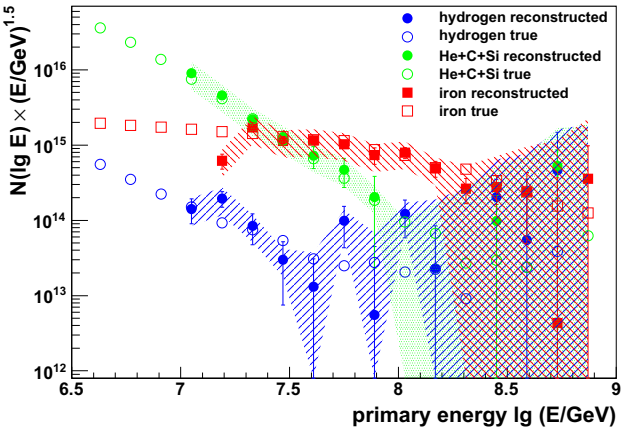


Figure 7.25: True and reconstructed energy spectra at an iteration level $\Delta\chi^2 = 0.00005$. Helium, carbon and silicon are combined to one component.

one component, i. e. helium, carbon and silicon are combined to one energy spectrum. The resulting graphs can be found in Figure 7.25. For the reconstructed hydrogen and iron spectra nothing changes. The combination of helium, carbon and silicon leads to a better reconstruction characteristic, but also to a loss of information on the individual elemental spectra. Up to an energy of $10^8$ GeV the reconstructed and the true combined flux agree well. For higher energies large deviations become apparent (some values in the reconstructed flux are missing), which are insignificant in the view of the size of the systematic reconstruction uncertainties.

### 7.3.3 The effect of the detector resolution

Another important question is the effect of the detector resolution on the results of the unfolding analysis. For that purpose the response functions are recalculated, but without any detector effects. For the discussion the same test spectra (same knee positions and abundances) are used

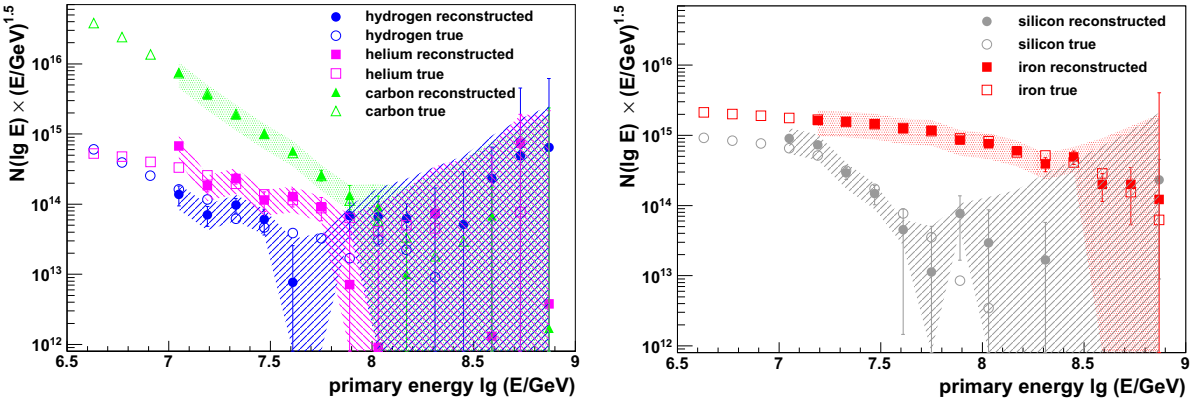


Figure 7.26: True and reconstructed energy spectra of hydrogen, helium and carbon (on the left) and of silicon and iron (on the right) at an iteration level $\Delta\chi^2 = 0.0004$. The test spectra are consistent with the one shown in Figure 7.24, but the response functions are calculated without the detector resolution.

as in Section 7.3.2.4, but now the two-dimensional shower size spectrum of electron and muon numbers are calculated on basis of the response functions without the detector resolution. In the left part of Figure 7.26 the energy spectra of hydrogen, helium and carbon are displayed, in the right part the spectra of silicon and iron are depicted. The energy spectra of all 5 primary particle types are reconstructed well up to an energy of approximately $10^8$ GeV. For higher energies the reconstruction suffers from large statistical and systematic uncertainties. Iron, being the most abundant primary particle type is reconstructed well even up to the highest energies. Comparing Figure 7.24 and Figure 7.26, which are based upon the same energy spectra but on different response functions, an improvement of the reconstruction characteristics can be found if the detector resolution is switched off. The successful reconstruction, assuming a perfect detector, reveals the impact of the resolution on the results of the analysis.

### 7.3.4 The effect of the statistics

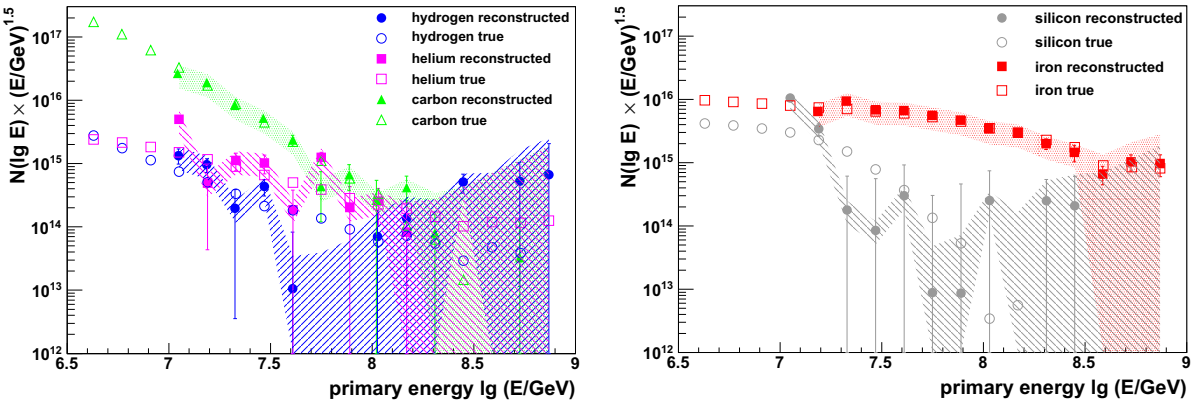


Figure 7.27: True and reconstructed energy spectra of hydrogen, helium and carbon (on the left) and of silicon and iron (on the right) at an iteration level $\Delta\chi^2 = 0.00001$. The data set comprises a factor of 5 times more statistics than the set shown in Figure 7.24.

Compared to the number of events measured by the KASCADE experiment, the statistics of KASCADE-Grande is poor. To test the effect of the data statistics on the results of the analysis a set of test spectra with 5 times the statistics as in the set, discussed in Section 7.3.2.4, is generated. The shape of the test spectra and the relative abundances of the elements are chosen equally to the spectra shown in Figure 7.24. Concerning real data an increase of the statistics by a factor of 4 corresponds to more than 15 years of further data taking. In Figure 7.27 the true and the reconstructed test spectra with the increased statistics can be found. Compared to Figure 7.24 the reconstruction characteristics of the energy spectra does not improve by the use of 5 times the statistics, which leads to the assumption that the overall statistics only plays a minor role in the reconstruction of energy spectra by means of deconvolution and only helps to improve the results at the highest energy bins.

## 7.4 Conclusion

Regarding the discussion in Section 7.3.2 on the reconstruction of the fluxes of different sets of test spectra and the tests concerning the effect of the detector resolution (Section 7.3.3) and the statistics (Section 7.3.4), a deconvolution analysis of KASCADE-Grande data, i. e. the

determination of energy spectra of individual mass groups is possible, but with less precision as for KASCADE. The less precise reconstruction of energy spectra using the KASCADE-Grande experiment, can be explained by the interplay of different facts. For KASCADE the energy spectra in the range from $10^{15} - 10^{17}$ eV can be reconstructed. The energy spectra of different primary particle types are supposed to have different knee positions. Their indices $\gamma$ after the knee decrease, i. e. the spectra become steeper. An extrapolation of the individual energy spectra, obtained by the analysis of KASCADE data (see Chapter 8.1), results in small elemental abundances in the measurement range of the KASCADE-Grande experiment, especially of the light elements (H, He and C) and sometimes also of silicon. The small relative abundances of these elements in the energy region of the Grande array together with the detector resolution results in a less precise reconstruction of energy spectra. A reconstruction of the energy spectra of the elements lighter than iron is possible up to energies of $\approx 10^8$GeV. As it was shown in Section 7.3.2.4, the reconstruction of the energy spectra of 5 elemental groups does not succeed for all test spectra used. The use of the sum of helium, carbon and silicon as representative of the medium heavy elements leads to a more stable solution. The flux of iron, which is supposed to be the most abundant primary particle type in the energy range of KASCADE-Grande array as well as the all-particle flux can be accurately determined up to the highest energies.

# Chapter 8

# Deconvolution of KASCADE and KASCADE-Grande data

In Chapter 7 the reconstruction capabilities of energy spectra of both experiments are discussed. The experiments vary highly in the number of events used for the analysis and differ significantly in their reconstruction quality of the unfolded spectra. The present chapter deals with the deconvolution of data measured with the KASCADE array and the Grande array respectively. First an additional source of systematic uncertainties is discussed and then the results based upon response matrices, which are calculated on basis of different hadronic interaction models, are presented.

## 8.1 Uncertainties arising from parameterisations

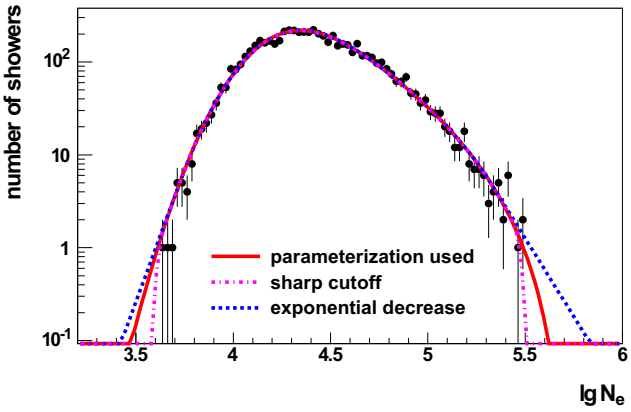


Figure 8.1: Parameterisation of the intrinsic shower fluctuations in the electron number of hydrogen induced air showers of an energy of $5 \cdot 10^{14}$ eV. Additionally the two described models are depicted (exponential decrease and sharp cutoff).

Section 7.2.1 deals with the systematic and statistical uncertainties of the method. For the calculation of the response matrices simulations, which only offer a limited statistics, are used. Systematic uncertainties, arising from a parameterisation of distributions with limited statistics and statistical uncertainties, originating from the errors of the parameters, have to be taken into account.

When examining the intrinsic shower fluctuations in the electron and the muon number (see Section 6.1.1 and 6.1.2), it becomes obvious that the fluctuations in the electromagnetic component exceed those of the muonic one and that they are the dominant part in the calculation of the response matrices. The examination of the reconstruction uncertainties in the electron number $N_e$ as well as in the truncated muon number $N_\mu^{tr.}$ for KASCADE, which are reviewed in detail in Section 6.2, makes clear that the statistical reconstruction uncertainties, i.e the detector resolution, are negligible compared to the size of the shower fluctuations. For these reasons as additional source of systematic deviations the uncertainties of the paramaterisation of the lg $N_e$ distribution are taken into consideration. Figure 8.1 depicts the shower fluctuations in the electron number and the corresponding parameterisation (red line), used in the calculation of the response matrices. Whereas in the region around the maximum the statistics is sufficiently high for a proper fitting, in the tails of the distribution the exact shape can not be definitely determined. Due to the steepness of the energy spectra the description of the tails makes a significant contribution to the uncertainties. To estimate the systematic uncertainties, arising from this impreciseness, two different models, which describe two extreme cases, are adopted. The first model is characterised by an exponential decrease at the edges of the distribution. The second model describes a sharp cutoff of the distribution. For both models (sharp cut-off and exponential decrease) the response functions are recalculated and the measured data set is deconvolved. The differences of the energy spectra derived by the use of both models are interpreted as an additional systematic uncertainty. The whole procedure has to be done for each interaction model used. As it is described in Section 6.1.1 and 6.1.2 the parameters of the functions, describing the shower fluctuations of the electron and the muon number, are determined at fixed energies and afterwards interpolated. The determination of the interpolated parameters itself is liable to uncertainties, which can be neglected in comparison to all other uncertainties.
For test spectra the systematic uncertainties arising from the parametrization of the lg $N_e$-distribution (see Figure 8.1) are not taken into consideration, because for the deconvolution analysis as well as for the generation of the two-dimensional size spectra the same response functions are used.

The uncertainties arising from the parameterisation of the shower fluctuations in the electron number and the systematic uncertainties of the methods (see Chapter 7) are combined and displayed as error band in the following plots. The error bars of the energy spectra represent the statistical error.

## 8.2 Uncertainties arising from different interaction models

Since for the generation and the unfolding of test spectra the same response functions are used, these response functions can be considered as the absolute truth. This assumption is not valid for measured data, since the probability distributions derived by Monte Carlo simulations, using different interaction models, do not necessarily describe the truth. Figure 8.2 depicts the two-dimensional size spectrum of electron and muon numbers measured by the KASCADE array. Additionally the lines of the most probable values, derived from Monte Carlo simulations on basis of different models, are plotted for hydrogen and iron induced air showers. The maximum positions allow to draw conclusions on the varying abundances for different interaction models. The most probable values are determined on basis of the response functions, being calculated for different interaction models. The maxima of the two-dimensional probabilities for different energies are located along these lines (higher muon numbers correspond to higher energies).

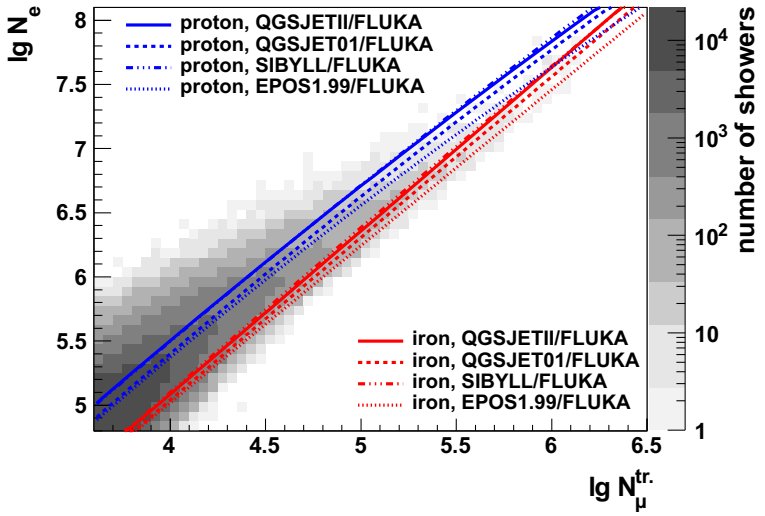


Figure 8.2: Two-dimensional size spectrum of electron and muon numbers. Additionally plotted are the lines of the most probable values for different interaction models.

The lines vary significantly for different interaction models. These differences lead to differences of the results, based upon different interaction models. The connection of the most probable values to the elemental abundances and the shape of the energy spectra are discussed in detail in the following sections, which comprise the results of the analysis of measured data for different interaction models. The exact shape of the energy spectra and the abundances of the elements, resulting from the analysis, are determined by an interplay of the most probable values, the resolution in the electron and the muon number and the predicted shower-to-shower fluctuations of the corresponding models. The width of the response functions, which comprise (statistical) reconstruction uncertainties as well as shower fluctuations, is in case of the KASCADE array in general dominated by the intrinsic shower fluctuations.
For completeness it should be noted that a large uncertainty of the individual energy spectra arises from the interaction models, which of course do not render the absolute truth. In the following sections the energy spectra, resulting from response functions derived from different interaction models, are discussed. The cross sections of hadronic interactions occurring at cosmic ray energies can be deduced from well measured nucleus-nucleus scattering by means of extrapolation. These extrapolations are a source of large uncertainties. In addition, different models make use of different approaches of modelling hadronic interactions. It is still ambiguous, which models are able to describe the truth best, since all models reveal insufficiencies in the description of both cosmic ray and accelerator data [Ent11]. A new generation of particle accelerators, reaching almost the energies of particles, which are measured in cosmic ray experiments, will allow a further development of the hadronic interaction models. From this point of view analysing KASCADE data will still be interesting in several years, since for example the unfolding analysis offers extensive studies on composition and can, with improved interaction models, give new results on the acceleration and propagation mechanisms.
In the following chapter the results obtained by the use of different interaction models, which are currently available, are discussed.

## 8.3 Deconvolution of KASCADE array data

The determination of the energy spectra of different elemental groups and of the all-particle spectrum in the primary energy range around the knee is the main goal of the KASCADE experiment. The data set used for the KASCADE unfolding analysis, comprising air showers below 18°, is shown in Figure 5.2. Due to the large intrinsic shower fluctuations and the computing time consumption of simulations it is impossible to account for all primary particle types, being present in cosmic rays. The elements used in the deconvolution analysis rather represent mass groups of primary particle masses. These individual mass groups are hydrogen, helium, carbon represents the CNO group, silicon is the representative of the intermediate elements and iron stands for the heavy elements. For this reason the reconstructed energy spectra do not describe the course of one individual element, but of a mixture of elements with similar properties.

### 8.3.1 Effect of the low energy interaction model

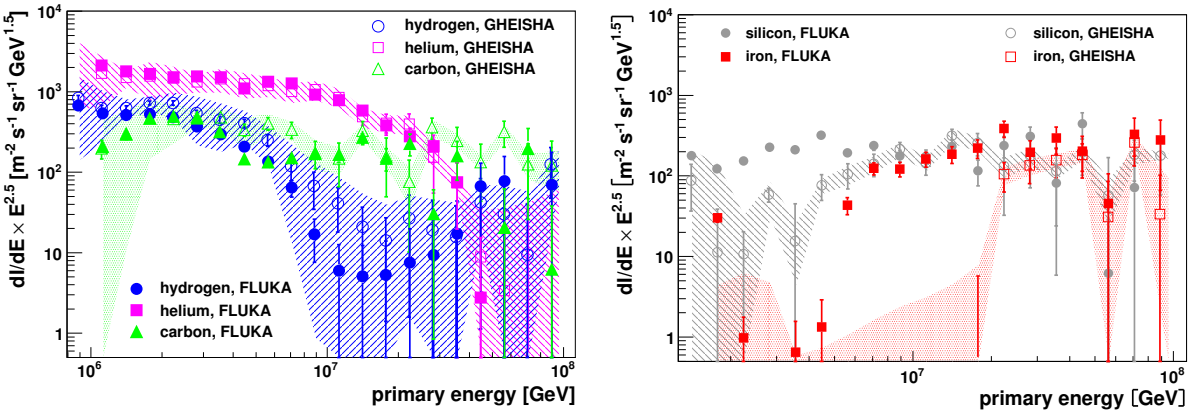


Figure 8.3: Energy spectra of hydrogen, helium and carbon (left part) and silicon and iron (right part) in the zenith angle range from $0 - 18°$, using two different low-energy interaction models, FLUKA and GHEISHA. As hadronic high-energy interaction model QGSJET01 was used. The error bars represent the statistical uncertainties and the error band displays the systematic uncertainties of the QGSJET/ GHEISHA solution (taken from [Ape09]).

In [Ape09] it is shown that the choice of the hadronic low-energy interaction model does not influence the analysis significantly. For that analysis a slightly modified algorithm compared to the one in the present analysis was used, but both are based upon the Gold algorithm. Although the algorithm was minimally changed, the findings are as well valid for the present analysis. Figure 8.3 shows a comparison of the individual energy spectra, derived by the use of the same high-energy interaction model (QGSJET01), but different low energy interaction models (GHEISHA and FLUKA). The left part of Figure 8.3 comprises the energy spectra of hydrogen, helium and carbon, on the right the energy spectra of silicon and iron are depicted. The error band displays the systematic uncertainties of the QGSJET/ GHEISHA solution, the error band for QGSJET/ FLUKA is left out due to illustration purposes, but it is of similar order. Taking into account systematic (error bands) as well as statistical (error bars) reconstruction uncertainties the differences of the two solutions are small for the light elements H, He and C. This also holds for the heavier mass groups, Si and Fe, except for energies below $10^7$ GeV, where the differences are larger. In the low energy range more heavy elements are reconstructed using

FLUKA instead of GHEISHA. By the use of FLUKA the overall data description is slightly improved. Furthermore, the predictions of the FLUKA code [Fas00] describe experimental data properly, whereas simulations based upon GHEISHA suffer from deficiencies in the data description (see [Ape09]). Hence in all simulations, used in the present analysis, the low-energy interaction model FLUKA is applied and only the high-energy models are varied.

### 8.3.2 Energy spectra of different angular ranges

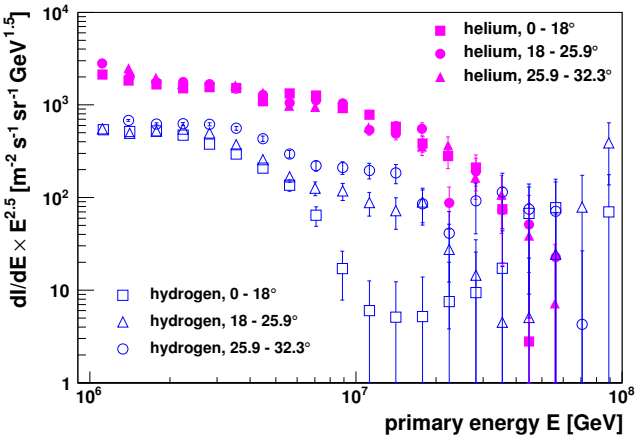


Figure 8.4: Energy spectra of hydrogen and helium for different zenith angle ranges. As hadronic interaction models QGSJET01 and FLUKA are used (taken from [Ape09]).

In the present analysis only air showers in the zenith angle range from 0° to 18° are applied, but in [Ape09] additionally the energy spectra of more inclined showers have been investigated. Significantly varying energy spectra, obtained on basis of data originating from different inclinations, would imply inconsistencies in either the analysis method or the simulations. Thus the use of data from different angular ranges serves as a consistency check. The angular ranges are chosen according to the same acceptance on the sky, i. e. assuming an isotropic arrival direction the flux in each angular bin is the same. Due to the limited reproduction of the measured correlations and the differences in the shower fluctuations, the same results for different inclinations are not expected. Figure 8.4 displays the hydrogen and the helium spectra, derived on basis of data of different zenith angle ranges, but the findings hold for the other elements as well. For a better illustration the representation of the systematic uncertainties are omitted, but they are of the same order of magnitude as displayed for example in Figure 8.3 or 8.6. The energy spectra of helium, being the most abundant element for an analysis on basis of QGSJET01, agree well over the entire energy range. For hydrogen the agreement of the energy spectra of different angular ranges is not as good as for helium, especially above the knee. With increasing inclination the index change is less pronounced, i. e. a higher hydrogen flux is reconstructed for more inclined showers. But taking into account the size of the total reconstruction uncertainties (systematic uncertainties are omitted in this depiction) still an agreement of the spectra is found. The use of data of different angular ranges does not change the results of the analysis significantly. Thus, no inconsistencies concerning the simulation chain or the analysis technique are observed.

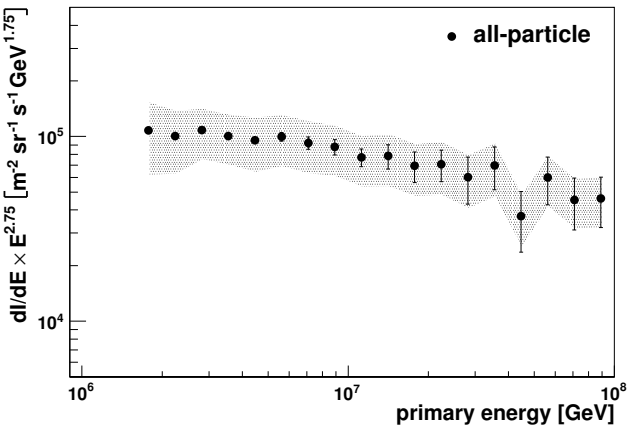


Figure 8.5: All-particle energy spectra in the zenith angle range from $0-18°$, using QGSJET01 and FLUKA. The error band indicates the systematic uncertainties, the error bars assign the statistical uncertainties.

### 8.3.3 QGSJET01 and FLUKA, $0-18°$

QGSJET01 is the first hadronic high-energy interaction model being investigated in this section. Figure 8.5 shows the all-particle spectrum in the zenith angle range from $0-18°$ derived by the unfolding analysis, using as hadronic interaction models QGSJET01 and FLUKA. The course of the WMSE can be found in Figure D.1 in the appendix.
For illustration purposes the all-particle flux is multiplied by $E^{2.75}$. The error band comprises the systematic uncertainties arising from the parameterisation as well as methodical systematic uncertainties, and the error bars indicate the statistical error. At an energy of $\approx 6 \times 10^{15}$eV a kink in the energy spectrum can be found, which is referred to as the knee in the energy spectrum of cosmic rays.
Figure 8.6 displays the energy spectra of 5 different mass groups with the systematic (error bands) and the statistical uncertainties (error bars). In the left part of the depiction the energy spectra of hydrogen, helium and carbon are shown. The shape of the hydrogen spectrum for QGSJET01 and FLUKA indicates a change of the spectral index at an energy of $\approx 4 \times 10^{15}$eV. Above an energy of $\approx 9 \times 10^{15}$eV the flux drops to values below 1 and rises again at higher energies. This increase of the flux at higher energies can be interpreted as an artificial effect of the unfolding analysis. For QGSJET01 and FLUKA the most abundant element is helium. Just like the hydrogen spectrum the helium spectrum obviously shows a knee-like structure, but at an higher energy ($\approx 8 \times 10^{15}$eV). Differing by approximately a factor of 2, the position of the index changes of the hydrogen and the helium spectrum are indicative for a rigidity dependence of the knee positions of different elements ($E_Z^{knee} \propto Z \cdot E_{prot}^{knee}$). In contrast to the hydrogen and helium spectrum the carbon spectrum does not reveal a significant change of slope.
The right part of Figure 8.6 displays the silicon and the iron spectrum. Both, silicon and iron flux, do not show any knee-like features. The index of the silicon spectrum is almost constant over the entire energy range. When examining the iron spectrum it can be noticed that at low energies up to $\approx 7 \times 10^{15}$eV nearly no iron is present, but with increasing energy the iron flux reaches the same values as the silicon flux. Regarding the extrapolations of direct measurements, the absence of iron at low energies can be interpreted as a non-physical result, which originates from insufficiencies of the interaction model used in describing the measured data.
These deficiencies become also apparent when studying the $\chi^2$ distribution shown in Figure

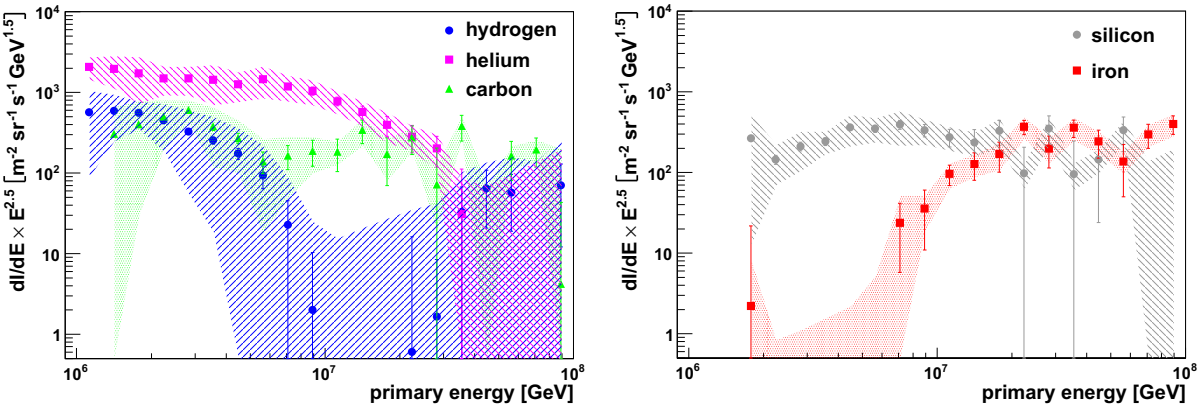


Figure 8.6: Energy spectra of hydrogen, helium and carbon (left part) and silicon and iron (right part) in the zenith angle range from $0 - 18°$, using as hadronic interaction models QGSJET01 and FLUKA. The error band displays the systematic uncertainties and the error bars represent the statistical uncertainties.

8.7. The $\chi^2$ of each cell of the two-dimensional size spectrum of electron and muon numbers is calculated using the measured number of showers of each cell i, which is denoted as $N_i^{meas.}$, the number of showers $N_i^{rec.}$ being reconstructed ($N_i^{rec.}$ is calculated by a convolution of the reconstructed energy spectra with the response matrices) and the statistical error $\sigma_i$ of each cell. The $\chi_i^2$ of a cell i is given by

$$\chi_i^2 = \frac{(N_i^{meas.} - N_i^{rec.})^2}{\sigma_i^2}. \tag{8.1}$$

The $\chi_{ndf}^2$ calculated as $\sum_i \chi_i^2/ndf$ is 1.34 and the examination of the $\chi^2$-distribution reveals a good overall description of the measured data by the hadronic interaction models used. The distribution of the $\chi_i^2$ is rather homogeneous, but also irregularities can be found. With increasing energy, i. e. with increasing electron and muon number, the distribution becomes more homogeneously and the data description improves with increasing energy. At the lower edge of

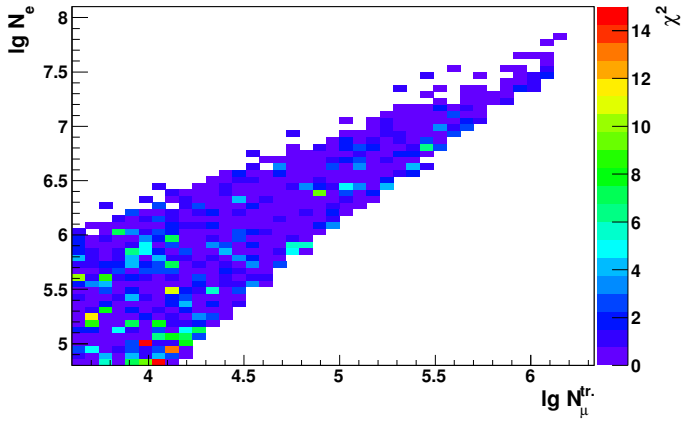


Figure 8.7: $\chi^2$ distribution of the solution of QGSJET01 and FLUKA for zenith angles in the range $0 - 18°$.

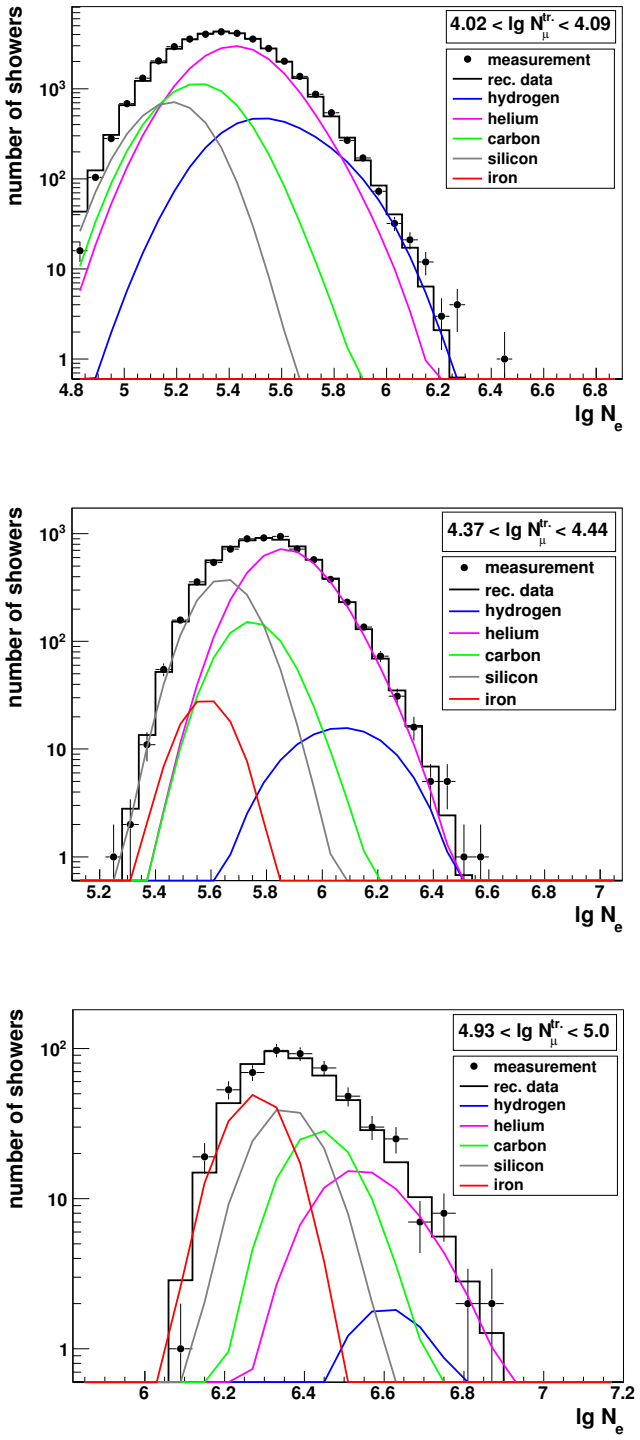


Figure 8.8: Projection along the lg $N_e$-axis of the two-dimensional size spectra of electron and muon numbers for different lg $N_\mu^{tr.}$-intervals. Plotted are the lg $N_e$-distributions of measured showers (dots) and via forward folding reconstructed showers (lines). The upper graph corresponds to approximately the energy of the knee, the lower graphs to energies above the knee.

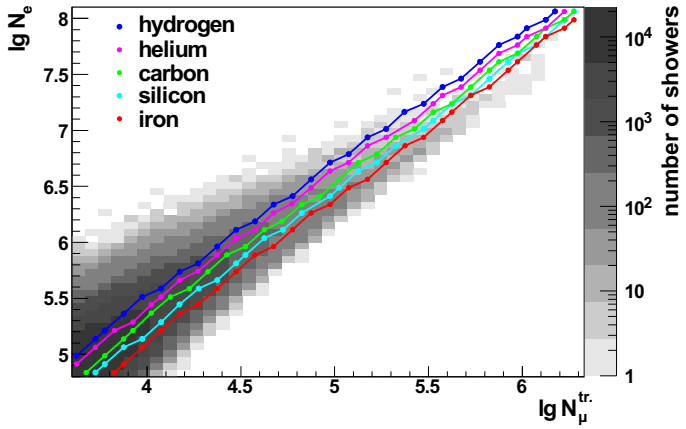


Figure 8.9: Most probable values for QGSJET01 and FLUKA, using the calculated two-dimensional response functions. Additionally the measured two-dimensional size spectrum (the data used) is depicted.

the distribution, the iron edge, in the region of small electron and muon numbers, the largest deviations can be found. The absence of iron at low energies is correlated with these insufficiencies in the data description.
The projection of the two-dimensional size spectrum of electron and muon numbers along the lg $N_\mu^{tr.}$-axis for certain lg $N_\mu^{tr.}$-intervals and its comparison with the reconstructed data offers another possibility of studying the performance of this particular interaction model. In Figure 8.8 the projections of the measured and reconstructed all-particle distributions and the reconstructed distributions of the individual mass groups are displayed for three different lg $N_\mu^{tr.}$ intervals. These projections are similar to the lg $N_e$-distributions for certain energies. The reconstructed distributions are obtained by means of convolution of the resulting energy spectra with the response functions. The plots shown in Figure 8.8 correspond to different energy ranges in the region of the knee (upper graph) and above it (lower graphs), whereat a small number of muons implies a low-energy.
The overall data description within the statistical uncertainties seems to be satisfactorily, but for values of lg $N_\mu^{tr.}$ between 4.02 and 4.07 at small electron numbers, i. e. at the so-called iron edge, some deviations can be found. With increasing energy (increasing muon number) the data description at the heavy edge improves.
In addition the plots also demonstrate the contribution of the different elemental groups to the total distribution. At low energies (see upper graph of Figure 8.8) no iron can be present as the mean value and the tail of iron predicted from simulations are not able to describe the distribution. The contribution of iron to the all-particle flux rises with increasing energy. The plot for values of lg $N_\mu^{tr.}$ between 4.02 and 4.07 even reveals that although no iron is present at the heavy edge, there are more showers reconstructed than measured.
At low energies, the light primary particles, especially hydrogen and helium, are most abundant, but with increasing energy the composition becomes heavier, i. e. the contribution of the heavy elements to the total distribution rises and implies a decrease of the light primary particles. The decreasing abundances can be detected as kinks in the energy spectrum of hydrogen and helium.

With the help of Figure 8.8 it is feasible to clarify, which is the most dominant element or which element is not necessary for the data description, but for a more precise understanding the knowledge of the position of the most probable values of each elemental group is indispensable.

Not only the size of the fluctuations, but also the position of the maxima with respect to the measured distribution has an essential impact on the results of the analysis. For clarification purposes in Figure 8.9 the maximum values of all primary particle types are displayed together with the measured two-dimensional size spectrum of electron and muon numbers. The lines of the most probable values are determined using the calculated two-dimensional response functions. Each data point of a line corresponds to a different energy, whereat the energy increases with increasing shower sizes. On basis of this depiction it is possible to clarify roughly some of the features of the energy spectra. For example the knee-like structures in the hydrogen as well as in the helium spectrum can be explained by the course of their most probable values with respect to the maximum of the measured distribution. At low energies (small electron and muon numbers) the most probable values of helium are located almost in the maximum of the measured distribution, and for this reason at low energies helium is the dominant primary particle. But going to higher energies the helium lines and the maximum of the data more and more diverge, which leads to a change of the index in the helium spectrum. A similar argumentation can be applied for hydrogen, but with the difference that the lines for hydrogen are slightly shifted (to the left) with respect to the maximum of the data, leading to hydrogen appear less abundant.
The energy spectra of carbon and silicon do not exhibit any index changes, as the positions of their lines of the maximum values do not change significantly with respect to the ridge of the data. Regarding the most probable values for iron, an increasing contribution to the all-particle flux is expected, since the maximum of the two-dimensional histogram and the lines of the most probable values more and more converge with increasing energy. The total absence of iron at low energies can not be absolutely clarified by the analysis of the most probable values, because the shower fluctuations can also influence the elemental abundances.
The conclusion of the discussion on Figure 8.8 and Figure 8.9 is that the shape of the energy spectra and the elemental abundances is affected by the width of the distributions of different primary particle types and energies as well as by the positions of the maximum values.

### 8.3.4 EPOS1.99 and FLUKA, $0 - 18°$

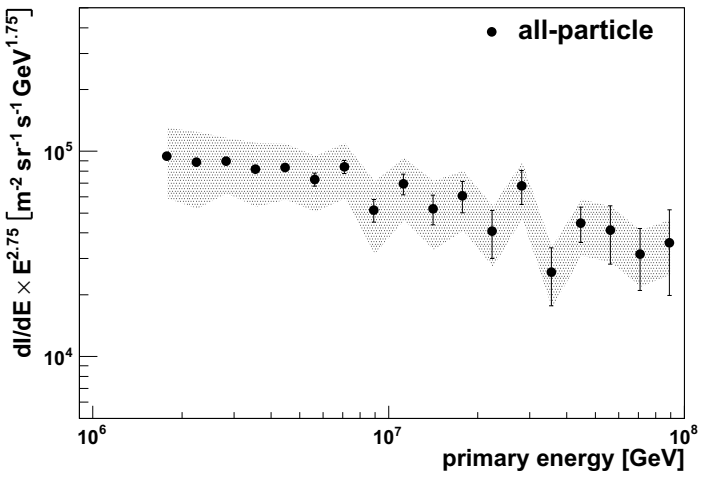


Figure 8.10: All-particle energy spectrum, using EPOS1.99 and FLUKA. The error band indicates the systematic uncertainties, the error bars display the statistical uncertainties.

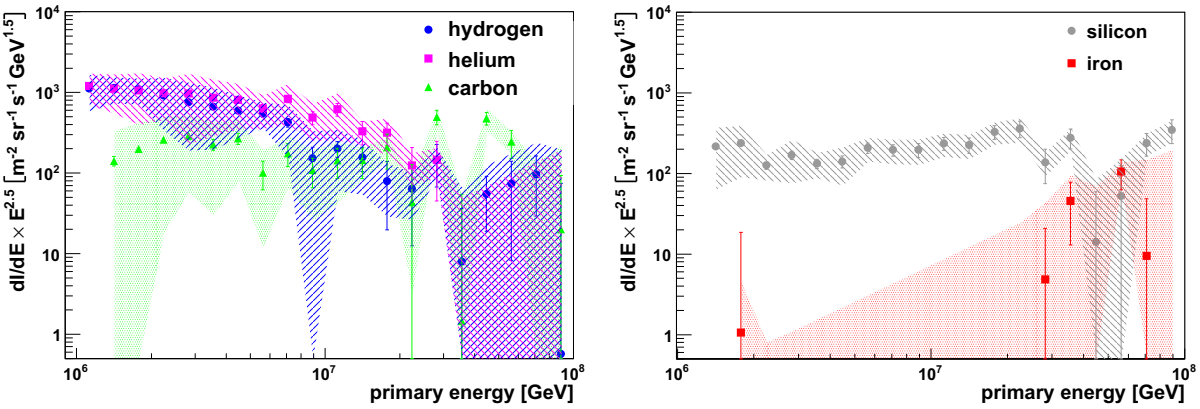


Figure 8.11: Energy spectra of hydrogen, helium and carbon (left part) and silicon and iron (right part), using as hadronic interaction models EPOS1.99 and FLUKA. The error band displays the systematic uncertainties and the error bars represent the statistical uncertainties.

Figure 8.10 displays the all-particle energy spectrum for zenith angles from 0° to 18° obtained by the unfolding analysis using as hadronic interaction models EPOS1.99 and FLUKA. The iteration level is chosen according to Figure D.2 in the appendix. At an energy of $\approx 7 \times 10^{15}$ eV a change of index in the all-particle spectrum can be observed. In comparison with QGSJET01 and FLUKA this index change is less significant.
The energy spectra of the individual mass groups, which are shown in Figure 8.11, exhibit different elemental abundances compared to QGSJET01/ FLUKA. Hydrogen and helium are almost equally abundant in the energy range from $10^6$ to $10^8$ GeV. The index change in both cases is only weak. At an energy of $\approx 5 - 6 \times 10^{15}$ eV the hydrogen knee can be found and the position of the knee in the helium spectrum can be determined to $\approx 1 \times 10^{16}$ eV. Again the positions of both knees to one another indicate a rigidity dependence. The energy spectra of carbon and silicon exhibit similar abundances and do not show any knee-like feature. Compared to QGSJET01/ FLUKA the situation for iron becomes even worse, when using EPOS1.99/ FLUKA. Nearly no iron is present over the whole energy range. Solely at high energies some iron induced air showers are reconstructed, but being liable to large fluctuations. The systematic uncertainties, mainly being dominated by the uncertainties arising from the parameterisation of the lg $N_e$-distribution, are larger than the uncertainties for QGSJET01/ FLUKA, only the systematic uncertainties of the silicon spectrum are of comparable size. The inspection of the $\chi^2$-distribution (see Figure 8.12) reveals deficiencies in the data description at low energies (small electron and muon numbers), especially at the heavy edge (right side of the distribution). With increasing energy the $\chi^2$-distribution becomes more and more homogeneous, but compared to QGSJET01 the overall data description, characterised by a $\chi^2_{ndf}$ of 1.79, is worse.
The lg $N_e$-distribution for the same three lg $N_\mu^{tr.}$-intervals as in the section before can be found in Figure E.1 in the appendix. The distributions of the first lg $N_\mu^{tr.}$-interval show similarities to the one of QGSJET01. Again a large amount of light primary particles, but no iron is required to describe the measured data. Even with increasing energy the situation for iron does not improve, which can be directly observed in the iron spectrum as well (up to $3 \times 10^{16}$ eV no iron is present). Furthermore, with increasing energy the contribution of the light elements (H, He) to the overall distribution decrease, leading to knee-like structures in the individual spectra.
Depiction 8.13 shows the most probable values for EPOS1.99 and FLUKA compared to the measurement. The lines for hydrogen and helium start almost in the maximum of the data

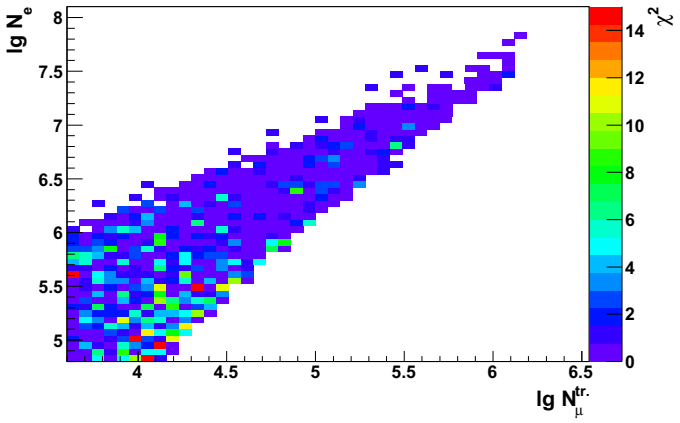


Figure 8.12: $\chi^2$-distribution of the solution of EPOS1.99 and FLUKA for zenith angles in the range $0 - 18°$.

distribution, which helps to explain the dominant contribution of these elements at low energies. With increasing energy the most probable values leave the maximum, leading to an alteration of their elemental abundances. The similar abundances of hydrogen and helium can be explained by the shift of the lines of the most probable values towards the heavy edge compared to QGSJET01. For QGSJET01 the lines of the most probable values of helium are almost consistent with the maximum and the lines for hydrogen are shifted to the left with respect to the maximum. For EPOS1.99 a shift of the lines of hydrogen towards the heavy edge is equivalent to a shift towards the maximum of the measured two-dimensional distribution, which leads to a increase of the hydrogen contribution and decrease of the amount of helium. An almost constant slope can be found for carbon and silicon, which can be explained by the almost constant position of the maximum values with respect to the maximum of the two-dimensional size spectrum. Comparing the lines of the most probable values with those of QGSJET01/ FLUKA it becomes obvious that they are shifted in the direction of the heavy edge, which leads to a reduction of the iron flux compared to QGSJET01/ FLUKA.

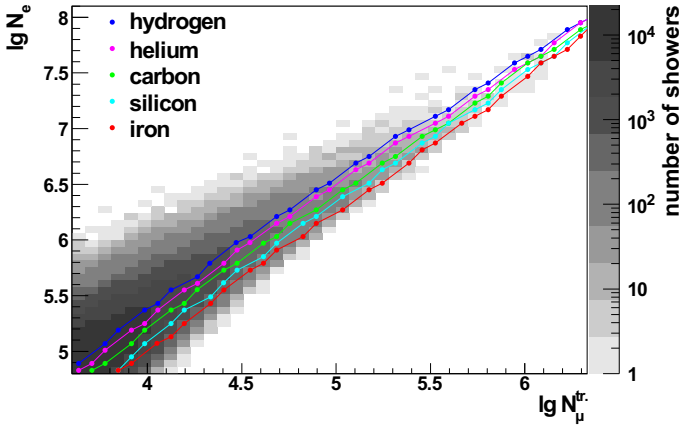


Figure 8.13: Most probable values for EPOS1.99 and FLUKA, using the calculated two-dimensional response functions. Additionally the measured two-dimensional size spectrum (the data used) is depicted.

### 8.3.5 QGSJETII and FLUKA, $0 - 18°$

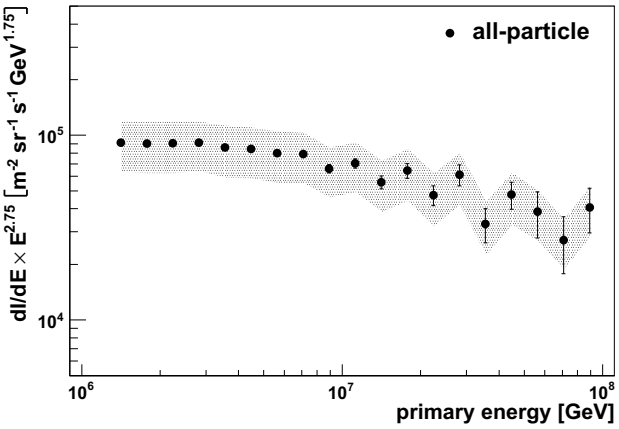


Figure 8.14: All-particle energy spectra, using QGSJETII and FLUKA. The error band indicates the systematic uncertainties, the error bars display the statistical uncertainties.

In Figure 8.14 the all-particle spectrum from $0-18°$, using QGSJETII and FLUKA, is depicted. The stop criterion was chosen on basis of Figure D.3 in the appendix. At an energy of approximately $4-5\times10^{15}$eV a kink in the all-particle flux can be observed.
The left side of Figure 8.15 shows the energy spectra of hydrogen, helium and carbon. Hydrogen is less abundant than helium and carbon. At an energy of $\approx 4\times10^{15}$eV a kink in the hydrogen spectrum can be found. An examination of the energy spectrum of helium and carbon, which are the most abundant nuclei, illustrates an almost equal abundance of both elements, but the two primary particle types differ in their knee positions. Whereas the helium spectrum is characterised by a kink at $\approx 7-8\times10^{15}$eV, the change of index in the carbon spectrum can be found at approximately $2-3\times10^{16}$eV. Like for the models discussed before the knee positions of the three elements (H, He, C) relative to each other demonstrate a compatibility with a rigidity dependence of the knees of the individual spectra. It should be mentioned that in case of the

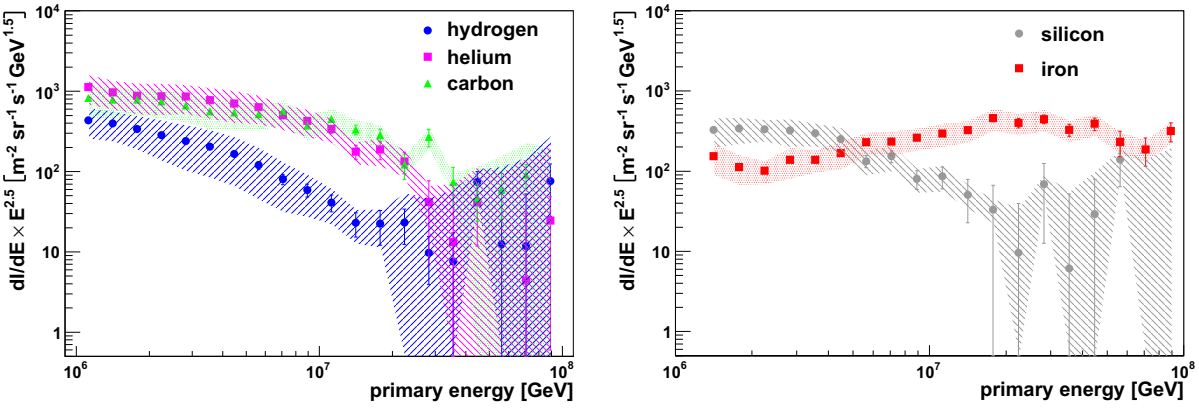


Figure 8.15: Energy spectra of hydrogen, helium and carbon (left part) and silicon and iron (right part), using as hadronic interaction models QGSJETII and FLUKA. The error band displays the systematic uncertainties and the error bars represent the statistical uncertainties.

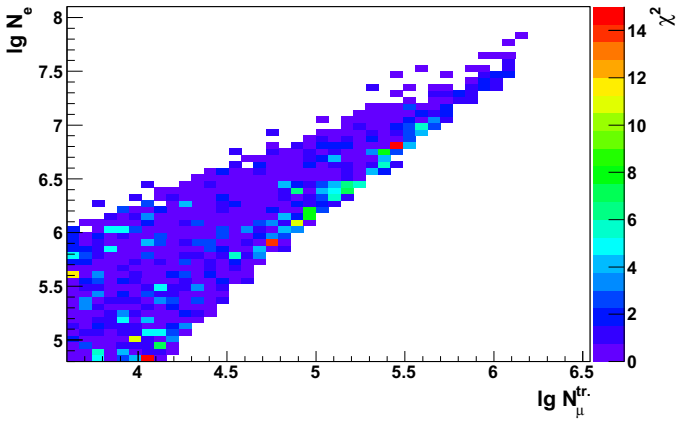


Figure 8.16: $\chi^2$-distribution of the solution of QGSJETII and FLUKA for zenith angles in the range $0 - 18°$.

steepening of the carbon spectrum the statistics in this energy region becomes poor and the spectrum is liable to large fluctuations, but a general trend can be seen.
The right part of Figure 8.15 comprises the energy spectra of silicon and iron. The silicon spectrum reveals a kink at an energy of $\approx 4 \times 10^{15}$eV, but the spectrum of iron does not show a knee-like feature. Assuming a rigidity dependence the kink in the silicon spectrum is not expected in this energy region. Its existence can be explained by the problems in the data description. Compared to the results of QGSJET01 and EPOS1.99, the use of QGSJETII as hadronic interaction model results in a reconstruction of more iron induced air showers at low energies. An examination of the $\chi^2$-distribution, displayed in Figure 8.16, reveals deficiencies mainly in the medium energy range especially at the heavy edge, which can explain the course of the silicon spectrum. The $\chi^2_{ndf}$ of 1.27, which is only slightly better than the one of QGSJET01/ FLUKA, indicates a good overall data description. To clarify in which energy range the description of data by simulations works best and in which region problems can be

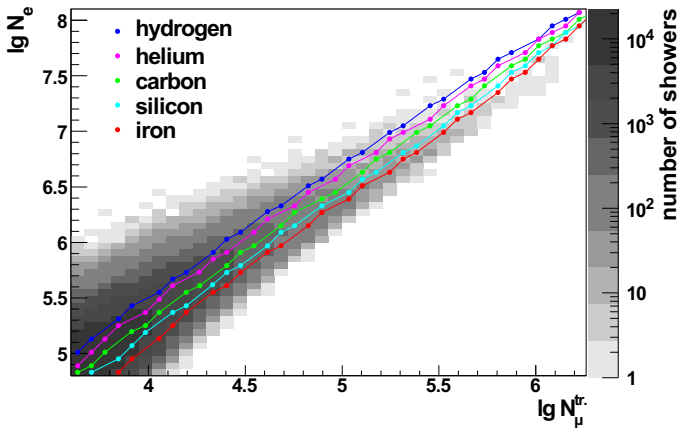


Figure 8.17: Most probable values for QGSJETII and FLUKA, using the calculated two-dimensional response functions. Additionally the measured two-dimensional size spectrum (the data used) is depicted.

found, the projections along the lg $N_\mu^{tr.}$-axis for different lg $N_\mu^{tr.}$-intervals (see Figure E.2 in the appendix) can be used. At low energies (small muon numbers) the contribution of the light elements is dominant, but reduces with increasing energy. Thus the course of the energy spectra of the light elements exhibit index changes. In contrast to the models discussed before, for QGSJETII in all three intervals a remarkable contribution of iron is found.
Figure 8.17 shows the two-dimensional shower size spectrum of electron and muon numbers and additionally the lines of the most probable values for all elements used. Whereas the lines of helium and carbon, being the most abundant elements at low energies, start almost in the maximum of the two-dimensional size spectrum, the line of hydrogen is located on the left-hand side of the maximum, which causes a minor frequency of hydrogen. With increasing energy the most probable values more and more leave the maximum region, leading to a kink in the individual energy spectra. For silicon the situation seems to be more complicated. Although the lines start on the right-hand side of the maximum of the data distribution and converge with increasing energy towards the maximum, a sharp kink in the silicon spectrum can be found. Solely from an examination of the course of the most probable values this change of index is not expected. With respect to the most probable values of silicon the values for iron are shifted to the heavy edge. The deficit of iron at low energies as well as the kink in the silicon spectrum can not be clarified by analysing only the most probable values. This reveals the importance of the shower fluctuations on the results of the analysis.

### 8.3.6 SIBYLL2.1 and FLUKA, $0 - 18°$

The all-particle spectrum from $0 - 18°$, using SIBYLL2.1 and FLUKA, can be found in Figure 8.18. By means of Figure D.4 in the appendix the stop criterion can be estimated. At an energy of approximately $4 - 5 \times 10^{15}$eV a kink in the all-particle flux can be found.
In the left part of Figure 8.19 the energy spectra of hydrogen, helium and carbon are depicted. Hydrogen is less abundant than helium and carbon. At an energy of $\approx 5 \times 10^{15}$eV a steepening of the hydrogen spectrum can be found. Comparing the size of the error band for hydrogen with the error bands of hydrogen, derived by the use of the other hadronic high-energy interaction models it becomes obvious that the error band for SIBYLL2.1 is broader. The difference in the size of the error bands can be explained by the larger impact of the parameterisations of the edges of the lg $N_e$-distributions (see Section 8.1) in case of SIBYLL. Helium and carbon, the

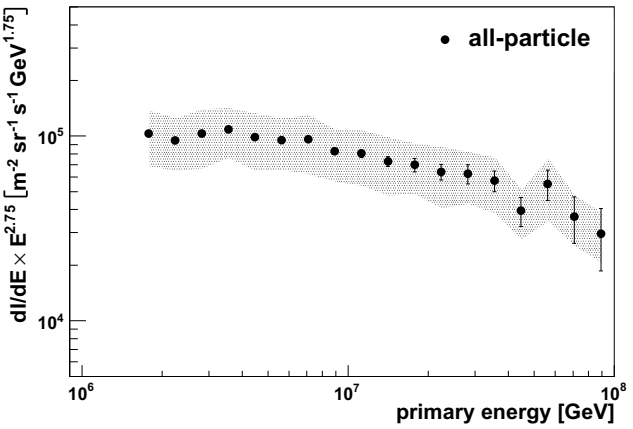


Figure 8.18: All-particle energy spectrum, using SIBYLL2.1 and FLUKA. The error band indicates systematic uncertainties, the error bars display the statistical uncertainties.

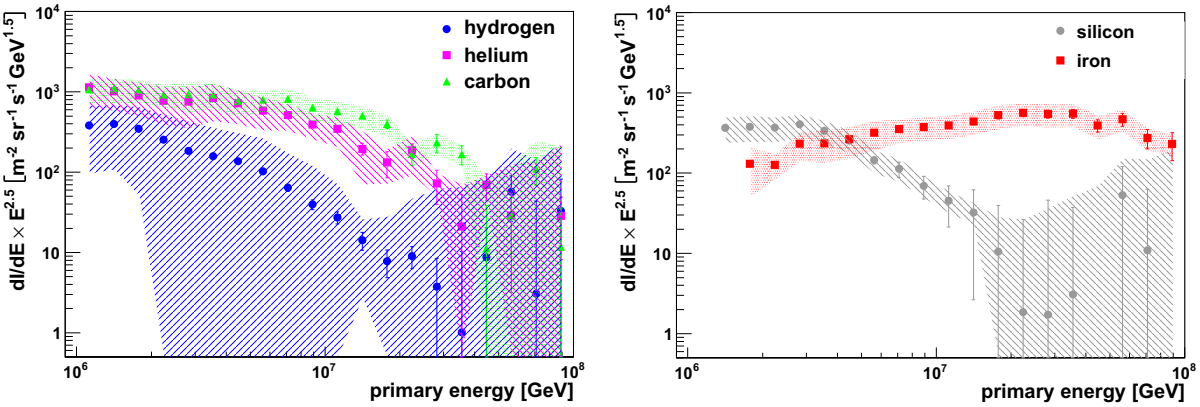


Figure 8.19: Energy spectra of hydrogen, helium and carbon (left part) and silicon and iron (right part), using as hadronic interaction models SIBYLL2.1 and FLUKA. The error band displays the systematic uncertainties and the error bars represent the statistical uncertainties.

most abundant nuclei, exhibit a similar abundance, but vary in the position of their kink. The helium spectrum shows a knee-like feature at $\approx 8 \times 10^{15}$eV, whereas the index of the carbon spectrum changes at approximately $2 - 3 \times 10^{16}$eV. Like for QGSJETII the kinks in the energy spectra of hydrogen, helium and carbon are consistent with a rigidity dependence.
The right part of Figure 8.19 shows the energy spectra of silicon and iron. The silicon spectrum reveals a kink at an energy of $\approx 4 \times 10^{15}$eV, which is not compatible with a rigidity dependence of the knee positions. Like for QGSJETII this kink is due to problems in the description of measured data by simulations. The spectrum of iron does not show any knee-like feature.
A comparison of the energy spectra of the various elements using QGSJETII/ FLUKA and SIBYLL/ FLUKA illustrates that the use of these two different hadronic high-energy interaction models changes only slightly the results of the unfolding analysis.
But having a look at the $\chi^2$-distribution, which is displayed in Figure 8.20, it becomes obvious that using SIBYLL/ FLUKA leads to similar problems as the use of QGSJETII/ FLUKA.

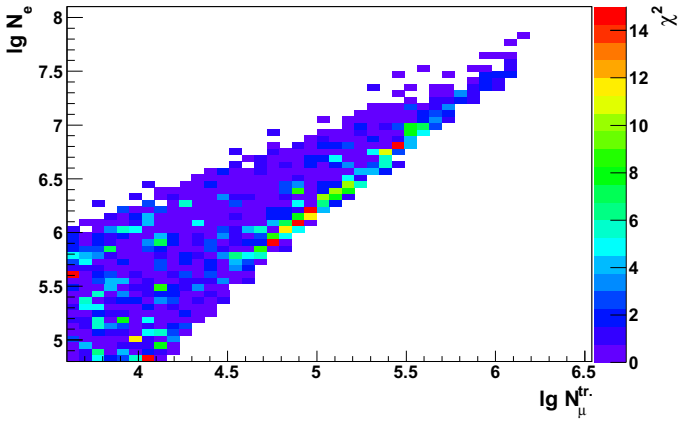


Figure 8.20: $\chi^2$-distribution of the solution using SIBYLL2.1 and FLUKA for zenith angles in the range $0 - 18°$.

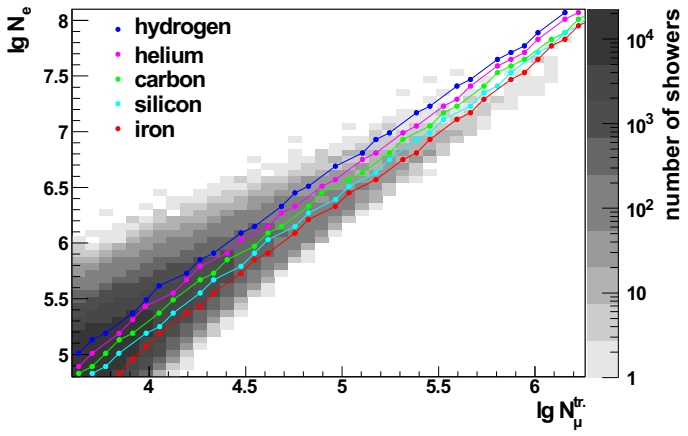


Figure 8.21: Most probable values for SIBYLL2.1 and FLUKA, using the calculated two-dimensional response functions. Additionally the measured two-dimensional size spectrum (the data used) is depicted.

Except the problems in the medium energy range at the iron edge the overall data description is good, which is indicated by an almost homogeneous $\chi^2$-distribution. The problems at the iron edge in the medium energy range are more pronounced compared to QGSJETII/ FLUKA, which also becomes evident when comparing the $\chi^2_{ndf}$ of 1.27 for QGSJETII/ FLUKA to 1.82 for SIBYLL/ FLUKA.
The lg $N_e$-distribution for three different lg $N_\mu^{tr.}$-intervals, which is shown in Figure E.3 in the appendix, can be used to clarify in which energy range problems in the data description occur and where the simulations describe the data properly. The graphs reveal a good agreement of measured data and reconstructed data at low up to medium energies, but at higher energies problems in the data description at the lower edge (iron edge) become apparent.
The lines of the most probable values together with the measured two-dimensional size spectrum can be found in Figure 8.21. The most probable values for QGSJETII/ FLUKA and SIBYLL/ FLUKA are almost identical, which can be seen in Figure 8.2 for hydrogen and iron induced air showers and therefore the discussion of the most probable values for QGSJETII/ FLUKA in the section before is also valid for SIBYLL/ FLUKA and is not reconsidered. On basis of Figure 8.2 the similarity of the results of the unfolding analysis for QGSJETII and SIBYLL2.1 can be understood.

## 8.4 Comparison of the all-particle spectra

Figure 8.22 shows the all-particle spectra of all hadronic high-energy interaction models used in this analysis. For illustration purposes the energy spectra are multiplied by $E^{2.75}$ and the systematic errors (error bands) are not depicted for reasons of clarity, but they are of similar size for all models. Each of the all-particle energy spectra is characterised by a knee-like structure, but the positions vary from one model to the other from 4 to $7 \times 10^{15}$ eV. The spectral index $\gamma$ before the knee is for each of the unfolded energy spectra approximately 2.7 and changes to $\gamma \approx 3.1$ after the knee.
The all-particle energy spectra derived, using different interaction models, agree within the systematic and statistical reconstruction uncertainties, but a more precise examination reveals distinct differences. Whereas the all-particle spectra of QGSJET01 and SIBYLL2.1 agree well,

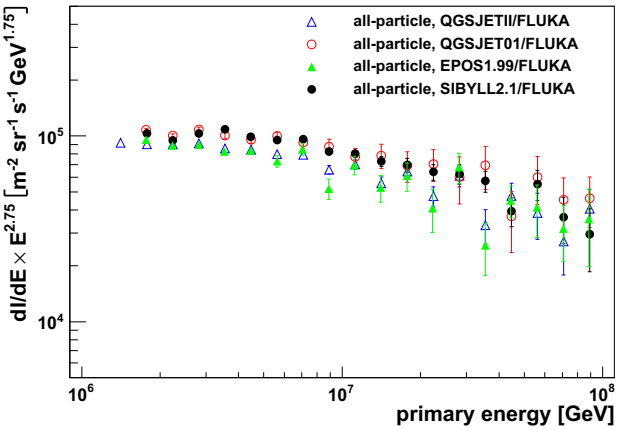


Figure 8.22: Comparison of the all-particle spectra derived by the use of different hadronic high-energy interaction models. As low-energy interaction model in all simulations FLUKA is used.

the all-particle fluxes for QGSJETII and EPOS1.99 are shifted to lower values. The differences in the all-particle flux, arising from the use of different hadronic high-energy interaction models, can be explained by the varying mean energy assignment of different models. It is conspicuous that the fluctuations of the all-particle flux of EPOS1.99 and also QGSJETII (but less pronounced) start at lower energies compared to QGSJET01 and SIBYLL. These fluctuations are mainly due to the varying energy assignment, which leads for EPOS1.99 and QGSJETII to a lower number of reconstructed showers in an individual energy bin. In addition the all-particle energy spectra, which are shifted to lower flux values, are characterised by knee positions at higher energies.

## 8.5 Qualitative comparison of results for different interaction models

None of the interaction models discussed in the previous sections is able to describe the measured data properly over the entire energy range. The most probable values together with the $\chi^2$-distributions allow a qualitative comparison of the different interaction models and can give hints on the origin of the mismatching of data by model predictions. On basis of the $\chi^2$-distributions for different interaction models (see Figures 8.7, 8.12, 8.16 and 8.20) the insufficiencies in the data description can be visualised. The lines of the most probable values (see Figures 8.9, 8.13, 8.17 and 8.21) can help to draw conclusions on the shape of the individual energy spectra, like for example the varying abundances. QGSJET01 and QGSJETII describe the data equally well, the data description for SIBYLL2.1 and EPOS1.99 is worse. Considering the $\chi^2$-distributions it becomes obvious that for all models the largest discrepancies between measured and reconstructed data appear at the heavy edge, but in different energy regions. Whereas for QGSJET01 and EPOS1.99 these discrepancies occur at low energies, i. e. at low muon numbers, for QGSJETII and SIBYLL2.1 they can be found in the medium to high energy range, i. e. at medium to high muon numbers.
The two-dimensional shower size spectrum together with the most probable values for hydrogen and iron induced showers for all models used in the analysis are displayed in Figure 8.2. For a better illustration in Figure 8.23 the residuals in the electron number $\lg N_e$ with respect to QGSJETII are plotted subject to the truncated muon number $\lg N_\mu^{tr.}$ for hydrogen and

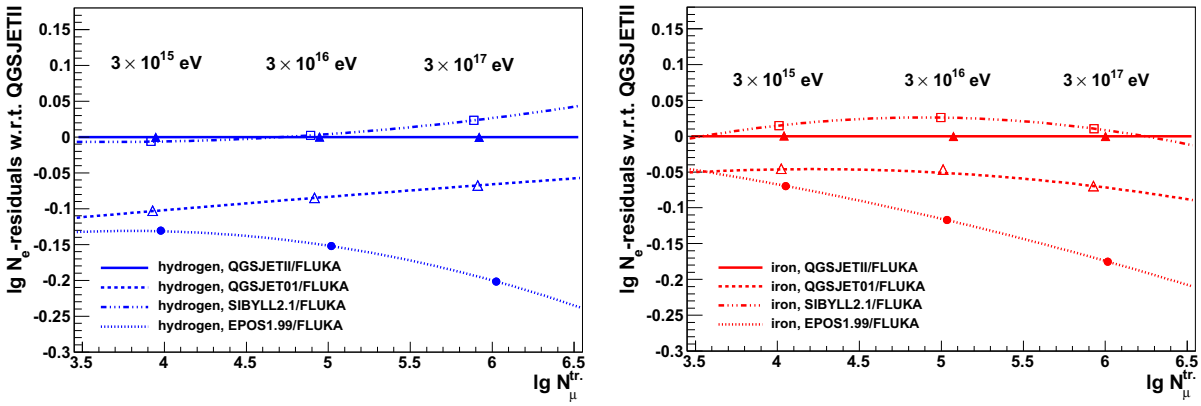


Figure 8.23: lg $N_e$-residuals with respect to QGSJETII and FLUKA subject to the truncated muon number. The markers illustrate three different energies.

iron initiated events. The lines of QGSJET01 and SIBYLL2.1 are almost parallel but slightly shifted to each other. Also the lines for QGSJETII are characterised by a similar slope. Solely the lines of EPOS1.99 exhibit a lower gradient. The lines of QGSJETII and SIBYLL2.1 are nearly on top of each other, leading to similar shapes of the individual spectra and to similar elemental abundances. But the mean energy assignment is different for both models, which can be explained by the fact that on average an air shower simulated with SIBYLL2.1 produces at the same energy less electrons and less muons than an air shower simulated with QGSJETII. In Figure 8.23 additionally the marker for three different energies are displayed. Whereas the markers for QGSJET01 and SIBYLL2.1agree in the energy and the muon number, the markers for EPOS1.99 and QGSJETII are slightly shifted to higher energies. This shift, which can be observed for hydrogen as well as iron induced showers, illustrates the varying energy assignment of different models. The shift of the all-particle energy spectrum of QGSJETII to lower flux values with respect to SIBYLL2.1 is due to this varying mean energy assignment. With increasing energy the most probable values of iron more and more converge with the maximum of the measured distribution and thus for a description of the heavy edge a large amount of iron is needed to fit the measured data (see also lower graphs in Figure E.2 and E.3). This results in a sharp decrease of the silicon spectrum and leads to inconsistencies in the data description. On the one hand a reduction of the slope of the most probable values would improve the data description at the heavy edge. A lower gradient can be achieved by either a faster rise of the muon number or a slower rise of the electron number with increasing energy. On the other hand a less rapid decrease of the shower fluctuations with increasing energy could also lead to an improvement of the compatibility of data and simulations.
Compared to QGSJETII and SIBYLL2.1 the lines of the most probable values for QGSJET01 are shifted towards the heavy edge, which results in different elemental abundances. The absence of iron at low energies is correlated with the problems in the data description. There are two possibilities of eliminating these problems. One possibility could be the shift of the most probable values at low energies away from the heavy edge towards the maximum of the two-dimensional shower size spectrum. An alternative solution would be the reduction of the shower fluctuations at low energies.
The lines of the most probable values for EPOS1.99 at low energies are even shifted more towards the heavy edge compared to QGSJET01. Additionally the slope of the lines for EPOS1.99 is flatter. The combination of both results in a lack of iron over almost the entire

energy range and causes problems in the data description mainly at low energies at the heavy edge. In the low energy region the same statements as for QGSJET01 can be applied. Since with increasing energy for QGSJET01 the data description becomes more consistent, the convergence of the maximum values for EPOS1.99 with the lines of QGSJET01 at higher energies would lead to a more compatible description of measured data.
A change of the slopes of the most probable values or a variation of the size of the shower fluctuations would not only affect the heavy primary particles, but also have an impact on the light elements. Since the compatibility of the interaction model used is affected by an interplay of the maximum values and the shower fluctuations, an alteration of the properties of the interaction models can result in problems in other regions of the measured two-dimensional shower size spectrum.

To summarize, all discussed models exhibit problems especially at the heavy edge, but at different energies. On basis of the unfolding analysis incapabilities of describing measured data by the interaction models can be observed, but none of the models completely fails in the data description. A similar statement can be found in [Ent11], where the predictions of the interaction models QGSJET01, QGSJETII, SIBYLL2.1 and EPOS1.99 are compared to CERN LHC data. In [Ent11] the authors point out that none of the models indeed provides a very good description of all considered observables, but that no new or exotic physics is needed to describe the data. At present the LHC is running with a center of mass energy $\sqrt{s} = 7\,\mathrm{TeV}$, corresponding to a fixed-target energy of $2.4 \times 10^{16}\,\mathrm{eV}$, and thus is the first collider experiment reaching an energy higher than the knee energy. The data derived by LHC measurements can be used to tune the parameters of the models and therefore improve the reliability of air shower simulations, but there is no evidence from the present results that the extrapolation to higher energies have to be changed significantly. Furthermore the authors mention that the interpretation of air shower data in the energy range of the knee as a change from a light to heavy mass composition is supported by LHC measurements. The statements in [Ent11] are absolutely compatible with the findings of the present work.

## 8.6 Deconvolution of KASCADE-Grande data

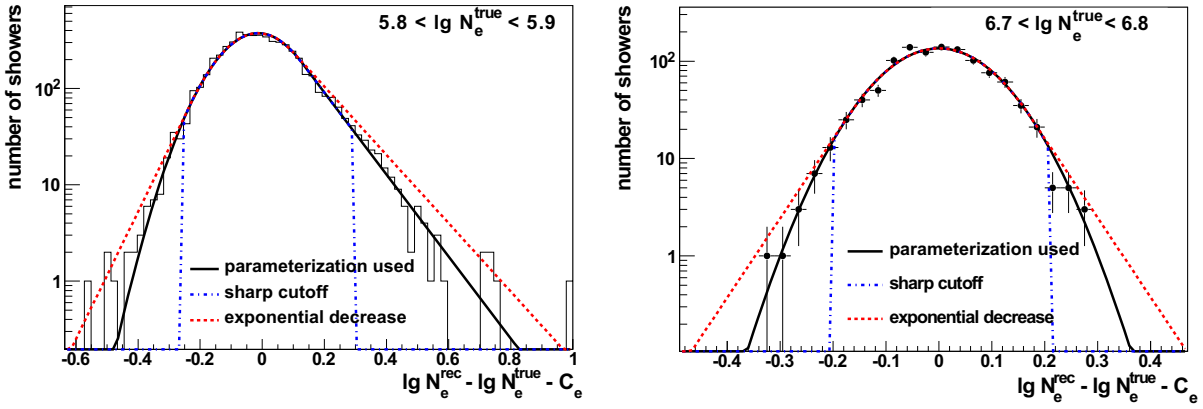


Figure 8.24: Distribution of the reconstruction uncertainties in the electron number for $5.8 < \lg N_e^{true} < 5.9$ (asymmetric function) on the left and for $6.7 < \lg N_e^{true} < 6.8$ (Gaussian) on the right. Additionally in both cases the two extreme assumptions are shown (exponential decrease and sharp cutoff).

In Section 8.1 of this chapter an additional source of systematic uncertainties, arising from the parameterisation of the shower fluctuations, is discussed. In case of KASCADE-Grande also the parameterisations of the distribution of the reconstruction uncertainties have to be accounted for. As shown in Figure 7.1 and Figure 7.2 the detector resolution for KASCADE-Grande is not as good as for KASCADE. Whereas the resolution of the electron number of both experiments differ significantly, the differences in the resolutions of the number of muons (KASCADE uses the truncated muon number, KASCADE-Grande the total muon number) are less distinct. In particular, the edges of the parametrization of the intrinsic shower fluctuations are an additional source of systematic uncertainties. The lower resolution in lg $N_e$ for KASCADE-Grande compared to KASCADE leads to the necessity of taking also into account the edges of the distribution of the reconstruction uncertainties as an further source of systematic uncertainties. Figure 8.24 shows the parameterisations of the distribution of the reconstruction uncertainties for two different electron number intervals. For electron numbers lg $N_e^{true}$ up to 6.3 an asymmetric function and above a Gaussian is used. The red and the blue dashed lines display the two extreme assumptions, whereas the solid black curve represents the original parameterisations. The blue dashed line shows the functions with a sharp cutoff at 1/10 of the maximum of the distribution and red one the parameterisation assuming an exponential decrease at 1/5 of the maximum. Solely the right edge of the red curve is treated differently. Since the original distribution already exhibits an exponential decrease, in order to obtain a broader distribution the slope of the original exponential decrease is enlarged by 20%. To estimate the uncertainties the extreme assumptions of the shower fluctuations (see Figure 8.1) and the distribution of the reconstruction uncertainties are combined. Since the shower fluctuations in the electron number are the dominant contribution to the shower fluctuations only the parameterisation of the reconstruction uncertainties in lg $N_e$ are considered. One set of response functions is calculated with a combination of the exponential decrease of the parameterisation of the shower fluctuations and the exponential decrease of the parameterisation of the distribution of the reconstruction uncertainties. Another set is calculated with a combination of the two sharp cutoffs. For both sets the measured data is unfolded. The differences of the two solutions describe an additional

source of systematic uncertainties (included in the bands), which originates from the parameterisation of the shower fluctuations in combination with the parameterisation of the distribution of the reconstruction uncertainties.

### 8.6.1 QGSJETII and FLUKA, $0 - 18^{\circ}$

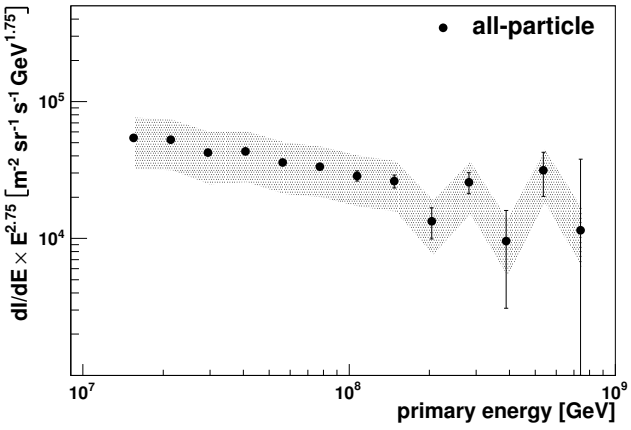


Figure 8.25: All-particle energy spectra, using QGSJETII and FLUKA. The error band indicates the systematic uncertainties, the error bars display the statistical uncertainties.

A deconvolution analysis on basis of KASCADE-Grande data allows the reconstruction of the energy spectra in the energy range from $10^{16}$ eV to $10^{18}$ eV. The WMSE, on basis of which the stop criterion ($\Delta\chi^2$) is determined, can be found in Figure D.5 in the appendix. Figure 8.25 shows the unfolded all-particle spectrum based upon KASCADE-Grande data. The all-particle flux does not reveal any knee-like features.
Figure 8.26 comprises the energy spectra of the individual elements. On the left-hand side the spectra of the light elements, hydrogen, helium and carbon, are depicted. Regarding the reconstruction of energy spectra of different test sets, which are discussed in Section 7.3.2, it becomes obvious that the reconstruction of energy spectra works in most cases up to an energy of $\approx 10^8$ eV. For higher energies the reconstruction uncertainties are very large and do not allow to draw any conclusion on the shape nor on the abundances of the elements.

Using QGSJETII and FLUKA, hydrogen is the least abundant primary particle type in the energy range of Grande. The increase of the hydrogen spectrum at high energies ($E > 10^8$ GeV) is most probably an artificial effect of the unfolding method itself, which is also observed in the reconstruction of the test spectra (see Figure 7.24). Up to an energy of $\approx 10^8$ GeV the course of the helium spectrum is almost parallel to the hydrogen spectrum, but shifted to higher flux values. For energies higher than $\approx 2 \times 10^8$ GeV the helium flux disappears. Solely at an energy of $5 - 6 \times 10^8$ GeV a further single flux value is reconstructed, but as already mentioned the reconstruction for energies higher than $\approx 10^8$ GeV is afflicted by large uncertainties. The carbon spectrum is characterised by a steep course with an index $\gamma \approx 5.7$. Above $\approx 2 \times 10^8$ GeV the same problems as in case of the helium spectrum occur. Nearly no carbon is reconstructed above this energy, only at $5 - 6 \times 10^8$ GeV a single flux value can be found. In the right part of Figure 8.26 the fluxes of the elements silicon and iron are shown. The course of the silicon spectrum is similar to the one of the carbon spectrum. It is characterized by approximately the same spectral index and a similar abundance. At energies above $\approx 2 \times 10^8$ GeV the silicon flux is smaller than $10^{-1}\mathrm{m}^{-2}\mathrm{sr}^{-1}\mathrm{s}^{-1}\mathrm{GeV}^{1.5}$ and at larger energies one single flux value is

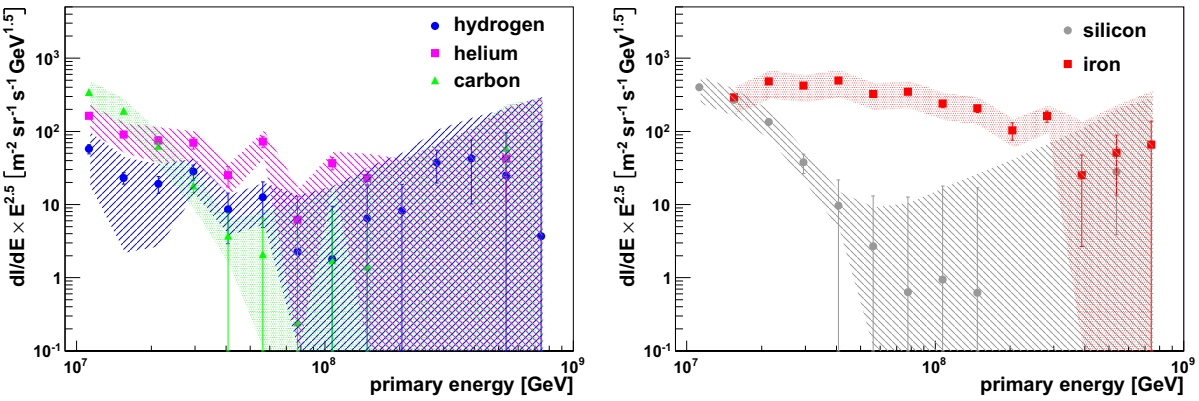


Figure 8.26: Unfolded energy spectra of hydrogen, helium and carbon (left part) and silicon and iron (right part), using as hadronic interaction models QGSJETII and FLUKA. The error band displays the systematic uncertainties and the error bars represent the statistical uncertainties.

reconstructed. The reconstructed energy spectra of the elements hydrogen, helium, carbon and silicon all reveal problems for energies larger than $2 \times 10^8$ GeV, which also becomes apparent by comparing the reconstructed and the true energy spectra (see Section 7.3.2.4). The reason for the absence of H, He, C and Si at this energies can mainly be explained by the low statistics of these elements in this energy range. The sizes of the systematic (error bands) and the statistical uncertainties (error bars) do not allow to draw any conclusion on the course and the abundances of these elements for energies higher than $2 \times 10^8$ GeV. The iron spectrum does not show any of these effects and can be reconstructed up to the highest energies. Solely the first point of the spectrum, near the threshold of the experiment, seems to be shifted to a lower flux value. Considering the true and the reconstructed iron spectra in Section 7.3.2.1, 7.3.2.2 and 7.3.2.4, it is conceivable that this is an threshold effect. The interaction models used can be another possible explanation for the increase of the iron flux near the threshold. Compared to the results of the KASCADE unfolding for the same interaction models (QGSJETII and FLUKA) in Section 8.3.5 a similar trend for both iron spectra is observable, where the interaction model as possi-

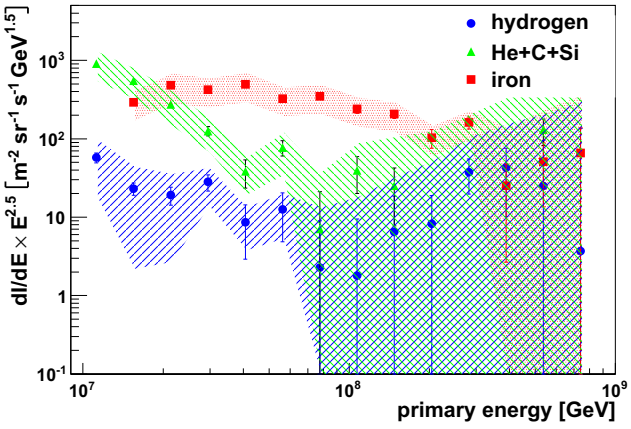


Figure 8.27: Unfolded energy spectra. Helium, carbon and silicon are combined to one component.

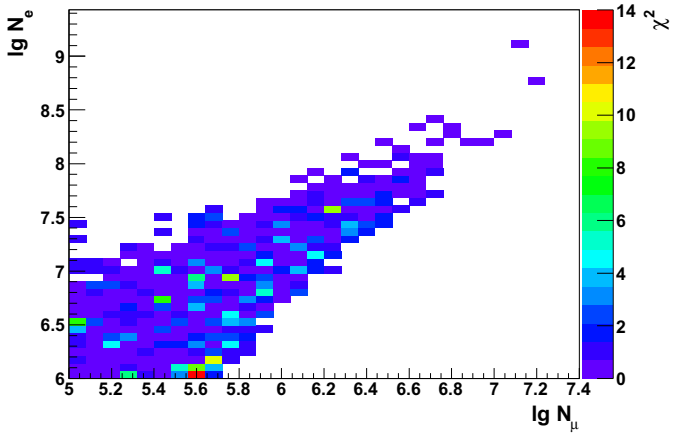


Figure 8.28: $\chi^2$-distribution of the solution of QGSJETII and FLUKA for zenith angles in the range $0 - 18°$.

ble source seems more likely. The size of the statistical and systematic uncertainties indicate that the reconstruction works properly up to an energy of $4 \times 10^8$ GeV. At higher energies the reconstruction uncertainties increase. A kink in the iron spectrum can be found at an energy of $\approx 8 - 9 \times 10^8$ GeV. Considering the knee positions of hydrogen, helium and carbon, derived from the QGSJETII analysis of KASCADE data, the determined position of the knee in the iron spectrum for KASCADE-Grande is also consistent with a rigidity dependence. The earlier as expected kink can be explained by the fact that the reconstructed iron spectrum does not only contain showers of the iron group, but also of the lighter elements. As a consequence of this mixture the knee position of iron is shifted to lower energies.
As shown in Chapter 7.3.2 the reconstruction of 5 primary particle types in the unfolding analysis can, in some special cases, cause problems and lead to unstable solutions. The origin of the instabilities can not be exactly clarified, but they are most probably due to the interplay of the steepness of the individual energy spectra, the abundances of the elements and the detector resolution. As it is shown in Figure 7.25 a more stable solution can be achieved, when using indeed 5 primary particle types for the deconvolution, but then summing up the elements helium, carbon and silicon to a medium heavy component. The corresponding spectra can be found in Figure 8.27. In the medium heavy component no knee-like feature can be found. A further indication for summing up the elements helium, carbon and silicon to a medium-heavy component can be found in the next section, in which a comparison of the KASCADE-Grande and the KASCADE results is shown.
The two-dimensional $\chi^2$-distribution, indicating a good overall data description, can be found in Figure 8.28. The largest deviations between measured and reconstructed data can be found at the iron edge at low muon numbers. On basis of this distribution no severe problems in describing measured by reconstructed data can be observed.
Another way to analyse the data description is shown in Figure 8.29. The illustration comprises a comparison of measured and reconstructed KASCADE-Grande data according to Figure 8.8. The graphs show projections of the measured and the reconstructed two-dimensional size spectrum of electron and muon numbers along the lg $N_\mu$-axis for certain lg $N_\mu$-intervals. Additionally the distributions of the individual elements are depicted. All depictions reveal a good description of measured data by the reconstructed one. At low energies (small lg $N_\mu$) all primary particle types are present, but the dominant part of events is induced by heavy elements, especially iron. With increasing energy, i. e. with an increasing number of muons, the contribution of the

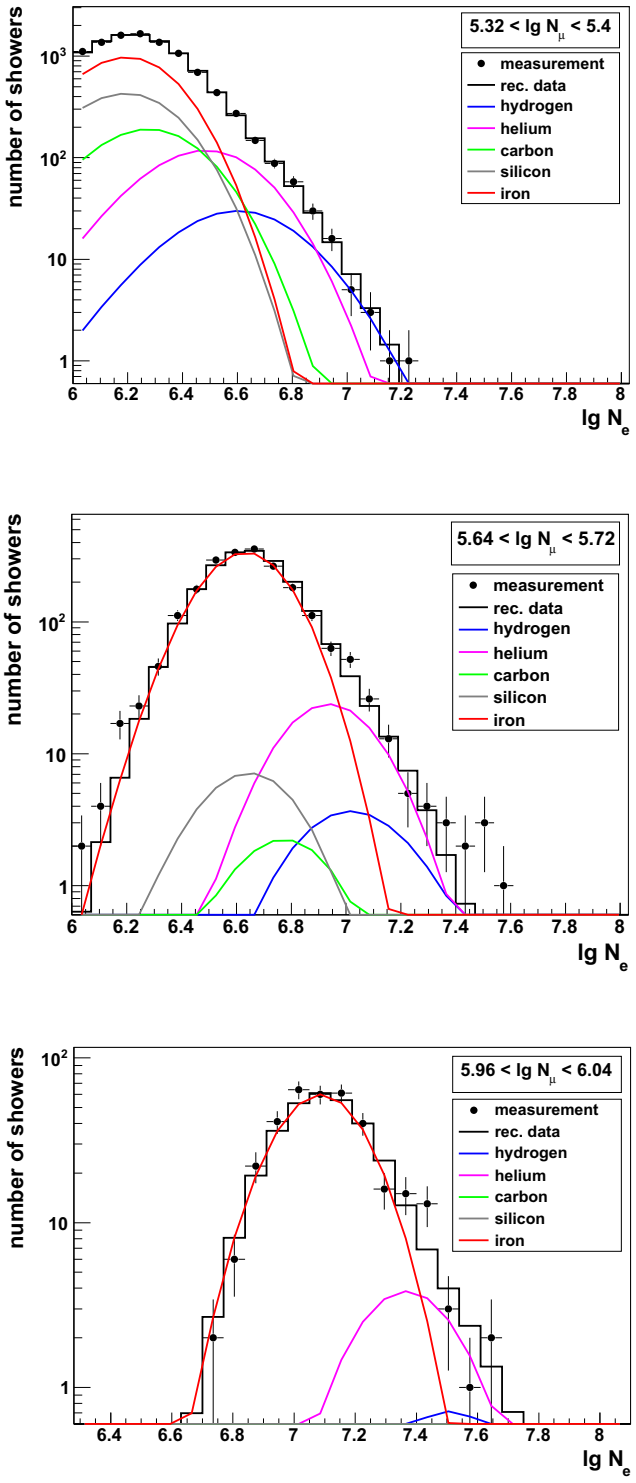


Figure 8.29: Projection along the lg $N_e$-axis of the two-dimensional size spectra of electron and muon numbers for different lg $N_\mu$-intervals. Plotted are the lg $N_e$-distributions of measured showers (dots) and via forward folding reconstructed showers (lines).

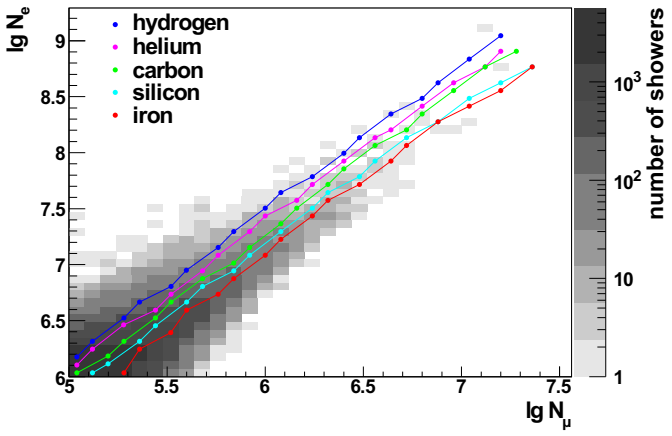


Figure 8.30: two-dimensional size distribution of electron and muon number. Additionally the lines of the most probable values are shown for each primary particle.

elements lighter than iron diminishes. In the lg $N_\mu$-interval from 5.64 to 5.72 iron is the dominant primary particle. Carbon and silicon are in this interval even less abundant than helium, which can be explained by the steep spectra of both elements. Going to even higher energies ($5.96 < \lg N_\mu < 6.04$) almost all primary particles measured by KASCADE-Grande are iron-like. Figure 8.30 comprises the two-dimensional shower size distribution of electron and muon numbers measured with KASCADE-Grande superimposed with the lines of the most probable values. In Section 8.3.5 the lines of the most probable values are discussed for KASCADE. As mentioned in this previous section not only the lines of the most probable values, but also the shape and the size of the shower fluctuations are of importance for the results of the analysis. Observing the lines of the most probable values at low energies, i. e. at small muon numbers, the lines of carbon and silicon are located in the maximum of the distribution, which leads to the assumption that these primary particle types (added up) are most abundant. Examining the energy spectra (see Figure 8.26) this is only valid for low energies. Both, carbon and silicon, are characterised by a steep spectrum. Solely from an investigation of the most probable values the course of these spectra cannot be deduced. For an understanding of the steepness of the energy spectra also the shower fluctuations and in case of KASCADE-Grande additionally the distribution of the reconstruction uncertainties have to be accounted for. Compared to silicon the line of iron is shifted towards the heavy edge of the distribution. With increasing energy the line more and more converges with the maximum, leading to an iron dominant composition. The lines of hydrogen and helium are shifted to higher electron numbers with respect to the maximum, for which reason it is expected that hydrogen and helium are less abundant than carbon and silicon. Solely from the course of the lines of the most probable values the shape of the energy spectra as well as the abundances cannot be explained, which clarifies that the shape and the width of the shower fluctuations as well as of the distribution of the reconstruction uncertainties are of great importance for the results of the analysis.

## 8.7 Comparison of KASCADE and KASCADE-Grande results

Figure 8.31 shows a comparison of the all-particle spectra of KASCADE and KASCADE-Grande for zenith angles from 0° to 18°, which are achieved using as hadronic interaction model QGSJETII and FLUKA. For illustration purposes no error bands are depicted. The re-

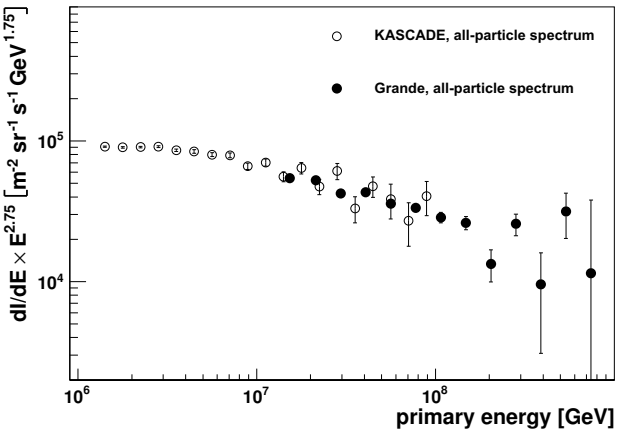


Figure 8.31: Comparison of the unfolded all-particle energy spectra of KASCADE and KASCADE-Grande $(0 - 18°)$.

constructed energy spectra of KASCADE and KASCADE-Grande agree well. With increasing energy the overall statistics decreases. In case of KASCADE this becomes obvious for energies above $2 \times 10^7$ GeV, where the unfolded all-particle flux is liable to statistical fluctuations. In the energy range from $2 \times 10^7$ GeV to $2 \times 10^8$ GeV the unfolded all-particle spectrum of KASCADE-Grande is smoother compared to the one of KASCADE, which reveals that the use of KASCADE-Grande data leads to an improvement in the determination of the all-particle flux. At energies above $2 \times 10^8$ GeV the all-particle flux of KASCADE-Grande is also affected by statistical fluctuations.
In Figure 8.32 a comparison of the reconstructed fluxes of the individual elements is shown. The systematic error bands are left out for reasons of depiction. The left part shows the energy spectra of the light elements. The hydrogen fluxes, reconstructed by unfolding KASCADE and KASCADE-Grande array data, are compatible within the systematic and statistical uncer-

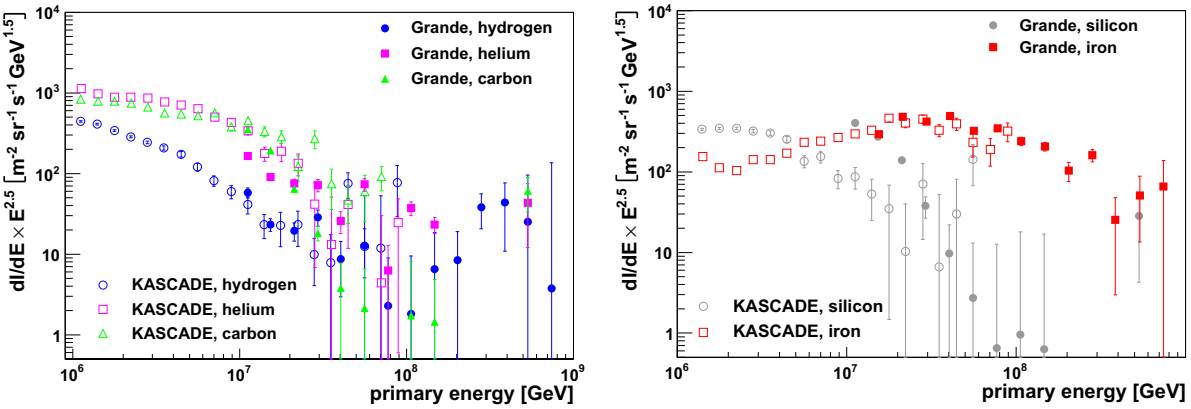


Figure 8.32: Comparison of the unfolded energy spectra of the individual elements for KASCADE and KASCADE-Grande, using as hadronic interaction models QGSJETII and FLUKA. Only showers in the zenith angle range from 0° to 18° are used. For illustration purposes no error bands are depicted.

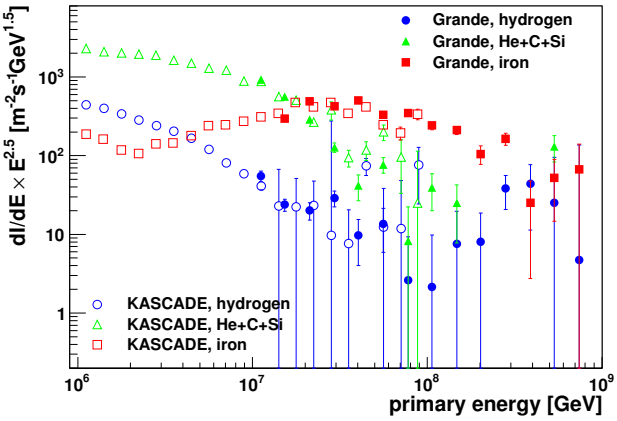


Figure 8.33: Unfolded energy spectra. Helium, carbon and silicon are combined to one component.

tainties. In comparison to KASCADE the helium flux of KASCADE-Grande is smaller. The unfolded helium spectra of both experiments do not agree well, but are compatible within the uncertainties. The carbon flux reconstructed using KASCADE-Grande data is characterised by a steeper spectrum and by smaller fluxes, but the carbon fluxes of both experiments agree within the uncertainties. The right part of the depiction displays the spectra of silicon and iron for KASCADE and KASCADE-Grande. The silicon spectra of both experiments differ significantly, even regarding the systematic and statistical uncertainties. In Section 7.3.2.4 similar differences are observed, when comparing the true and reconstructed silicon test spectra. The iron spectra of both experiments agree well within the uncertainties. Using KASCADE-Grande data allows to reconstruct the iron flux more precisely up to higher energies. Whereas with KASCADE it is possible to reconstruct the energy spectrum of iron up to an energy of $10^{17}$ eV, the unfolding analysis of KASCADE-Grande allows to extend this range up to several $10^{17}$ eV.
Figure 8.32 reveals that the KASCADE and the KASCADE-Grande results are not compatible for all individual elements. Especially in the silicon flux large deviations can be found. For this reason as well as for reasons of unstable solutions (see Section 7.3.2.4) the energy spectra of helium, carbon and silicon are summed up to one component, the medium heavy component. The resulting spectra are shown in Figure 8.33. For hydrogen and iron the energy spectra do not change, since only the helium, carbon and silicon are summed up to one component. When comparing the medium heavy component reconstructed by an unfolding analysis of KASCADE and KASCADE-Grande data a good agreement of the energy spectra of the medium heavy component can be found.
Regarding the combined energy spectra of KASCADE and KASCADE-Grande a clear change of index (knee) in the iron spectrum can be observed, whereas the other spectra do not show any knee-like features. At an energy of $\approx 10^{16}$ eV the energy spectra of hydrogen and the medium heavy component agree well, but with increasing energy the reconstruction uncertainties of the energy spectra increase and do hardly allow a conclusion on the course of the energy spectra above $7 \times 10^{16}$ eV. However, the combination of the results of KASCADE and KASCADE-Grande clearly evidence that the mass composition around the knee changes from light to more heavy.

# Chapter 9

# Conclusion

The present unfolding analysis on basis of KASCADE and KASCADE-Grande data allows the reconstruction of the all-particle energy spectrum as well as the energy spectra of individual elements in the energy range from $10^{15}$ eV to $10^{18}$ eV. The data of KASCADE and KASCADE-Grande are treated separately. Using KASCADE data the determination of the energy spectra in the range from $10^{15}$ eV to $10^{17}$ eV is possible. The analysis of KASCADE-Grande data provides the opportunity of investigating the energy spectra in the range from $10^{16}$ eV to $10^{18}$ eV. Whereas for KASCADE a precise reconstruction of the energy spectra of 5 different mass groups (H, He, C, Si, Fe) can be achieved (see Section 7.2.2), due to the lower statistics and the lower reconstruction quality, for KASCADE-Grande the separation of only 3 mass groups can be performed. For the unfolding in case of KASCADE-Grande the same 5 primary particles as for KASCADE are used, but the elements He, C and Si are added up to one component, referred to as medium heavy component (see Section 7.3.2). The combination of He, C and Si to one component leads indeed to a loss of information, but on the other hand also to a reduction of the reconstruction uncertainties. The accurate determination of the all-particle spectrum together with the knowledge of the energy spectra of the individual mass groups give hints on the origin of the knee reconstructed at around $4 \times 10^{15}$ eV and the existence of the iron knee. For making general statements on these two structures the use of different hadronic interaction models is indispensable. The required response functions, describing the probabilities of reconstructing the electron number $\lg N_e$ and the muon numbers $\lg N_\mu$ for certain energies and different primary particles, are based upon CORSIKA simulations. As shown in [Ape09] the effect of the hadronic low-energy interaction model is of minor importance and therefore as low-energy interaction model in all cases the sophisticated model FLUKA was applied. Due to the fact that the measurement range of the Grande array exceeds the one of KASCADE by one decade in energy, the air shower simulations are very time consuming. For this reason the generation of simulations with sufficient statistics for the variety of hadronic interaction models is barely possible. Thus, in the present KASCADE-Grande unfolding analysis the use of only one hadronic high-energy interaction model (QGSJETII) was possible, while for KASCADE four different high-energy interaction models (QGSJET01, QGSJETII, SIBYLL and EPOS1.99) are applied.

For KASCADE all hydrogen, helium and the all-particle spectra obtained on basis of different interaction models (see Section 8.3) exhibit index changes. The results of the KASCADE unfolding reveal that the knee in the all-particle spectrum is caused by index changes in the spectra of the light elements and can therefore be interpreted as a change from a light to a more heavy mass composition. This finding is also supported by LHC measurements [Ent11]. The positions of the knees vary from one model to the other, but the difference between the

knee positions of the hydrogen and the helium spectra is in all cases approximately a factor of $\approx 2$, suggesting a rigidity dependence of the knee positions of different mass groups. As explained in Section 2.4.1 a dependence of the knee positions of the individual elements on the valence $Z$ would favour astrophysical models based upon acceleration and propagation mechanisms. Theories, trying to explain the origin of the knee by interactions of cosmic rays with background particles in the Galaxy or by new physics, seem unlikely considering the results of the KASCADE unfolding analysis. For SIBYLL and QGSJETII further kinks in the carbon and the silicon spectrum can be found. Whereas the knee positions of the carbon spectra are also compatible with a rigidity dependence, the kink in the silicon spectrum is not expected at this energy. The sharp cut-off of the silicon spectra using QGSJETII and SIBYLL respectively can be explained by the insufficiencies in describing the measured data by the simulations. These insufficiencies are for both models (QGSJETII and SIBYLL) mainly observed at the heavy edge in the range of medium to high muon numbers, i. e. in the region where the silicon spectrum starts to steepen. The iron spectra for QGSJET01 and EPOS1.99 look fairly unexpected. For QGSJET01 below an energy of $7 \times 10^{15}\,\mathrm{eV}$ almost no iron is reconstructed. Compared to QGSJET01 the situation for iron becomes even worse when using EPOS1.99. For energies below $3 \times 10^{16}\,\mathrm{eV}$ no iron is present and at higher energies the iron flux suffers from large fluctuations. Regarding direct measurements, the absence of iron at low energies appears to be unphysical (see lower graphs in Figure 9.2). Again the curious shapes of the iron spectra of QGSJET01 and EPOS1.99 originate from the incapability of the interaction models used to describe the measured data. The iron spectra based upon the interaction models QGSJETII and SIBYLL are characterised by a rather flat course with a slight index change at an energy of $1-2\times10^{16}\,\mathrm{eV}$.

Assuming a rigidity dependence of the knee positions of different primary particles ($E_Z^{knee} \propto Z \cdot E_H^{knee}$), at an energy around $10^{17}\,\mathrm{eV}$ a knee-like structure is expected, being caused by the steepening of the iron spectrum and therefore being referred to as iron knee. For an investigation of this structure and to produce proof for its existence the data of the KASCADE-Grande experiment can be used. The energy spectra obtained by a deconvolution analysis on basis of QGSJETII simulations are discussed in Section 8.6.1. The low overall statistics of the measured KASCADE-Grande data does hardly allow a conclusion on the all-particle energy spectrum for energies above $2 \times 10^{17}\,\mathrm{eV}$. Up to this energy no index change in the all-particle spectrum can be found. In the spectra of hydrogen and the medium elements (He+C+Si) no obvious change of index can be observed, too. Both spectra are affected by large reconstruction uncertainties for energies above $10^{17}\,\mathrm{eV}$ and for this reason it is hardly possible to draw conclusions on the shape of the spectra in this energy region. However, the flux of iron, being the most abundant primary particle mass in the energy range from $10^{16}\,\mathrm{eV}$ to $10^{18}\,\mathrm{eV}$, can be precisely determined up to an energy of $3 \times 10^{17}\,\mathrm{eV}$. The results of the KASCADE-Grande deconvolution analysis also support the interpretation of knee as a change of the mass composition of cosmic rays. The iron spectrum multiplied by $E^{2.5}$ is characterised by a flat course up to an energy of approximately $80 - 90\,\mathrm{PeV}$ and then the spectrum steepens, i. e. exhibits a knee-like feature. A comparison of the KASCADE and the KASCADE-Grande results for QGSJETII, using in both cases only three mass groups (see Figure 8.33) indicates a good agreement of the energy spectra for both experiments and approves that an unfolding analysis is also possible for KASCADE-Grande, but with less precision. The less accurate determination of the elemental abundances for KASCADE-Grande can be explained by an interplay of the low statistics and the reconstruction properties of KASCADE-Grande. The occurrence of the kink in the iron spectrum earlier than expected can have different explanations. On the one hand the hadronic interaction models used may be responsible, on the other hand it is conceivable that the iron spectrum does not only contain

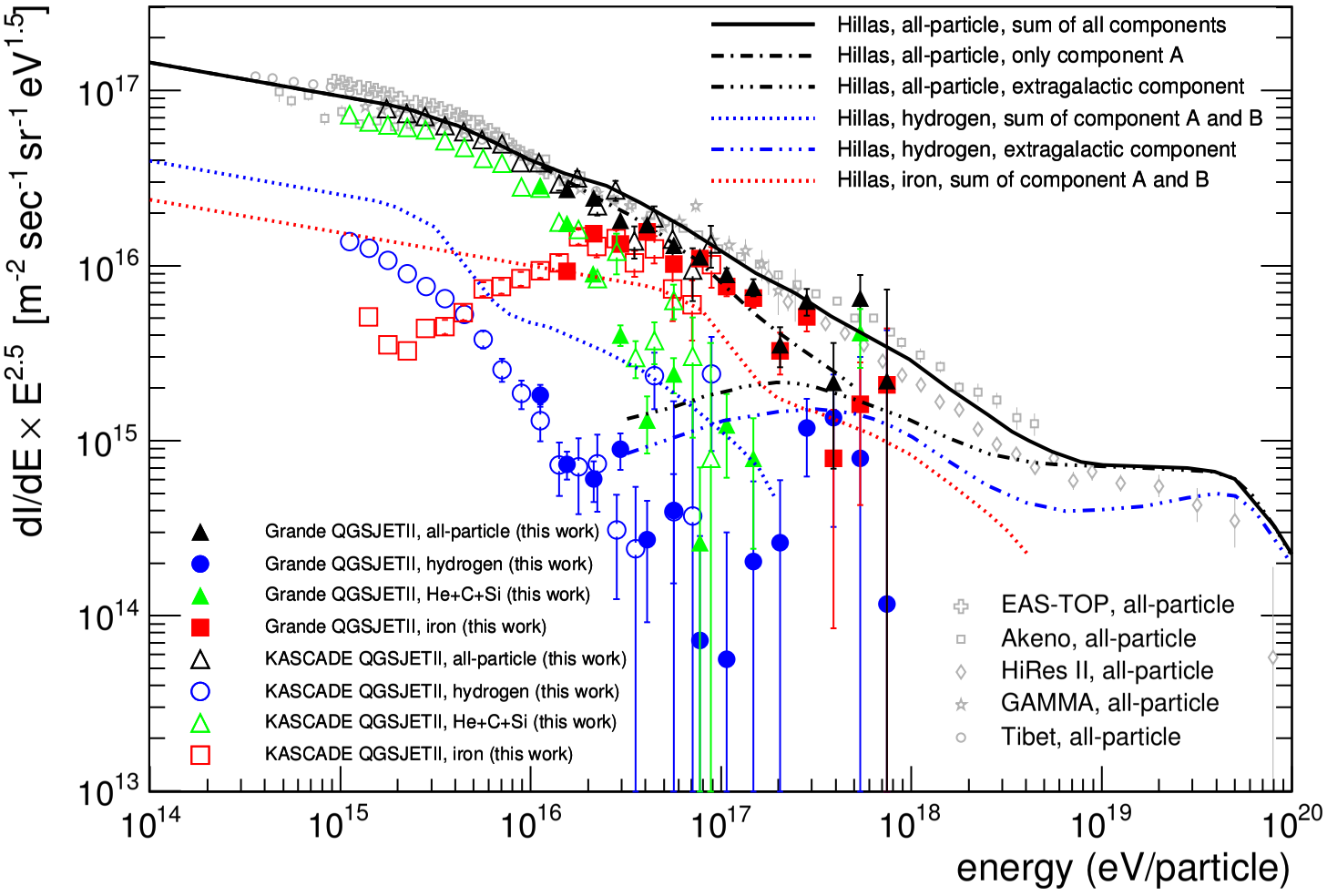


Figure 9.1: Comparison of the results of the KASCADE and KASCADE-Grande unfolding analysis, using QGSJETII and FLUKA, and the Hillas model [Hil04] and [Hil05].

primary particles of the iron group, but also comprises contributions of lighter elements, causing an earlier as expected steepening. In spite of the earlier appearance of the knee in the iron flux the results suggest a dependence of the knee positions on the valence $Z$ of the primary particle. Although a kink in the iron spectrum is observed, no knee in the all-particle spectrum can be discovered. A possible explanation for this may be an additional component (source) as it is introduced for example in [Hil04] and [Hil05]. Hillas describes three basic parts, which are the component 'A', spanning the energy range from below $10^{10}$ eV up to at least $10^{16}$ eV, the extragalactic component (EG) at the highest energies and a component 'B', being required to describe the intermediate energy region. The component A comprises cosmic rays of galactic origin driven by diffusive shock acceleration in supernova remnants, producing a sharp knee at about 3 PeV and being observed by KASCADE measurement, the second rigidity dependent component (B) may be due to special supernova remnants, and the extragalactic component (EG) is dominated by hydrogen and helium. As a consequence of the superposition of these three components it seems possible that a kink, originating from a steepening in the spectra of the heavy elements (mainly iron) is washed out and cannot be detected. A comparison of the unfolded energy spectra of KASCADE and KASCADE-Grande data, derived on basis of QGSJETII and FLUKA simulations, with the Hillas model can be found in Figure 9.1. The abundances of the elements in the Hillas model are obtained by the extrapolation of direct measurements and the turn-down shape at the knee is based upon results of the KASCADE experiment [Hau03]. From the point of view that the abundances in the Hillas model are derived on basis of direct measurements and that the unfolding results are strongly dependent on the hadronic interaction models used in the simulations, it is in general not expected that the model predictions match the reconstructed energy spectra. Both, the iron and the hydrogen spectra are shifted with respect to the Hillas spectra of these elements (for carbon in [Hil04] and [Hil05] no predictions are made). Due to the large uncertainties on the unfolded flux values for energies above $7 \times 10^{16}$ eV a statement on the validity of the Hillas model is hardly possible. But the observations show that a description of measured data at energies in the region of $10^{17}$ eV and above is not possible entirely without the light elements H and He (see lower graph of Figure 8.29, which corresponds to $\approx 10^{17}$ eV) and therefore indicate the existence of some component similar to the component B introduced by Hillas. Comparing the shape of the hydrogen spectra with the shape of the iron, it is conspicuous that the steepening of the iron spectra after the knee is less pronounced. This less pronounced knee structure may also be an indication for a component B. From observations of the hydrogen and the helium spectra the existence of a component B can neither be verified nor excluded.
Examining the reconstructed all-particle fluxes for QGSJETII and FLUKA at low energies. i. e. at the beginning of the KASCADE spectrum, a good agreement with the all-particle flux predicted by Hillas can be found. Only a shift of the unfolded spectra to slightly lower flux values can be observed. Taking into account this shift the existence of a component B is conceivable, but for the interaction model combination used (QGSJETII and FLUKA) the importance of this component seems less distinct. Nevertheless, the underlying idea of the Hillas model seems a possible explanation for a less pronounced or even a missing structure in the all-particle energy spectrum at an energy corresponding to the iron knee.

Finally in Figure 9.2 the results of the KASCADE and the KASCADE-Grande unfolding analysis are compared to different experiments. Due to illustration purposes not all cosmic ray experiments are included and systematic uncertainties are omitted. The error bars in the depictions represent the statistical uncertainties. In the upper graph the all-particle spectra obtained by the unfolding analysis are compared to selected experiments like EAS-TOP ([Agl99]), Akeno ([Nag84]), HiResII ([Abb08]), GAMMA ([Gar08]) and Tibet ([Ame96]).

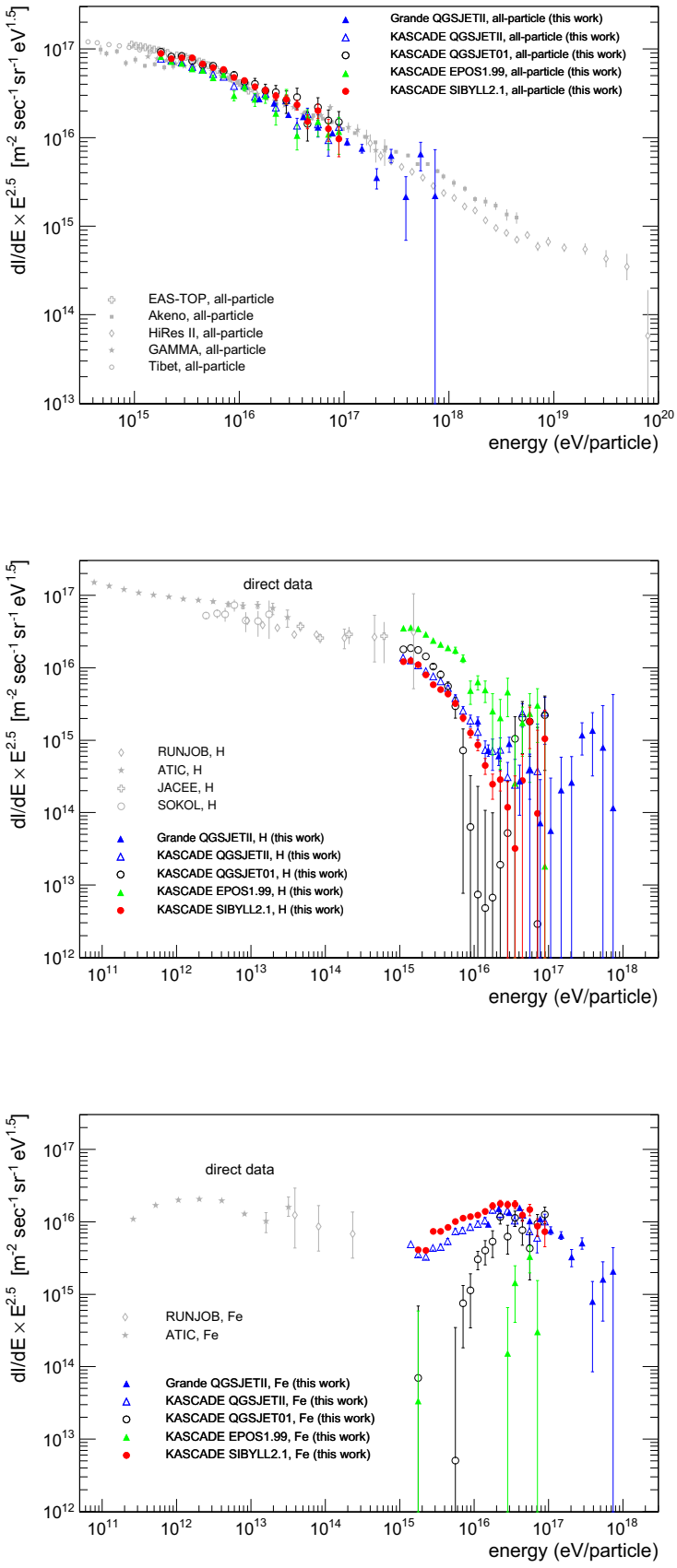


Figure 9.2: Compilation of the energy spectra of different experiments and the present work.

Within the uncertainties a good agreement of both the slope and the absolute intensity can be observed. The central depiction comprises the resulting hydrogen spectra of the present analysis in comparison with the findings of direct measurements (RUNJOB ([Der05]), ATIC ([Pan09]), JACEE ([Tak98]) and SOKOL ([Gri90])). An extrapolation of the results of direct measurements to the energies measured with KASCADE shows that the directly measured proton fluxes are in general compatible with the unfolded fluxes. The fact that either the direct measurements do not reach the KASCADE energy range or they are affected by large uncertainties does not allow to exclude any of the tested models.
The lower graph of Figure 9.2 displays the iron spectra obtained in the present work and the iron data of two direct measurements, RUNJOB ([Der05]) and ATIC ([Pan09]). An extrapolation of direct data to the measurement range of KASCADE indicates that a compatibility of the reconstructed iron fluxes with direct data is not given for QGSJET01 and EPOS1.99, but for QGSJETII and SIBYLL the results seem consistent.
A general statement, which hadronic high-energy interaction model describes the process of the shower development best, can hardly be made, since all models used reveal insufficiencies in some part of the measurement range. From this point of view an analysis of KASCADE and KASCADE-Grande data will still be interesting in several years, since collider experiments like the LHC will help to improve the interaction models.

# Appendix A

# Parameters of the correlated lg $N_e$-lg $N_\mu^{tr.}$-distribution

As an example the parameters of the correlated lg $N_e$-lg $N_\mu^{tr.}$-distribution for hydrogen are listed for KASCADE as well as for KASCADE-Grande. The parameters are determined on basis of simulations with QGSJETII and FLUKA. Some of the parameters are constant over the entire energy range, the others are described by polynomials not exceeding third order

$$g_n = p_0 + p_1 \cdot \lg(\mathrm{E/GeV}) + p_2 \cdot (\lg(\mathrm{E/GeV}))^2 + p_3 \cdot (\lg(\mathrm{E/GeV}))^3, \tag{A.1}$$

with $n = 1, ..., 10$, being the number of parameters used to fit the lg $N_e$-lg $N_\mu^{tr.}$-distribution.

## KASCADE, QGSJETII/FLUKA

### Hydrogen

$$g_3 = -1.1,\ g_5 = 2.5,\ g_7 = 0.2573,\ g_9 = 3.561,\ g_{10} = 0.08012$$

| parameter | value | error |
|---|---|---|
| $p_0$ | $-2.82$ | 0.14 |
| $p_1$ | 1.336 | 0.038 |
| $p_2$ | $-0.01079$ | 0.00266 |

Table A.1: Parameter $g_1$.

| parameter | value | error |
|---|---|---|
| $p_0$ | 3.234 | 0.484 |
| $p_1$ | $-1.049$ | 0.215 |
| $p_2$ | 0.121 | 0.031 |
| $p_3$ | $-0.004793$ | 0.001495 |

Table A.2: Parameter $g_2$.

| parameter | value | error |
|---|---|---|
| $p_0$ | 0.6016 | 0.2424 |
| $p_1$ | 0.8375 | 0.0694 |
| $p_2$ | 0.009291 | 0.004876 |

Table A.3: Parameter $g_4$.

| parameter | value | error |
|---|---|---|
| $p_0$ | 0.6797 | 0.0157 |
| $p_1$ | $-0.05559$ | 0.00223 |

Table A.4: Parameter $g_6$.

| parameter | value | error |
|---|---|---|
| $p_0$ | 3.929 | 0.365 |
| $p_1$ | $-1.861$ | 0.163 |
| $p_2$ | 0.00568 | 0.02394 |
| $p_3$ | 0.00204 | 0.00115 |

Table A.5: Parameter $g_8$.

**Helium**

$$g_3 = -1.1,\ g_5 = 3.5,\ g_7 = 0,\ g_9 = 3.5,\ g_{10} = 0$$

| parameter | value | error |
|---|---|---|
| $p_0$ | $-2.385$ | 0.172 |
| $p_1$ | 1.351 | 0.048 |
| $p_2$ | $-0.01234$ | 0.00331 |

Table A.6: Parameter $g_1$.

| parameter | value | error |
|---|---|---|
| $p_0$ | 2.749 | 0.446 |
| $p_1$ | −0.8749 | 0.1967 |
| $p_2$ | 0.09971 | 0.02848 |
| $p_3$ | −0.003904 | 0.001354 |

Table A.7: Parameter $g_2$.

| parameter | value | error |
|---|---|---|
| $p_0$ | −2.174 | 1.334 |
| $p_1$ | 1.782 | 0.590 |
| $p_2$ | −0.1094 | 0.0856 |
| $p_3$ | −0.005156 | 0.004077 |

Table A.8: Parameter $g_4$.

| parameter | value | error |
|---|---|---|
| $p_0$ | −0.6376 | 0.4097 |
| $p_1$ | 0.461 | 0.182 |
| $p_2$ | −0.07112 | 0.02662 |
| $p_3$ | 0.003352 | 0.001274 |

Table A.9: Parameter $g_6$.

| parameter | value | error |
|---|---|---|
| $p_0$ | 2.208 | 0.298 |
| $p_1$ | −1.054 | 0.134 |
| $p_2$ | −0.1255 | 0.0197 |
| $p_3$ | 0.004945 | 0.000951 |

Table A.10: Parameter $g_8$.

**Carbon**

$$g_3 = -1.1,\ g_5 = 5.5,\ g_7 = 0,\ g_9 = 3.5,\ g_{10} = 0$$

| parameter | value | error |
|---|---|---|
| $p_0$ | −2.183 | 0.037 |
| $p_1$ | 1.167 | 0.005 |

Table A.11: Parameter $g_1$.

| parameter | value | error |
|---|---|---|
| $p_0$ | 3.012 | 0.451 |
| $p_1$ | −1.002 | 0.197 |
| $p_2$ | 0.1175 | 0.0284 |
| $p_3$ | −0.004675 | 0.001345 |

Table A.12: Parameter $g_2$.

| parameter | value | error |
|---|---|---|
| $p_0$ | −1.947 | 0.273 |
| $p_1$ | 1.359 | 0.079 |
| $p_2$ | −0.01924 | 0.00558 |

Table A.13: Parameter $g_4$.

| parameter | value | error |
|---|---|---|
| $p_0$ | −1.59 | 0.35 |
| $p_1$ | 0.7968 | 0.1552 |
| $p_2$ | −0.1149 | 0.0226 |
| $p_3$ | 0.005316 | 0.001081 |

Table A.14: Parameter $g_6$.

| parameter | value | error |
|---|---|---|
| $p_0$ | 0.77 | 0.23 |
| $p_1$ | −0.5668 | 0.1027 |
| $p_2$ | −0.1902 | 0.0152 |
| $p_3$ | 0.007863 | 0.000732 |

Table A.15: Parameter $g_8$.

**Silicon**

$$g_3 = -1.1,\ g_5 = 7.5,\ g_7 = 0,\ g_9 = 3.5,\ g_{10} = 0$$

| parameter | value | error |
|---|---|---|
| $p_0$ | −3.281 | 0.220 |
| $p_1$ | 1.444 | 0.060 |
| $p_2$ | −0.01789 | 0.00408 |

Table A.16: Parameter $g_1$.

| parameter | value | error |
|---|---|---|
| $p_0$ | 2.268 | 0.370 |
| $p_1$ | −0.7674 | 0.1634 |
| $p_2$ | 0.09345 | 0.02369 |
| $p_3$ | −0.003911 | 0.001127 |

Table A.17: Parameter $g_2$.

| parameter | value | error |
|---|---|---|
| $p_0$ | −2.002 | 0.324 |
| $p_1$ | 1.321 | 0.093 |
| $p_2$ | −0.01472 | 0.00660 |

Table A.18: Parameter $g_4$.

| parameter | value | error |
|---|---|---|
| $p_0$ | −1.294 | 0.304 |
| $p_1$ | 0.609 | 0.013 |
| $p_2$ | −0.08349 | 0.01943 |
| $p_3$ | 0.003683 | 0.000925 |

Table A.19: Parameter $g_6$.

| parameter | value | error |
|---|---|---|
| $p_0$ | −0.5364 | 0.1797 |
| $p_1$ | −0.1354 | 0.0810 |
| $p_2$ | −0.2448 | 0.0120 |
| $p_3$ | 0.0102 | 0.0006 |

Table A.20: Parameter $g_8$.

**Iron**

$$g_3 = -1.1,\ g_5 = 12,\ g_7 = 0,\ g_9 = 3.5,\ g_{10} = 0$$

| parameter | value | error |
|---|---|---|
| $p_0$ | −3.588 | 0.286 |
| $p_1$ | 1.498 | 0.080 |
| $p_2$ | −0.02046 | 0.00557 |

Table A.21: Parameter $g_1$.

| parameter | value | error |
|---|---|---|
| $p_0$ | 0.7866 | 0.0607 |
| $p_1$ | −0.1565 | 0.0173 |
| $p_2$ | 0.008717 | 0.001217 |

Table A.22: Parameter $g_2$.

| parameter | value | error |
|---|---|---|
| $p_0$ | −2.544 | 0.531 |
| $p_1$ | 1.472 | 0.153 |
| $p_2$ | −0.02391 | 0.01089 |

Table A.23: Parameter $g_4$.

| parameter | value | error |
|---|---|---|
| $p_0$ | −0.01302 | 0.04237 |
| $p_1$ | 0.0448 | 0.0123 |
| $p_2$ | −0.00375 | 0.00088 |

Table A.24: Parameter $g_6$.

| parameter | value | error |
|---|---|---|
| $p_0$ | −0.1017 | 0.1553 |
| $p_1$ | −0.4528 | 0.0701 |
| $p_2$ | −0.192 | 0.010 |
| $p_3$ | 0.007485 | 0.000502 |

Table A.25: Parameter $g_8$.

## KASCADE-Grande, QGSJETII/FLUKA

### Hydrogen

$$g_3 = 0.12,\ g_5 = 3.6,\ g_7 = 0.23,\ g_9 = 5.5,\ g_{10} = 0.13$$

| parameter | value | error |
|---|---|---|
| $p_0$ | −3.302 | 0.263 |
| $p_1$ | 1.448 | 0.069 |
| $p_2$ | −0.01729 | 0.00445 |

Table A.26: Parameter $g_1$.

| parameter | value | error |
|---|---|---|
| $p_0$ | 1.062 | 0.173 |
| $p_1$ | −0.1965 | 0.0452 |
| $p_2$ | 0.01002 | 0.00291 |

Table A.27: Parameter $g_2$.

| parameter | value | error |
|---|---|---|
| $p_0$ | 1.109 | 0.490 |
| $p_1$ | 0.7344 | 0.1284 |
| $p_2$ | 0.01522 | 0.00829 |

Table A.28: Parameter $g_4$.

| parameter | value | error |
|---|---|---|
| $p_0$ | 1.318 | 0.218 |
| $p_1$ | −0.1735 | 0.0573 |
| $p_2$ | 0.006399 | 0.003706 |

Table A.29: Parameter $g_6$.

| parameter | value | error |
|---|---|---|
| $p_0$ | 4.875 | 0.164 |
| $p_1$ | −3.829 | 0.043 |
| $p_2$ | 0.08204 | 0.00279 |

Table A.30: Parameter $g_8$.

**Helium**

$$g_3 = -1.1,\ g_5 = 3.5,\ g_7 = 0,\ g_9 = 3.5,\ g_{10} = 0$$

| parameter | value | error |
|---|---|---|
| $p_0$ | −2.797 | 0.373 |
| $p_1$ | 1.35 | 0.10 |
| $p_2$ | −0.01254 | 0.00628 |

Table A.31: Parameter $g_1$.

| parameter | value | error |
|---|---|---|
| $p_0$ | 1.105 | 0.164 |
| $p_1$ | −0.2076 | 0.0429 |
| $p_2$ | 0.0108 | 0.0028 |

Table A.32: Parameter $g_2$.

| parameter | value | error |
|---|---|---|
| $p_0$ | −0.2553 | 0.0710 |
| $p_1$ | 1.012 | 0.010 |

Table A.33: Parameter $g_4$.

| parameter | value | error |
|---|---|---|
| $p_0$ | 0.8418 | 0.1389 |
| $p_1$ | −0.1181 | 0.0364 |
| $p_2$ | 0.004651 | 0.002355 |

Table A.34: Parameter $g_6$.

| parameter | value | error |
|---|---|---|
| $p_0$ | 4.485 | 0.104 |
| $p_1$ | −3.799 | 0.027 |
| $p_2$ | 0.07545 | 0.00175 |

Table A.35: Parameter $g_8$.

**Carbon**

$g_3 = 0.13$, $g_5 = 8.5$, $g_7 = 0.1$, $g_9 = 5.5$, $g_{10} = 0.13$

| parameter | value | error |
|---|---|---|
| $p_0$ | −2.104 | 0.050 |
| $p_1$ | 1.159 | 0.007 |

Table A.36: Parameter $g_1$.

| parameter | value | error |
|---|---|---|
| $p_0$ | 0.9169 | 0.1382 |
| $p_1$ | −0.1706 | 0.0363 |
| $p_2$ | 0.008899 | 0.002347 |

Table A.37: Parameter $g_2$.

| parameter | value | error |
|---|---|---|
| $p_0$ | $-0.5255$ | 0.0920 |
| $p_1$ | 1.042 | 0.012 |

Table A.38: Parameter $g_4$.

| parameter | value | error |
|---|---|---|
| $p_0$ | 0.7323 | 0.1169 |
| $p_1$ | $-0.1232$ | 0.0308 |
| $p_2$ | 0.005776 | 0.001998 |

Table A.39: Parameter $g_6$.

| parameter | value | error |
|---|---|---|
| $p_0$ | 4.624 | 0.073 |
| $p_1$ | $-3.944$ | 0.019 |
| $p_2$ | 0.09339 | 0.00124 |

Table A.40: Parameter $g_8$.

**Silicon**

$g_3 = 0.13.1$, $g_5 = 8.5$, $g_7 = 0.1$, $g_9 = 5.5$, $g_{10} = 0.13$

| parameter | value | error |
|---|---|---|
| $p_0$ | $-3.31$ | 0.43 |
| $p_1$ | 1.444 | 0.113 |
| $p_2$ | $-0.01774$ | 0.00729 |

Table A.41: Parameter $g_1$.

| parameter | value | error |
|---|---|---|
| $p_0$ | 0.6515 | 0.1271 |
| $p_1$ | $-0.1123$ | 0.0333 |
| $p_2$ | 0.005497 | 0.002152 |

Table A.42: Parameter $g_2$.

| parameter | value | error |
|---|---|---|
| $p_0$ | $-1.086$ | 0.077 |
| $p_1$ | 1.09 | 0.01 |

Table A.43: Parameter $g_4$.

| parameter | value | error |
|---|---|---|
| $p_0$ | 0.3166 | 0.0114 |
| $p_1$ | −0.02888 | 0.00155 |

Table A.44: Parameter $g_6$.

| parameter | value | error |
|---|---|---|
| $p_0$ | 4.005 | 0.058 |
| $p_1$ | −3.854 | 0.015 |
| $p_2$ | −0.08901 | 0.00099 |

Table A.45: Parameter $g_8$.

**Iron**

$g_3 = 0.13$, $g_5 = 4.5$, $g_7 = 0$, $g_9 = 5.5$, $g_{10} = 0.13$

| parameter | value | error |
|---|---|---|
| $p_0$ | −4.15 | 0.19 |
| $p_1$ | 1.613 | 0.049 |
| $p_2$ | −0.02677 | 0.00313 |

Table A.46: Parameter $g_1$.

| parameter | value | error |
|---|---|---|
| $p_0$ | 0.5659 | 0.0912 |
| $p_1$ | −0.1001 | 0.0240 |
| $p_2$ | 0.005037 | 0.001552 |

Table A.47: Parameter $g_2$.

| parameter | value | error |
|---|---|---|
| $p_0$ | −3.127 | 0.292 |
| $p_1$ | 1.494 | 0.077 |
| $p_2$ | −0.0222 | 0.0051 |

Table A.48: Parameter $g_4$.

| parameter | value | error |
|---|---|---|
| $p_0$ | 0.4819 | 0.0987 |
| $p_1$ | $-0.07709$ | 0.02632 |
| $p_2$ | 0.003143 | 0.001733 |

Table A.49: Parameter $g_6$.

| parameter | value | error |
|---|---|---|
| $p_0$ | 3.299 | 0.051 |
| $p_1$ | $-3.729$ | 0.013 |
| $p_2$ | 0.08224 | 0.00086 |

Table A.50: Parameter $g_8$.

# Appendix B

# Parameterization of the reconstruction uncertainties

## B.1 KASCADE, QGSJETII/FLUKA

### Electrons

#### Systematic deviation

The systematic deviation of lg $N_e^{rec.}$ and lg $N_e^{true}$ is given by a polynomial of third order according to

$$C_e = p_0 + p_1 \cdot (\lg\ N_e^{true} - \lg\ N_\mu^{tr.,rec.}) + p_2 \cdot (\lg\ N_e^{true} - \lg\ N_\mu^{tr.,rec.})^2 + p_3 \cdot (\lg\ N_e^{true} - \lg\ N_\mu^{tr.,rec.})^3. \tag{B.1}$$

| parameter | value | error |
|---|---|---|
| $p_0$ | $-0.07533$ | 0.00931 |
| $p_1$ | 0.05664 | 0.02206 |
| $p_2$ | $-0.01649$ | 0.01692 |
| $p_3$ | 0.00266 | 0.00421 |

Table B.1: Parameters of the systematic deviation of lg $N_e^{rec.}$ and lg $N_e^{true}$ (valid for all primary particles).

#### Remaining systematics

The remaining systematics are parameterized according to

$$f(\lg\ N_e^{true}) = \begin{cases} p_2 + p_1 \cdot (\lg\ N_e^{true} - p_0)^2 & : \ \lg\ N_e^{true} \leq p_0 \\ p_2 + p_3 \cdot (\lg\ N_e^{true} - p_0) & : \ p_0 < \lg\ N_e^{true} < p_4 \\ p_2 + p_3 \cdot (p_4 - p_0) + (p_5 \cdot (\lg\ N_e^{true} - p_4)^2 & : \ \lg\ N_e^{true} \geq p_4 \end{cases} \tag{B.2}$$

| parameter | value | error |
|---|---|---|
| $p_0$ | 3.913 | 0.018 |
| $p_1$ | 0.5554 | 0.0837 |
| $p_2$ | −0.003423 | 0.000263 |
| $p_3$ | 0.002968 | 0.000180 |
| $p_4$ | 6.268 | 0.017 |
| $p_5$ | −0.04169 | 0.00157 |

Table B.2: Parameters of the systematics remaining after applying the correction function $C_e$ (see Equation 6.7).

### Distribution of the reconstruction uncertainties

The parameters $e_1$ and $e_2$ of Equation 6.8 (Gaussian function) describe the distributions of the reconstruction uncertainties.

$$e_1(\lg N_e^{true}) = \begin{cases} p_0 + p_1 \cdot \lg N_e^{true} & : \quad \lg N_e^{true} \leq p_2 \\ p_0 + p_1 \cdot p_2 + p_3 \cdot (\lg N_e^{true} - p_2)^2 & : \quad \lg N_e^{true} > p_2 \end{cases} . \tag{B.3}$$

| parameter | value | error |
|---|---|---|
| $p_0$ | −0.0174 | 0.0010 |
| $p_1$ | 0.003391 | 0.000193 |
| $p_2$ | 6.249 | 0.013 |
| $p_3$ | −0.04125 | 0.00177 |

Table B.3: Parameterization of the parameter $e_1$ (valid for all primary particles).

$$e_2(\lg N_e^{true}) = p_0 + p_2 \cdot (\lg N_e^{true})^{p_1} \cdot (0.5 \cdot \mathrm{erf}(-p_4 \cdot \lg N_e^{true} + p_3) + 0.5) \tag{B.4}$$

| parameter | value | error |
|---|---|---|
| $p_0$ | 0.00642 | 0.00032 |
| $p_1$ | −6.477 | 0.046 |
| $p_2$ | 530.6 | 34.7 |
| $p_3$ | 7.822 | 0.525 |
| $p_4$ | 1.396 | 0.103 |

Table B.4: Parameterization of the parameter $e_2$ (valid for all primary particles).

## Muons

### Systematic deviation

The systematic deviation of $\lg N_\mu^{tr.,rec.}$ and $\lg N_\mu^{tr.,true}$ is

$$C_\mu = p_0 + p_1 \cdot (\lg N_e^{true}) + p_2 \cdot (\lg N_e^{true})^2 + p_3 \cdot (\lg N_e^{true})^3. \tag{B.5}$$

| parameter | value | error |
|---|---|---|
| $p_0$ | $-0.9632$ | 0.1468 |
| $p_1$ | 0.541 | 0.082 |
| $p_2$ | $-0.1052$ | 0.0151 |
| $p_3$ | 0.007065 | 0.000918 |

Table B.5: Parameters of the systematic deviation of lg $N_\mu^{tr.,rec.}$ and lg $N_\mu^{tr.,true}$.

**Remaining systematics**

The remaining systematics are given by

$$f(\lg N_\mu^{tr.,true}) = \begin{cases} p_2 + p_1 \cdot (\lg N_\mu^{tr.,true} - p_0)^2 & : \lg N_\mu^{tr.,true} \leq p_0 \\ p_2 + p_3 \cdot (\lg N_\mu^{tr.,true} - p_0) & : p_0 < \lg N_\mu^{tr.,true} < p_4 \\ p_2 + p_3 \cdot (p_4 - p_0) + (p_5 \cdot (\lg N_\mu^{tr.,true} - p_4)^2 & : \lg N_\mu^{tr.,true} \geq p_4 \end{cases} \tag{B.6}$$

| parameter | value | error |
|---|---|---|
| $p_0$ | 3.01 | 0.02 |
| $p_1$ | 0.5648 | 0.0541 |
| $p_2$ | $-0.0008957$ | 0.0007932 |
| $p_3$ | $-0.002044$ | 0.000664 |
| $p_4$ | 5.215 | 0.023 |
| $p_5$ | $-0.2397$ | 0.0169 |

Table B.6: Parameters of the systematics remaining after applying the correction function $C_\mu$ (see Equation 6.7).

**Distribution of the reconstruction uncertainties**

The parameters $m_1$, $m_2$ and $m_3$ of Equation 6.9 describe the distribution of the reconstruction uncertainties. For muon numbers above $10^4$ the asymmetric function passes into a Gaussian function with parameters $m_1$ and $m_2$.

$$m_1 = p_0 + p_1 \cdot \lg N_\mu^{tr.,true} + p_2 \cdot (\lg N_\mu^{tr,true})^2 + p_3 \cdot (\lg N_\mu^{tr.,true})^3 + p_4 \cdot (\lg N_\mu^{tr.,true})^4. \tag{B.7}$$

| parameter | value | error |
|---|---|---|
| $p_0$ | $-3.99$ | 0.06 |
| $p_1$ | 4.336 | 0.569 |
| $p_2$ | $-1.703$ | 0.200 |
| $p_3$ | 0.2887 | 0.0308 |
| $p_4$ | $-0.01793$ | 0.00176 |

Table B.7: Parameterization of the parameter $m_1$ (valid for all primary particles).

$$m_2(\lg N_\mu^{tr.,true}) = p_0 + p_2 \cdot \lg N_\mu^{tr.,true^{p_1}} \cdot (0.5 \cdot \mathrm{erf}(-p_4 \cdot \lg N_\mu^{tr.,true} + p_3) + 0.5). \tag{B.8}$$

| parameter | value | error |
|---|---|---|
| $p_0$ | 0.0164 | 0.0008 |
| $p_1$ | 4.162 | 0.048 |
| $p_2$ | 3076 | 179 |
| $p_3$ | −2.562 | 0.010 |
| $p_4$ | 0.3072 | 0.0012 |

Table B.8: Parameterization of the parameter $m_2$ (valid for all primary particles).

$$m_3(\lg N_\mu^{tr.,true}) = p_0 + p_1 \cdot \lg N_\mu^{tr.,true} + p_2 \cdot (\lg N_\mu^{tr,true})^2 + p_3 \cdot (\lg N_\mu^{tr.,true})^3. \quad \text{(B.9)}$$

| parameter | value | error |
|---|---|---|
| $p_0$ | −11.01 | 3.37 |
| $p_1$ | 10.22 | 2.97 |
| $p_2$ | −3.086 | 0.869 |
| $p_3$ | 0.3058 | 0.0845 |

Table B.9: Parameterization of the parameter $m_3$ (valid for all primary particles).

## B.2 KASCADE-Grande, QGSJETII/FLUKA

### Electrons

#### Systematic deviation

The systematic deviations of lg $N_e^{rec.}$ and lg $N_e^{true}$ for all primary particles can be described by a polynomial of third order according to

$$C_e = p_0 + p_1 \cdot \lg N_e^{true} + p_2 \cdot (\lg N_e^{true})^2 + p_3 \cdot (\lg N_e^{true})^3. \quad \text{(B.10)}$$

| parameter | value | error |
|---|---|---|
| $p_0$ | −2.325 | 0.738 |
| $p_1$ | 1.091 | 0.342 |
| $p_2$ | −0.1701 | 0.0526 |
| $p_3$ | 0.00889 | 0.00267 |

Table B.10: Parameters of the systematic deviation of lg $N_e^{rec.}$ and lg $N_e^{true}$ for hydrogen.

| parameter | value | error |
|---|---|---|
| $p_0$ | $-2.19$ | 0.76 |
| $p_1$ | 1.04 | 0.35 |
| $p_2$ | $-0.1633$ | 0.0544 |
| $p_3$ | 0.008544 | 0.002771 |

Table B.11: Parameters of the systematic deviation of lg $N_e^{rec.}$ and lg $N_e^{true}$ for helium.

| parameter | value | error |
|---|---|---|
| $p_0$ | $-2.488$ | 0.759 |
| $p_1$ | 1.2 | 0.4 |
| $p_2$ | $-0.1912$ | 0.0547 |
| $p_3$ | 0.01013 | 0.00280 |

Table B.12: Parameters of the systematic deviation of lg $N_e^{rec.}$ and lg $N_e^{true}$ for carbon.

| parameter | value | error |
|---|---|---|
| $p_0$ | $-0.419$ | 0.797 |
| $p_1$ | 0.2483 | 0.3723 |
| $p_2$ | $-0.04633$ | 0.05754 |
| $p_3$ | 0.002816 | 0.002943 |

Table B.13: Parameters of the systematic deviation of lg $N_e^{rec.}$ and lg $N_e^{true}$ for silicon.

| parameter | value | error |
|---|---|---|
| $p_0$ | 0.02338 | 0.81523 |
| $p_1$ | 0.06909 | 0.38113 |
| $p_2$ | $-0.02222$ | 0.05893 |
| $p_3$ | 0.00173 | 0.00301 |

Table B.14: Parameters of the systematic deviation of lg $N_e^{rec.}$ and lg $N_e^{true}$ for iron.

**Distribution of the reconstruction uncertainties**

The parameters e1, e2 and e2 of Equation 6.10 describe the distribution of the reconstruction uncertainties. For electron numbers above $10^{6.3}$ the distribution passes into a Gaussian function with parameters $e_1$ and $e_2$.

$$e_1(N_e^{true}) = p_0 + p_1 \cdot \lg N_e^{true} + p_2 \cdot (\lg N_e^{true})^2 + p_3 \cdot (\lg N_e^{true})^3. \tag{B.11}$$

| parameter | value | error |
|---|---|---|
| $p_0$ | 0.7561 | 0.3667 |
| $p_1$ | −0.4075 | 0.1705 |
| $p_2$ | 0.06927 | 0.02624 |
| $p_3$ | −0.003776 | 0.001335 |

Table B.15: Parameterization of the parameter $e_1$ (valid for all primary particles).

$$e_2(N_e^{true}) = p_0 + p_1 \cdot \lg\, N_e^{true} + p_2 \cdot (\lg\, N_e^{true})^2. \tag{B.12}$$

| parameter | value | error |
|---|---|---|
| $p_0$ | 0.469 | 0.030 |
| $p_1$ | −0.09044 | 0.00931 |
| $p_2$ | 0.005208 | 0.000729 |

Table B.16: Parameterization of the parameter $e_2$ (valid for all primary particles).

$$e_3(N_e^{true}) = p_0 + p_1 \cdot \lg\, N_e^{true} + p_2 \cdot (\lg\, N_e^{true})^2. \tag{B.13}$$

| parameter | value | error |
|---|---|---|
| $p_0$ | 2.627 | 0.431 |
| $p_1$ | −0.9954 | 0.1522 |
| $p_2$ | 0.09041 | 0.01343 |

Table B.17: Parameterization of the parameter $e_3$ (valid for all primary particles).

## Muons

### Systematic deviation

The parametrization of the systematic deviations of $\lg\, N_\mu^{rec.}$ and $\lg\, N_\mu^{true}$ for all primary particles is given by a polynomial of third order

$$C_\mu = p_0 + p_1 \cdot \lg\, N_\mu^{true} + p_2 \cdot (\lg\, N_\mu^{true})^2 + p_3 \cdot (\lg\, N_\mu^{true})^3. \tag{B.14}$$

| parameter | value | error |
|---|---|---|
| $p_0$ | −4.481 | 0.592 |
| $p_1$ | 2.476 | 0.330 |
| $p_2$ | −0.446 | 0.061 |
| $p_3$ | 0.0264 | 0.0037 |

Table B.18: Parameters of the systematic deviation of $\lg\, N_\mu^{rec.}$ and $\lg\, N_\mu^{true}$ for hydrogen.

| parameter | value | error |
|---|---|---|
| $p_0$ | 4.885 | 0.652 |
| $p_1$ | 2.694 | 0.361 |
| $p_2$ | −0.4854 | 0.0663 |
| $p_3$ | 0.02873 | 0.00403 |

Table B.19: Parameters of the systematic deviation of lg $N_\mu^{rec.}$ and lg $N_\mu^{true}$ for helium.

| parameter | value | error |
|---|---|---|
| $p_0$ | −6.259 | 0.622 |
| $p_1$ | 3.426 | 0.338 |
| $p_2$ | −0.6139 | 0.0609 |
| $p_3$ | 0.03616 | 0.00362 |

Table B.20: Parameters of the systematic deviation of lg $N_\mu^{rec.}$ and lg $N_\mu^{true}$ for carbon.

| parameter | value | error |
|---|---|---|
| $p_0$ | −7.98 | 0.62 |
| $p_1$ | 4.381 | 0.333 |
| $p_2$ | −0.7891 | 0.0594 |
| $p_3$ | 0.04679 | 0.00350 |

Table B.21: Parameters of the systematic deviation of lg $N_\mu^{rec.}$ and lg $N_\mu^{true}$ for silicon.

| parameter | value | error |
|---|---|---|
| $p_0$ | −7.539 | 0.661 |
| $p_1$ | 4.117 | 0.355 |
| $p_2$ | −0.7382 | 0.0630 |
| $p_3$ | 0.04359 | 0.00370 |

Table B.22: Parameters of the systematic deviation of lg $N_\mu^{rec.}$ and lg $N_\mu^{true}$ for iron.

**Distribution of the reconstruction uncertainties**

The parameters $m_1$, $m_2$ and $m_3$ of Equation 6.9 describe the distribution of the reconstruction uncertainties. For muon numbers above $10^{5.2}$ the asymmetric function passes into a Gaussian function with parameters $m_1$ and $m_2$.

$$m_1(N_\mu^{true}) = p_0 + p_1 \cdot \lg N_\mu^{true} + p_2 \cdot (\lg N_\mu^{true})^2 + p_3 \cdot (\lg N_\mu^{true})^3. \tag{B.15}$$

| parameter | value | error |
|---|---|---|
| $p_0$ | 2.075 | 0.291 |
| $p_1$ | −1.029 | 0.159 |
| $p_2$ | 0.1693 | 0.0286 |
| $p_3$ | −0.00925 | 0.00171 |

Table B.23: Parameterization of the parameter $m_1$ (valid for all primary particles).

$$m_2(N_\mu^{true}) = p_0 + p_1 \cdot \lg N_\mu^{true} + p_2 \cdot (\lg N_\mu^{true})^2 + p_3 \cdot (\lg N_\mu^{true})^3. \tag{B.16}$$

| parameter | value | error |
|---|---|---|
| $p_0$ | 2.062 | 0.217 |
| $p_1$ | −0.8368 | 0.1177 |
| $p_2$ | 0.117 | 0.0212 |
| $p_3$ | −0.005579 | 0.001260 |

Table B.24: Parameterization of the parameter $m_2$ (valid for all primary particles).

$$m_3(N_\mu^{true}) = p_0 + p_1 \cdot \lg N_\mu^{true} + p_2 \cdot (\lg N_\mu^{true})^2. \tag{B.17}$$

| parameter | value | error |
|---|---|---|
| $p_0$ | 2.19 | 0.45 |
| $p_1$ | −0.7095 | 0.1882 |
| $p_2$ | 0.05718 | 0.01956 |

Table B.25: Parameterization of the parameter $m_3$ (valid for all primary particles).

# Appendix C

# Efficiencies

The efficiencies are parameterized according to

$$\epsilon(\lg N_e^{true}, \lg N_\mu^{tr.,true}) = \mathrm{erf}\left(\frac{\lg N_e - p_0}{p_1}\right) \cdot \mathrm{erf}\left(\frac{\lg N_\mu^{tr.} - p_2}{p_3}.\right) \tag{C.1}$$

In case of KASCADE the parameters $p_0$ and $p_1$ are only determined for hydrogen and then fixed for all other primary particles. For KASCADE-Grande all parameters are determined with the help of a fit and instead of the truncated muon number $\lg N_\mu^{tr.,true}$ the total number of muons $\lg N_\mu^{true}$ is used.

## C.1 KASCADE, QGSJETII/FLUKA

| parameter | value | error |
|---|---|---|
| $p_0$ | 2.110 | 0.127 |
| $p_1$ | 2.155 | 0.039 |
| $p_2$ | 5.876 | 0.124 |
| $p_2$ | 3.759 | 0.002 |

Table C.1: Parameters of the two-dimensional efficiency for hydrogen.

| parameter | value | error |
|---|---|---|
| $p_0$ | 2.110 | 0.127 |
| $p_1$ | 2.155 | 0.039 |
| $p_2$ | 5.876 | 0.124 |
| $p_2$ | 3.759 | 0.002 |

Table C.2: Parameters of the two-dimensional efficiency for hydrogen.

| parameter | value | error |
|---|---|---|
| $p_0$ | 2.110 | 0 |
| $p_1$ | 2.155 | 0 |
| $p_2$ | 6.329 | 0.112 |
| $p_2$ | 3.761 | 0.002 |

Table C.3: Parameters of the two-dimensional efficiency for helium.

| parameter | value | error |
|---|---|---|
| $p_0$ | 2.110 | 0 |
| $p_1$ | 2.155 | 0 |
| $p_2$ | 6.410 | 0.106 |
| $p_2$ | 3.763 | 0.002 |

Table C.4: Parameters of the two-dimensional efficiency for carbon.

| parameter | value | error |
|---|---|---|
| $p_0$ | 2.110 | 0 |
| $p_1$ | 2.155 | 0 |
| $p_2$ | 6.870 | 0.115 |
| $p_2$ | 3.776 | 0.002 |

Table C.5: Parameters of the two-dimensional efficiency for silicon.

| parameter | value | error |
|---|---|---|
| $p_0$ | 2.110 | 0 |
| $p_1$ | 2.155 | 0 |
| $p_2$ | 6.489 | 0.117 |
| $p_2$ | 3.801 | 0.204 |

Table C.6: Parameters of the two-dimensional efficiency for iron.

## C.2 KASCADE-Grande, QGSJETII/FLUKA

| parameter | value | error |
|---|---|---|
| $p_0$ | 3.891 | 0.177 |
| $p_1$ | 4.280 | 0.005 |
| $p_2$ | 3.249 | 0.065 |
| $p_2$ | 5.439 | 0.005 |

Table C.7: Parameters of the two-dimensional efficiency for hydrogen.

| parameter | value | error |
|---|---|---|
| $p_0$ | 4.266 | 0.175 |
| $p_1$ | 4.409 | 0.005 |
| $p_2$ | 3.392 | 0.131 |
| $p_2$ | 5.371 | 0.007 |

Table C.8: Parameters of the two-dimensional efficiency for helium.

| parameter | value | error |
|---|---|---|
| $p_0$ | 3.865 | 0.189 |
| $p_1$ | 4.468 | 0.007 |
| $p_2$ | 3.698 | 0.170 |
| $p_2$ | 5.336 | 0.008 |

Table C.9: Parameters of the two-dimensional efficiency for carbon.

| parameter | value | error |
|---|---|---|
| $p_0$ | 4.720 | 0.315 |
| $p_1$ | 4.492 | 0.009 |
| $p_2$ | 3.341 | 0.106 |
| $p_2$ | 5.343 | 0.008 |

Table C.10: Parameters of the two-dimensional efficiency for silicon.

| parameter | value | error |
|---|---|---|
| $p_0$ | 5.918 | 0.273 |
| $p_1$ | 4.541 | 0.008 |
| $p_2$ | 3.111 | 0.088 |
| $p_2$ | 5.308 | 0.008 |

Table C.11: Parameters of the two-dimensional efficiency for iron.

# Appendix D

# Weighted mean squared error WMSE

## D.1 KASCADE

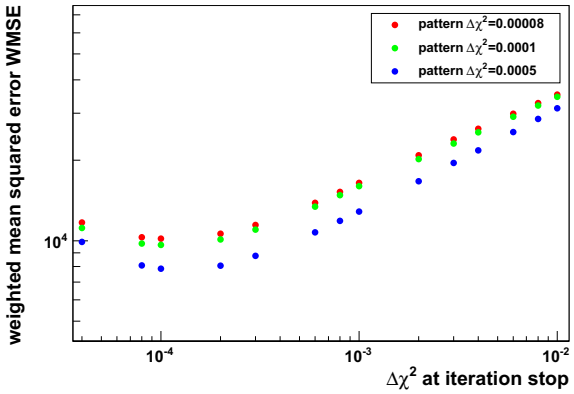


Figure D.1: Weighted mean squared error for three different patterns for QGSJET01 and FLUKA.

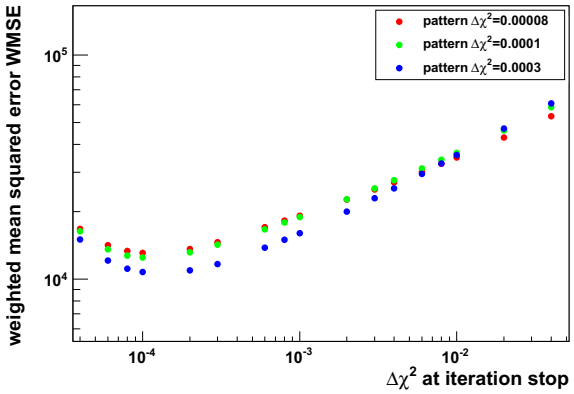


Figure D.2: Weighted mean squared error for three different patterns for EPOS1.99 and FLUKA.

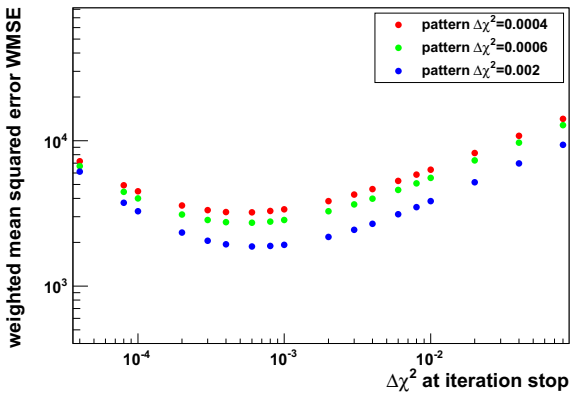


Figure D.3: Weighted mean squared error for three different patterns for QGSJETII and FLUKA.

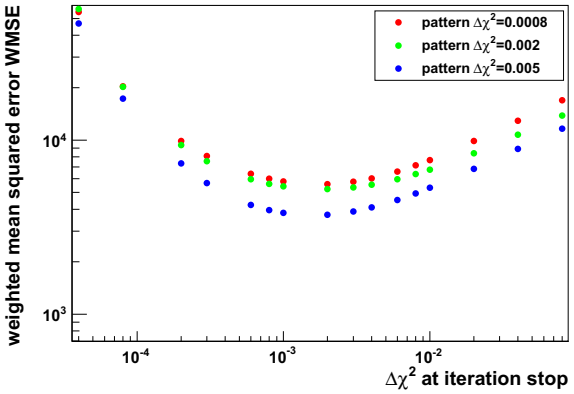


Figure D.4: Weighted mean squared error for three different patterns for SIBYLL and FLUKA.

## D.2 Grande

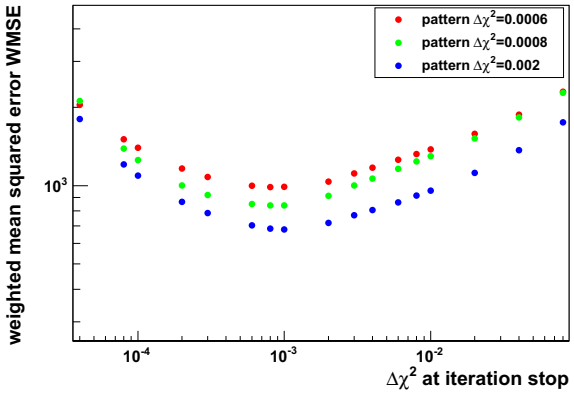


Figure D.5: Weighted mean squared error for three different patterns for QGSJETII and FLUKA.

# Appendix E

# Data description for KASCADE

## E.1 EPOS1.99 and FLUKA

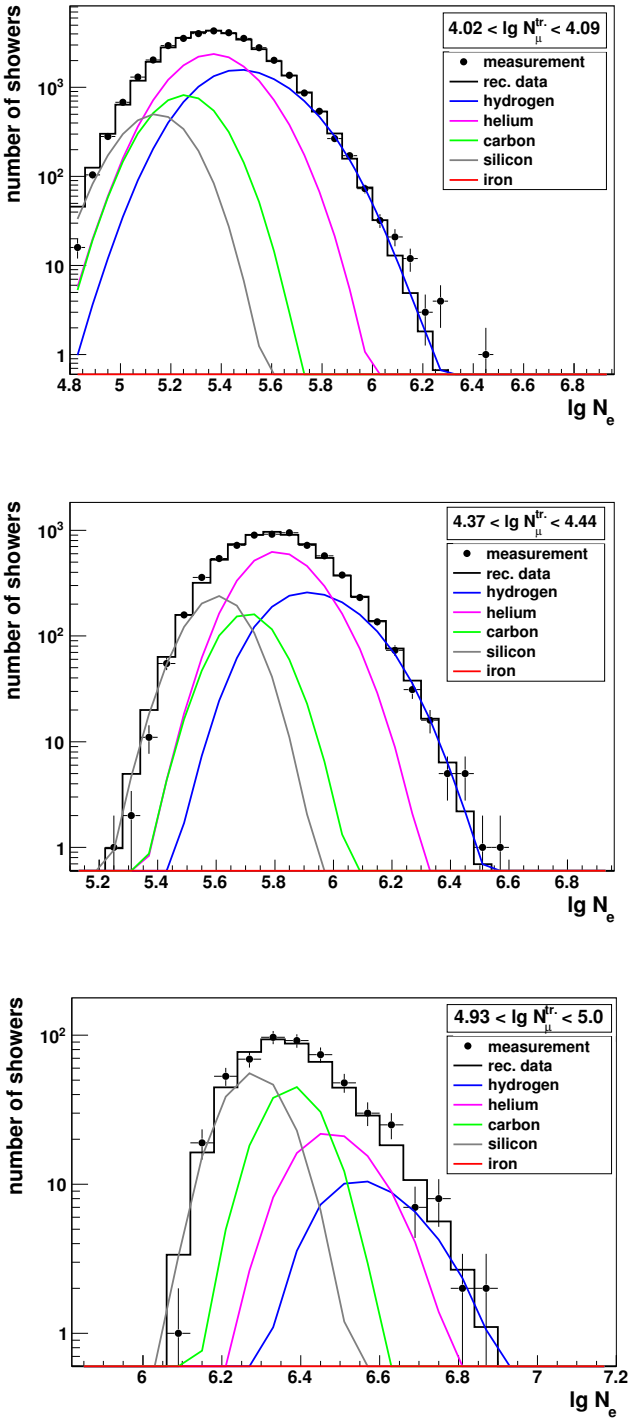


Figure E.1: Projection along the lg $N_\mu^{tr.}$-axis of the two dimensional size spectra of electron and muon numbers for different lg $N_\mu^{tr.}$ intervals. Plotted are the lg $N_e$ distributions of measured showers (dots) and via forward folding reconstructed showers (lines).

## E.2 QGSJETII and FLUKA

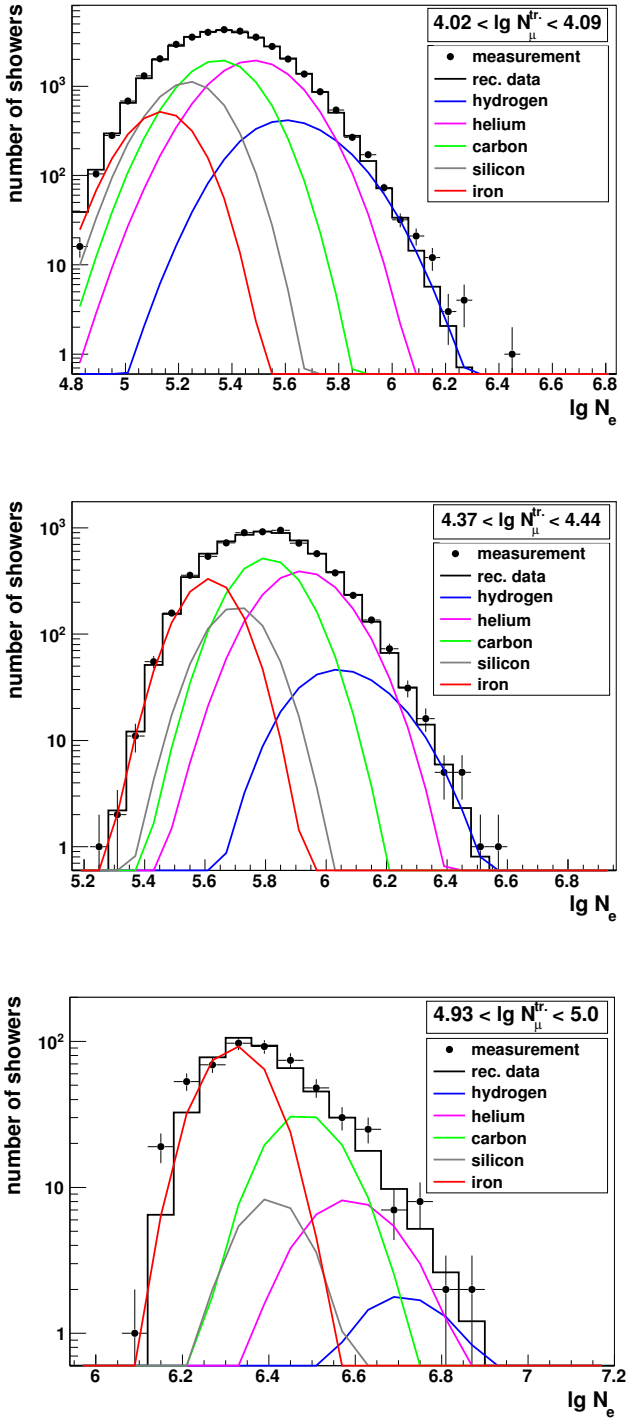


Figure E.2: Projection along the lg $N_\mu^{tr.}$-axis of the two dimensional size spectra of electron and muon numbers for different lg $N_\mu^{tr.}$ intervals. Plotted are the lg $N_e$-distributions of measured showers (dots) and via forward folding reconstructed showers (lines).

## E.3 SIBYLL and FLUKA

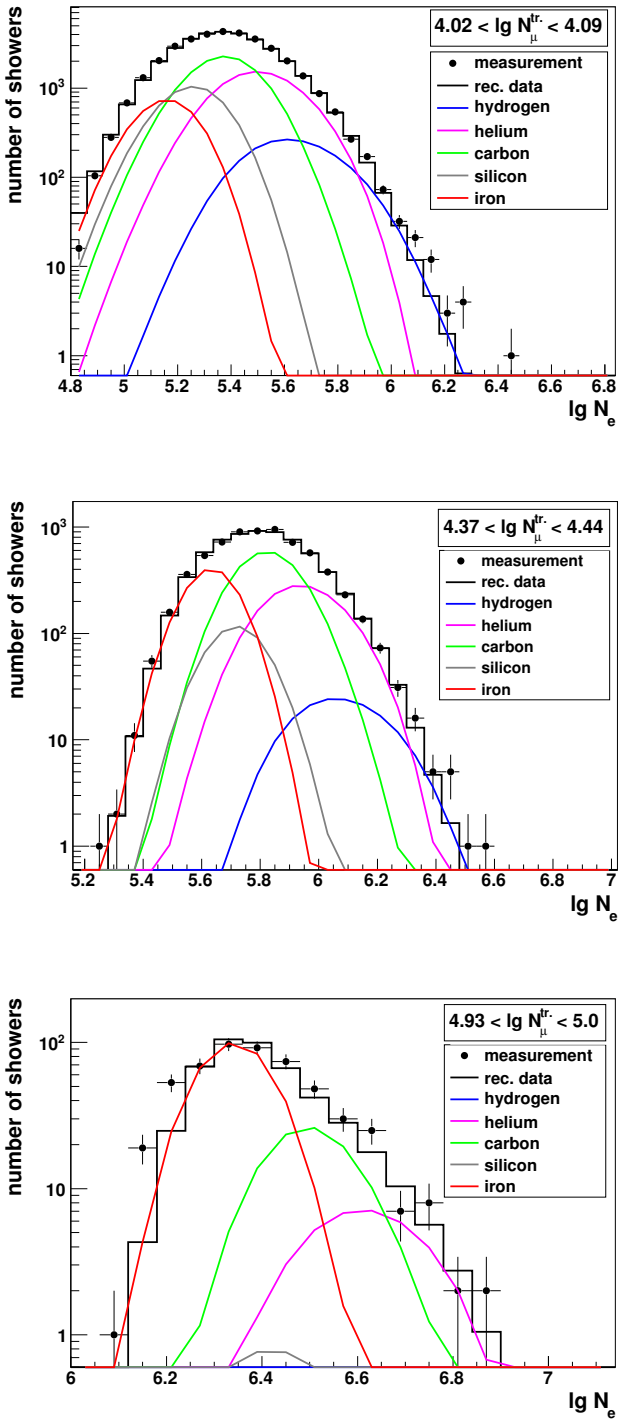


Figure E.3: Projection along the lg $N_\mu^{tr.}$-axis of the two dimensional size spectra of electron and muon numbers for different lg $N_\mu^{tr.}$ intervals. Plotted are the lg $N_e$-distributions of measured showers (dots) and via forward folding reconstructed showers (lines).

# Bibliography


[Abb08] R.U. Abbasi et al., Phys. Rev. Lett. **100** (2008) 101101.

[Abr08] J. Abraham, Phys. Rev. Lett. **101** (2008) 61101.

[Abr08a] J. Abraham et al., Astropart. Phys., **29** (2008) 243.

[Abu01] T. Abu-Zayyad et al., Astrophys. J. **557** (2001) 686

[Agl99] M. Aglietta et al., Astropart. Phys., **10** (1999) 1.

[Ago95] G. D'Agostini, Nucl. Instr. and Meth. A, **362** (1995) 487.

[Ame96] M. Amenomori et al., Astrophys. J., **46** (1996) 408.

[Ant03] T. Antoni et al., Nucl. Instr. and Meth. A, **513** (2003) 490.

[Ant04] T. Antoni et al., Astrophys. J., **612** (2004) 914.

[Ant05] T. Antoni et al., Astropart. Phys. **24** (2005) 1.

[Ant06] T. Antoni et al., Astropart. Phys., **24** (2006) 467.

[Ape09] W.D. Apel et al., Astropart. Phys. **31** (2009) 86.

[Ape10] W.D. Apel et al., Nucl. Instr. and Meth. A, **620** (2010) 202.

[Ave03] M. Ave et al., Astropart. Phys. **19** (2003) 47.

[Ave08] M. Ave et al., Phys. Rev. Lett. **100** (2008) 101101.

[Bas98] S.A. Bass et al., Prog. Part. Nucl. Phys. **41** (1998) 225.

[Ber99] E.G. Berezhko and L.T. Ksenofontov, JETP 89, **3** (1999) 391.

[Ber07] D.R. Bergmann and J.W. Belz, J. Phys. G:Nucl. Part Phys. **24** (2007) R359.

[Bir93] D.J. Bird et al., Phys. Rev. Lett. **71** (1993) 3401.

[Bir94] D.J. Bird et al., Astrophys. J. **424** (1994) 491.

[Blu09] J. Bluemer, R. Engel, and J. R. Hoerandel, Prog. Part. Nucl. Phys. **63** (2009) 293.

[GEA93] Cern Software Division, GEANT Detektor Description and Simulation Tool, Cern Program Library Long Writeup **W5013**, 1993.

[Can02] J. Candia et al., Astropart. Phys. **17** (2002) 23.

[Cap89] J.N. Capdevielle, J. Phys. G: Nucl. Part. Phys. **15** (1989) 909.

[Che86] K. S. Cheng, C. Ho and M. Ruderman, Ap. J. **300** (1986) 500.

[Cit33] P.H. van Cittert, Z. Phys. **69** (1933) 298.

[Cow98] G. Cowan, *Statistical Data Analysis*; Oxford University Press (1998).

[Cow73] R. Cowsik and L. Wilson, Proc. 13th Int. Cosmic Ray Conf., Denver, **1** (1973) 577.

[Dar00] A. Dar, A. De Rújula, preprint astro-ph/0008474.

[Der05] V.A. Derbina et al, Astrophys. J., **628** (2005) L41.

[Dol02] P. Doll et al, Nucl. Instr. and Meth. A, **488** (2002) 517.

[Dov01] M.T. Dova et al., preprint astro-ph/0112191.

[Dre99] H.J. Drescher, M. Hladik, S.S. Ostapchenko and K. Werner, J. Phys. G: Nucl. Part. Phys. **25** (1999) L91.

[Eng99] R. Engel, T.K. Gaisser, P. Lipari and T. Stanev, Proc. $26^{th}$ Int. Cosmic ray Conf., Salt Lake City (USA), **1** (1999) 415.

[Eng99a] J. Engler et al., Nucl. Instr. and Meth. A, **427** (1999) 528.

[Ent11] David d'Enterria, R. Engel, T. Pierog, S. Ostapchenko and K. Werner, Constraints from the first LHC data on hadronic event generators for ultra-high energy cosmic-ray physics, 2011, arXiv:astro-ph.HE/1101.5596.

[Erl01] A.D. Erlykin and A. W. Wolfendale, J. Phys. G: Nucl. Part. Phys. **27** (2001) 1005.

[Fas00] A. Fassò et al., FLUKA: Status and Prospective for Hadronic Applications, in: A. Kling et al. (Eds.), Proceedings of the Monte Carlo 2000 Conference, Lisbon, October 23-26, 2000, Springer, Berlin, vol. 955, 2001, Available from: <http://www.fluka.org>.

[Fes85] H. Fesefeldt, Report **PITHA-85/02** (1985), RWTH Aachen.

[Fle94] R. S. Fletcher, T. K. Gaisser, P. Lipari and T. Stanev; Phys. Rev. **D50** (1994) 5710.

[Gai90] T. K. Gaisser, Cosmic Rays and Particle Physics, Cambridge University Press, Cambridge (1990).

[Gin80] V. L. Ginzburg, Y. M. Khazan and V. S. Ptuskin, Astr. Space Sci. **68** (1980) 295.

[Gar08] A.P. Garyaka et al., J. Phys. G: Nucl. Part. Phys. **35** (2008) 115201.

[Gol64] R. Gold Argonne National Laboratory Report ANL-6984; Argonne (1964).

[Gre66] K. Greisen, Phys. Rev. **16** (1966) 748.

[Gri90] N.L. Grigorov, Sov. J. Nucl. Phys. **51** (1990) 99.

[Hau03] A. Haungs, J. Phys. G: Nucl. Part. Phys. **29** (2003) 809.

[Hec98] D. Heck et al., FZK-Bericht 6019, Forschungszentrum Karlsruhe (1998).

[Hil81] A.M. Hillas, Proc. 17th Int. Cosmic Ray Conf., Paris, **8** (1981) 193.

[Hil97] A.M. Hillas, Nucl. Phys. B (Proc. Suppl.) **52B** (1997) 29.

[Hil04] A.M. Hillas, Nucl. Phys. B (Proc. Suppl.) **136** (2004) 139.

[Hil05] A.M. Hillas, J. Phys. G: Nucl. Part. Phys. **31** (2005) R95.

[Hör04] J.R. Hörandel, Astropart. Phys. **21** (2004) 241.

[Kal93] N.N. Kalmykov and S.S. Ostapchenko, Yad. Fiz. **56** (1993) 105.

[Kam57] K. Kamata and J. Nishimura, Suppl. Prog. Theo. Phys. **4** (1957) 93.

[Kan01] D. Kazanas and A. Nicolaidis, preprint astro-ph/0103147.

[Kan01a] D. Kazanas and A. Nicolaidis, preprint astro-ph/0109247.

[Kla97] H.V. Klapdor-Kleingrothaus and K. Zuber, Teilchenastrophysik (1997), B.G. Teubner Stuttgart, Stuttgart 1997.

[Kra96] H. Krawczynski et al., Nucl. Instr. Meth. **A383** (1996) 431.

[Kob02] K. Kobayakawa et al., Phys. Rev. D **66** (2002) 083004.

[Kri92] W. Kriegleder, KfK-Bericht 5023, Kernforschungszentrum Karlsruhe (1992).

[Kul58] G.V. Kulikov and G. B. Khristiansen, Zh. Eksp. Teor. Fiz. 35 (1958) 635.

[Lag01] A.A. Lagutin et al., Nucl. Phys. B (Proc. Suppl.) **97** (2001) 267;
Proc. 27th Int. Cosmic Ray Conf., Hamburg **5** (2001) 1896 and 1900.

[Lag01a] A.A. Lagutin et al., Nucl. Phys. B (Proc. Suppl.) **97** (2001) 274.

[Law91] M.A Lawrence,R. J. O. Reid and A. A. Watson, J. Phys. G: Nucl. Part. Phys. **17** (1991) 733.

[Mai03] G. Maier, Dissertation **2003** Universität Karlsruhe.

[May92] H.J. Mayer, Nucl. Instr. and Meth. **A317** (1992) 339.

[May93] H.J. Mayer, Nucl. Instr. and Meth. **A330** (1993) 339.

[Mül03] M. Müller, FZK-Bericht 6912, Forschungszentrum Karlsruhe (2003).

[Nag84] M. Nagano et al., J. Phys. G: Nucl. Part. Phys. **10** (1984) 1295.

[Nag92] M. Nagano et al., J. Phys. G: Nucl. Part. Phys. **18**(1992) 423

[Nel85] W.R. Nelson, H. Hirayama and D.W.O. Rogers, Report SLAC 265, Stanford Linear Accelerator Center (1985).

[Ogi03] S. Ogio and F. Kakimoto, Proc. 28th Int. Cosmic Ray Conf., Tsukuba **1** (2003) 315.

[Ost06] S.S. Ostapchenko, Nucl. Phys. B (Proc. Suppl.) **151** (2006) 143.

[Pan09] A.D. Panov, Bulletin of the Russian Academy of Sciences: Physics, 2009, **73** (2009) 564.

[Phi62] D.L. Phillips, J. ACM **9** (1962) 84.

[Pla02] R. Plaga, New Astronomy **7** (2002) 317.

[Ptu93] V.S. Ptuskin et al., Astron. & Astroph. **268** (1993) 726.

[Rou03] R. Roulet, preprint astro-ph/0310367.

[Ran95] J. Ranft, Phys. Rev. **D51** (1995) 64.

[Ran95] I.L. Rasmussen and B. Peters, Nature **258** (1975) 412.

[Sch96] H. Schieler, Development and test of the local data acquisition system for the structured detector array of the KASCADE experiment. Doktorarbeit, Universit"at Karlsruhe, 1996.

[Sha70] M.M. Shapiro and M. Silberberg, Ann. Rev. Nucl. Part. Sci. **20** (1970) 323.

[Sha48] C.E. Shannon, Bell Sys. Tech. J. **27** (1948) 379.

[Sig03] G. Sigl, Annals Phys. **303** (2003) 117.

[Sta93] T. Stanev et al., Astron. & Astroph. **274** (1993) 902.

[Sve03] L. G. Sveshnikova, Astron. & Astroph. **409** (2003) 799.

[Swo95] S. P. Swordy, Proc. 24th Int. Cosmic Ray Conf., Rome, **2** (1995) 697.

[Tak98] Y. Takahashi, Nucl. Phys. B (Proc. Suppl.) **60B** (1998) 82.

[Tka01] W. Tkaczyk, Proc. 27th Int. Cosmic Ray Conf., Hamburg, **5** (2001) 1979;
S. Karakula and W. TKaczyk, Astropart. Phys. **1** (1993) 229.

[Tik63] A.N. Tikhonov, Sov. Math **5** (1963) 1035.

[Van06] J. van Buren, Investigations of the Muon Component of Extensive Air Showers measured by KASCADE-Grande. PhD thesis, Universität Karlsruhe, 2006.

[Völ92] G. Völker, KfK-Bericht 4983, Kernforschungszentrum Karlsruhe (1992).

[Völ03] H.J. Völk and V.N. Zirakashvili, Proc. 28th Int. Cosmic Ray Conf., Tsukuba **4** (2003) 2031.

[Web99] J. Weber, FZK-Bericht 6339, Forschungszentrum Karlsruhe (1999).

[Wei06] K. Weiglein, Phys. Report **426** (2006) 47.

[Wer93] K. Werner, Phys. Report **232** (1993) 87.

[Wer08] K. Werner, Nucl. Phys. B (Proc. Suppl.) **175-176** (2008) 81.

[Zat66] V.I. Zatsepin and V.A. Kuz'min, JETP **4** (1966) 78.

# Danksagung

An dieser Stelle möchte ich allen danken, die zum Gelingen dieser Arbeit beigetragen haben, d.h. allen Mitgliedern der KASCADE-Grande Kollaboration sowie allen Technikern.

Ich danke Herrn Prof. Dr. Johannes Blümer für die Übernahme des Referats und die Ermöglichung dieser Arbeit am Institut für Kernphysik.

Des Weiteren möchte ich Herrn Prof. Dr. Wim de Boer danken, der sich zur Übernahme des Korreferats bereit erklärt hat.

Ein besonderer Dank gilt Herrn Dr. Andreas Haungs, der mit vielen Rätschlägen und ständigem Interesse an dieser Arbeit sehr zum Gelingen selbiger beigetragen hat.

Weiterhin danke ich allen Kolleginnen und Kollegen:

- Frau Dr. Donghwa Kang, Herrn Dipl. Phys. Michael Wommer, Herrn Dr. Paul Doll, Herrn Dr. Jürgen Wochele, Herrn Dr. Harald Schieler, Herrn Dipl. Phys. Andreas Weindl und Herrn Dr. Joachim Engler für die ständige Hilfs- und Diskussionsbereitschaft.
- Frau Dr. Doris Wochele, Herrn Dr. Wolf-Dieter Apel, Herrn Dr. Klaus Bekk und Herrn Thomas Csabo für die Unterstützung bei computerbezogenen Problemen.
- Frau Sabine Bucher und Frau Brigitte Gering für die Hilfe bei organisatorischen und verwaltungstechnischen Dingen.

Ganz besonders möchte ich mich bei meiner Familie und meinen Freunden für die ständige Unterstützung bedanken.